

FAKULTÄT FÜR BAUINGENIEUR-
UND VERMESSUNGSWESEN

Reprocessing of a global GPS network

Dissertation
von

Peter Steigenberger



TECHNISCHE UNIVERSITÄT MÜNCHEN

Technische Universität München

Institut für Astronomische und Physikalische Geodäsie

Reprocessing of a global GPS network

Peter Steigenberger

Vollständiger Abdruck der von der Fakultät für Bauingenieur- und Vermessungswesen der Technischen Universität München zur Erlangung des akademischen Grades eines

Doktor – Ingenieurs

genehmigten Dissertation.

Vorsitzender: Univ.-Prof. Dr.-Ing. habil. Th. Wunderlich

Prüfer der Dissertation:

1. Univ.-Prof. Dr. phil. nat. U. Hugentobler
2. Univ.-Prof. Dr. phil. nat. habil. M. Rothacher,
Eidgenössische Technische Hochschule Zürich, Schweiz
3. a.o. Prof. Dr. techn. Robert Weber,
Technische Universität Wien, Österreich

Die Dissertation wurde am 08.04.2009 bei der Technischen Universität München eingereicht und durch die Fakultät für Bauingenieur- und Vermessungswesen am 23.06.2009 angenommen.

Abstract

Scientific applications of the Global Positioning System (GPS) in geosciences have attained an important position during the past 15 years. The analysis centers of the International GNSS Service (IGS) process observations of global GPS networks on a regular basis in near real-time in order to determine, e.g., satellite orbits and station coordinates. The models and strategies applied for this processing have been significantly improved since the official start of the IGS in 1994. Therefore, the long time series of GPS-derived parameters are degraded by discontinuities and inconsistencies. Changes in the definition of the geodetic datum further decrease the consistency of these time series. Thus, a geophysical interpretation of such series is difficult and questionable.

This problem can only be overcome by a complete reprocessing of the raw GPS observation data. For this thesis, observations of a global GPS network have been homogeneously reprocessed with the Bernese GPS Software for a time period of more than 11 years. Consistent station coordinates, troposphere and ionosphere parameters as well as satellite orbits and Earth orientation parameters have been estimated with different temporal resolutions. First, the theoretical background and the processing strategy for global GPS solutions are discussed. To avoid misinterpretations a proper detection of outliers, discontinuities and systematic effects is essential. The presence of the latter is sometimes more evident in the reprocessed than in the inconsistent time series due to the homogeneity of the solution.

The second part of the thesis focusses on selected results of the reprocessing. The general results are sorted by the different parameter types: station coordinates and velocities, troposphere zenith delays and gradients, satellite orbits as well as Earth orientation parameters. The internal consistency of these parameters is evaluated by GPS/GPS co-locations, repeatabilities and overlap tests. Intra-technique comparisons with the Center for Orbit Determination in Europe (CODE) and IGS products document the benefits of a complete and homogeneous reprocessing. An independent validation of selected results is performed by comparisons with parameters determined by other space geodetic techniques such as VLBI (Very Long Baseline Interferometry) and SLR (Satellite Laser Ranging). The impact of important model improvements is demonstrated by comparing solutions with different troposphere mapping functions or antenna phase center models applied.

Zusammenfassung

Die wissenschaftliche Nutzung des Global Positioning System (**GPS**) hat innerhalb der letzten 15 Jahre eine bedeutende Stellung innerhalb der Geowissenschaften erlangt. Die Rechenzentren des International **GNSS** Service (**IGS**) verarbeiten Beobachtungen globaler Stationsnetze jeweils zeitnah. Dabei werden beispielsweise Satellitenbahnen und Stationskoordinaten bestimmt. Die hierfür verwendeten Modelle und Auswertestrategien wurden seit der Gründung des **IGS** im Jahre 1994 laufend verbessert. Aufgrund dieser Änderungen weisen Langzeitreihen der jeweils zeitnah aus **GPS** bestimmten Parameter Sprünge und Inkonsistenzen auf. Wechsel des zugrunde liegenden Referenzrahmens führen zu einer weiteren Verschlechterung der Konsistenz. Eine geophysikalische Interpretation dieser Zeitreihen ist daher schwierig oder gar fragwürdig.

Abhilfe kann hier lediglich eine komplette Neuverarbeitung der **GPS**-Beobachtungsdaten schaffen. Für die vorliegende Arbeit wurden originäre **GPS**-Beobachtungen eines globalen Stationsnetzes aus einem Zeitraum von mehr als 11 Jahren mit der Bernese **GPS** Software homogen reprozessiert. Dabei wurden Stationskoordinaten, Troposphären- und Ionosphärenparameter, Satellitenbahnen sowie Erdorientierungsparameter mit unterschiedlicher zeitlicher Auflösung bestimmt. Zunächst werden die hierzu benötigten theoretischen Grundlagen sowie die verwendete Auswertestrategie erläutert. Um Fehlinterpretationen zu vermeiden wurde eine sorgfältige Suche nach Ausreißern, Diskontinuitäten und systematischen Effekten vorgenommen. Es zeigte sich, daß letztere zum Teil auch in den reprozessierten Zeitreihen auftreten und sich infolge deren Homogenität sogar deutlicher äußern als in inkonsistenten Zeitreihen.

Im zweiten Teil der Arbeit werden ausgewählte Ergebnisse der Reprozessierung diskutiert. Diese sind nach den verschiedenen Parametertypen geordnet: Stationskoordinaten und -geschwindigkeiten, Troposphärenzenitverzögerungen und -gradienten, Satellitenbahnen sowie Erdorientierungsparameter. Die interne Konsistenz dieser Parameter wird durch **GPS/GPS**-Kokationen, Wiederholbarkeiten und Überlappungstests belegt. Vergleiche mit **GPS**-Lösungen des Center for Orbit Determination in Europe (**CODE**) und des **IGS** veranschaulichen die Vorzüge einer vollständigen und homogenen Neuverarbeitung der Daten. Eine unabhängige Validierung ausgewählter Resultate erfolgt überdies durch Vergleiche mit Lösungen der geodätischen Raumverfahren **VLBI** (Very Long Baseline Interferometry) und **SLR** (Satellite Laser Ranging). Der Einfluß wichtiger Modellverbesserungen wird anhand der Auswirkungen unterschiedlicher Troposphären-Mappingfunktionen sowie verschiedener Modelle für die Phasenzentren der **GPS**-Sende- und Empfangsantennen dargelegt.

Contents

1. Introduction	1
1.1. The International GNSS Service	1
1.2. Motivation	3
1.3. Subject of the Thesis	5
I. Global GPS Solutions	7
2. Modeling of GPS Observations	8
2.1. The Global Positioning System Space Segment	8
2.2. GPS Observables	10
2.3. Ambiguity Resolution	13
2.4. Station Coordinates and Velocities	13
2.5. Atmospheric Refraction	16
2.6. Satellite Orbits	21
2.7. Earth Orientation Parameters	26
2.8. Antenna Phase Center Variations and Offsets	27
2.9. Other Parameters and Effects	28
2.10. Basics of Least-Squares Adjustment	30
3. Data Processing	33
3.1. Modeling	33
3.2. Processing Strategy	35
4. Data	45
4.1. Tracking Station Network and Satellite Constellation	45
4.2. Detection of Outliers and Discontinuities	51
4.3. Other Systematic Effects	57
II. Reprocessing Results	61
5. Station Coordinates and Velocities	62
5.1. Coordinate Repeatabilities	62
5.2. GPS-GPS Co-locations	63
5.3. Reference Frame Solution	64
5.4. Time Series Solutions	68
6. Troposphere Parameters	73
6.1. Troposphere Zenith Delays	73
6.2. Troposphere Gradients	85
6.3. Impact of different Troposphere Modeling	88
7. Satellite Orbits	95
7.1. Formal Accuracy	95
7.2. Internal Consistency	96
7.3. Intra-Technique Comparisons	100
7.4. Validation with Satellite Laser Ranging	102
8. Earth Orientation Parameters	109
8.1. Earth Rotation Parameters with Daily Resolution	110

8.2. Subdaily Earth Rotation Parameters	118
8.3. Nutation Parameters	133
9. Antenna Phase Center Models and their Influence on Global GPS Solutions	138
9.1. Calibration of Receiver and Satellite Antennas	138
9.2. Effects on Global Solutions	139
10. Summary, Conclusions, and Outlook	153
III. Appendices	155
A. Datum Stations	156
B. Tracking Stations	158
C. Discontinuities in Coordinate Time Series	163
D. Subdaily ERP Model TUM05G	166
E. Nutation Model TUM05N	169
F. Abbreviations	172
Bibliography	176

1. Introduction

Scientific applications of Global Navigation Satellite Systems (GNSS) like the Global Positioning System (GPS) have attained an important position in geosciences during the past 15 years. Whereas the determination of precise satellite orbits and station coordinates in a global reference frame was the most important task in the first years, additional topics are of interest nowadays, e.g., monitoring of the Earth's rotation, remote sensing of the neutral atmosphere as well as of the ionosphere, time transfer and orbit determination for spacecrafts equipped with GPS receivers. Starting from the very beginning, the scientific community coordinated its GPS-related activities under the umbrella of an international organization, namely the International GNSS Service (IGS). As the development of scientific GPS applications is closely connected to the IGS, this introduction will briefly describe the history of the IGS as well as the resulting demand for the reprocessing of a global GPS network.

1.1. The International GNSS Service

The major motivation for the establishment of the IGS was the recognition that “the most demanding users of the GPS satellites, the geophysical community, were purchasing receivers in exceedingly large numbers and using them as more or less black boxes, using software packages which they did not completely understand, mainly for relative positioning. The observation as well as the subsequent data analyses were not based on common standards; thus the geodynamic interpretation of the results ... could not be trusted. Standards for equipment, site selection and preparation, data handling, data analysis, etc. were needed.” (Mueller, 1993).

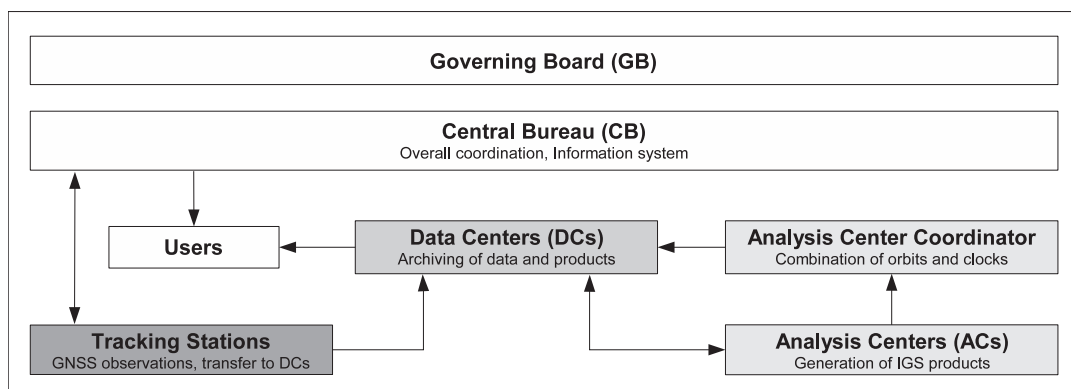


Fig. 1.1: Structure of the International GNSS Service (IGS).

These problems were discussed at the International Association of Geodesy (IAG) General Meeting in August 1989 in Edinburgh (Neilan *et al.*, 1989), and shortly after this meeting the IGS Planning Committee was established. After several meetings, the IGS Call for Participation to generate “precision GPS products in support of the international Earth science community” could be issued on 1 February 1991. In August 1991, at the 20th General Assembly of the International Union of Geodesy and Geophysics (IUGG) in Vienna, the exploration of the concept of the IGS within the following four years was recommended. From 21 June till 23 September 1992, an IGS Test Campaign was conducted as a proof of concept for the IGS: seven Analysis Centers (ACs) participated in this campaign, processing a network of about 30 stations. The resulting orbit accuracy was in the order of 50 cm (Beutler, 1993b). Starting with 1 November 1992, the IGS Pilot Service was established to bridge the gap until the start of the official service. In October 1993, it was decided to generate an official combined IGS orbit whose generation started on 5 December 1993. On 1 January 1994, the International GPS Service for Geodynamics started its activities as an official service of the IAG (Beutler *et al.*, 1994b).

Analysis Center	Abbrev.	Ultra-Rapid	Rapid	Final
Center for Orbit Determination in Europe	CODE	16.03.2000	30.06.1996	05.12.1993
European Space Operations Centre	ESOC	06.03.2000	30.06.1996	05.12.1993
GeoForschungsZentrum Potsdam	GFZ	05.03.2000	14.07.1996	05.12.1993
Jet Propulsion Laboratory	JPL	06.03.2000 – 28.03.2003	30.06.1996	05.12.1993
National Oceanic and Atmospheric Admin.	NOAA	–	18.08.1996	05.12.1993
National Resources Canada	NRCan	26.03.2000	07.07.1996	05.12.1993
Scripps Institute of Oceanography	SIO	05.03.2000	07.07.1996	05.12.1993
United States Naval Observatory	USNO	30.03.2000	27.04.1997	–
Massachusetts Institute of Technology	MIT	–	–	12.11.2003
Geodetic Observatory Pecny	GOP	06.01.2004	–	–

Tab. 1.1: Start (and end) dates of the [IGS](#) analysis center’s contributions to the Ultra-Rapid, Rapid and Final products.

The Terms of Reference¹ specify the objectives of the [IGS](#): the primary objective is the support (through [GNSS](#) data products) of geodetic and geophysical research activities. The [IGS](#) collects, archives and distributes [GNSS](#) observation data sets by its Data Centers ([DCs](#)). The [ACs](#) use this data to generate their contributions to the combined [IGS](#) products (see Tab. 1.1) which are produced by the Analysis Center Coordinator ([ACC](#)). An overview of the structure of the [IGS](#) is given in Fig. 1.1.

The major task in the early years was the generation of precise satellite orbits to support geodetic and geophysical research activities, e.g., the monitoring of regions of tectonic interest. Over the years, the accuracy of the orbits has increased by an order of magnitude from about 50 cm before the start of the [IGS](#) to below 5 cm (see Fig. 1.2). On 1 January 1999, the name of the [IGS](#) was changed to International [GPS](#) Service. To account for the activities in processing [GLONASS](#) data and the future Galileo system, the [IGS](#) was renamed to International [GNSS](#) Service on 14 March 2005. More details on the history of the [IGS](#) are given in [Beutler \(1993a\)](#), [Beutler et al. \(1996\)](#), [Kouba et al. \(1998a\)](#), [Beutler et al. \(1999\)](#), [Mireault and Kouba \(1999\)](#), [Dow et al. \(2005\)](#) as well as [Moore and Neilan \(2005\)](#).

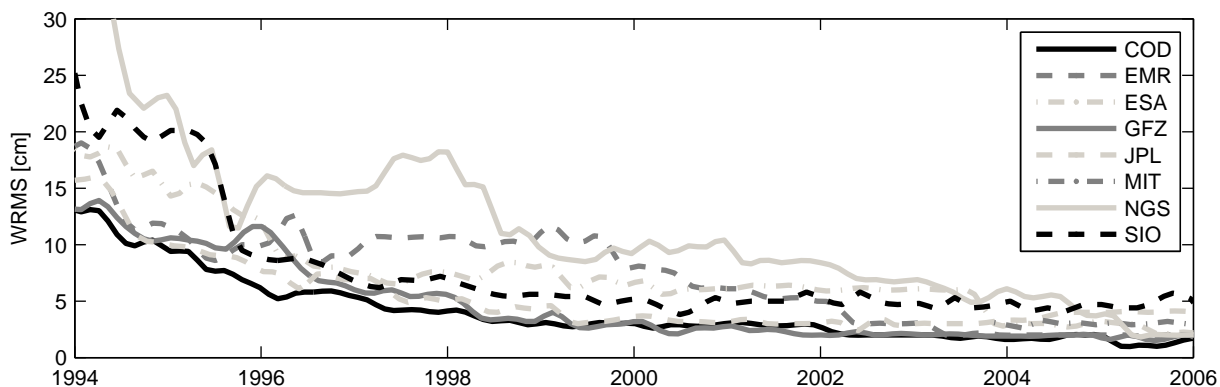
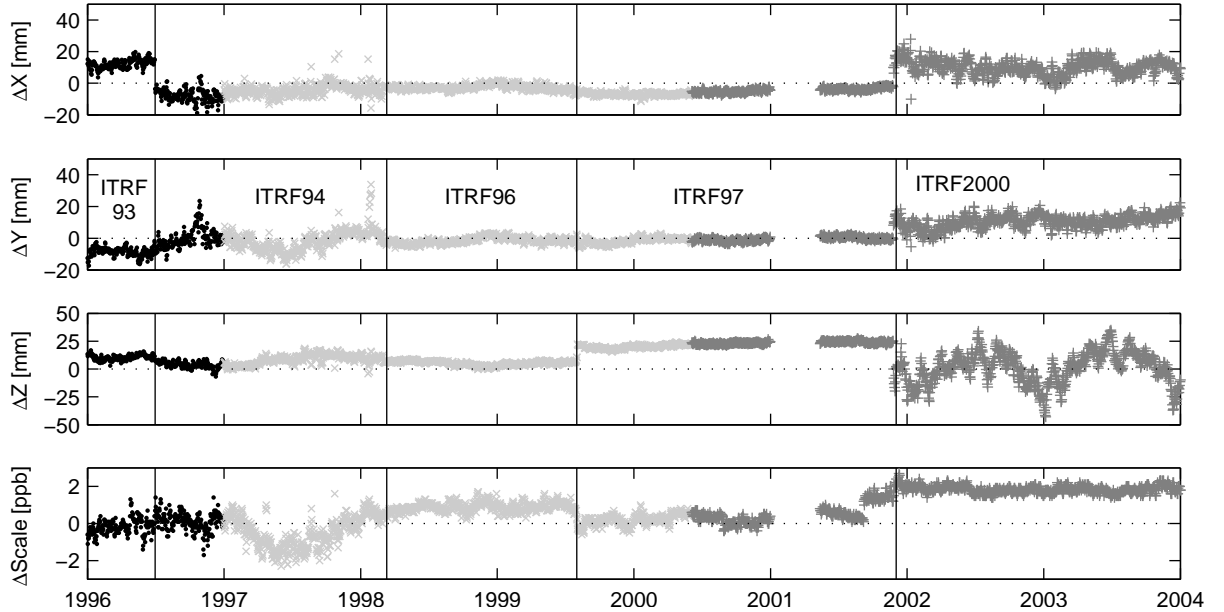


Fig. 1.2: Weighted [RMS](#) of the individual [IGS](#) analysis center solutions w.r.t. the [IGS](#) final orbits as given in the weekly orbit combination summary files (available at <ftp://cddis.gsfc.nasa.gov/pub/gps/products/>).

Whereas precise orbit determination was the major task of the [IGS](#) in the first years, the number of [GPS](#) applications has grown in the meantime: The dense tracking network provides a global access to the International Terrestrial Reference Frame ([ITRF](#)) and contributes to its improvement. Highly accurate station coordinates allow for the monitoring of deformations of the solid Earth and the detection of sea level variations. [GPS](#) receivers located at timing laboratories contribute to precise time and frequency transfer and a network of high-rate [GPS](#) stations supports the orbit determination of Low Earth Orbiters ([LEOs](#)). The refraction of the [GPS](#) signals in the atmosphere (originally seen as a disturbing effect) allows for the mapping of the ionosphere and the monitoring of the tropospheric water vapor content. These applications are also reflected in the increasing number of [IGS](#) products.

¹<http://igs.cb.jpl.nasa.gov/organization/bylaws.html>

The number of [IGS](#) tracking stations has increased from about 30 in the beginning to 384 in July 2008. The observation data of these tracking stations, stored in Receiver Independent Exchange ([RINEX](#)) format, is provided by global, regional and local [DCs](#) of the [IGS](#). Individual subnetworks of the [IGS](#) network are processed in near real-time by altogether ten [IGS ACs](#) (see [Tab. 1.1](#)). Three categories of products are generated by the [ACs](#) differing in latency and accuracy: ultra-rapid (delay of 3 hours, updated 4 times per day with an observed and a predicted half), rapid (delay of 17 hours) and final products (delay of 11 days). The Weighted [RMS](#) ([WRMS](#)) of the [ACs](#) contributing to the final orbit product (extracted from the final [IGS](#) orbit combination summaries) is shown in [Fig. 1.2](#).



[Fig. 1.3](#): Translations and scale differences of daily 7-parameter similarity transformations between [CODE](#) 3-day solutions and [ITRF2000](#). Reference frame changes are indicated by vertical lines. The symbols denote different internal solution types. Due to a data outage, the solutions for the beginning of 2001 are not available. Together with the last reference frame change the strategy for datum definition was changed. Instead of constraining a certain number of fiducial sites to their a priori coordinates, a no-net-rotation condition is used.

1.2. Motivation

Since the start of the [IGS](#) in 1994, the models and processing strategies of the [IGS ACs](#) have been continuously changed. As an example, important changes of the processing at the [CODE IGS AC](#) are listed in [Tab. 1.2](#). Although this list is long, it is by far not complete as smaller changes or changes that are assumed not to significantly change the results are not included. In addition, the realization of the terrestrial reference system has been changed four times (from [ITRF93](#) to [ITRF94](#), [ITRF96](#), [ITRF97](#), [ITRF2000](#)) during the time interval considered in [Tab. 1.2](#). As an example, [Fig. 1.3](#) shows the translations and the scale difference of the [CODE](#) 3-day solutions w.r.t. [ITRF2000](#). Discontinuities at all reference frame changes are evident. The last reference frame change is accompanied by a change of the type of datum definition: instead of constraining the coordinates of a number of fiducial sites to their a priori values, a No-Net-Rotation ([NNR](#)) condition w.r.t. these coordinates is used. Whereas reference frame changes can be overcome by a quite fast reprocessing of solutions based on variance-covariance information, changes in the modeling or parameterization require a complete reprocessing starting with the raw observation data to generate homogeneous results.

Although the importance of such [GPS](#) reprocessing activities was emphasized by several authors (e.g., [Angermann et al., 2005](#); [Ferland et al., 2005](#)), only a few attempts have already been completed. One example is the reprocessing performed by [Nikolaidis \(2002\)](#). However, this reprocessing is not completely homogeneous (small inconsistencies concerning ocean loading, pole tide and station-dependent weighting).

Changes in modeling, parameterization, processing	Date	
Constraints on pseudo-stochastic pulses changed	Oct	1994
Constraints on pseudo-stochastic pulses changed	Dec	1994
Change from ITRF92 to ITRF93	Jan	1995
Improved Earth shadow modeling	Mar	1995
Revised modeling of pseudo-stochastic pulses for eclipsing satellites	Apr	1995
Constraints on RPR parameters changed	May	1995
Correlations within the network clusters considered	Jun	1995
QIF ambiguity resolution	Jun	1995
Estimation of GIMs	Jan	1996
Pseudo-stochastic pulses for all satellites at 12:00 UT	Apr	1996
Change from ITRF93 to ITRF94	Jun	1996
Antenna phase center corrections for receivers	Jun	1996
Improved orbit model: gravity field, general relativity, Earth tide model, Love number	Jun	1996
Constraints on RPR parameters changed	Jul	1996
Constraints on RPR parameters changed	Aug	1996
IERS Conventions 1996	Oct	1996
Constraints on RPR parameters changed	Oct	1996
Conditions for arc-splitting changed	Sep	1997
Elevation cut-off angle: $20^\circ \Rightarrow 10^\circ$	Oct	1997
Elevation-dependent weighting	Oct	1997
Niell mapping function	Oct	1997
Change from ITRF94 to ITRF96	Mar	1998
Ocean loading implemented	Mar	1998
Changes in GIM estimation: height of single-layer, 2-hour resolution, reference frame	Apr	1998
Back-substitution of weekly coordinates and ERPs for final 3-day orbits	Oct	1998
Antenna offsets for Block IIR satellites corrected	Nov	1998
Change from ITRF96 to ITRF97	Aug	1999
Pseudo-stochastic pulses changed	Jun	2000
A priori delay mapped with the hydr. Niell mapping function (no a priori delay before)	Aug	2000
Estimated troposphere delay mapped with the wet Niell mapping function	Aug	2000
Considering of P1C1- DCBs for Melbourne-Wübbena ambiguity resolution	Oct	2000
Pseudo-stochastic pulses at day boundaries	Jun	2001
Estimation of troposphere gradients	Aug	2001
Elevation cut-off angle: $10^\circ \Rightarrow 3^\circ$	Aug	2001
Change from ITRF97 to ITRF2000	Dec	2001
Implementation of the Moon's shadow	Jan	2002
Refined ambiguity resolution	Mar	2002
Code-smoothing for Melbourne-Wübbena ambiguity resolution	Jul	2002
Ocean tide model for ocean loading: FES95.2 \Rightarrow GOT00.2	Mar	2003
Automatic check of datum stations	Apr	2003
Relativistic range correction and TCG/TT range correction implemented	Jun	2003
Continuous piecewise linear representation of the troposphere	Jun	2003
Subdaily ERP model: RAY96 \Rightarrow IERS2003	Oct	2003
Computation of solid Earth tides, step 2 corrected	Jul	2004
Relativistic range correction disabled	Jul	2004
TCG to TT time scale correction switched off	Jul	2004
JPL ephemeris: DE200 \Rightarrow DE405	Dec	2004
Ocean tide model: CSR 2.0 \Rightarrow CSR 3.0	Dec	2004
Clock jump detection	Apr	2005
Change from IGS00 to IGb00	Jun	2005
Nutation model: IAU80 \Rightarrow IAU2000A	Nov	2005
Solar radiation pressure a priori model: ROCK \Rightarrow CODE	Nov	2005
Sign of general relativistic acceleration corrected	Nov	2005

Tab. 1.2: Important changes in the processing strategy of the [CODE IGS](#) analysis center, see [Rothacher et al. \(1995\)](#), [Rothacher et al. \(1996\)](#), [Rothacher et al. \(1997\)](#), [Rothacher et al. \(1998b\)](#), [Rothacher et al. \(1999b\)](#), [Hugentobler et al. \(2000\)](#), [Hugentobler et al. \(2001\)](#), [Hugentobler et al. \(2004\)](#) and [Hugentobler et al. \(2008\)](#). For an explanation of the abbreviations see Appendix F.

In 2005 the IGS announced a call for participation for an IGS re-analysis effort (IGSMail² 5175). At the 2006 IGS Workshop in Darmstadt a special session on “Reprocessing Issues, Standardization, New models” was held. One of the recommendations of this workshop was that “(efficient) reprocessing must become a permanent feature of the IGS”. A few months later, the most significant discontinuity in the history of the IGS products was caused by the so-called “week 1400-switch”: the transition from a relative to an absolute antenna phase center model and the adoption of ITRF2005 in GPS week 1400 (5 November 2006).

As regards the inconsistent and inhomogeneous time series of IGS products, the situation is similar like before the establishment of the IGS that was already mentioned above: “the geodynamic interpretation of the results ... could not be trusted”. Therefore, a complete, homogeneous and consistent reprocessing starting with the raw observations is crucial for the proper interpretation of GPS-derived long time series.

1.3. Subject of the Thesis

The generation of homogeneous long time series was the main motivation for the reprocessing of a global network in a joint effort of Forschungseinrichtung Satellitengeodäsie (FESG), Technische Universität München (TUM) and Institut für Planetare Geodäsie (IPG), Technische Universität Dresden (TUD). This project started in fall 2002 and was funded by Deutsche Forschungsgemeinschaft (DFG). A modified version of the Bernese GPS Software (*Dach et al., 2007*) and a processing scheme similar to that of the CODE IGS AC (*Hugentobler et al., 2005a*) were used for the reprocessing of more than a decade of GPS observations. This thesis gives an overview of the reprocessing and describes the quality control as well as selected results.

Part I deals with theory and practice of global GPS solutions. Chapter 2 gives a short introduction into the GPS and its observables. The parameters estimated in global GPS solutions and the models applied during the data processing with the Bernese GPS Software are summarized. The implementation of these models and the detailed processing scheme are discussed in Chapter 3. Details on the tracking stations and the satellites used for reprocessing are given in Chapter 4. Examples for several systematic effects and discontinuities affecting the parameter time series are shown.

Part II focuses on the results of the reprocessing. The improvements of the reprocessed time series of station coordinates and velocities (Chapter 5), troposphere parameters (Chapter 6), satellite orbits (Chapter 7) and Earth orientation parameters (Chapter 8) are demonstrated by intra- and inter-technique comparisons with other time series and models. The reprocessing capabilities are used to compare long time series of the above mentioned parameters from solutions applying different troposphere modeling (hydrostatic a priori delays and mapping functions, Sec. 6.3) as well as different antenna phase center models (Chapter 9). Chapter 10 summarizes the most important results and gives the conclusions of this thesis as well as an outlook.

Finally, Part III includes tables of datum stations, tracking stations and discontinuities as well as a subdaily ERP model and a nutation model determined from the reprocessed time series.

²IGS electronic mail, available at <http://igs.cb.jpl.nasa.gov/mail/>

Part I.

Global GPS Solutions

2. Modeling of GPS Observations

This chapter gives a review of the parameters and models relevant for the GPS reprocessing. The description focusses on the parameterization and models implemented in the Bernese GPS Software and used for the work described in this thesis. For a more complete description of the Global Positioning System see, e.g., *Hofmann-Wellenhof et al. (2001)*, *Kaplan and Hegarty (2006)*, *Parkinson and Spilker (1996)*, *Teunissen and Kleusberg (1998)* and *Xu (2003)*.

2.1. The Global Positioning System Space Segment

The Navigation System with Time and Ranging (NAVSTAR) GPS is operated by the American Department of Defense (DoD). The space segment consists of nominally 24 satellites, its assembly began with the launch of the first out of eleven Block I satellites in 1978. The satellites are deployed in six evenly spaced orbital planes in near-circular orbits with an inclination of 55° , orbit height of $\approx 20,200$ km and a revolution period of $11^{\text{h}} 58^{\text{m}}$ (half a sidereal day). Since 1989 the Block II and later the Block IIA (A denotes “advanced”) satellites have been launched to build up the full GPS constellation. Block IIA satellites are very similar to the Block II satellites but have a mutual communication capability and two of them are equipped with laser retroreflector arrays. When the constellation reached a number of 21 spacecrafts, the initial operational capability was declared on 8 December 1993. After completing the full expansion of the satellite constellation full operational capability was declared by the DoD on 17 July 1995. Since 1997 altogether 12 Block IIR satellites (R denotes “replenishment” or “replacement”) have been launched to replace satellites that have reached the end of their lifetime and to further increase the number of satellites.

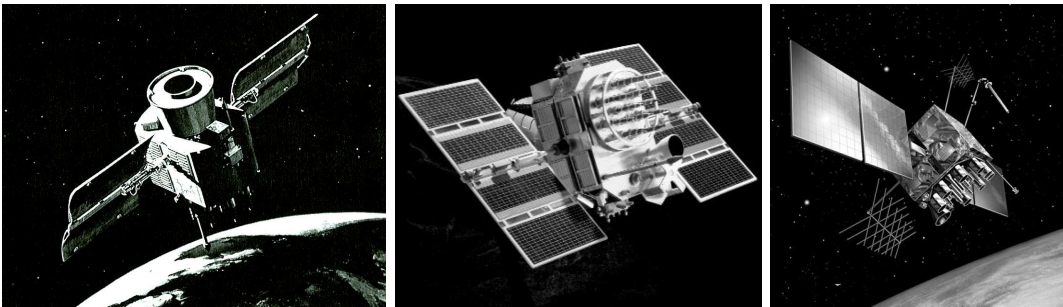


Fig. 2.1: Block I (*Parkinson and Spilker, 1996*), Block II (*Yinger, 2002*) and Block IIR (Lockheed Martin) GPS satellites.

Block IIR satellites represent a new generation of satellites disposing of several modifications w.r.t. the older Block II/IIA satellites: e.g., a time-keeping system with greater accuracy and stability, a new attitude control and acquisition system, improved inter-satellite cross-links and some other modifications, see *Kiser and Vaughan (1998)*. Starting with Block IIR-10 an improved antenna panel design (instead of the legacy antenna panel design used so far) is being used, providing a greater performance and power especially on L_2 and for low elevations (*Marquis and Reigh, 2005*). To distinguish these changes the earlier Block IIR satellites are referred to (within the IGS) as Block IIR-A, the ones with advanced antenna panel design as Block IIR-B. In October 2005 the first Block IIR-M (M denotes “modernized”) satellite was launched, providing for the first time a new military M-code on L_1 and L_2 and a civil signal on L_2 called L2C (*Rajan and Tracy, 2002*). The same improved antenna panel design as for the Block IIR-B satellites is used and, in addition, some other hardware modifications (e.g., a modernized transmitter to further increase the signal strength) have been implemented. Fig. 2.1 shows the different types of GPS satellites, Fig. 2.2 gives an overview of the temporal evolution of the different satellite blocks. For a detailed list of the satellites used in the reprocessing see Tab. 4.2.

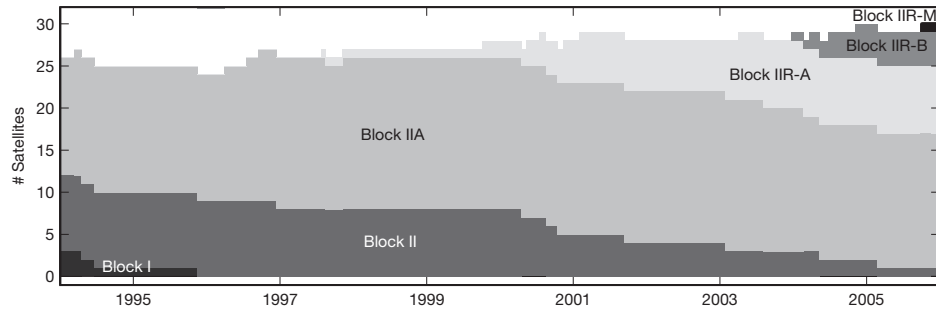


Fig. 2.2: Evolution of the GPS satellite constellation.

The GPS satellites transmit different signals on the two frequencies L_1 and L_2 in the microwave band which are listed in Tab. 2.1. Both frequencies are deduced from a nominal frequency of $f_0=10.23$ MHz (the true frequency is slightly smaller to correct for relativistic effects, see Sec. 2.9.5). This frequency is generated by Caesium (Cs) or Rubidium (Rb) frequency standards. Block I satellites were equipped with one Cs and two Rb standards. Block II/IIA satellites are equipped with two Cs and two Rb clocks, Block IIR satellites with three Rb clocks. If the clock in use fails, the satellites automatically switch to one of the backup clocks (if available). The codes modulated on the two frequencies are different for each satellite and consist of Pseudo-Random Noise (PRN) sequences, see *ICD-GPS-200* (2000). In addition, the navigation message (*IS-GPS-200*, 2004) is transmitted (including, e.g., a health indicator, satellite clock corrections and the broadcast orbits).

Carrier	Multiplier	Frequency	Wavelength	Civil code	Military code(s)
L_1	154	1575.43 MHz	19.0 cm	C/A	P1, M1 ^a
L_2	120	1227.60 MHz	24.4 cm	L2C ^a	P2, M2 ^a

^a Block IIR-M satellites only

Tab. 2.1: GPS frequencies and codes.

As the GPS is a military system two mechanisms have been implemented to limit the accuracy for unauthorized users:

- Selective Availability (SA): artificial degradation of the satellite clock accuracy (activated until 2 May 2000)
- Anti-Spoofing (AS): encryption of the military codes (activated during the time periods listed in Tab. 2.2).

These mechanisms were implemented starting with the Block II satellites, the signals of the Block I satellites were neither degraded nor encrypted.

Start		End	
31.01.1994	00:00:00	19.04.1995	20:59:59
10.05.1995	20:00:01	18.06.1995	23:59:59
11.07.1995	00:00:02	09.10.1995	23:59:59
01.11.1995	00:00:01	01.02.1997	23:59:59
24.02.1997	00:00:00		

Tab. 2.2: Time periods with anti-spoofing. AS periods in 1993 are given in *Zumberge et al.* (1994).

2.2. GPS Observables

Code Observations

The code observation equation for receiver R observing satellite S reads as

$$P_R^S = \rho_R^S + c \cdot (\Delta t_R - \Delta t_S + b_R + b_S) \quad (2.1)$$

with

P_R^S	pseudorange in units of length
c	vacuum speed of light
ρ_R^S	raw range satellite – receiver including corrections described below
$\Delta t_R, \Delta t_S$	receiver and satellite clock correction
b_R, b_S	receiver and satellite hardware delays.

P_R^S is called pseudorange as in addition to the geometric range it also contains the clock corrections and hardware delays. The raw range ρ_R^S includes corrections that are described below (e.g., the signal delay due to the atmosphere). The hardware delays in the receiver and satellite electronics are fully correlated with the clock parameters. Therefore, these biases can only be determined in a differential way for different observables as Differential Code Biases (DCBs), see Sec. 2.9.1.

Phase Observations

The phase observation equation expressed in units of length reads as

$$L_R^S = \rho_R^S + c \cdot (\Delta t_R - \Delta t_S) + \lambda \cdot B_R^S \quad (2.2)$$

where B_R^S is a constant bias term containing the unknown number of integer wavelengths λ , the so-called initial phase ambiguity term n_R^S :

$$B_R^S = n_R^S + \delta n_R^S + \frac{c}{\lambda} (b_R + b_S) \quad (2.3)$$

with the phase polarization effect δn_R^S , see Sec. 2.9.4. As the hardware delays cannot be separated from n_R^S , B_R^S is a real number. To fix the ambiguity term to an integer number (see Sec. 2.3), the hardware delays can be eliminated by forming double-differences between two stations and two satellites, see Sec. 2.2.1. Splitting the raw range ρ_R^S into its constituents, the more detailed phase observation equation can be written as

$$L_R^S = |\mathbf{x}_R(t_r) - \mathbf{x}_S(t_t)| + \Delta \rho_{trp} + \Delta \rho_{ion} + \Delta \rho_{mp} + \Delta \rho_{rel} + \Delta \rho_{pc} + c(\Delta t_R - \Delta t_S) + \lambda \cdot B_R^S + \epsilon_R^S \quad (2.4)$$

with

\mathbf{x}_R	position of the receiver at the time of reception t_r
\mathbf{x}_S	position of the satellite at the time of transmission t_t
$\Delta \rho_{trp}$	tropospheric delay
$\Delta \rho_{ion}$	ionospheric delay
$\Delta \rho_{mp}$	influence of multipath
$\Delta \rho_{rel}$	relativistic effects
$\Delta \rho_{pc}$	phase center variations and offsets
ϵ_R^S	measurement error.

The influence of multipath can reach up to several centimeters for the phase observations and can be minimized by using adequate antenna types (choking, groundplane), mounting the antenna far away from possible reflecting objects, and the use of microwave absorbing material when mounting the antenna (Elosegui et al., 1995). The measurement noise of the L_1 and L_2 phase observations is on the level of 0.2 to 5 mm (Hofmann-Wellenhof et al., 2001). The other terms of the observation equation will be discussed in the following sections.

Smoothing of Code Measurements

For receivers tracking code and phase observations on L_1 and L_2 , phase smoothed code observations $\tilde{P}_{R,i}^S$ with the frequency index $i = 1, 2$ can be generated by ([Schaer, 1999](#))

$$\tilde{P}_{R,1}^S = \bar{P}_{R,1}^S + \Delta L_{R,1}^S(t) + 2 \frac{f_2^2}{f_1^2 - f_2^2} (\Delta L_{R,1}^S(t) - \Delta L_{R,2}^S(t)) \quad (2.5a)$$

$$\tilde{P}_{R,2}^S = \bar{P}_{R,2}^S + \Delta L_{R,2}^S(t) + 2 \frac{f_1^2}{f_1^2 - f_2^2} (\Delta L_{R,1}^S(t) - \Delta L_{R,2}^S(t)) \quad (2.5b)$$

with

$$\Delta L_{R,1}^S(t) = L_{R,1}^S(t) - \bar{L}_{R,1}^S \quad (2.6a)$$

$$\Delta L_{R,2}^S(t) = L_{R,2}^S(t) - \bar{L}_{R,2}^S \quad (2.6b)$$

and

$\bar{P}_{R,i}^S$	mean code measurements of the current observation arc
$\bar{L}_{R,i}^S$	mean phase measurements of the current observation arc
$L_{R,i}^S(t)$	phase measurements at epoch t .

The noise of these smoothed code observations is significantly smaller than the noise of the original code observations and depends on the number of epochs of the current observation arc. Smoothed code observations are used in the reprocessing for the estimation of ionosphere parameters, [DCBs](#) and clocks.

2.2.1. Forming Differences

As the receiver and satellite clock errors Δt_R and Δt_S in Eq. 2.4 are unknown, these quantities have to be estimated as additional parameters when processing undifferenced (Zero-Difference – [ZD](#)) data. As these clock errors are usually estimated for each epoch, the number of clock parameters is very large. On the other hand the clock parameters can be eliminated by forming differences between satellites and receivers. The satellite clock error can be eliminated by differencing the observations of two receivers tracking the same satellite at the same time (forming a baseline). These Single-Differences ([SDs](#)) still contain the receiver clock error. A further differencing between two satellites tracked by both receivers eliminates the receiver clock errors. As these Double-Differences ([DDs](#)) are free of receiver and satellite clock errors, the number of unknowns in the parameter estimation process is highly reduced. A third differencing process between consecutive epochs results in Triple-Differences ([TDs](#)) which can be used for preprocessing and outlier detection as the phase ambiguity parameter is eliminated.

2.2.2. Linear Combinations

Based on the two frequencies L_1 and L_2 one can form different linear combinations with new properties reducing or eliminating certain effects in Eqs. 2.1 and 2.4. The phase and code linear combinations L_i and P_i are based on the coefficients $\kappa_{1,i}$ and $\kappa_{2,i}$:

$$L_i = \kappa_{1,i} \cdot L_1 + \kappa_{2,i} \cdot L_2 \quad (2.7a)$$

$$P_i = \kappa_{1,i} \cdot P_1 + \kappa_{2,i} \cdot P_2 \quad (2.7b)$$

The noise of the linear combination i is given by

$$\sigma_i = \sigma_0 \cdot \sqrt{\kappa_{1,i}^2 + \kappa_{2,i}^2} \quad (2.8)$$

assuming that the noise of the observations σ_0 is the same for L_1 and L_2 . The ambiguity term $n_{R,i}^S$ of the linear combination L_i can be expressed as

$$\lambda_i \cdot n_{R,i}^S = \kappa_{1,i} \cdot \lambda_1 \cdot n_{R,1}^S + \kappa_{2,i} \cdot \lambda_2 \cdot n_{R,2}^S \quad (2.9)$$

with the wavelength of the linear combination λ_i . Note that the integer character of $n_{R,i}^S$ depends on the selection of $\kappa_{1,i}$ and $\kappa_{2,i}$.

Ionosphere-free Linear Combination

The coefficients $\kappa_{1,3} = \frac{f_1^2}{f_1^2 - f_2^2}$ and $\kappa_{2,3} = \frac{-f_2^2}{f_1^2 - f_2^2}$ form the ionosphere-free linear combination

$$L_3 = \frac{1}{f_1^2 - f_2^2} (f_1^2 L_1 - f_2^2 L_2) . \quad (2.10)$$

The first order ionospheric effect ($\sim 1/f^2$) is eliminated by this linear combination; higher order effects are still included and should be modeled according to Sec. 2.5.2. In future, the second order ionospheric effect can be eliminated by forming linear combinations from triple-frequency observations (Xu, 2003). Disadvantages of the L_3 linear combination are the increased noise which is larger by a factor of three compared to L_1 and L_2 and the small wavelength of 0.6 cm making a direct ambiguity resolution impossible. However, if the wide-lane ambiguity $n_{R,5}^S$ is known, the ionosphere-free linear combination (after inserting Eq. 2.2 into 2.10) can be modified: the L_2 ambiguity $n_{R,2}^S$ in Eq. 2.9 can be replaced by

$$n_{R,2}^S = n_{R,1}^S - n_{R,5}^S \quad (2.11)$$

resulting in

$$\lambda_3 \cdot n_{R,3}^S = \frac{c}{f_1 + f_2} \cdot n_{R,1}^S + \frac{c \cdot f_2}{f_1^2 - f_2^2} \cdot n_{R,5}^S \quad (2.12)$$

As the multiplier of $n_{R,1}^S$ results in a wavelength of 10.7 cm, this term is called narrow-lane ambiguity.

Geometry-free Linear Combination

With $\kappa_{1,4} = 1$ and $\kappa_{2,4} = -1$ one gets the geometry-free linear combination

$$L_4 = L_1 - L_2 . \quad (2.13)$$

The receiver clock error and the geometry (satellite orbits and station coordinates) are eliminated. The ambiguity-term is not integer anymore. Ionospheric effects and the ambiguities are still included. By eliminating the geometric errors, this linear combination is particularly suitable for the estimation of ionosphere parameters.

Wide-Lane Linear Combination

The coefficients $\kappa_{1,5} = \frac{f_1}{f_1 - f_2}$ and $\kappa_{2,5} = \frac{-f_2}{f_1 - f_2}$ form the wide-lane linear combination

$$L_5 = \frac{1}{f_1 - f_2} (f_1 L_1 - f_2 L_2) . \quad (2.14)$$

Due to its large wavelength of 86.2 cm it is particularly suitable for ambiguity resolution and fixing cycle slips (integer number of cycle discontinuities in the phase measurements caused by temporary interruptions of the signal tracking).

Melbourne-Wübbena Linear Combination

For this linear combination phase and code measurements are used:

$$L_6 = \frac{1}{f_1 - f_2} (f_1 L_1 - f_2 L_2) - \frac{1}{f_1 + f_2} (f_1 P_1 + f_2 P_2) . \quad (2.15)$$

This Melbourne-Wübbena linear combination is the difference between the phase wide-lane and the code wide-line. Therefore, it also has a wavelength of 86.2 cm. As geometry and the effects of troposphere, ionosphere and clocks are eliminated, it is also well-suited for resolving the wide-lane ambiguities but also for [ZD](#) data screening.

2.3. Ambiguity Resolution

The fixing of the phase ambiguities n_R^S to their integer values (Ambiguity Resolution – AR) significantly improves the accuracy of the estimated parameters. In the following only the methods used in the reprocessing effort are described, for further details see, e.g., *Mervart (1995)*.

2.3.1. Melbourne-Wübbena Ambiguity Resolution

In a first step, the wide-lane ambiguities are fixed with the Melbourne-Wübbena (MW) linear combination using phase and code measurements. These ambiguities are subsequently introduced to fix the narrow-lane ambiguities. For the MW AR high-quality code observations are essential but with this method it is possible even to fix the ambiguities to their integer values on very long baselines. It was described independently by *Melbourne (1985)* and *Wübbena (1985)*. To account for the differences between the C/A-code and the P-code observations on L_1 , P1C1-DCBs should be estimated within the MW AR, see Sec. 2.9.1.

2.3.2. Wide-Lane/Narrow-Lane Ambiguity Resolution

This approach is very similar to the MW AR: again the wide-lane ambiguities are fixed first – but without code observations, i.e. using L_5 (see Eq. 2.14). In a second step the fixed L_5 ambiguities are introduced into a solution solving for the narrow-lane ambiguities. This approach is capable to solve ambiguities for baselines up to several hundred kilometers as the ionospheric error on L_5 is smaller than the corresponding L_2 error. Thus, even during periods with high ionospheric activity, the L_5 ambiguities can still be fixed when the L_1 and L_2 ambiguities cannot be fixed anymore.

2.3.3. Quasi-Ionosphere-Free Ambiguity Resolution

The Quasi-Ionosphere-Free (QIF) ambiguity resolution method (described by, e.g., *Mervart, 1995*) is capable of directly solving the L_1 and L_2 ambiguities without code measurements. For each epoch and each satellite Stochastic Ionosphere Parameters (SIPs) are estimated to account for ionospheric biases. The SIPs are usually estimated with constraints of several decimeters to properly solve for the ambiguities. Due to the huge number of SIPs these parameters are pre-eliminated epoch by epoch. The consideration of a priori ionosphere information (e.g., global ionosphere models, see Sec. 2.5.2) helps to increase the number of resolved ambiguities.

2.3.4. Direct Solution of the L_1 and L_2 Ambiguities

For short baselines the influence of the ionospheric refraction can be assumed to be identical for both receivers on each frequency and thus can be neglected. Therefore, the ambiguities can be independently solved on L_1 and L_2 using the SIGMA strategy, which considers the full variance-covariance information (*Dach et al., 2007*).

2.4. Station Coordinates and Velocities

2.4.1. Modeling of Site Displacement

Station coordinates are usually represented by constant offsets for solutions covering time intervals where the movement of the station due to plate tectonics can be neglected. The instantaneous station position $\mathbf{x}_R(t)$ at epoch t is expressed by

$$\mathbf{x}_R(t) = \mathbf{x}_R(t_0) + \dot{\mathbf{x}}_R \cdot (t - t_0) + \Delta\mathbf{x}_{R,set}(t) + \Delta\mathbf{x}_{R,pt}(t) + \Delta\mathbf{x}_{R,ol}(t) + \Delta\mathbf{x}_{R,al}(t) \quad (2.16)$$

with

\mathbf{x}_R	station position at reference epoch t_0
$\dot{\mathbf{x}}_R$	station velocity
$\Delta\mathbf{x}_{R,set}$	site displacement due to solid Earth tides
$\Delta\mathbf{x}_{R,pt}$	site displacement due to pole tide
$\Delta\mathbf{x}_{R,ol}$	site displacement due to ocean loading
$\Delta\mathbf{x}_{R,al}$	site displacement due to atmospheric loading.

The solid Earth tides are caused by the deformation of the Earth due to gravitational forces of the Sun and the Moon and can reach up to 40 cm for the radial component and several centimeters for the horizontal component. The deformation of the Earth induced by the changes of the Earth's rotation axis due to polar motion is called pole tide and can reach up to 25 mm in the radial component and up to 7 mm in the horizontal component. The deformation of the Earth due to tidal changes of the mass distribution of the oceans (tidal ocean loading) has its largest effect for stations near the coast in areas with a large tidal range. The radial displacement can reach several centimeters for these sites and is less than one centimeter for continental sites. State-of-the-art correction formulas for these three effects are given in the IERS Conventions 2003 (*McCarthy and Petit, 2004*).

Whereas the effect of ocean loading has the largest magnitude for sites near the coast, the site displacements due to atmospheric loading are most pronounced for continental sites far away from the oceans. Limited time series and grids of atmospheric loading corrections are provided by the IERS Special Bureau for Loading¹, complete time series starting in 1976 are provided by *Petrov and Boy (2004)*². Vertical peak-to-peak displacements can reach up to 15–20 mm (*van Dam and Wahr, 1987*). The annual amplitude of the atmospheric displacement can reach up to 4 mm for the radial component and is usually smaller than 0.5 mm for the horizontal component (*Dong et al., 2002*). *Tregoning and van Dam (2005)* showed that applying S_1 and S_2 models for atmospheric tides improves the height repeatability for stations near the equator but generally degrades stations at higher latitudes indicating that these models are not accurate enough at the moment. Although applying non-tidal atmospheric loading corrections on the observation level improved the height estimates for most of the stations, *Tregoning and van Dam (2005)* concluded that it is sufficient to apply daily-averaged a posteriori corrections for the non-tidal atmospheric loading to correct for the height time series. Regional and local displacements like post glacial rebound (e.g., *Johansson et al., 2002*; *Scherneck et al., 2003*) and hydrological effects (e.g., *Munekane et al., 2004*) are usually not modeled a priori in global analyses.

For solutions covering one to several days only, the station velocity is usually taken from an existing reference system realization like ITRF2000 (*Altamimi et al., 2002*) or the second IGS implementation of ITRF2000 called IGB00 (*Ray et al., 2004*). The offset errors of the latter reference frame are ± 0.5 mm for the x - and y -translations of the origin, ± 1.0 mm for the z -translation, ± 0.068 mas for the orientation and ± 0.24 ppb for the scale. The instability errors are ± 0.2 mm/y, ± 0.35 mm/y, ± 0.0065 mas/y and ± 0.07 ppb/y for the corresponding rates. However, these numbers seem to be too optimistic. The accuracy of the station coordinates of the accumulated IGS weekly solutions is about 3 mm for the station coordinates and 1.5 mm/y for the station velocities (*Ferland et al., 2005*). For stations that are not included in existing reference frames, plate motion models like NNR-NUVEL1A (*DeMets et al., 1994*) can be used to compute approximate velocities. When processing several years of data station velocities can be estimated as additional parameters, see Sec. 2.4.3.

2.4.2. Datum Definition

To preserve the inner geometry of the network and to avoid distortions (due to fixing or constraining stations), global GPS solutions are usually adjusted as free networks with additional conditions to cope with the datum defect. This type of datum definition (see *Brockmann, 1997*) is based on a 7-parameter similarity transformation between the a priori coordinates $\mathbf{x}_i = [x_i, y_i, z_i]^T$ and the estimated coordinates $\tilde{\mathbf{x}}_i = [\tilde{x}_i, \tilde{y}_i, \tilde{z}_i]^T$ with the transformation parameter vector $\mathbf{T} = [T_x, T_y, T_z, \alpha, \beta, \gamma, s]^T$ composed of the translations T_x, T_y, T_z , the rotations α, β, γ (assuming that these angles are small) and the scale factor s :

¹<http://www.sbl.statkart.no/>

²<http://gemini.gsfc.nasa.gov/aplo/>

$$\begin{bmatrix} \tilde{x}_i \\ \tilde{y}_i \\ \tilde{z}_i \end{bmatrix} = \begin{bmatrix} x_i \\ y_i \\ z_i \end{bmatrix} + \begin{bmatrix} 1 & 0 & 0 & 0 & -z_i & y_i & x_i \\ 0 & 1 & 0 & z_i & 0 & -x_i & y_i \\ 0 & 0 & 1 & -y_i & x_i & 0 & z_i \end{bmatrix} \cdot \begin{bmatrix} T_x \\ T_y \\ T_z \\ \alpha \\ \beta \\ \gamma \\ s \end{bmatrix} \quad (2.17)$$

or in matrix notation

$$\tilde{\mathbf{x}}_i = \mathbf{x}_i + \mathbf{B}_i \mathbf{T} \quad (2.18)$$

With the superior vectors $\tilde{\mathbf{x}}$, \mathbf{x} and the matrix \mathbf{B}

$$\tilde{\mathbf{x}} = \begin{bmatrix} \tilde{\mathbf{x}}_1 \\ \tilde{\mathbf{x}}_2 \\ \vdots \end{bmatrix}, \quad \mathbf{x} = \begin{bmatrix} \mathbf{x}_1 \\ \mathbf{x}_2 \\ \vdots \end{bmatrix}, \quad \mathbf{B} = \begin{bmatrix} \mathbf{B}_1 \\ \mathbf{B}_2 \\ \vdots \end{bmatrix} \quad (2.19)$$

one can set up the minimum constraint condition (*Altamimi et al., 2004*)

$$\mathbf{B}^T (\tilde{\mathbf{x}} - \mathbf{x}) = 0 \quad (2.20)$$

With the weight matrix \mathbf{P} these pseudo-observations in the form of

$$\Delta \mathbf{N} = \mathbf{B} \mathbf{P} \mathbf{B}^T \quad (2.21)$$

can be added to the normal equation matrix \mathbf{N} , see Sec. 2.10. Similar conditions for the rates of the transformation parameter vector \mathbf{T} can be set up when estimating velocities. If \mathbf{T} is limited to a subset of transformation parameters \mathbf{T}_s , the following conditions (or combinations of them) can be realized:

- No-Net-Translation (**NNT**): $\mathbf{T}_s = [T_x, T_y, T_z]^T$
- No-Net-Rotation (**NNR**): $\mathbf{T}_s = [\alpha, \beta, \gamma]^T$
- No-Net-Scale (**NNS**): $\mathbf{T}_s = s$

As global **GPS** solutions including the estimation of satellite orbits and Earth Rotation Parameters (**ERPs**) can be rotated by small angles without changing the inner geometry, a **NNR** condition is mandatory to remove the datum defect; the translations and the scale can be determined by the **GPS** observations. A **NNT** condition has to be applied when coordinates of the origin of the tracking network are estimated as additional parameters, see Sec. 2.9.2. A **NNS** condition is necessary when estimating parameters that are highly correlated with the terrestrial scale, e.g. satellite antenna offsets (Sec. 2.8). If velocities are estimated (see next section), the same set of conditions can be applied for the velocities, too.

2.4.3. Velocity Estimation

Station velocities can be added as additional parameters on the Normal Equation (**NEQ**) level, see Sec. 2.10. Two offset vectors (\mathbf{x}_{t_1} at the beginning and \mathbf{x}_{t_2} at the end of the time interval considered for velocity estimation) per station are set up. Each single coordinate solution $\mathbf{x}(t)$ contributes to these offsets weighted according to the time intervals between the epoch of the actual solution and the epochs of the two offsets:

$$\mathbf{x}(t) = \mathbf{x}_{t_1} \frac{t_2 - t}{t_2 - t_1} + \mathbf{x}_{t_2} \frac{t - t_1}{t_2 - t_1} \quad (2.22)$$

After the adjustment (considering the full variance-covariance information of the contributions to the velocity estimation) these two offsets can be transformed to an offset (station coordinate) and a drift (station velocity) (*Brockmann, 1997*). To get reasonable velocities, the observed time interval of stations contributing to the velocity estimation should be at least 2.5 years (*Blewitt and Lavallée, 2002*).

2.5. Atmospheric Refraction

While propagating from the satellite to the receiver, GPS signals are diffracted and delayed by the atmosphere. In this section the influence of the troposphere (0 to 10 km height above the Earth's surface) and the ionosphere (50 to 1000 km height above the Earth's surface) on microwave signals will be discussed. For GPS signals the troposphere is non-dispersive, that means the velocity of propagation does not depend on the wavelength. The ionosphere on the other hand is dispersive – the velocity of propagation depends on the wavelength. The tropospheric delay has to be modeled and/or estimated, the first order effect of the ionosphere can be eliminated by forming the ionosphere-free linear combination (Eq. 2.10). In the following only the equations for the phase observations will be shown.

The atmospheric delay depends on the refraction index n along the signal path. As deviations of the refractive index from 1 (vacuum, no delay) are very small, usually the refractivity $N = (n - 1) \cdot 10^6$ is used. The atmospheric delay $\Delta\rho_{atm}$ can be described by the integral

$$\Delta\rho_{atm} = \Delta\rho_{trp} + \Delta\rho_{ion} = 10^{-6} \int_S^R N(s) ds \quad (2.23)$$

along the signal propagation path s .

2.5.1. Influence of the Troposphere

The tropospheric delay in zenith direction (Zenith Total Delay – ZTD) can be separated into a hydrostatic component $\Delta\rho_{trp}^h$ and a wet component $\Delta\rho_{trp}^w$ and has an order of magnitude of about 2.4 m. About 90% are caused by the hydrostatic component, the other approximately 10% by the wet component including the influence of liquid water-drops and water vapor:

$$\Delta\rho_{trp} = \Delta\rho_{trp}^h + \Delta\rho_{trp}^w = 10^{-6} \int_S^R N_{trp}^h ds + 10^{-6} \int_S^R N_{trp}^w ds . \quad (2.24)$$

Expressions for N_{trp}^h and N_{trp}^w are given in, e.g., *Solheim et al. (1999)*. Due to the unpredictable short-term variations of the wet part of the troposphere, merely modeling the tropospheric delay is in most cases inadequate for high-precision GPS applications. Usually an a priori model $\Delta\rho_{apr}$ is only used for the hydrostatic part. The model described by *Saastamoinen (1973)* uses

p	atmospheric pressure [mbar]
e	partial water vapor pressure [mbar]
T	temperature [K]

to compute the troposphere zenith delay

$$\Delta\rho_{trp,saast} = 0.002277 \cdot \left[p + \left(\frac{1255}{T} + 0.05 \right) \cdot e \right] . \quad (2.25)$$

This model contains the hydrostatic and the wet part of the troposphere delay. If one wants to compute the hydrostatic part only, e has to be set to zero. If continuous meteorological measurements are not available, the model atmosphere of *Berg (1948)* with the reference values p_{ref} [mbar], T_{ref} [°C] and the humidity H_{ref} [%] at reference height h_{ref} can be used to compute the input arguments of Eq. 2.25 at the actual height h [m]:

$$p = p_{ref} \cdot [1 - 0.0000226 \cdot (h - h_{ref})]^{5.225} \quad [\text{mbar}] \quad (2.26a)$$

$$T = T_{ref} - 0.0065 \cdot (h - h_{ref}) \quad [^\circ\text{C}] \quad (2.26b)$$

$$H = H_{ref} \cdot e^{-0.0006396 \cdot (h - h_{ref})} \quad [\%] . \quad (2.26c)$$

The partial water vapor pressure e and the humidity H are approximately related by

$$e = \frac{H}{100} \cdot e^{-37.2465 + 0.213166 \cdot T - 0.000256908 \cdot T^2} . \quad (2.27)$$

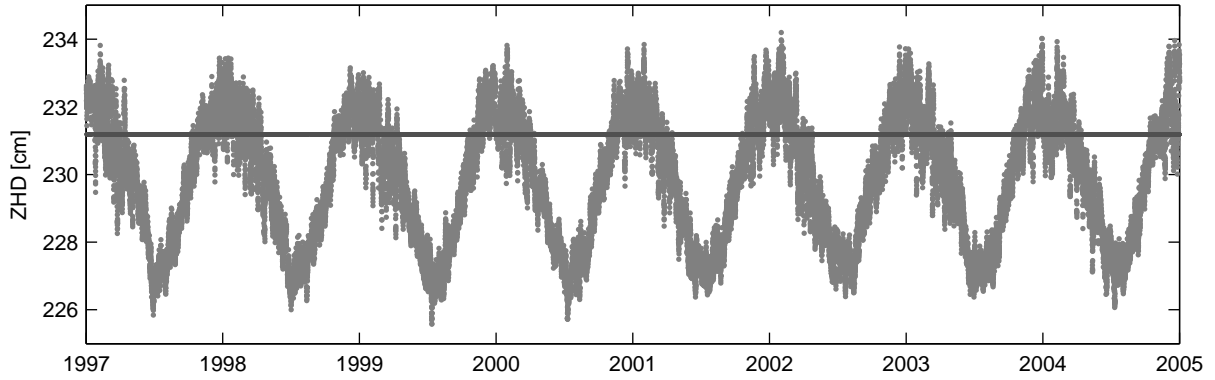


Fig. 2.3: Hydrostatic troposphere zenith delays from [ECMWF](#) for Bahrain. The solid line represents the constant delay computed from Eqs. 2.25 and 2.26a.

Due to deficiencies of this a priori model, the estimated delay $\Delta\rho_{est}$ is the sum of the Zenith Wet Delay ([ZWD](#)) and the errors of the hydrostatic a priori model.

Hydrostatic zenith delays derived from numerical integration through pressure level data of numerical weather models provide a more realistic a priori model. If the delays from the weather model are given on the height of a Digital Elevation Model ([DEM](#)) h_M that differs from the actual station height h , they have to be extrapolated to the station height. [Brunner \(2001\)](#) proposed the following extrapolation

$$\Delta\rho_{trp}^h(h) = \Delta\rho_{trp}^h(h_M) - 2.277 \cdot 10^{-3} \frac{g}{R} \frac{p(h_M)}{T(h_M)} \cdot (h - h_M) \quad (2.28)$$

with

g	gravity
R	gas constant
$p(h_M)$	pressure at height h_M
$T(h_M)$	temperature at height h_M .

Fig. 2.3 shows the Zenith Hydrostatic Delay ([ZHD](#)) computed from European Centre for Medium-Range Weather Forecasts ([ECMWF](#)) data (extrapolation to station height according to Eq. 2.28) and the [ZHD](#) computed from Eqs. 2.25 and 2.26a for Bahrain. As Bahrain is a station with quite large pressure variations, a clear annual signal with an amplitude of 2.4 cm can be seen in the [ECMWF ZHD](#). In addition a mean bias of 1.3 cm between both models is present. The mean biases are largest in Antarctica (up to 9 cm) with maximum differences of up to 19 cm. When applying constant a priori delays computed with a standard atmosphere, the difference between this delay and the true hydrostatic delay is mapped with the wet instead of the hydrostatic mapping function. The results of this erroneous mapping will be discussed in Sec. 6.3.2.

The observation equation of the tropospheric delay reads as

$$\Delta\rho_{trp}(z_R^S) = f_{apr}(z_R^S)\Delta\rho_{apr} + f_{est}(z_R^S)\Delta\rho_{est} \quad (2.29)$$

$f_{apr}(z_R^S)$ and $f_{est}(z_R^S)$ are mapping functions for the a priori and estimated part of the zenith delay to map these delays to the actual zenith angle z_R^S . The simplest mapping function is given by

$$f(z_R^S) = \frac{1}{\cos z_R^S} \quad (2.30)$$

Up-to-date mapping functions are based on the continued fraction form of [Herring \(1992\)](#)

$$f(\epsilon_R^S) = \frac{1 + \frac{a}{b}}{1 + \frac{1+c}{a}} \frac{\sin \epsilon_R^S + \frac{b}{\sin \epsilon_R^S + c}}{\sin \epsilon_R^S + \frac{b}{\sin \epsilon_R^S + c}} \quad (2.31)$$

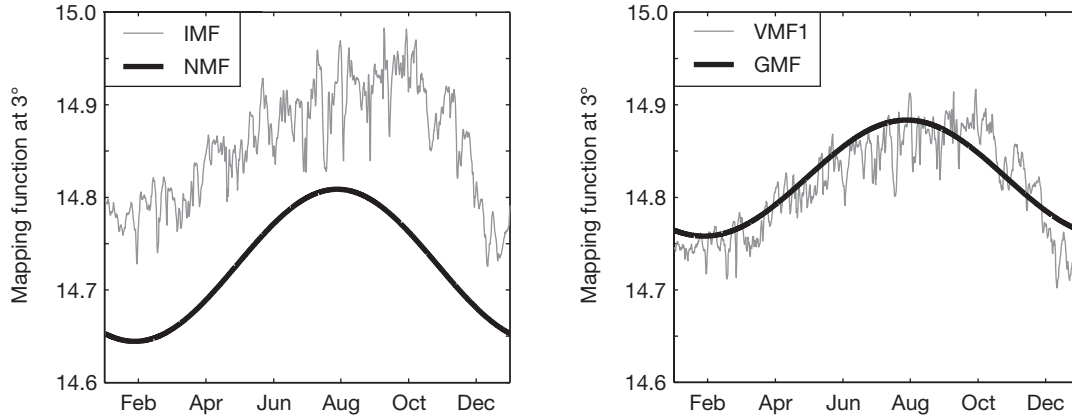


Fig. 2.4: Hydrostatic mapping functions at an elevation of 3° for Syowa (Antarctica) in 2005.

with the mapping function parameters a , b , c and the elevation of the satellite $\epsilon_R^S = 90^\circ - z_R^S$. Usually different sets of coefficients are used for the hydrostatic and the wet delays. The Niell mapping function (NMF) described by [Niell \(1996\)](#) was determined from radiosonde data and has the advantage that the only input arguments are the site location and the day of year. The spatial resolution is 15° in latitude, dependence on longitude is not modeled, and the time resolution is one day. The mapping function parameters for the hydrostatic part of the tropospheric delay are computed from latitude-dependent tabulated values for offset, amplitude and phase of an annual signal and a height correction for each of the three parameters. The wet NMF only depends on the latitude of the tracking station. However, the hydrostatic NMF has three major deficiencies: it is assumed that (1) the seasonal behavior of the southern and the northern hemisphere is the same (phase difference of 180°), (2) the equatorial region from 15°S to 15°N is described by the 15°N latitude profile, and (3) the polar regions with latitudes larger than 75° are described by the 75°N latitude profile. Another disadvantage is that short-term variations (several hours till days) are not considered ([Niell, 2001](#)).

More recent mapping functions are based on data of numerical weather models which provide the best globally available description of the atmospheric state. One of these is the Isobaric Mapping Function (IMF) developed by [Niell \(2000\)](#). IMF uses the geopotential height of the 200 hPa pressure level (z_{200}) and the ratio of the wet path delay along a straight line at 3.3° elevation and its zenith delay (smfw3) as meteorologic input parameters. The hydrostatic IMF depends on the z_{200} -value, the latitude and height of the station, the wet IMF depends on the smfw3-value and the height of the station. For further details on IMF and comparisons with NMF see [Vey et al. \(2006\)](#). For the Vienna Mapping Function 1 (VMF1, [Boehm et al., 2006b](#)) the coefficients a_h and a_w are derived from a rigorous raytracing through pressure layers of the ECMWF numerical weather model. These coefficients are provided by TU Vienna³ as site-specific or global grid time series with 6-hour temporal spacing. The coefficients b_h and c_h were derived from one year of ECMWF data in a least squares fit. Whereas b_h is constant, c_h depends on the day of year and the latitude. b_w and c_w were taken from the NMF at 45° latitude as the coefficient a_w is sufficient to model the dependence of the wet mapping function on latitude ([Boehm and Schuh, 2004](#)). The Global Mapping Function (GMF, [Boehm et al., 2006a](#)) is an empirical mapping function (input arguments are only the day of year and the site location) that is consistent with VMF1. Expressions for the coefficients a_h and a_w were derived from three years of ECMWF data and are provided as a spherical harmonic expansion of degree and order nine. The coefficients b and c are taken from the VMF1.

Fig. 2.4 shows the four hydrostatic mapping functions described above for Syowa (Antarctica). A clear bias between the two empiric mapping functions (NMF and GMF) as well as a difference in the amplitude can be seen. IMF and VMF1 show in general the same structure but there is also a small bias between both mapping functions. More details of the effects of different mapping functions on the estimated parameters will be discussed in Sec. 6.3.

Azimuthal variations of the tropospheric delay can be taken into account by additionally estimating troposphere gradients:

³<http://mars.hg.tuwien.ac.at/~ecmwf1/>

$$\Delta\rho_{trp}(z_R^S, A_R^S) = f_{apr}(z_R^S)\Delta\rho_{apr} + f_{est}(z_R^S)\Delta\rho_{est} + \Delta\rho_n \frac{\partial f_{est}}{\partial z} \cos(A_R^S) + \Delta\rho_e \frac{\partial f_{est}}{\partial z} \sin(A_R^S) \quad (2.32)$$

with the gradient in north-south direction $\Delta\rho_n$ and the gradient in east-west direction $\Delta\rho_e$ depending on the azimuth A_R^S . These gradients can be seen as a tilting of the zenith direction in the direction with the azimuth

$$A_{grd} = \arctan \frac{\Delta\rho_e}{\Delta\rho_n} \quad (2.33)$$

and the norm

$$s_{grd} = \sqrt{\Delta\rho_n^2 + \Delta\rho_e^2} . \quad (2.34)$$

The estimation of troposphere gradients significantly improves the coordinate repeatability (in particular the horizontal component), see [Rothacher et al. \(1998a\)](#) and [Meindl et al. \(2004\)](#).

2.5.2. Influence of the Ionosphere

The molecules of the ionosphere are highly ionized by the strong ultraviolet radiation and the X-rays of the Sun. The free electrons generated in this ionization process affect the signal propagation. For frequencies higher than 1 GHz the ionospheric refraction index reads as

$$n_{ion} = \sqrt{1 - \frac{f_p^2}{f^2}} \quad (2.35)$$

with the signal frequency f and the natural oscillation frequency of electrons in a plasma f_p . The latter depends on the electron density n_e in electrons/m³: $f_p^2 = c_x \cdot n_e$ with

$$c_x = \frac{e^2}{4\pi^2\epsilon_0 m_e} \approx 80.6 \frac{\text{m}^3}{\text{s}^2} \quad (2.36)$$

composed of the fundamental constants

e	charge of one electron
ϵ_0	permittivity in the vacuum
m_e	electron mass.

With the first order approximation of the refraction index

$$n_{ion,1} = 1 - \frac{1}{2} \frac{c_x \cdot n_e}{f^2} \quad (2.37)$$

the ionospheric delay of phase observations is the integral along the path of the signal

$$\Delta\rho_{ion,1}(f) = -\frac{1}{2} \frac{c_x}{f^2} \int_S^R n_e(s) ds . \quad (2.38)$$

The integral in Eq. 2.38 represents the Total Electron Content (**TEC**)

$$E = \int_S^R n_e(s) ds \quad (2.39)$$

expressed in **TEC** units (1 **TECU** = 10¹⁶ electrons/m²). The first order effect (up to 150 m at low elevations during the ionospheric maximum) can be eliminated by forming the ionosphere-free linear combination L_3 , see Sec. 2.2.2. Formulations for the second and third order effects are given in [Bassiri and Hajj \(1993\)](#), [Kedar et al. \(2003\)](#) and [Fritsche et al. \(2005\)](#). For the computation of these effects the ionosphere is modeled as an infinitesimal layer (single-layer) at a height of H_{sl} above the Earth's surface, see Fig. 2.5. The second order term depends on the magnetic field vector

$$\mathbf{B}_0 = B_g \left(\frac{R_e}{R_e + H_{sl}} \right)^3 \cdot (\sin \theta_m \cdot \mathbf{E}_m - 2 \cos \theta_m \cdot \mathbf{U}_m) \quad (2.40)$$

with

B_g	magnetic field magnitude; $B_g \approx 3.12 \cdot 10^{-5}$ T near the equator at surface height
R_e	radius of the Earth
$\mathbf{E}_m, \mathbf{U}_m$	unit vectors of magnetic east and up
θ_m	colatitude of the ionospheric intersection point.

In Eq. 2.40 the Earth's magnetic field is approximated by a tilted magnetic dipole ([Fraser-Smith, 1987](#)). The coordinates of the geomagnetic pole used for reprocessing are given in Tab. 3.1. With the signal propagation vector \mathbf{k} , the constant

$$c_y = \frac{\mu_0 e}{2\pi m_e} \quad (2.41)$$

with the permeability in the vacuum μ_0 , the second order ionospheric effect reads as

$$\Delta\rho_{ion,2}(f) = -\frac{1}{2} \frac{c_x \cdot c_y}{\mu_0 \cdot f^3} (\mathbf{B}_0 \cdot \mathbf{k}) \cdot E \quad (2.42)$$

The order of magnitude of this effect is up to 4 cm at 10° elevation. For the third order effect [Brunner and Gu \(1991\)](#) introduced the shape factor $\eta \approx 0.66$:

$$\Delta\rho_{ion,3}(f) = -\frac{1}{8} \frac{c_x^2}{f^4} N_{max} \cdot \eta \cdot E \quad (2.43)$$

with the peak electron density along the signal propagation path $N_{max} \approx 4.42 \cdot 10^{-6} \frac{1}{\text{m}} \cdot E$. The order of magnitude of the third order effect is about 1 to 4 mm. The impact of considering the higher order ionospheric corrections on stations coordinates, troposphere parameters and satellite orbits is discussed in [Fritsche et al. \(2005\)](#).

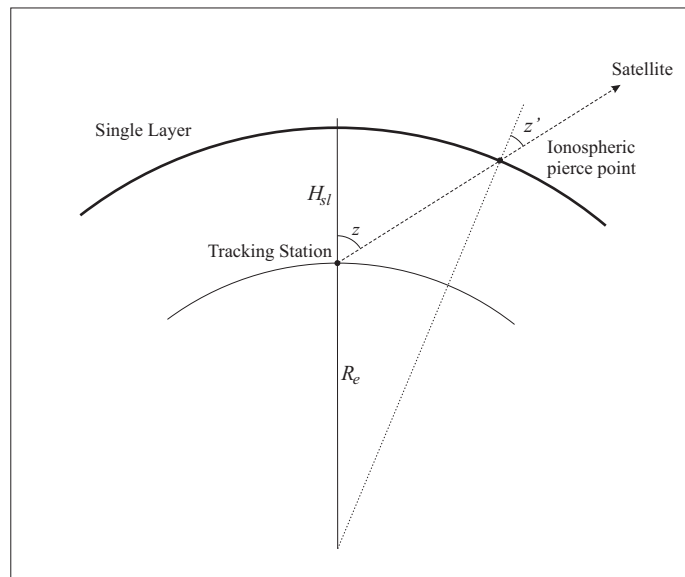


Fig. 2.5: Ionospheric single-layer model: radius of the Earth R_e , altitude of the single-layer above the Earth's surface H_{sl} , zenith distance z , zenith distance at the ionospheric pierce point z' .

Ionosphere parameters themselves (which are also needed for the computation of the higher order ionospheric corrections) can be estimated from undifferenced code observations using the geometry-free linear combination L_4 : the ionosphere is again modeled as a single-layer at altitude H_{sl} above the Earth's surface in a geomagnetic reference frame, for details see [Schaer \(1999\)](#). The vertical total electron content E_v (sometimes also called **VTEC**) can be described by the spherical harmonic coefficients a_{nm} and b_{nm} of an expansion with maximum degree and order n_{max} :

$$E_v(\beta_m, s) = \sum_{n=0}^{n_{max}} \sum_{m=0}^n \bar{P}_{nm}(\sin \beta_m) (a_{nm} \cos ms + b_{nm} \sin ms) \quad (2.44)$$

with

β_m	geomagnetic latitude of the intersection point of the single-layer and the line of sight receiver-satellite (ionospheric pierce point)
s	sun-fixed geomagnetic longitude of the ionospheric pierce point (difference between the longitude of the ionospheric pierce point and the longitude of the Sun)
\bar{P}_{nm}	normalized associated Legendre polynomials of degree n and order m (e.g., Heiskanen and Moritz, 1967).

Together with the estimation of such Global Ionosphere Maps (GIMs) one should estimate P1P2-DCBs (see Sec. 2.9.1) to reduce systematic effects due to different hardware delays for P_1 and P_2 in the satellite and receiver electronics. As E_v represents the vertical electron density, an elevation-dependent mapping function $f_{ion}(z_R^S)$ is required to relate the slant TEC with E_v :

$$\text{TEC} = E(z_R^S) = f_{ion}(z_R^S) \cdot E_v \quad (2.45)$$

The basic form of the ionospheric mapping function is similar to Eq. 2.30, but instead of the zenith distance at the receiver the zenith distance at the ionospheric pierce point z' is used. Thus, the Modified Single-Layer Model (MSLM) mapping function ([Schaer, 1999](#)) can be written as

$$f_{ion}(z_R^S) = \frac{1}{\cos z'} = \frac{1}{\sqrt{1 - \sin^2 z'}} \quad \text{with} \quad \sin z' = \frac{R_e}{R_e + H_{sl}} \sin(\alpha \cdot z_R^S) \quad (2.46)$$

and

H_{sl}	height of the single-layer; $H_{sl} = 506.7$ km
α	scaling factor; $\alpha = 0.9782$.

2.6. Satellite Orbits

The equation of motion of a satellite orbiting the Earth reads as (e.g., [Springer, 2000](#))

$$\ddot{\mathbf{x}}_S = -GM \frac{\mathbf{x}_S}{x_S^3} + \mathbf{a}(t, \mathbf{x}_S, \dot{\mathbf{x}}_S, q_1, q_2, \dots, q_n) \quad (2.47)$$

with

GM	gravitational coefficient of the Earth (gravity constant G times mass of the Earth M)
\mathbf{x}_S	position vector of the satellite; $x_S = \mathbf{x}_S $
$\dot{\mathbf{x}}_S$	velocity vector of the satellite
\mathbf{a}	disturbing acceleration
q_i	dynamical parameters.

For a unique solution of the system of 2nd order differential equations (Eq. 2.47), six initial conditions are necessary. Instead of an initial position and velocity the osculating orbital elements

a	semi-major axis
e	eccentricity
i	inclination
Ω	right-ascension of the ascending node
ω	argument of perigee
u	argument of latitude

are usually used. The solution of the equation of motion by numerical integration is described in, e.g., [Beutler \(2005\)](#).

The most important disturbing accelerations for Medium Earth Orbiters (MEOs) like the GPS satellites are:

- Solar Radiation Pressure (RPR)
- Non-sphericity of the Earth's gravity field

- Gravitational acceleration of 3rd bodies (Moon, Sun, planets)
- Earth tidal potential
- Ocean tidal potential
- Thruster firing.

Smaller accelerations are caused by relativistic effects (see Sec. 2.9.5), radiation emitted and reflected by the Earth, outgassing (especially in the very first weeks after the launch), thermal re-emission (*Duha et al., 2006*) and antenna thrust (acceleration on the satellite due to the transmission of the GPS navigation signals, *Ziebart et al., 2004*). For MEOs the solar radiation pressure is the largest uncertainty in the orbit determination process. To account for this effect usually dynamical parameters are estimated. The Enhanced CODE Orbit Model (ECOM) described by *Beutler et al. (1994a)* has nine dynamical parameters:

$$\mathbf{a}_{RPR} = \nu \cdot [\mathbf{a}_{ROCK} + D(u) \cdot \mathbf{e}_D + Y(u) \cdot \mathbf{e}_Y + X(u) \cdot \mathbf{e}_X] \quad (2.48)$$

with

$$D(u) = D_0 + D_C \cdot \cos u + D_S \cdot \sin u \quad (2.49a)$$

$$Y(u) = Y_0 + Y_C \cdot \cos u + Y_S \cdot \sin u \quad (2.49b)$$

$$X(u) = X_0 + X_C \cdot \cos u + X_S \cdot \sin u \quad (2.49c)$$

and

\mathbf{a}_{RPR}	acceleration due to solar radiation pressure
ν	eclipse factor, see Sec. 2.6.2
\mathbf{a}_{ROCK}	acceleration of the corresponding ROCK model (<i>Fliegel et al., 1992; Fliegel and Gallini, 1996</i>)
\mathbf{e}_D	unit vector pointing to the Sun
\mathbf{e}_Y	unit vector in the direction of the solar panel axis
\mathbf{e}_X	$\mathbf{e}_D \times \mathbf{e}_Y$, pointing to the hemisphere containing the Earth.

The three coefficients with index 0 (D_0 , Y_0 , X_0) represent constant terms whereas the coefficients with indices C and S describe periodic variations in the three directions. Together with the six orbital elements, altogether 15 deterministic parameters are used to characterize an orbital arc. The additional stochastic parameters are described in the next paragraph.

Pseudo-Stochastic Pulses Pseudo-stochastic pulses are additional parameters (small velocity changes) introduced into the equation of motion (*Beutler et al., 1994a*). They allow for compensating deficiencies of the solar radiation pressure model which is the largest error source of MEOs as already mentioned above. For these pulses the a priori weight

$$w_a = \frac{\sigma_0^2}{\sigma_a^2} \quad (2.50)$$

is applied with

σ_a^2	a priori variance
σ_0^2	a priori variance of the unit weight.

For GPS satellites pseudo-stochastic pulses are usually set up twice per day (corresponding to the time of revolution) and in three directions.

2.6.1. Nominal Attitude

The satellite-fixed coordinate system has its origin in the center of mass of the satellite and is defined by:

1. the z -axis \mathbf{Z} is parallel to the Earth-pointing antenna axis
2. the y -axis \mathbf{Y} points along the solar panel axis

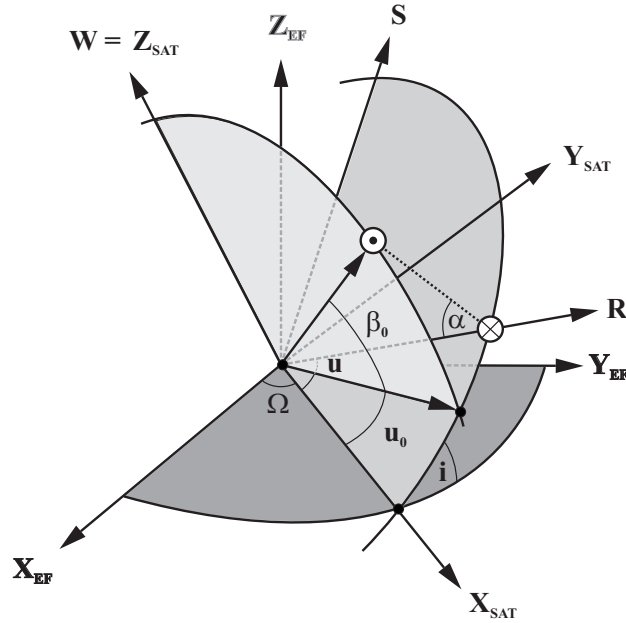


Fig. 2.6: Elevation of the Sun w.r.t. the orbital plane: Earth-fixed system $[X_{EF}, Y_{EF}, Z_{EF}]$, orbit system $[X_{SAT}, Y_{SAT}, Z_{SAT}]$, accompanying tripod of the satellite position $[R, S, W]$, i.e. radial, along-track and cross-track. Right ascension of the ascending node Ω , argument of latitude u , inclination i , argument of latitude and elevation of the Sun u_0 and β_0 . \odot symbolizes the Sun, \otimes the satellite.

3. the x -axis \mathbf{X} completes a right-handed system and points into the hemisphere containing the Sun

$$\mathbf{X} = \mathbf{Y} \times \mathbf{Z} . \quad (2.51)$$

The GPS attitude control system has two major tasks:

1. the transmitting antenna has to point towards the center of the Earth

$$\mathbf{Z} = -\frac{\mathbf{x}_s}{|\mathbf{x}_s|} \quad (2.52)$$

2. the vector perpendicular to the solar panels has to point toward the Sun, i.e. the solar panel axis has to be perpendicular to the direction of the Sun

$$\mathbf{Y} = -\frac{\mathbf{Z} \times \mathbf{x}_\odot}{|\mathbf{Z} \times \mathbf{x}_\odot|} . \quad (2.53)$$

For Block I and Block II/IIA satellites there is a third condition: the angle α between the Sun and the satellite's z -axis ($=-R$) has to be between 0° and 180° . To fulfill these conditions, the satellite has to rotate around its z -axis. During periods with low elevations β_0 of the Sun w.r.t. the orbital plane (see Fig. 2.6) the satellite rotates quickly when passing the subsolar point (so-called noon-turn) and after leaving the Earth's shadow (so-called midnight-turn). During periods with high elevations β_0 the satellite rotates continuously and very slowly once per revolution around its z -axis. As an example, the elevation of the Sun above the orbital plane β_0 for the year 2003 is shown in Fig. 2.7 for all satellites. Satellites in orbit plane B show the largest, satellites in plane E the smallest variations of the β_0 angle. The peak-to-peak amplitude varies with time due to the precession of the orbital planes. The time period between minimum and maximum peak-to-peak amplitude is about 13 years (*Schmid et al., 2007*). Block IIR satellites have the same attitude algorithm as the Block II/IIA satellites for $|\beta_0| > 1.6^\circ$. In contrast to Block II/IIA satellites (see below), this attitude mode includes the eclipse phases. For $|\beta_0| < 1.6^\circ$, the Block IIR satellites initially followed a fixed yaw mode (x -axis approximately points in the satellite velocity direction, see IGSMAIL 1653). According to *Kouba (2009)* the Block IIR satellites maintain nominal attitude even during eclipses nowadays.

The actual attitude is permanently measured by Sun sensors mounted on each solar panel and a Earth sensor mounted on the same side of the satellite as the antenna panel. Deviations from nominal attitude are

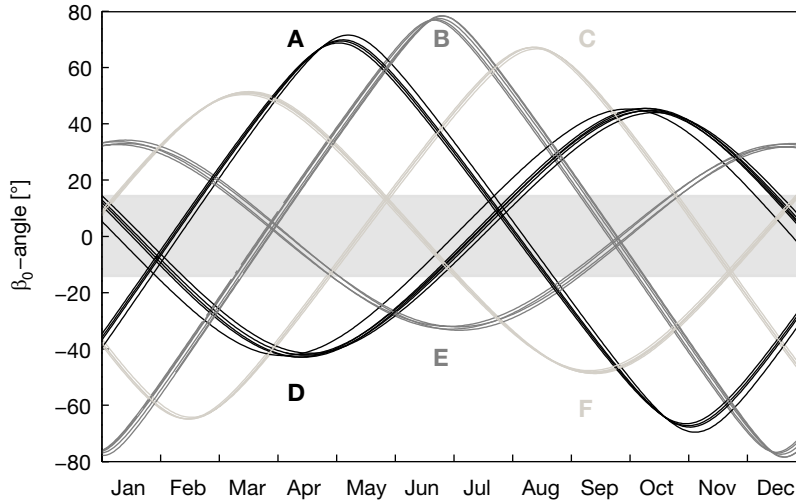


Fig. 2.7: Elevation of the Sun above the orbital plane β_0 for the year 2003. The gray-shaded area marks eclipse periods with $|\beta_0| < 14^\circ$.

corrected for by torques created by either a system of four Reaction Wheels (RWs) (primary system) or by hot gas thrusters (backup system). The alignment of the RWs w.r.t. the satellite axes allows to maintain nominal attitude even if one RW fails (*Violet et al., 1999*). External torques by the Earth's gravity and magnetic field and the solar RPR increase the rotation speed of the RWs. Therefore, the momentum stored in the RWs has to be reduced periodically by so-called momentum dumps. These momentum dumps are usually performed by electro-magnetic torquers (primary system, *Eller and Fuchs, 2008*) controlled by the Autonomous Magnetic Momentum Management (AMMM) or by thruster firing (backup system).

2.6.2. Satellite Eclipses

When the angle α between the Sun and the satellite's z -axis is smaller than about 14° (gray-shaded area in Fig. 2.7) the satellite passes the Earth's shadow and is eclipsed by the Earth. Such eclipses can last up to 55 minutes and happen twice per year for a specific orbital plane for a period of several weeks. During these eclipses no solar radiation pressure acts on the satellite. Using a simple cylinder model for the shadow of the Earth, as shown in Fig. 2.8, the eclipse factor ν (1 if satellite in the sunlight, 0 if satellite in the umbra) can be computed as

$$\nu = \begin{cases} 1 & \text{if } \cos \gamma_e < 0 \text{ and } y < R_e \\ 0 & \text{else} \end{cases} \quad (2.54)$$

with

$$\cos \gamma_e = \frac{\mathbf{x}_s \cdot \mathbf{x}_\odot}{|\mathbf{x}_s| \cdot |\mathbf{x}_\odot|} \quad (2.55a)$$

$$y = |\mathbf{x}_s| \sqrt{1 - \cos^2 \gamma_e} . \quad (2.55b)$$

A severe problem during eclipses is the attitude of the satellite. As Sun sensors are responsible for the determination of the attitude, the maintenance of the nominal attitude with these sensors during the eclipses is impossible. After entering the shadow, the Block II/IIA satellites start to rotate with a rate of up to $0.13^\circ/\text{s}$ (*Bar-Sever, 1996*) around their z -axis. As the satellite re-enters the sunlight with an almost arbitrary orientation of the solar panels, the time until reestablishing nominal attitude (up to 20 minutes, see *Fliegel and Gallini, 1996*) will cause orbit modeling problems.

Eclipses by the Moon are less frequent and shorter but also have to be considered for high precision applications. For these eclipses an umbra/penumbra model has to be used. The occultation of the Sun by the Moon depends on the angle γ_s between the Sun, the satellite and the Moon

$$\cos \gamma_s = \frac{(\mathbf{x}_\zeta - \mathbf{x}_s) \cdot (\mathbf{x}_\odot - \mathbf{x}_s)}{|\mathbf{x}_\zeta - \mathbf{x}_s| \cdot |\mathbf{x}_\odot - \mathbf{x}_s|} . \quad (2.56)$$

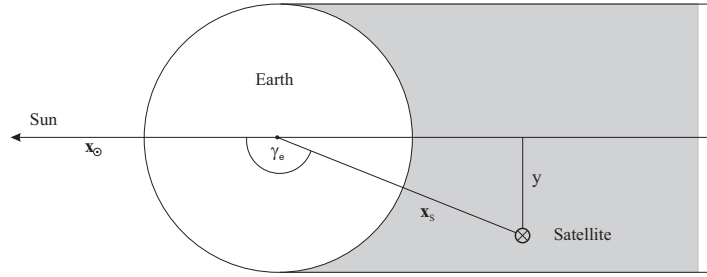


Fig. 2.8: Modeling of satellite eclipses by the Earth with a cylindric shadow model.

The satellite is completely in the sunlight if

$$\gamma_s \geq \gamma_\odot + \gamma_\zeta \quad (2.57)$$

in the umbra if

$$\gamma_s \leq \gamma_\zeta - \gamma_\odot \quad (2.58)$$

and in the penumbra if

$$\gamma_s < \gamma_\zeta + \gamma_\odot . \quad (2.59)$$

For the definition of the angles see Fig. 2.9. According to *Montenbruck and Gill (2000)* the area A occulted by the Moon during the partial phase can be expressed by

$$A = 2(A_{BCF} - A_{BCE}) + 2(A_{ACD} - A_{ACE}) . \quad (2.60)$$

This area can be computed from angular separations and diameters:

$$A = r_\odot^2 \arccos \frac{x_\odot}{r_\odot} + r_\zeta^2 \arccos \frac{x_\zeta}{r_\zeta} - (x_\zeta + x_\odot) \cdot y \quad (2.61)$$

with

$$x_\odot = \frac{(x_\zeta + x_\odot)^2 + r_\odot^2 - r_\zeta^2}{2(x_\zeta + x_\odot)} \quad \text{and} \quad y = \sqrt{r_\odot^2 - x_\odot^2} = \sqrt{r_\zeta^2 - x_\zeta^2} . \quad (2.62)$$

For the definition of the quantities x_ζ , x_\odot , r_ζ and r_\odot see Fig. 2.9b. The eclipse factor is hence

$$\nu = 1 - \frac{A}{r_\odot^2 \pi} . \quad (2.63)$$

Eclipses by the Moon can last up to 2.5 hours although the average duration is only half an hour.

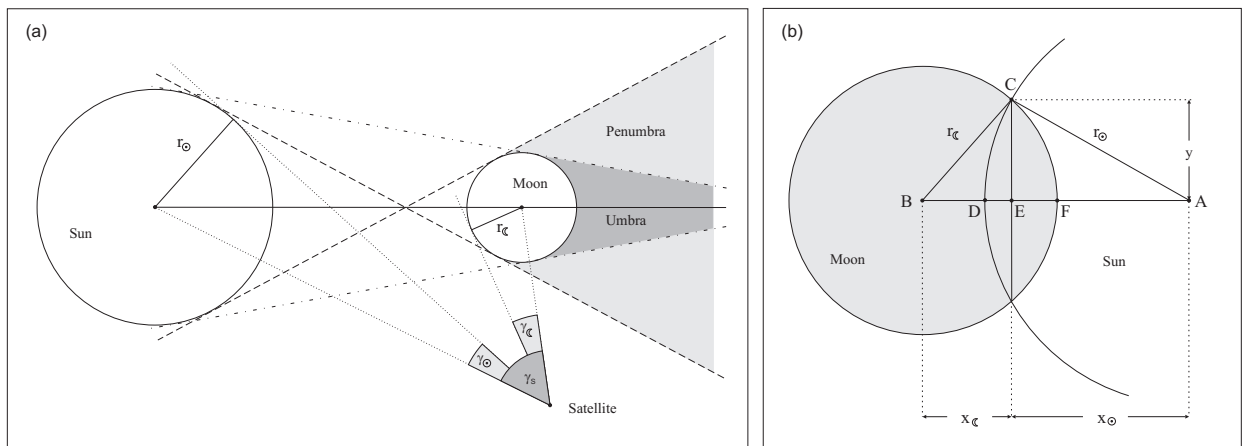


Fig. 2.9: Satellite eclipses by the Moon: (a) conical shadow model with umbra and penumbra; (b) occultation of the Sun by the Moon.

2.7. Earth Orientation Parameters

The Earth orientation parameters, namely the pole coordinates x_p and y_p , Universal Time 1 (**UT1**) and the nutation parameters in longitude $\Delta\psi$ and obliquity $\Delta\epsilon$, provide the transformation between the inertial system (realized by the satellite orbits) and the terrestrial system (realized by the coordinates of the tracking stations). For the pole coordinates and **UT1** the expression **ERPs** will be used whereas the Earth Orientation Parameters (**EOPs**) additionally include the two nutation angles. The pole coordinates are directly accessible by **GPS** whereas **UT1** (which is one-to-one correlated with the right ascension of the ascending node) and the nutation parameters cannot be determined in an absolute sense. On the other hand the rate of **UT1**, called Length of Day (**LOD**)

$$\text{LOD} = -\frac{d}{dt}(\text{UT1} - \text{UTC}) \quad (2.64)$$

as well as the nutation rates (*Rothacher et al., 1999a*) can be determined by **GPS** due to their relation to the first derivatives of the orbital elements:

$$\text{LOD} = (\dot{\Omega} + \cos i \dot{u}_0) \cdot \frac{1}{b_1} \quad (2.65a)$$

$$\Delta\dot{\epsilon} = \cos \Omega \dot{i} + \sin i \sin \Omega \dot{u}_0 \quad (2.65b)$$

$$\Delta\dot{\psi} \sin \epsilon_0 = -\sin \Omega \dot{i} + \sin i \cos \Omega \dot{u}_0 \quad (2.65c)$$

with

b_1	ratio of universal time and sidereal time, see Eq. 2.70b
$\Delta\dot{\epsilon}$	nutation rate in obliquity
$\Delta\dot{\psi}$	nutation rate in longitude
ϵ_0	mean obliquity of the ecliptic.

The transformation between the coordinates in the terrestrial system \mathbf{x}_T and in the inertial system \mathbf{x}_I that is used to compute the partial derivatives of the Earth orientation parameters is given by

$$\mathbf{x}_I = \mathbf{P}(t)\mathbf{N}(t)\mathbf{R}_3(-\Theta)\mathbf{R}_1(y_P)\mathbf{R}_2(x_P) \cdot \mathbf{x}_T \quad (2.66)$$

with the rotation matrices \mathbf{R}_i and the precession matrix

$$\mathbf{P}(t) = \mathbf{R}_3(\zeta)\mathbf{R}_2(-\vartheta)\mathbf{R}_3(z) \quad (2.67)$$

computed from the precession parameters z , ϑ and ζ and the nutation matrix

$$\mathbf{N}(t) = \mathbf{R}_1(-\epsilon_0)\mathbf{R}_3(\Delta\psi)\mathbf{R}_1(\epsilon_0 + \Delta\epsilon) \quad (2.68)$$

composed of the nutation in longitude $\Delta\psi$ and obliquity $\Delta\epsilon$ and the mean obliquity of the ecliptic ϵ_0 . The Greenwich Sidereal Time Θ describes the rotation of the Earth. Eq. 2.66 is the traditional formulation of the transformation between the terrestrial and the celestial reference system as implemented in the Bernese **GPS** Software. In August 2000 the International Astronomical Union (**IAU**) recommended a new transformation approach (*Guinot, 2002*) based on:

- coordinates X and Y of the Celestial Intermediate Pole (CIP) in the celestial system instead of the precession and nutation quantities
- Earth Rotation Angle θ instead of Greenwich Sidereal Time Θ .

The transformation equations using these quantities as well as expressions of the old nutation and precession quantities compatible with the **IAU** 2000 recommendations are given in *McCarthy and Petit (2004)*. An expression for Θ compatible with the **IAU** 2000 recommendations is described in more detail by *Capitaine et al. (2003)*:

$$\Theta = \Theta_M + \Delta\psi \cos \epsilon_0 + \Delta\text{GMST} \quad (2.69)$$

with

$$\Theta_M = \theta(t_u) + a_0 + a_1 t + a_2 t^2 + a_3 t^3 + a_4 t^4 \quad (2.70a)$$

$$\theta(t_u) = 2\pi(b_0 + b_1 t_u) \quad (2.70b)$$

$$\Delta\text{GMST} = -\sum_{i=1}^{12} c_i \sin \alpha_i - 0.87 \mu\text{as } t \sin \Omega_\zeta \quad (2.70c)$$

and

t_u	UT1 Julian day number since J2000.0
a_i	correction terms for Θ referring to the Celestial Ephemeris Origin (CEO)
t	time in centuries after J2000.0
ΔGMST	correction to Greenwich Mean Sidereal Time
Ω_ζ	mean longitude of the ascending node of the Moon.

The coefficients a_i , b_i , c_i and α_i are listed in [McCarthy and Petit \(2004\)](#). The latter two terms in Eq. 2.69 are also known as equation of equinoxes. As the pole of the celestial reference system and direction of the Celestial Intermediate Pole (CIP) at epoch J2000.0 are not identical one has to correct for this frame bias by

$$\Delta\psi_b = -41.775 \text{ mas} \quad (2.71a)$$

$$\Delta\epsilon_b = -6.8192 \text{ mas}. \quad (2.71b)$$

The frame bias also includes an offset in right ascension. As GPS is not sensitive to this small rotation of about 15 mas, this effect can be neglected.

2.8. Antenna Phase Center Variations and Offsets

GPS observations correspond to the distance between the electromagnetic phase centers of the transmitting and receiving antenna. These are usually not identical with the point the observations are referred to: the center of mass for the satellite and a mechanically well-defined Antenna Reference Point (ARP) for the receiver antenna. The ARP is usually defined by the intersection of the vertical antenna axis of symmetry with the bottom of the antenna. The correction for the difference of the mean electromagnetic and the mechanic reference point is called Phase Center Offset (PCO), see Fig. 2.10. The location of the electromagnetic reference point in addition depends on the direction of the received signal: this dependence is called Phase Center Variation (PCV). The influence of phase center variations and offsets of the satellite and receiver antenna $\Delta\rho_{pc}$ is given by

$$\Delta\rho_{pc}(A_R^S, z_R^S, A_S^R, n_S^R) = \Delta\rho'_R(A_R^S, z_R^S) - \Delta\mathbf{r}_R \cdot \mathbf{e}_R^S + \Delta\rho'_S(A_S^R, n_S^R) + \Delta\mathbf{r}_S \cdot \mathbf{e}_R^S \quad (2.72)$$

with

A_R^S	azimuth of the observed satellite
z_R^S	zenith distance of the observed satellite
A_S^R	azimuth at the satellite
n_S^R	nadir angle at the satellite
$\Delta\rho'_R$	receiver antenna phase center variations
$\Delta\rho'_S$	satellite antenna phase center variations
$\Delta\mathbf{r}_R$	receiver antenna phase center offset: position of the mean phase center w.r.t. the antenna reference point

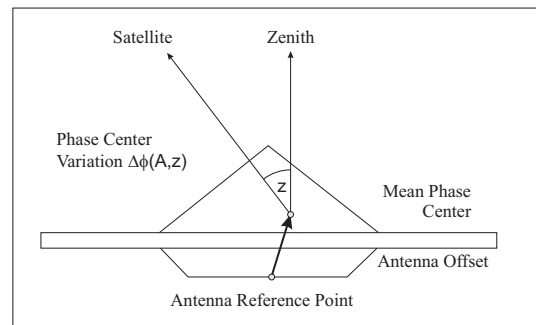


Fig. 2.10: Geometry of the receiver antenna.

$\Delta \mathbf{r}_S$	satellite antenna phase center offset: position of the mean phase center w.r.t. the center of mass of the satellite
\mathbf{e}_R^S	unit vector receiver – satellite.

The connection between z_R^S and n_S^R is given by

$$\sin(n_S^R) = \frac{R_e}{\rho_S} \sin(z_R^S) \quad (2.73)$$

with the radius of the Earth R_e and the geocentric distance of the satellite ρ_S , see [Schmid and Rothacher \(2003\)](#). Further details on the calibration of receiver and satellite antennas are given in [Sec. 9.1](#).

2.9. Other Parameters and Effects

2.9.1. Differential Code Biases

P1C1 In principle one can distinguish three classes of receivers concerning the code registration on L_1 : C1/X2 receivers with cross-correlation technique (e.g., Rogue, TurboRogue, Trimble 4000) track the C/A-code on L_1 and provide $X2 = C1 + (P2 - P1)$. P1/P2 receivers (e.g., Ashtech, AOA Benchmark ACT) on the other hand directly track the P-code on both frequencies. Some recent receiver models (e.g., Leica and Trimble) also only provide the C/A-code and not the P-code on L_1 (C1/P2 receivers). The bias between these two types of L_1 code measurements is different for each satellite and has to be considered when estimating satellite clocks or solving ambiguities using code measurements (Melbourne-Wübbena linear combination), see [Jefferson et al. \(2001\)](#). If these DCBs are unknown, they can be set up as additional parameters within the clock estimation or ambiguity resolution. As DCBs cannot be determined in an absolute sense, an additional condition has to be introduced for datum definition: either the code bias of one reference satellite has to be fixed or the sum of the DCBs has to be zero

$$\frac{1}{n} \sum_{j=1}^n \text{DCB}_j = 0 \quad (2.74)$$

with the DCBs of the individual satellites DCB_j and the number of satellites n . Both approaches have the disadvantage that changes in the satellite constellation can also cause jumps in the DCB time series although this effect is smaller when using the sum-condition. Therefore, this sum-condition is the approach used within the IGS.

P1P2 Frequency-dependent delays in the electronics of the satellites and the receivers cause a bias between the code signals on L_1 and L_2 . This effect can be accounted for by estimating P1P2 differential code biases for satellites and receivers. The application or estimation of these P1P2-DCBs is essential for the determination of absolute ionosphere parameters from dual-frequency code observations ([Newby, 1992](#)). Ignoring the P1P2-DCBs may cause errors in the TEC determination of up to 9 TECUs due to satellite DCBs and up to 30 TECUs due to receiver DCBs ([Rideout and Coster, 2006](#)). For ROGUE receivers, the DCBs can be measured directly by the receiver and are stable at the level of ± 0.1 ns (in a temperature-controlled environment). Receiver DCBs are very sensitive to hardware changes concerning the receiver, the antenna cable and the antenna. As all receivers of a tracking network contribute to the estimation of satellite DCBs, this type of DCBs can be determined more accurately than receiver DCBs.

2.9.2. Origin of the Tracking Network

The GPS satellite orbits are sensitive to the Earth's center of mass. When setting up a NNT condition w.r.t. the a priori coordinates in addition to the NNR condition necessary for global GPS solutions (see [Sec. 2.4.2](#)), the origin of the tracking network $\mathbf{o}_{nw} = [X_{nw}, Y_{nw}, Z_{nw}]^T$ w.r.t. the a priori reference frame as represented by the currently observed stations $i = 1, \dots, N$ can be explicitly estimated as an additional parameter

$$\mathbf{x}_{R_i} = \overset{\circ}{\mathbf{x}}_{R_i} + \mathbf{o}_{nw} \quad (2.75)$$

with the estimated receiver position \mathbf{x}_{R_i} of station i and the a priori receiver position $\mathring{\mathbf{x}}_{R_i}$. Instead of setting up these parameters during the parameter estimation they can also be added on the normal equation level ([Brockmann, 1997](#)). The origin determined in such a way depends on the distribution of the tracking stations and also contains artifacts of the orbit modeling ([Hugentobler et al., 2005b](#)), in particular the mismodelling of non-gravitational forces ([Heflin et al., 2002](#)) resulting in much larger variations than expected by geophysical effects (e.g., [Chen et al., 1999](#)) and observed by other space geodetic techniques (e.g., [Angermann et al., 2002](#)).

2.9.3. Receiver and Satellite Clocks

The clock terms for receivers Δt_R and satellites Δt_S in Eq. 2.4 can be eliminated by forming double-differences between two stations and two satellites. On the other hand, the clock parameters can be estimated from undifferenced GPS data. As GPS is a differential technique, clock offsets cannot be estimated for all receivers of a tracking network and each satellite at once. One has to fix either a single reference clock or an ensemble of reference clocks (usually highly accurate hydrogen masers located at fundamental stations or time laboratories). When estimating clock parameters from code observations of a tracking network incorporating P1- and C1-receivers, the estimation of P1C1-DCBs (as described in Sec. 2.9.1) is recommended. As the work described in this thesis is primarily based on DD observations, no further details on clock determination are discussed here. For more details see, e.g. [Bock et al. \(2000\)](#) and [Dach et al. \(2003\)](#).

2.9.4. Phase Polarization Effect

The GPS phase observation depends on the orientation of the satellite and receiver antenna as well as the direction of the line of sight of the two antennas. According to [Wu et al. \(1993\)](#) an effective dipole model \mathbf{D} can be used for the receiver and the satellite antenna

$$\mathbf{D}_R = \bar{\mathbf{x}}_R - \mathbf{k}(\mathbf{k} \cdot \bar{\mathbf{x}}_R) + \mathbf{k} \times \bar{\mathbf{y}}_R \quad (2.76a)$$

$$\mathbf{D}_S = \bar{\mathbf{x}}_S - \mathbf{k}(\mathbf{k} \cdot \bar{\mathbf{x}}_S) - \mathbf{k} \times \bar{\mathbf{y}}_S \quad (2.76b)$$

with

\mathbf{k}	phase propagation vector (pointing from the satellite to the receiver)
$\bar{\mathbf{x}}_R, \bar{\mathbf{y}}_R$	unit vectors of the receiver antenna
$\bar{\mathbf{x}}_S, \bar{\mathbf{y}}_S$	unit vectors of the satellite antenna.

The phase correction for right circularly polarized signals (like the GPS signals) is given by

$$\Delta\Phi = 2N\pi + \Delta\phi \quad (2.77)$$

where

$$\Delta\phi = \text{sign}(\zeta) \arccos \frac{\mathbf{D}_S \cdot \mathbf{D}_R}{|\mathbf{D}_S| \cdot |\mathbf{D}_R|} \quad \text{with} \quad \zeta = \mathbf{k} \cdot (\mathbf{D}_S \times \mathbf{D}_R) \quad (2.78a)$$

$$N = \text{NINT} \left(\frac{\Delta\Phi_{prev} - \Delta\phi}{2\pi} \right) . \quad (2.78b)$$

$\Delta\Phi_{prev}$ is the previous value of the phase polarization correction. On very long baselines this effect can reach up to several centimeters.

2.9.5. Relativistic Effects

General Relativistic Effect for the Equation of Motion The acceleration due to the general relativistic curvature of the space-time caused by the Earth's gravity field (e.g., [Zhu and Groten, 1988](#)) on a GPS satellite solely depends on the position \mathbf{x}_S and the velocity $\dot{\mathbf{x}}_S$ of the satellite and fundamental constants

$$\ddot{\mathbf{x}}_{rel} = \frac{GM}{c^2 x_S^3} \left[\left(4 \frac{GM}{x_S} - \dot{\mathbf{x}}_S \cdot \dot{\mathbf{x}}_S \right) \mathbf{x}_S + 4(\mathbf{x}_S \cdot \dot{\mathbf{x}}_S) \dot{\mathbf{x}}_S \right] . \quad (2.79)$$

This acceleration can reach up to $0.3 \cdot 10^{-9} \text{ m} \cdot \text{s}^{-2}$. The much smaller effects of geodesic precession and the Lense-Thirring effect, which are included in the [IERS Conventions 2003](#), can be neglected for [GPS](#) satellites.

Shapiro Effect According to the general theory of relativity, the propagation time of an electro-magnetic wave is affected by the gravitational potential along its path. For the [GPS](#) signals, the Earth's gravity field increases the propagation time. This Shapiro effect expressed in units of length reads as

$$\Delta\rho_{sh} = \frac{2GM}{c^2} \ln \frac{\rho_S + \rho_R + \rho_R^S}{\rho_S + \rho_R - \rho_R^S} \quad (2.80)$$

ρ_S	geocentric distance of the satellite
ρ_R	geocentric distance of the receiver
ρ_R^S	distance between receiver and satellite.

This range correction can reach a maximum value of 19 mm ([Zhu and Groten, 1988](#)).

Effects on Satellite Clocks General as well as special relativistic effects affect the clocks onboard the [GPS](#) satellites (e.g., [Ashby, 2003](#)). These effects can be separated into a constant and a periodic part. The constant part is corrected for by shifting the nominal frequency of the satellite frequency standards by $-4.4647 \cdot 10^{-10}$ Hz. The origin of the constant part is the gravitational potential difference between the mean height of the receiver and the satellite clock (general relativity) and the mean velocity of the satellite w.r.t. the receiver (special relativity). The periodic relativistic correction $\Delta\rho_{per}$ (which is also applied for the broadcast clock information) is given by

$$\Delta\rho_{per} = \frac{2}{c} \sqrt{a \cdot GM_e} \sin E \quad (2.81)$$

a	semi-major axis
e	eccentricity
E	eccentric anomaly.

This correction accounts for deviations of the satellite height from the mean height (general relativity) and the satellite velocity from mean velocity (special relativity) due to the non-circularity of the satellite orbit. According to [Kouba \(2002\)](#) this correction may also be written as

$$\Delta\rho_{per} = \frac{2}{c} \mathbf{x}_S \cdot \dot{\mathbf{x}}_S \quad (2.82)$$

\mathbf{x}_S	position vector of the satellite
$\dot{\mathbf{x}}_S$	velocity vector of the satellite.

As this effect is a pure clock effect, it cancels completely when processing double-differenced [GPS](#) data. For [ZD](#) data the effect can reach up to 14 m, depending mainly on the eccentricity of the [GPS](#) satellite orbit. If satellite clocks are estimated, this effect is completely absorbed by the clock estimates.

2.10. Basics of Least-Squares Adjustment

As the Least-Squares Adjustment ([LSA](#)) method is used for the parameter estimation of the reprocessing, some basics will be summarized here, for further details see, e.g. [Brockmann \(1997\)](#) and [Koch \(1999\)](#). The mathematical model is described by

$$\hat{\mathbf{b}} = \mathbf{b} + \hat{\mathbf{v}} = f(\hat{\mathbf{x}}) \quad (2.83)$$

with

$\hat{\mathbf{b}}$	adjusted observations
\mathbf{b}	original observations
$\hat{\mathbf{v}}$	observation corrections (residuals)
$\hat{\mathbf{x}}$	adjusted parameters (unknowns)
$f(\hat{\mathbf{x}})$	functional model.

For the least-squares adjustment (Gauß-Markoff model), the weighted squared sum of the residuals is minimized, i.e.

$$\hat{\mathbf{v}}^T \mathbf{P}_{bb} \hat{\mathbf{v}} = \min \quad (2.84)$$

where \mathbf{P}_{bb} is the weight matrix (stochastic model) of the observations. The partial derivatives of the functional model w.r.t. the unknown parameters form the design matrix

$$\mathbf{A} = \frac{\partial f(\hat{\mathbf{x}})}{\partial \hat{\mathbf{x}}} \quad (2.85)$$

computed with the a priori values of the unknown parameters $\hat{\mathbf{x}}$. The linearized observation equation is given by

$$\hat{\mathbf{v}} = \mathbf{A} \Delta \hat{\mathbf{x}} - \mathbf{w} \quad (2.86)$$

with

$\mathbf{w} = \mathbf{b} - f(\hat{\mathbf{x}})$	observed – computed
$\Delta \hat{\mathbf{x}}$	improvements of the a priori values.

Inserting Eq. 2.86 in Eq. 2.84 gives

$$\underbrace{\mathbf{A}^T \mathbf{P}_{bb} \mathbf{A}}_{\mathbf{N}} \Delta \hat{\mathbf{x}} = \underbrace{\mathbf{A}^T \mathbf{P}_{bb} \mathbf{w}}_{\mathbf{r}} \quad (2.87)$$

with

\mathbf{N}	normal equation matrix
\mathbf{r}	right hand side of the normal equation system.

By solving this equation system for the improvements $\Delta \hat{\mathbf{x}}$ of the a priori values of the unknowns

$$\Delta \hat{\mathbf{x}} = (\mathbf{A}^T \mathbf{P}_{bb} \mathbf{A})^{-1} \mathbf{A}^T \mathbf{P}_{bb} \mathbf{w} \quad (2.88)$$

one gets the adjusted parameters

$$\hat{\mathbf{x}} = \hat{\mathbf{x}} + \Delta \hat{\mathbf{x}} \quad (2.89)$$

The a posteriori variance factor $\hat{\sigma}_0^2$ is computed from the weighted squared sum of the observation corrections:

$$\hat{\sigma}_0^2 = \frac{\hat{\mathbf{v}}^T \mathbf{P}_{bb} \hat{\mathbf{v}}}{r} \quad (2.90)$$

with

$r = n - u$	redundancy or degree of freedom
n	number of observations
u	number of unknowns.

The covariance matrix of the unknowns $\hat{\mathbf{K}}_{\hat{\mathbf{x}}\hat{\mathbf{x}}}$ is given by

$$\hat{\mathbf{K}}_{\hat{\mathbf{x}}\hat{\mathbf{x}}} = \hat{\sigma}_0^2 \mathbf{N}^{-1} \quad (2.91)$$

When saving the normal equation, the right hand side, the a priori values, $\mathbf{w}^T \mathbf{P}_{bb} \mathbf{w}$ and the numbers of observations and unknowns of different NEQ systems, one can combine and manipulate these NEQs in an efficient and mathematically correct way. The most important operations are:

- Stacking of parameters
- Parameter transformations:

- Changing a priori values
- Changing of the parameter spacing
- Offset/drift \Leftrightarrow 2 offsets (import/export of Solution Independent Exchange ([SINEX](#)) files)
- Adding additional unknown parameters, e.g. station velocities
- Applying constraints, e.g. for datum definition
- Deletion of parameters (fixing to their a priori values)
- Pre-elimination of parameters (reducing the dimension of the normal equation system).

For more details see [Brockmann \(1997\)](#) and [Mervart \(2000\)](#).

3. Data Processing

In this chapter the realization of the models and parameters discussed in Chapter 2 and the processing strategy are described. This processing strategy is based on the one used at the [CODE IGS](#) analysis center to generate the contribution to the final [IGS](#) products ([Hugentobler et al., 2005a](#)), but was moderately modified and enhanced to fulfil the requirements of the reprocessing.

3.1. Modeling

General Aspects The time system is Terrestrial Time ([TT](#)) realized by the [GPS](#) time (as given by the observation epochs) which differs only by a constant offset (51.184 s) from Terrestrial Dynamical Time ([TDT](#)). Double-differenced phase and code observations are the main observables. Zero-difference data is only used for the estimation of ionosphere parameters, [DCBs](#) and clock parameters. The preprocessing is done with the full sampling rate of 30 seconds, the final parameter estimation with a sampling of 3 minutes. The a priori weight for the L_1 and L_2 phase observations at the zenith is one millimeter, the corresponding weight for the code observations is 10 cm. A cut-off angle of 3° and elevation-dependent weighting (weight $w = \cos^2 z$ with zenith angle z) are used to properly decorrelate the height component and the troposphere zenith delay.

Station Coordinates The geodetic datum is defined by a [NNR](#) condition for a subset of the 106 IGB00 stations ([Ray et al., 2004](#)). The coordinates and velocities of these stations are given in the file `IGS03P33_RS106.snx`, available at <ftp://igs.cb.jpl.nasa.gov/igs/cb/station/coord/>. This reference frame is the [IGS](#) implementation of the [ITRF2000](#) ([Altamimi et al., 2002](#)). Stations with data problems or discontinuities are temporarily or permanently excluded from datum definition (e.g., IGSMAILs 4666, 4748, 4928). The datum stations and the exclusions are listed in Appendix A. Scale and origin of the network are determined by the [GPS](#) observations. Solid Earth tides are modeled according to the [IERS Conventions 2003](#) ([McCarthy and Petit, 2004](#)). The permanent tidal contribution is left in the tide model but is not included in the station coordinates. Corrections for the pole tide are applied using constant pole offsets ($\bar{x}_p = 0.033$ as, $\bar{y}_p = 0.331$ as). The oceanic pole tide is neglected. Ocean loading is corrected for with the GOT00.2 model, the successor of the model described by [Ray \(1999\)](#). The coefficients were provided by the ocean loading service¹ of [Scherneck \(1991\)](#), corrections for the center of mass movement of the solid Earth due to the periodical water mass displacements of the oceans are not applied. Atmospheric tides, atmospheric loading as well as other loading effects are not corrected for. Vertical antenna offsets are applied as given in the file <ftp://igs.cb.jpl.nasa.gov/igs/cb/station/general/igs.snx> for active [IGS](#) stations. For non-[IGS](#) stations and inactive stations the information has been extracted from the station log files and from the Scripps Orbit and Permanent Array Center ([SOPAC](#)) Site Information Manager². Horizontal antenna offsets are applied (from the stations listed in Appendix B only NYAL and WUHN have horizontal offsets). As these offsets were initially not given in the `igs.snx` file, they were taken from the station log files.

Atmospheric Parameters and Effects The a priori troposphere zenith delay of the [Saastamoinen \(1973\)](#) model (hydrostatic part only, standard atmosphere according to Eq. 2.26a with reference height $h_{ref} = 0$ m and reference pressure $p_{ref} = 1013.25$ mbar) is mapped to the actual zenith angle with the hydrostatic Isobaric Mapping Function ([IMF](#)). The height of the 200 hPa pressure layer (z_{200}) is linearly interpolated from [ECMWF](#) data provided by the Institute of Geodesy and Geophysics, TU Vienna³ with a temporal resolution of 6 hours and a spatial resolution of $2.5^\circ \times 2.0^\circ$.

¹<http://www.oso.chalmers.se/~loading/>

²http://sopac.ucsd.edu/scripts/SIMpl_launch.cgi

³<http://mars.hg.tuwien.ac.at/~ecmwf1/Z200/>

Year	1994	1995	1996	1997	1998	1999	2000	2001	2002	2003	2004
Lat. [°]	79.28	79.31	79.35	79.38	79.41	79.45	79.48	79.52	79.55	79.59	79.62
Lon. [°]	-71.38	-71.44	-71.51	-71.57	-71.64	-71.71	-71.78	-71.85	-71.92	-71.99	-71.06

Tab. 3.1: Coordinates of the geomagnetic north pole derived from the International Geomagnetic Reference Field (IGRF) 9th Generation model (*Macmillan et al., 2003*).

Continuous piecewise linear troposphere parameters are estimated in 2-hour intervals using the wet *Niell (1996)* mapping function. To avoid singularities in periods with very few observations, loose relative and absolute constraints of 2.5 m are applied for the estimation of the troposphere zenith delays. Troposphere gradients in north-south and east-west direction are modeled as continuous piecewise linear functions with a parameter interval of 24 hours applying the partial derivative of the wet Niell mapping function according to Eq. 2.32.

The first order term of the ionospheric refraction is eliminated by forming the ionosphere-free linear combination L_3 . Second and third order terms are modeled according to Eqs. 2.42 and 2.43. The TEC information needed for the computation of these corrections is taken from the global ionosphere maps estimated within the 1-day solution (see Sec. 3.2.1). The GIMs are determined from the L_4 linear combination of smoothed code observations (see Eq. 2.5) with an elevation cut-off angle of 10° and a sampling rate of 5 minutes. A continuous piecewise linear function with a time spacing of two hours is used for the spherical harmonic expansions up to degree and order 15 that represent the GIMs (i.e., $13 \times 256 = 3328$ parameters per day). Relative constraints of 0.03 TECUs are applied between consecutive spherical harmonic coefficients of the same degree and order to avoid unreasonably large TEC variations in regions not covered by the tracking network (*Schaer, 1999*). The coordinates of the geomagnetic pole needed for Eq. 2.40 and 2.44 are given in Tab. 3.1.

Satellite Orbits The radiation pressure model according to Eq. 2.48 is used but only five of the nine radiation pressure parameters are estimated: the three constant parameters and the periodic parameters in X -direction. The other parameters are heavily constrained to zero. Pseudo-stochastic pulses in radial, along-track and cross-track direction are set up at 12-hour intervals. These pulses are constrained to zero with 10^{-6} , 10^{-5} and 10^{-8} m/s², respectively. The absence of the radiation pressure of the Sun when the satellite passes the shadow of the Earth is considered with a cylindric model (see Sec. 2.6.2). For the Moon an umbra/penumbra model is used. For orbit integration the JGM3 gravity field (*Tapley et al., 1996*) up to degree and order 12 including secular variations for J_2 and the ocean tide model CSR 3.0 (*Eanes and Bettadpur, 1996*) are applied. The JPL ephemeris DE405 (*Standish, 1998*) is used to derive the positions of the Moon and the Sun for computing third-body forces. The positions of the planets Venus, Mars and Jupiter are computed according to *Seidelmann (1992)* and their third-body forces are also considered. The oceanic pole tide is neglected. The general relativistic effect for the equation of motion (Eq. 2.79) is applied but geodesic and Lense-Thirring precession are neglected as these effects have no significant influence on GPS orbits. Nominal attitude is applied according to Sec. 2.6.1. Epochs with large deviation from nominal attitude are excluded automatically during the residual screening.

Earth Orientation Parameters Earth orientation parameters are initially set up with a 2-hour resolution as continuous piecewise linear functions. The pole coordinates are estimated freely whereas the first UT1–UTC parameter of each individual solution is constrained to its a priori value (Bulletin A, *Luzum et al., 2001*) and the other parameters are estimated freely, too. Due to their high correlations with the orbital elements, retrograde terms of polar motion are blocked on the normal equation level (*Hefty et al., 2000*) when estimating ERPs with subdaily resolution. Subdaily variations of the Earth rotation caused by ocean tides are modeled with the IERS2003 subdaily ERP model (successor of the model described by *Ray et al., 1994*). The nutation is accounted for with the IAU2000A model (*Mathews et al., 2002*). Atmospheric subdaily Earth rotation variations as well as high-frequency nutation are not modeled. The nutation parameters $\Delta\psi$ and $\Delta\epsilon$ are usually heavily constrained to the values of the a priori model and their rates are only estimated freely in a special solution, see Sec. 3.2.2.

Antenna Phase Center Variations and Offsets Absolute models for antenna phase center variations and offsets for the receiver (*Menge et al., 1998*) as well as the satellite antennas (*Schmid and Rothacher, 2003*)

Block	Nadir angle														
	0°	1°	2°	3°	4°	5°	6°	7°	8°	9°	10°	11°	12°	13°	14°
I	-0.6	-3.8	-1.0	-1.0	0.4	1.3	2.0	2.1	2.0	0.9	0.3	-0.4	-0.8	-0.9	-0.6
II/IIA	-0.2	-0.7	-0.9	-0.9	-0.6	0.0	0.6	1.2	1.4	1.2	0.7	-0.1	-0.5	-0.7	-0.6
IIR-A	-4.6	-4.5	-2.8	-0.9	1.3	3.0	3.9	4.1	3.4	2.2	0.4	-1.2	-2.0	-1.7	-0.6
IIR-B/M	10.6	10.4	8.1	4.7	0.6	-3.9	-7.7	-9.8	-10.3	-9.5	-7.4	-4.2	0.1	5.9	12.4

Tab. 3.2: Block-specific satellite antenna phase center variations (TUM05) in millimeters.

Block	SVN/ z -Offset [m]														
I	9	10	11												
	1.7866	1.7414	1.7658												
II	13	14	15	16	17	18	19	20	21						
	2.5072	2.6585	2.2409	2.3426	2.2217	2.4020	2.7475	2.3822	2.3747						
IIA	22	23	24	25	26	27	28	29	30	31					
	2.2373	2.5530	2.3934	2.2660	2.2565	2.4218	2.3406	2.3158	2.3322	2.0421					
	32	33	34	35	36	37	38	39	40						
	2.1511	2.5686	2.2139	2.4282	2.6496	2.1563	2.3400	2.2666	2.3223						
IIR-A	41	43	44	45	46	51	54	56							
	1.1125	1.1635	0.8245	1.1640	0.8597	1.1266	1.0325	1.2682							
IIR-B	47	59	60	61											
	0.6287	0.5257	0.4429	0.4914											
IIR-M	53														
	0.5600														

Tab. 3.3: Satellite-specific vertical satellite antenna offsets (TUM05) in meters.

are applied. The block-specific satellite antenna *PCVs* are listed in Tab. 3.2 and the satellite-specific z -offsets in Tab 3.3. These values are the *TUM* contribution for the generation of the *IGS* absolute antenna model, see *Schmid et al. (2007)*. The value for the IIR-M satellite is the mean value of the analysis of 31 days of reprocessing solution M3 (see Tab. 3.7). The block-specific horizontal satellite antenna offsets are given in Tab. 7.1. Radome calibrations are not considered in the standard solutions. For receiver antennas with calibration values down to 10° only, the 10° -value is used for lower elevations. For more details on the estimation of satellite antenna offsets and *PCVs* as well as the effects of different antenna calibrations on other parameters see Sec. 9.

3.2. Processing Strategy

The reprocessing is based on four different solutions: 1-day solution, preliminary 3-day solution, weekly solution and final 3-day solution, see Fig. 3.1. In the latter solution, the coordinates and Earth rotation parameters of the weekly solution are kept fixed and the troposphere parameters and orbits are recomputed to get a consistent set of parameters. An overview of the parameters estimated within each individual solution is given in Tab. 3.4.

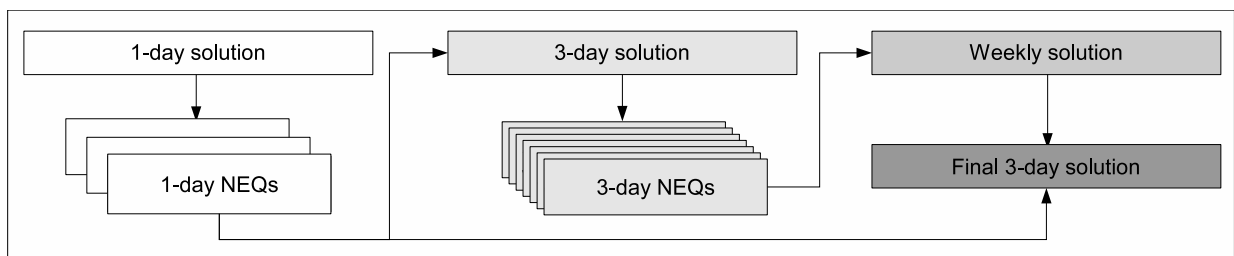


Fig. 3.1: Processing scheme used for reprocessing.

Parameter	Solution			
	1-day	prel. 3-day	weekly	final 3-day
Station coordinates	x	x	x	f
Earth rotation parameters	x	x	x	f
Satellite orbits	x	x	p	x
Troposphere parameters	x	x	p	x
Origin of the tracking network	x	x	x	x
Ambiguities	x	p	p	p
Differential code biases	x	–	–	–
Receiver and satellite clocks	x	–	–	–
Global ionosphere maps	x	–	–	–
Nutation rates	(x)	x	–	–
Subdaily ERPs	x	x	–	–
Satellite-specific PCVs	(x)	(x)	–	–
Station-specific Love numbers	(x)	–	–	–

Tab. 3.4: List of parameters estimated within the different solutions. (x) indicates that these parameters are setup but heavily constrained to their a priori values. p indicates that these parameters are pre-eliminated. f indicates that these parameters are fixed to the results of the weekly solution.

3.2.1. 1-day Solution

Fig. 3.2 shows the reprocessing scheme of the 1-day solution. Starting point are RINEX observation data available at the IGS⁴, EUREF⁵ and SOPAC⁶ data centers, merged IGS/CODE orbits and Bulletin A Earth rotation parameters as a priori information. Prior to 14 November 1993, where no IGS orbits are available, only CODE orbits are used. For some days in 1993 no broadcast clocks are contained in the CODE orbits, for these days the clocks are extracted from the RINEX navigation data.

In a first step receiver clock jumps are detected and corrected for by comparing the epoch-to-epoch differences of the phase and the code observations and the code observations are smoothed using the phase measurements. After synchronizing the receiver clocks using the code observations, stations with a code RMS of more than 999 m are deleted. Single-differences are formed with a strategy selecting the baselines with the highest number of common observations from all possible baselines, for details see Dach *et al.* (2007). After correcting cycle-slips on the triple-difference level a first ambiguity-free solution is computed. Based on this solution the observations are screened for outliers on the double-difference level. Bad stations and satellites (due to maneuvers or modeling problems) and satellites with less than 1000 observations per day are detected and automatically excluded from the processing. The number of 1000 observations has been determined empirically by comparing orbits of satellites with few observations with the IGS final orbits. If a bad satellite has been detected, this satellite is excluded for the whole day and the processing jumps back to the conversion of the RINEX files. If one or more bad stations have been detected, the corresponding zero-difference files are deleted and the forming of the single-differences is repeated. These iteration steps are repeated four times at maximum.

After an outlier detection step on the zero-difference level, the global ionosphere maps as well as P1P2-DCBs for receivers and satellites are estimated from smoothed code observations using the geometry-free linear combination L_4 . The a priori values for the DCBs are the result of a combination of the corresponding normal equations of the last 30 days. Afterwards, a second ambiguity-free solution is computed. As ambiguity resolution is crucial for high-precision geodetic applications (Mervart, 1995), ambiguities are resolved to integers for baselines up to 6000 km using different approaches depending on the baseline length, see Tab. 3.5.

For the Melbourne Wübbena approach (see Sec. 2.3.1) high-quality code observations are essential. As ROGUE receivers without ACT technology (ROGUE SNR-800, SNR-8000, SNR-8100) provide only low-quality code observations, baselines where one or both stations are equipped with such a receiver type are excluded from the MW AR. In addition to these ROGUE receivers, baselines with a RMS larger than 20 cm in the code residual screening performed within this ambiguity resolution step are also excluded from

⁴<http://igsceb.jpl.nasa.gov/components/data.html>

⁵http://www.epncb.oma.be/_dataproducts/datacentres/

⁶<http://sopac.ucsd.edu/dataArchive/>

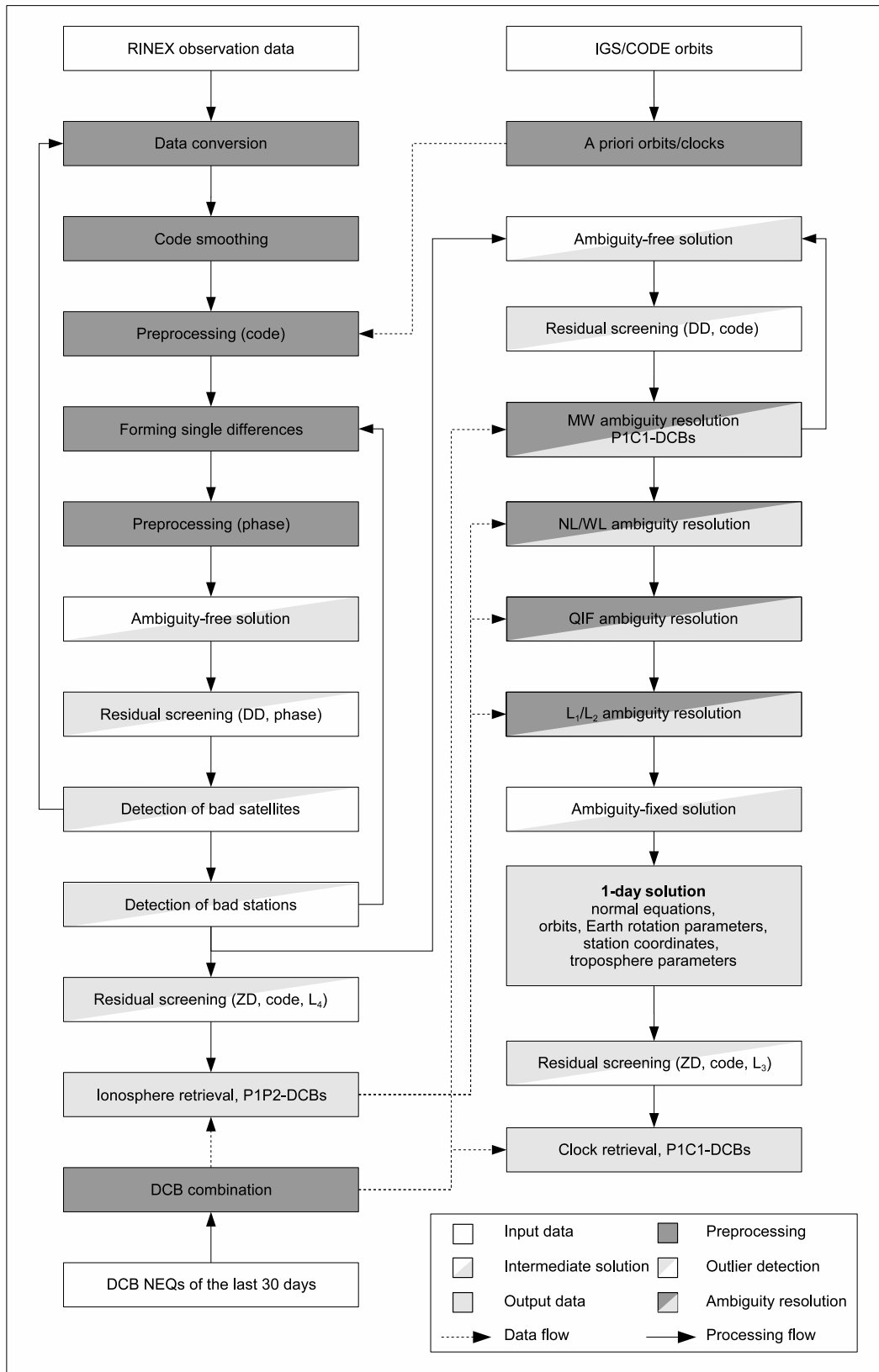


Fig. 3.2: Flow chart of the 1-day solution.

Method	Baseline length
Melbourne-Wübbena	≤ 6000 km
Quasi-Ionosphere-Free	≤ 2000 km
Wide-Lane/Narrow-Lane	≤ 200 km
Direct solution of L_1 and L_2	≤ 20 km

Tab. 3.5: Ambiguity resolution strategies depending on the baseline length.

the **MW AR**. As the network used for reprocessing contains C1- as well as P1-receivers, P1C1-DCBs for satellites have to be estimated within the **MW AR**. A combination of the DCBs over the last 30 days is used as a priori information. These DCBs are a refinement (fixed ambiguities) of the DCBs estimated in the DCB/clock solution described at the end of this section. In a first iteration of the **MW AR**, ambiguities for baselines up to 3000 km are solved. Subsequently, the second ambiguity-free solution and the residual screening already mentioned above and the **MW AR** for resolving remaining ambiguities of baselines up to 6000 km are repeated. The wide-lane/narrow-lane approach (see Sec. 2.3.2) is used for baselines up to 200 km. For the **QIF** ambiguity resolution strategy (see Sec. 2.3.3), which is used for baselines up to 2000 km, the previously estimated ionosphere maps are introduced as a priori ionosphere information. For short baselines up to 20 km the ambiguities are resolved independently on L_1 and L_2 .

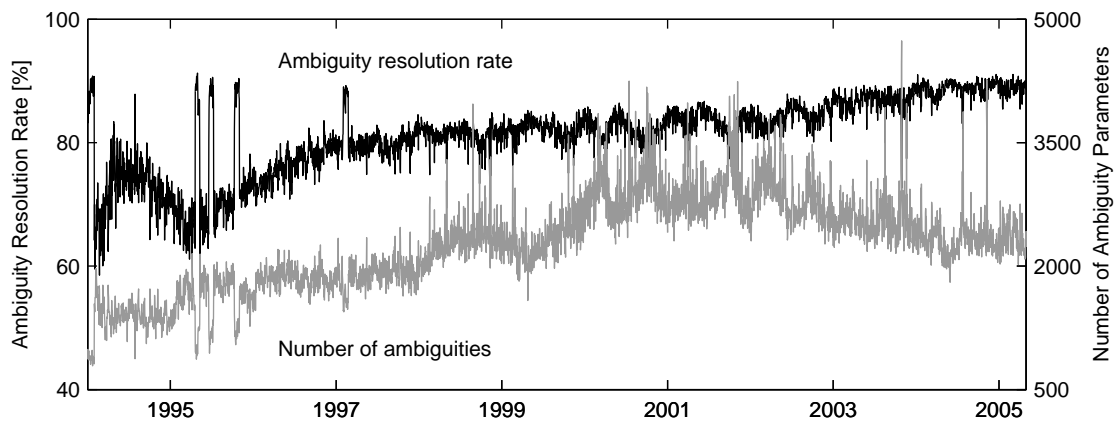


Fig. 3.3: Number of ambiguities (gray) and ambiguity resolution rate (black) in the 1-day solution. During periods with **AS** off (see Tab. 2.2) the ambiguity resolution rate is significantly higher.

Fig. 3.3 shows that the fraction of resolved ambiguities increases with time due to the densification of the global network and the corresponding decrease of the baseline lengths. In addition, new receiver technology led to a further improvement in the ambiguity resolution rate in 2002–2003 when the number of stations is almost constant, see Fig. 4.1. At the beginning of 1994 about 65% of the ambiguities can be resolved, whereas at present time almost 85% of the ambiguities can be fixed to their integer values. In some periods between 1994 and 1997 where **AS** was switched off (see Tab. 2.2 and Fig. 3.3) the ambiguity resolution rate was, with about 90%, even higher than nowadays, since the P-code was not encrypted and also the phase observations had a higher quality.

After the time-consuming ambiguity resolution steps, the final 1-day ambiguity-fixed solution is computed in four station clusters. The first cluster (number 0) contains redundant baselines, the other three clusters are formed by the geographic distribution of the stations:

1. Europe
2. North and South America
3. Asia, Australia, Africa and Antarctica

These three clusters are computed with full correlations. For the cluster with redundant baselines, only the correlations within each baseline are modeled correctly. The number of observations in this redundant cluster is small (10–15%) as these baselines are quite long, see Fig. 3.4. But even these few observations help to connect the other three clusters and to strengthen the stability of the polyhedron of stations, see [Brockmann \(1997\)](#). The normal equations of these four clusters are combined to the final 1-day solution. The station coordinates, **ERPs** and orbits of this solution are used to compute 5-min satellite clocks and

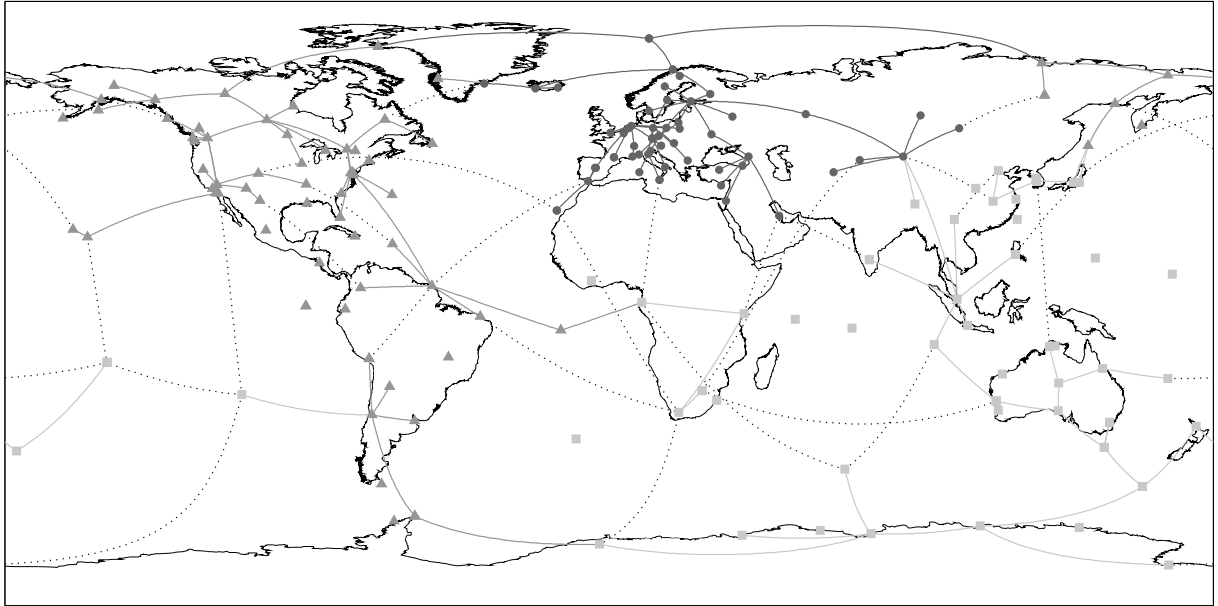


Fig. 3.4: Station cluster and baseline definition for 1 January 2003: stations belonging to cluster 1 (Europe) are represented by dots, cluster 2 (North and South America) by triangles, cluster 3 (Asia, Australia, Africa, Antarctica) by squares, redundant baselines (cluster 0) are represented by dotted lines. Stations with no baseline connections were not observed at that particular day.

P1C1-DCBs for satellites based on smoothed zero-difference code observations. A priori values for the DCB estimation are combination results of the last 30 days. In the early years there are several days with only cross-correlation receivers (that are not capable to track the P-code under AS conditions) observing: an estimation of P1C1-DCBs is not possible for these days and the corresponding parameter estimation step is skipped. Cleaned single-difference files with fixed ambiguities and normal equations of the 1-day solution (including station and origin coordinates, troposphere zenith delays and gradients, orbit parameters, EOPs, station-specific Love numbers and satellite-specific PCVs), the P1C1- and the P1P2-DCB retrieval results are saved for further investigations and the multi-day solutions. The computation time for a single 1-day solution depends on the number of stations and parameters and varies between 40 minutes (1994) and four hours (2005) on the hardware described in Sec. 3.2.5.

3.2.2. 3-day Solution

The multi-day solutions (preliminary 3-day, weekly and final 3-day solution, see Fig. 3.5) are handled on the normal equation level. A set of three normal equations from consecutive 1-day solutions is combined to a preliminary 3-day solution. The 3-day orbits are usually represented by one set of osculating elements, radiation pressure parameters and pseudo-stochastic pulses at 12-hour intervals, thus strengthening the stability of the arcs. If this is not possible due to modeling problems or maneuvers, a 3-day arc is split up at the day boundaries into two or even three arcs. In the basic 3-day solution the ERPs, which were set up at 2-hour intervals, are transformed to daily parameters. The ERPs as well as the troposphere parameters, which have discontinuities at the day boundaries, are stacked at the day boundaries to form a continuous piecewise linear function over the whole 3-day interval. Special 3-day solutions are generated in separate runs:

- Subdaily Earth rotation parameters (pole coordinates and length of day with 2-hour resolution)
- Nutation rates (corrections of the rates in longitude and obliquity with respect to the IAU2000A model, one rate in longitude and obliquity per 3-day interval)
- Origin of the tracking network (using a NNR/NNT condition for datum definition).

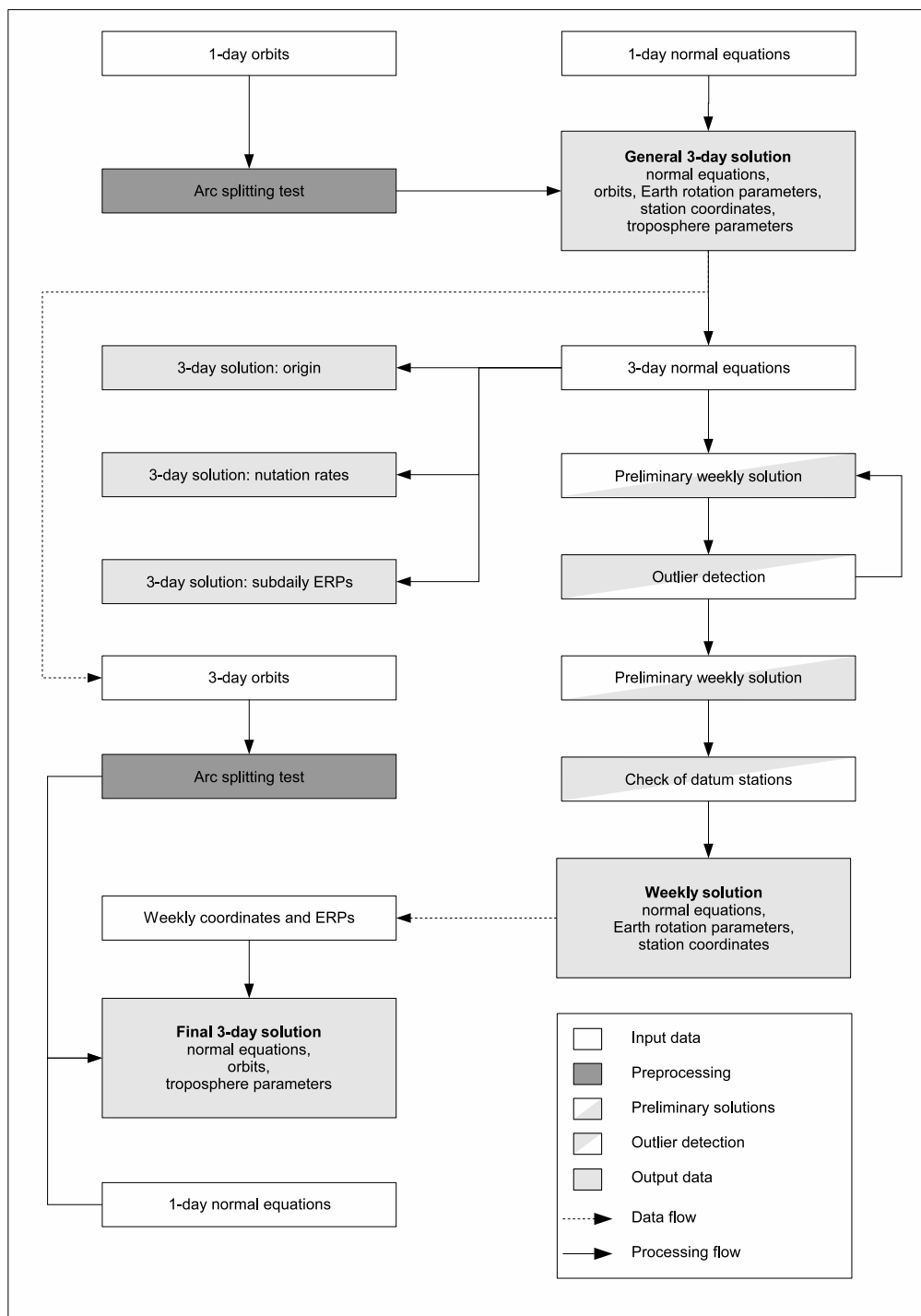


Fig. 3.5: Processing scheme of the preliminary 3-day solution, the weekly solution and the final 3-day solution.

3.2.3. Weekly Solution

A set of seven consecutive 3-day normal equations is combined to a weekly solution to estimate the final coordinates and Earth rotation parameters. Based on this weekly solution, stations with a bad repeatability or big residuals of the 3-day solutions compared to the weekly solution are excluded automatically. The limits defining, whether a station is excluded or not, depend on time, have been determined empirically and

Type	R_{max}			R_{min}			$s_{R,x}$		
	N	E	U	N	E	U	N	E	U
RMS	40 mm	40 mm	100 mm	8 mm	8 mm	20 mm	$\frac{32}{532900}$	$\frac{32}{532900}$	$\frac{32}{532900}$
Residuals	50 mm	50 mm	125 mm	10 mm	10 mm	25 mm	$\frac{40}{532900}$	$\frac{40}{532900}$	$\frac{100}{532900}$

Tab. 3.6: Outlier criteria for automated station pre-elimination in the weekly solution.

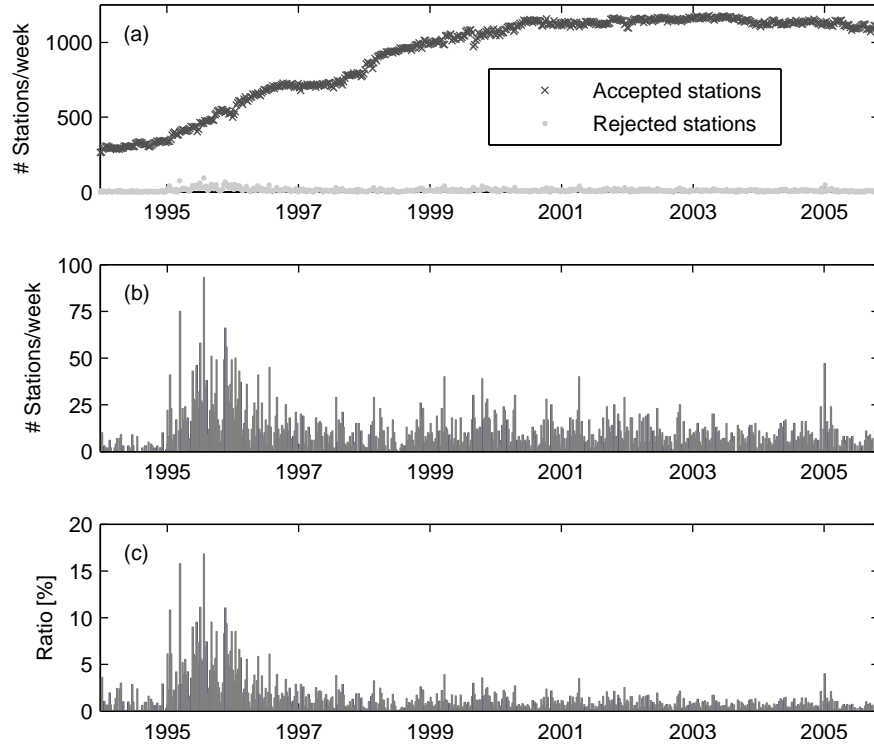


Fig. 3.6: Automatic pre-elimination of stations: (a) number of accepted and rejected stations per week; (b) number of rejected stations per week; (c) ratio of rejected number of stations w.r.t. total number of stations per week.

are given by

$$R_{max}(t, x) = (t - t_0)^2 \cdot s_{R,x} \cdot [R_{max,x} - R_{min,x}] \cdot k + R_{min,x} \quad \text{with} \quad \begin{cases} k = 1 & \text{for } t < t_0 \\ k = 0 & \text{for } t \geq t_0 \end{cases} \quad (3.1)$$

R_{max}	outlier criteria for maximum RMS or residuals
x	coordinate component in the local system (north, east, up)
t	time in MJD
t_0	reference epoch MJD
$s_{R,x}$	scale factor, see Tab. 3.6
$R_{min,x}$	coefficients for minimum RMS or residuals, see Tab. 3.6
$R_{max,x}$	coefficients for maximum RMS or residuals, see Tab. 3.6.

In the early years ($t < t_0 = 1$ January 1996) the limits are higher to avoid a further thinning of the already sparse tracking network.

In addition, stations with less than two observation days per week are pre-eliminated. The actual numbers of accepted and rejected stations according to these criteria are displayed in Fig. 3.6. In a second step stations defining the datum are compared to their a priori IGB00 coordinates using a 7-parameter similarity transformation. Stations with residuals larger than 10 mm for the horizontal components or 30 mm for the

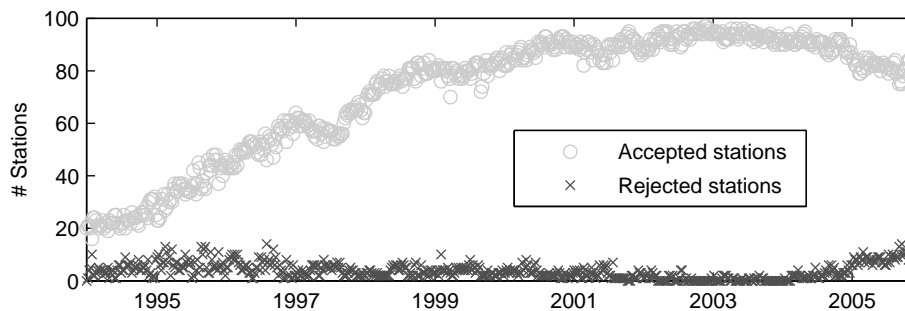


Fig. 3.7: Automatic check of datum stations: number of accepted and rejected stations per week.

height component are not used for datum definition. In Fig. 3.7 the number of datum stations passing this check and the number of stations excluded from datum definition are plotted. Due to deficiencies of the IGB00 reference frame (which includes data up to 17 August 2003) the number of rejected stations grows in 2004 and 2005.

3.2.4. Final 3-day Solution

The coordinates and Earth rotation parameters of the weekly solution are back-substituted into the final 3-day solution. Based on the 3-day orbits another arc-splitting test is performed to detect whether a further splitting is necessary that has not been detected with the 1-day orbits. A set of three consecutive 1-day normal equations is used to compute the final troposphere parameters and orbits. These form, together with the weekly coordinates and ERPs, a consistent set of products.

3.2.5. Hardware and Software Used for Reprocessing

The data processing was performed on the serial 32-bit part of the Linux cluster operated by the Leibniz-Rechenzentrum (LRZ) of the Bavarian Academy of Sciences. A maximum number of 16 nodes (Pentium IV, 3.06 GHz, 1.0–1.5 GB RAM), disk storage of one Terabyte and the storage archive could be used. For the GPS processing a modified version of the Bernese GPS Software 5.0 (Dach *et al.*, 2007) developed at the Astronomisches Institut der Universität Bern (AIUB) was used. Major modifications are the implementation of IMF, GMF, VMF1, hydrostatic troposphere a priori delays from ECMWF, 2nd and 3rd order ionosphere corrections and the estimation of site-specific Love numbers. By using the Bernese Processing Engine (BPE) a very high degree of automatization of the individual processing steps has been achieved so that the reprocessing can be performed with a minimum of human interaction. The CPU time for run M3 (see Tab. 3.7) and several special solutions based on this run (e.g., Tab. 9.1) was about 40,400 hours (almost 18,000 jobs).

3.2.6. Reprocessing Runs

Altogether three complete runs of the reprocessing have been performed, labeled M0, M1 und M3. The major differences of the three runs are listed in Tab. 3.7. The run M2 was not completed and is therefore not contained in Tab. 3.7. Run M0 is affected by the Bernese tide bug (BSWMAIL 190⁷), hence the results are not discussed in this thesis. It is only mentioned here, because it was used for the estimation of the satellite antenna PCVs and offsets used for run M1. Run M0 was also used for the first detection of station coordinate discontinuities and outliers, see Sec. 4.2. The additional parameters, namely the block-specific satellite antenna offsets, the satellite-specific PCVs and the station-specific Love numbers are heavily constrained to their a priori values in the solutions described above. The processing scheme described so far corresponds to run M3 as well as the results discussed in the next chapters, if not explicitly stated otherwise. Due to the very small tracking network in 1993, resulting in a degraded quality of the estimated parameters, that year was not considered for run M3 which starts on 1 January 1994 and ended on 31 March 2005 in a first version. It was later extended till 31 October 2005.

⁷<http://www.aiub.unibe.ch/download/bswmail/bswmail.0190>

	M0	M1	M3
Time interval	1993 – 2004	1993 – 2004	1994 – 2005
Number of stations	192	195	202
Mapping function for hydrostatic a priori delay	hydr. NMF	hydr. NMF	hydr. IMF
Satellite antenna PCVs	PHAS_ABS.03 ^a	PHAS_ABS.04 ^b	PHAS_ABS.05 ^c
Satellite antenna PCOs	SAT_ABS.03 ^a	SAT_ABS.04 ^b	SAT_ABS.05 ^c
2nd and 3rd order ionosphere	–	–	x
Exclusion ROGUE MW AR	–	–	x
Pre-elimination of bad stations in the weekly solution	–	x	x
Correction of clock jumps	–	–	x
Setup of block-specific satellite antenna PCOs	x	x	–
Setup of satellite-specific PCVs	–	–	x
Setup of station-specific Love numbers	–	–	x
C1 clock and DCB retrieval	x	–	x

^a block-specific satellite antenna [PCVs](#) and z -offsets estimated by [Schmid and Rothacher \(2003\)](#)

^b block-specific satellite antenna [PCVs](#) and z -offsets estimated from data of the M0 reprocessing run

^c block-specific satellite antenna [PCVs](#) and satellite-specific z -offsets estimated from data of the M1 reprocessing run, [TUM](#) contribution to [Schmid et al. \(2007\)](#)

Tab. 3.7: Important differences of the three reprocessing runs M0, M1 and M3.

4. Data

In the first part of this chapter, details on the tracking stations and the satellites used in the reprocessing are given. The second part discusses the detection of outliers and discontinuities in the station coordinate time series. Several examples of tracking problems and other deficiencies illustrate the consequences of systematic effects on GPS-derived parameter time series. The detection of such effects is essential to avoid misinterpretations of the resulting time series.

4.1. Tracking Station Network and Satellite Constellation

The station selection was primarily based on the following criteria:

- good global coverage
- long observation time span
- co-locations with other space geodetic techniques as well as tide gauges
- geo-scientific relevance
- contribution to existing reference frames.

The goal of a good global coverage is difficult to reach as the distribution of GPS tracking stations is very inhomogeneous. Whereas many stations are located in Europe and Northern America, the number of stations on the southern hemisphere is comparatively small. This fact is also reflected in the distribution of the stations used for the reprocessing: 142 stations are located on the northern, but only 60 on the southern hemisphere. The number of co-located stations and of stations contributing to existing reference frames is given in Tab. 4.1. The nominal number of stations is 202, but due to changes of the station distribution (deactivation/outages of stations) the number of stations per day rarely exceeds 165. Most stations (184) of the reprocessing network are IGS¹ stations, but also several non-IGS stations meeting the criteria mentioned above have been considered. These stations belong to the permanent networks EPN² (EUREF Permanent Network, 2 stations) and CORS³ (Continuously Operating Reference Stations, 9 stations), respectively. In addition, seven offline observing stations in Antarctica and Greenland contribute to the selected tracking network. A complete list of the tracking stations is given in Appendix B.

The Figs. 4.1, 4.2 and 4.3 show the temporal evolution of the number of stations and their spatial distribution. At the beginning, the tracking network is quite sparse with only about 40 stations. The decrease

¹<http://igsceb.jpl.nasa.gov/network/netindex.html>

²http://www.epncb.oma.be/_trackingnetwork/

³<http://www.ngs.noaa.gov/CORS/cors-data.html>

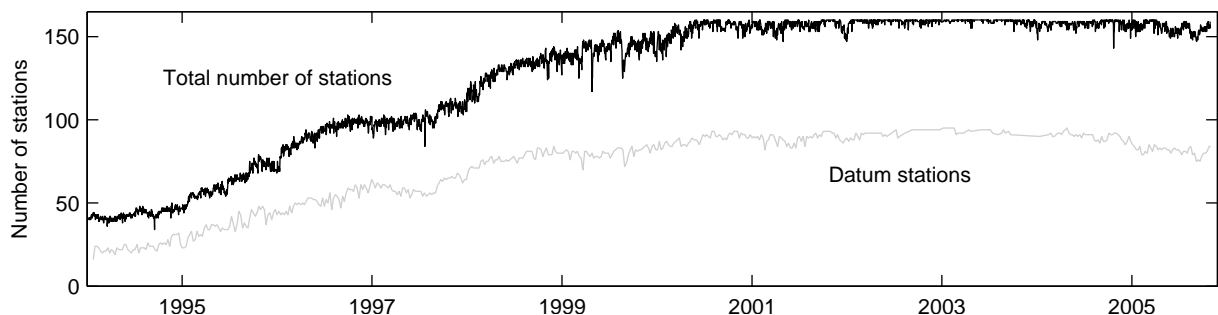


Fig. 4.1: Evolution of the number of stations: total number of stations (black) and number of datum stations (gray), respectively.

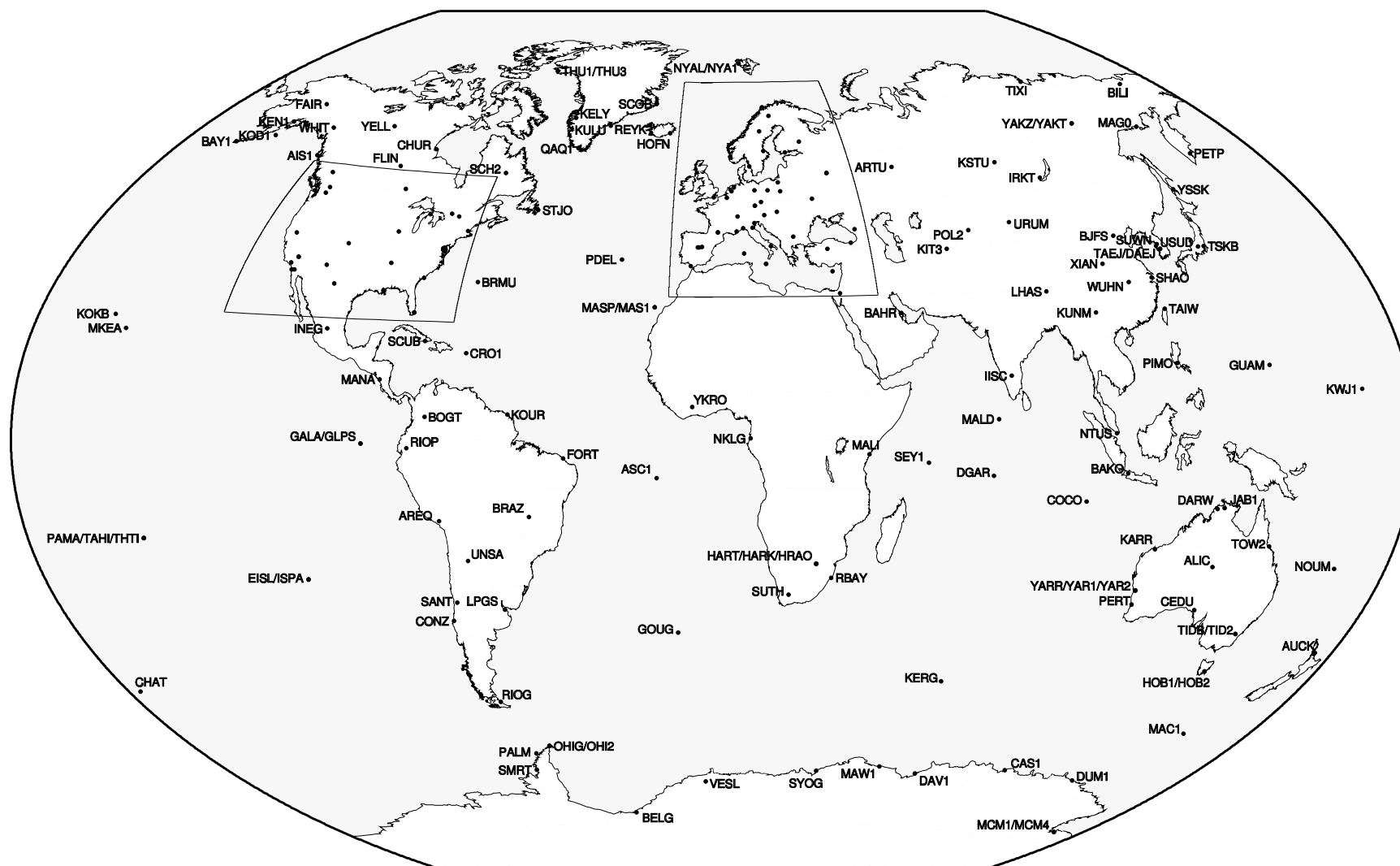


Fig. 4.2: Spatial distribution of the stations used for the reprocessing. Detailed maps for Europe and North America are shown in Fig. 4.3.

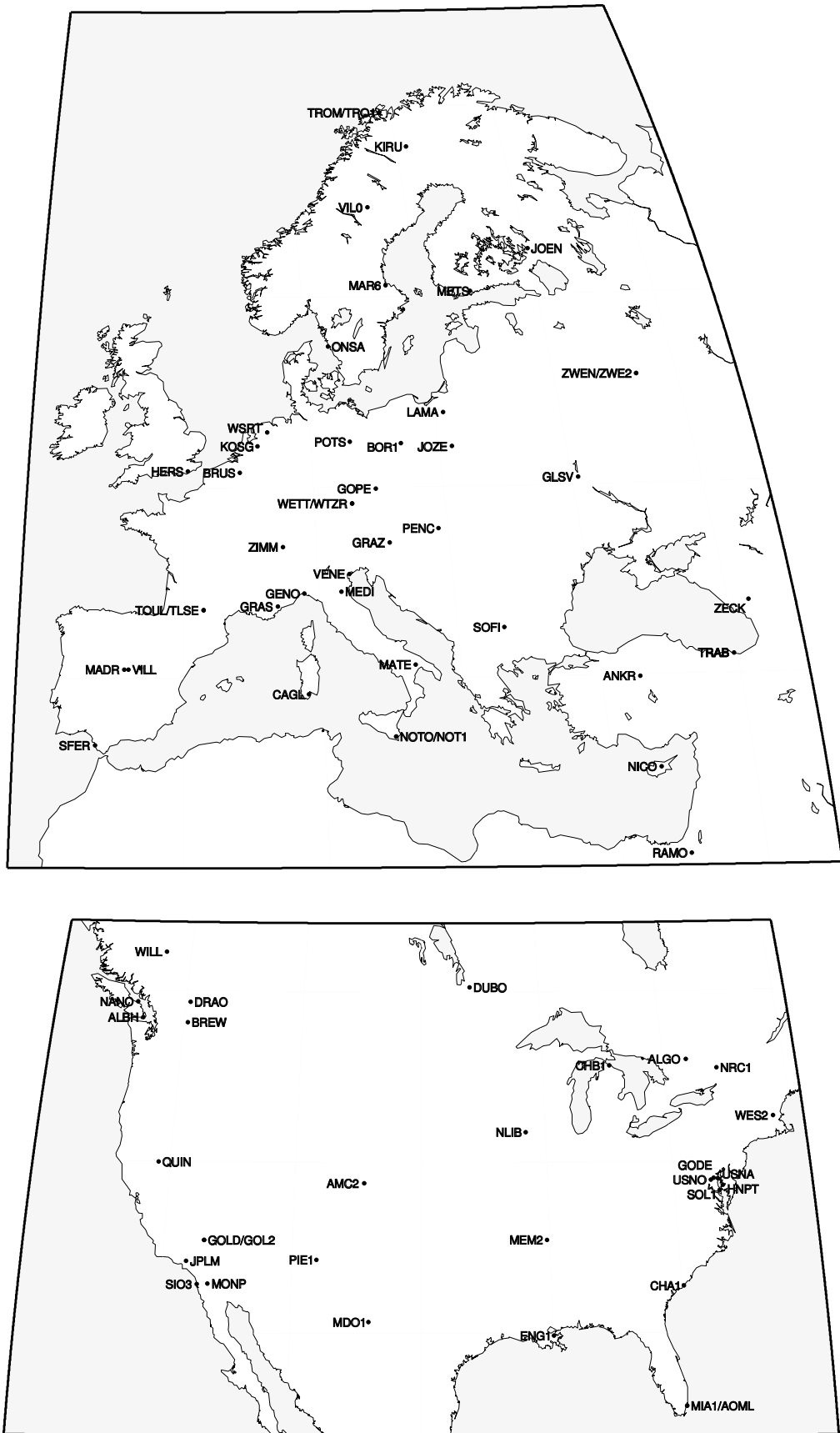


Fig. 4.3: Detailed station maps for Europe and North America.

Co-location with	# stat.
DORIS	45
SLR	32
VLBI	32
Tide gauges	19
IGS00	54
IGb00	99

Tab. 4.1: Number of co-located stations and contributions to existing reference frames.

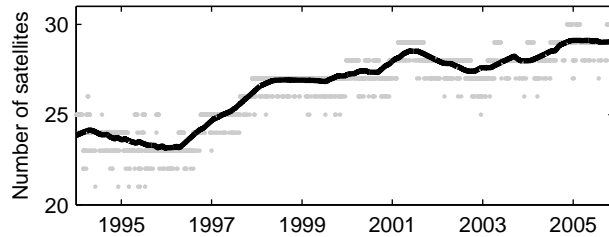


Fig. 4.4: Evolution of the number of satellites used for the reprocessing. The solid line represents a yearly running mean.

of the number of stations in August 1999 is related to an outage of the Crustal Dynamics Data Information System (CDDIS). The maximum number of about 160 stations is reached in the year 2000. If more than 160 stations are present for one day, the worst stations (selection based on the observation time and the number of tracked satellites) are excluded to comply with a maximum of 160 stations to limit the processing load. In 2005, the total as well as the number of datum stations slightly decreases due to the decommissioning of some stations.

All GPS satellites involved in the reprocessing are listed in Tab. 4.2, and the evolution of the number of satellites actually used in the 1-day solutions is shown in Fig. 4.4. As the PRN number is not unique, also the Space Vehicle Number (SVN) and the Committee on Space Research (COSPAR) ID are given to distinguish between the individual satellites. SVN 35 and 36 are equipped with a Laser Retroreflector Array (LRA) that can be used for an independent validation of the GPS-derived satellite orbits with Satellite Laser Ranging (SLR) measurements, see Sec. 7.4. SVN 23 suffers from problems with its solar panels: shortly after the launch of this satellite, the control system of one of the solar arrays failed and this array could not be pointed towards the Sun automatically. Therefore, the solar arrays had to be pitched manually in four different modes depending on the elevation β_0 of the Sun w.r.t. the orbital plane (see Fig. 2.6):

- $|\beta_0| > 45^\circ$ hold mode, arrays at 90°
- $30^\circ < |\beta_0| < 45^\circ$ scissor mode, one array at 70° and the other at 110° , the position of each array is swapped once per day
- $15^\circ < |\beta_0| < 30^\circ$ intermediate slew mode, the arrays are slewed to $135^\circ/95^\circ$ at each orbit dawn and to $45^\circ/85^\circ$ at each orbit dusk
- $|\beta_0| < 15^\circ$ hyper slew mode, the arrays are slewed to $155^\circ/115^\circ$ at each orbit dawn and to $25^\circ/65^\circ$ at each orbit dusk.

This so-called four season operation (Dieter and Taylor, 1999) resulted in severe orbit modeling problems. In January 2002, an automated mechanism to pitch the solar panels was implemented that significantly improved the orbit quality (Hugentobler et al., 2003, and Fig. 7.6).

Several satellites suffer from failures of RWs responsible for maintaining the satellite's attitude. Due to the Space Shuttle accident in 1986, the launch of several satellites was delayed. Thus, these satellites were put into storage that resulted in significant bearing lubricant leakage responsible for RW failures (Violet et al., 1999). As soon as this problem had been discovered, the satellites still on storage were refurbished. However, altogether 10 satellites already in orbit suffer from this problem (SVN 14–21, 23 and 24). Although the nominal attitude can be maintained with three operational RWs, satellites with RW failures are usually put into an operation mode that enables the attitude control thrusters to prevent a loss of stabilization in the case of another RW failure. Unfortunately, momentum dumps with electro-magnetic torquers cannot be performed in this operation mode. Therefore, the momentum has to be dumped by thruster firings. However, those introduce (as well as thruster firings to directly support the attitude control system) additional orbit perturbations resulting in a degraded orbit quality. Enabling the thrusters for attitude control purposes causes another problem, so-called glint firings during the eclipse season (Violet et al., 1999). The satellite's Earth sensor misinterprets the Sun's reflection off the Earth's surface as an attitude error. To correct for this apparent error, the thrusters are fired to maintain the nominal attitude resulting in significant orbit perturbations. In particular SVN 15 and 18 are prone to glint firings (Rivers, 2000). Examples of satellites with degraded performance will be discussed in Sec. 7.2.

For several satellites, two or even three different orbital slots are given. These satellites have been shifted to other slots within the same orbital plane as a result of changes in the satellite constellation. These shifts are

PRN	SVN	COSPAR ID	Block	Orbital plane	Start	End	Comment
1	32	1992-079A	IIA-16	F-1/F-4/F-6	22.11.1992	17.03.2008	PRN number of SVN 32 was changed from 32 to 1 on 28 January 1993 repositioned from slot 1 to 4 betw. 30 January 1999 and 28 January 2000 repositioned from slot 4 to 6 betw. 29 June and 18 November 2004
2	13	1989-044A	II-2	B-3/B-5	10.06.1989	12.05.2004	repositioned from slot 3 to 5 betw. 30 October 2001 and 10 April 2002
2	61	2004-045A	IIR-13	D-1	06.11.2004		Block IIR-B
3	11	1985-093A	I	C-4	09.10.1985	13.04.1994	
3	33	1996-019A	IIA-25	C-2	28.03.1996		
4	34	1993-068A	IIA-23	D-4	26.10.1993		
5	35	1993-054A	IIA-22	B-4	30.08.1993		LRA
6	36	1994-016A	IIA-24	C-1	10.03.1994		LRA
7	37	1993-032A	IIA-20	C-4/C-5	13.05.1993	20.12.2007	repositioned from slot 4 to 5 in 2006
8	38	1997-067A	IIA-28	A-5/A-3	06.11.1997		repositioned from slot 5 to 3 betw. 01 October 1999 and 08 March 2000
9	39	1993-042A	IIA-21	A-1	26.06.1993		
10	40	1996-041A	IIA-26	E-3	16.07.1996		
11	8	1983-072A	I	C-8	14.07.1983	04.05.1993	
11	46	1999-055A	IIR-3	D-2	07.10.1999		
12	10	1984-097A	I	A-1	08.09.1984	18.11.1995	
13	9	1984-059A	I	C-1	13.06.1984	20.06.1994	
13	43	1997-035A	IIR-2	F-5/F-3	23.07.1997		repositioned from slot 5 to 3 betw. 25 July and 10 October 2000
14	14	1989-013A	II-1	E-1	14.02.1989	14.04.2000	RW1 failure in August 1991 RW failure on 26 March 2000, satellite lost yaw control
14	41	2000-071A	IIR-6	F-1	10.11.2000		
15	15	1990-088A	II-9	D-2/D-5	01.10.1990	14.03.2007	RW1 disabled in April 1999 RW2 failure on 28 June 1999, RW1 re-enabled repositioned from slot 2 to 5 betw. 06 May 1999 and 29 July 1999 prone to glint firings (<i>Rivers, 2000</i>) since in AMMM Mode 5 working quite well
16	16	1989-064A	II-3	E-3/E-5	18.08.1989	13.10.2000	repositioned from slot 3 to 5 betw. 19 August 1996 and 02 January 1997 RW2 preemptively disabled before early 1996 RW4 failure in February 1996, RW2 re-enabled RW2 failure in March 1996 RW4 returned to life in late April 1996
16	56	2003-005A	IIR-8	B-1	29.01.2003		
17	17	1989-097A	II-5	D-3/D-6	11.12.1989	22.02.2005	repositioned from slot 3 to 6 betw. 17 April and 15 December 2003 RW3 failure in December 2000 supposed change in attitude control in mid of 2003
17	53	2005-038A	IIR-14/M-1	C-4	26.09.2005		
18	18	1990-008A	II-6	F-3	24.01.1990	18.08.2000	RW3 preemptively disabled before early 1996 RW failure in April 1996, RW3 re-enabled RW3 problems, start of thruster firings in January 1999

PRN	SVN	COSPAR ID	Block	Orbital plane	Start	End	Comment
							attitude control processor failure on 28 June 2000, lost Earth-pointing <i>RW</i> failure on 10 July 2000 prone to glint firings (<i>Rivers, 2000</i>)
18	54	2001-004A	IIR-7	E-4	30.01.2001		
19	19	1989-085A	II-4	A-4/A-5	21.10.1989	11.09.2001	<i>RW</i> 4 failure before early 1996 drifted from slot 4 to 5 in 1999
19	59	2004-009A	IIR-11	C-3	20.03.2004		Block IIR-B
20	20	1990-025A	II-7	B-2	26.03.1990	13.12.1996	<i>RW</i> 2 failure on 26 July 1991 <i>RW</i> 1 failure in April 1996
20	51	2000-025A	IIR-4	E-1	11.05.2000		
21	21	1990-068A	II-8	E-2	02.08.1990	27.01.2003	supposed <i>RW</i> failure in January 2001
21	45	2003-010A	IIR-9	D-3	31.03.2003		
22	22	1993-007A	IIA-18	B-1/B-6	03.02.1993	06.08.2003	repositioning from slot 1 to 6 started on 20 January 2003 no observations after 27 May 2003
22	47	2003-058A	IIR-10	E-2	21.12.2003		Block IIR-B
23	23	1990-103A	IIA-10	E-4/E-5	26.11.1990	13.02.2004	repositioned from slot 4 to 5 betw. 04 December 2002 and 27 May 2003 solar panel problem, see <i>Dieter and Taylor (1999)</i>
23	60	2004-023A	IIR-12	F-4	23.06.2004		Block IIR-B
24	24	1991-047A	IIA-11	D-1/D-7/D-6	04.07.1991		<i>RW</i> 3 disabled on 25 November 1999 in <i>AMMM</i> Mode 5 since 4 January 2005 repositioned from slot 1 to 7 betw. 23 November 2004 and 15 March 2005 official slot designation changed from 7 to 6 with demise of <i>SVN</i> 17
25	25	1992-009A	IIA-12	A-2	23.02.1992		
26	26	1992-039A	IIA-14	F-2	07.07.1992		
27	27	1992-058A	IIA-15	A-3/A-4	09.09.1992		drifted from slot 3 to 4 in 1999
28	28	1992-019A	IIA-13	C-2/C-5	10.04.1992	15.08.1997	repositioned from slot 2 to 5 betw. 06 March and 23 August 1996 navigational processor problems since November 1996
28	44	2000-040A	IIR-5	B-5/B-3	16.07.2000		repositioned from slot 5 to 3 betw. 02 August 2000 and 27 March 2001
29	29	1992-089A	IIA-17	F-4/F-1/F-5	18.12.1992	23.10.2007	repositioned from slot 4 to 1 in 1999 repositioned from slot 1 to 5 betw. 20 December 2001 and 27 June 2002 supposed change in <i>RW</i> performance in 2002 manual momentum dumps with thruster firing durations > 3 s (<i>Violet et al., 1999</i>)
30	30	1996-056A	IIA-27	B-2	12.09.1996		
31	31	1993-017A	IIA-19	C-3/C-5	30.03.1993	24.10.2005	repositioned from slot 3 to 5 betw. 04 May and 03 August 2004

Tab. 4.2: Satellites of the *GPS* constellation used for the reprocessing. Information based on the "Almanac" given in the August and December issues of *GPS World*, *CANSPACE NAVSTAR GPS Constellation Status* (<http://gge.unb.ca/Resources/GPSConstellationStatus.txt>), *USNO* satellite status (<ftp://tycho.usno.navy.mil/pub/gps/gpsb2.txt>), *Kammeyer (2000)* and *Losinski (2000)*. *RW* failures according to *Violet et al. (1999)* and *Losinski (2000)*.

usually the result of two so-called Delta-V maneuvers changing the speed of the satellite by thruster firings. The first maneuver decreases or increases the semi-major axis of the satellite. Afterwards, the satellite drifts continuously within the orbital plane into the direction of the new slot. As soon as this position is reached (after two months to one year), the semi-major axis is increased or decreased by a second maneuver to establish a stable position within the orbital plane.

4.2. Detection of Outliers and Discontinuities

Based on the time series of the first reprocessing run, discontinuities and outliers in the station coordinate time series were detected. The major part of the discontinuities is related to changes in the station equipment (antenna, receiver, antenna cable) and earthquakes, respectively. For a small part of the discontinuities the reason is unknown, but some of them are also visible in one or more time series of the [IGS ACs](#). If such an event occurred within a multi-day solution, two independent sets of coordinates were estimated for the corresponding station. Criteria for outliers were a 3-sigma limit and the behavior in the vicinity of the possible outliers. Stations that are temporarily excluded from the datum definition (due to suspicious behavior or recommendations of IGSMAIL/IGSSTATION) are listed in [Appendix A](#). The search for outliers and discontinuities was repeated for the complete time series after the second reprocessing run and for the time period of the third reprocessing run that was not covered by the previous runs until then.

4.2.1. Tracking Problems and Station Anomalies

To detect discontinuities caused by a changed tracking performance of the antenna and/or receiver without an equipment change, a *teqc* ([Estey and Meertens, 1999](#)) quality check was performed for all tracking stations of the reprocessing network. The time series of daily values for the number of observations, the observation rate (actual number of observations divided by the theoretical number of observations derived from the location of the station and the broadcast orbits), the multipath on L_1 (MP1) and L_2 (MP2), the number of cycle slips (CS) and the observation distribution w.r.t. the zenith distance were checked for anomalies. MP1 and MP2 are defined by

$$\text{MP1} = P_1 - \left(1 + \frac{2}{\alpha - 1}\right) L_1 + \frac{2}{\alpha - 1} L_2 = M_1 + B_1 - \left(1 + \frac{2}{\alpha - 1}\right) m_1 + \left(\frac{2}{\alpha - 1}\right) m_2 \quad (4.1a)$$

$$\text{MP2} = P_2 - \frac{2\alpha}{\alpha - 1} L_1 + \left(\frac{2\alpha}{\alpha - 1} - 1\right) L_2 = M_2 + B_2 - \left(\frac{2\alpha}{\alpha - 1}\right) m_1 + \left(\frac{2\alpha}{\alpha - 1} - 1\right) m_2 \quad (4.1b)$$

with

P_i	pseudorange measurement on frequency i
L_i	phase measurement on frequency i
M_i	pseudorange multipath on P_i
m_i	phase multipath on L_i
B_i	bias terms on L_i due to the phase ambiguities
$\alpha = \frac{f_1^2}{f_2^2}$.

In the following, some examples for different anomalies will be presented. The thorough detection of such anomalies is an important issue to avoid misinterpretations of the station-specific parameter time series.

Antenna Problems

Malfunctions of the tracking antenna resulting in a loss of observations or in an increased signal-to-noise ratio can significantly affect the [GPS](#)-derived parameter time series, in particular the station coordinates and the troposphere zenith delays.

RAMO After changing the antenna from an ASH700936D_M model to an ASH701945B_M type antenna on 17 July 2000, the station Mitzpe Ramon (Israel) shows a periodic signal with an initial peak-to-peak variation of 13 mm in the east component that is not visible before the antenna change, and also described by

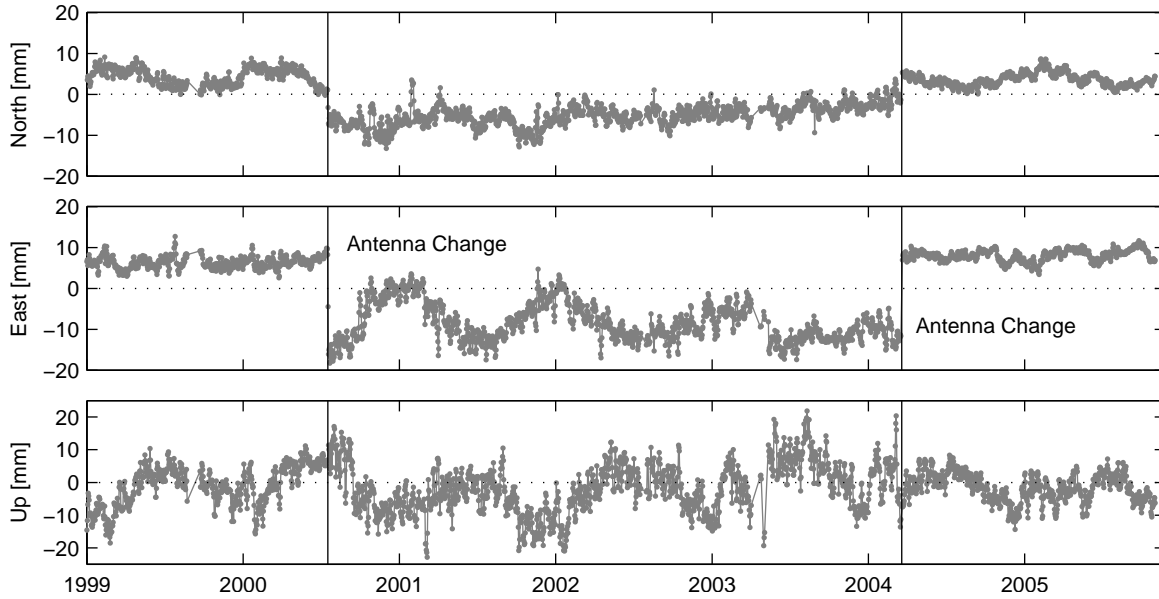


Fig. 4.5: Coordinate time series of Mitzpe Ramon (Israel). After an antenna change in July 2000 a periodic signal appears in the east component vanishing after another antenna change in March 2004.

Kenyeres and Bruyninx (2004). *Wdowinski et al.* (2004) report that the antenna had a hardware problem resulting in very noisy data (according to their paper, the antenna change took place in 2001, but Fig. 4 of this paper shows that the change was in fact in 2000). After another antenna replacement on 18 March 2004 the periodic signal disappears.

KOKB The comparison of **ZWD** parameters derived from the two independent techniques **GPS** and **VLBI** (further details are given in Sec. 6.1.3) allows to detect anomalies in one of both time series. Fig. 4.6 illustrates the effect of a tracking anomaly of the **GPS** site at Kokee Park (Hawaii): for a time period of several months, the **ZWD** difference between **VLBI** and **GPS** shows a bias of about 3.2 cm. This systematic offset is generated by a degraded tracking performance of the **GPS** antenna which resulted in a dramatically reduced observation rate. Especially satellites at elevations below 35° were only tracked sparsely, see Fig. 4.7. Due to the lack of observations at low elevations, the correlation between the troposphere zenith delay and the station height is unusually high, resulting in a systematic bias in the **ZWD** difference as well as in the height of the **GPS** station (4.2 cm w.r.t. the long-term mean). According to *Rothacher* (2002), errors in the station height δh are related to a tropospheric bias $\delta\rho_{\text{trp}}$ by the rule of thumb

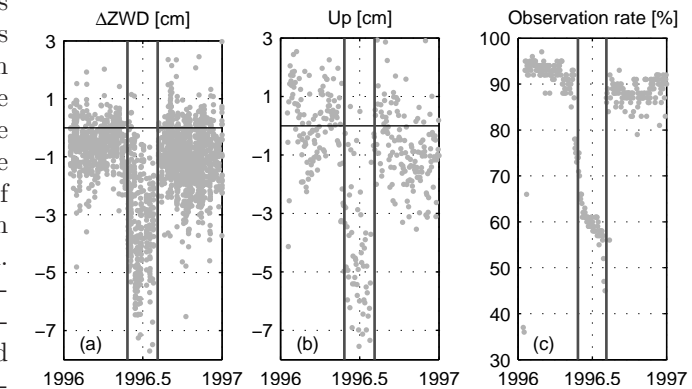


Fig. 4.6: Tracking anomaly of the **GPS** antenna at Kokee Park (start and end time are indicated by vertical lines): (a) **ZWD** difference between **VLBI** and **GPS**; (b) **GPS** station height w.r.t. the long-term mean; (c) observation rate of the **GPS** receiver.

According to *Rothacher* (2002), errors in the station height δh are related to a tropospheric bias $\delta\rho_{\text{trp}}$ by the rule of thumb

$$\delta h \approx \frac{\delta\rho_{\text{trp}}}{\cos z_{\text{max}}} \quad (4.2)$$

with the maximum zenith angle (cut-off angle) z_{max} . With a zenith delay bias of 3.2 cm and a height bias of 4.2 cm, the effective cut-off angle due to degraded tracking would be about 50° which only roughly agrees with the 35° derived from the observation statistics. One explanation for the difference might be the elevation-dependent weighting ($w = \cos^2 z$ with zenith angle z) of the **GPS** observations. After an antenna replacement in August 1996, the observation rate as well as the **ZWD** and the height estimates return to

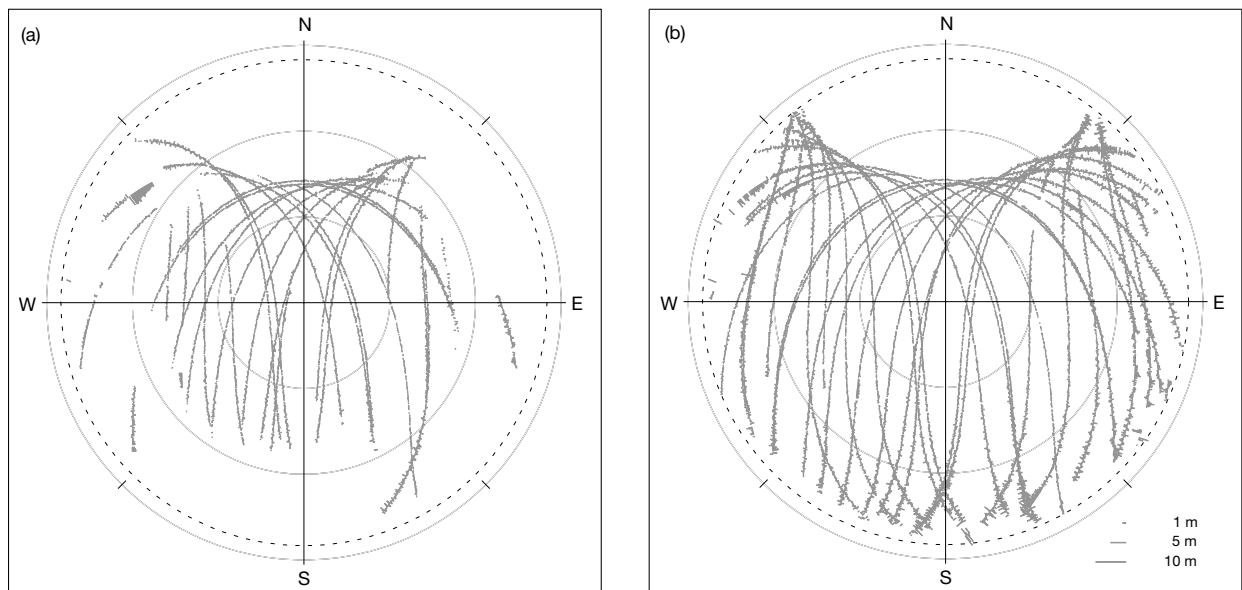


Fig. 4.7: Skyplots for Kokee Park: (a) during the tracking anomaly (1 August 1996); (b) after the antenna replacement (4 August 1996). The length of the lines perpendicular to the satellite tracks indicates the code multipath on L_1 .

normal. As a consequence, Kokee Park has been excluded from the set of datum stations for the time period of the tracking problem, see Tab. A.2.

Asymmetric Tracking

An asymmetric tracking can cause systematic effects in parameters that are sensitive to the azimuth. The troposphere gradients are an example for such a parameter type. The GPS site at the North Liberty VLBA station (USA) shows a large anomaly of up to 6 mm in the east-west component of the troposphere gradient in 2002 (Fig. 4.8). The reason for this anomaly (that is not present in the corresponding VLBI time series described in Sect. 6.1.3) might be the asymmetric distribution of the observations w.r.t. the east-west direction.

Skyplots of the observation distribution for days during (Fig. 4.9a) and after the anomaly (Fig. 4.9b) reveal such a tracking anomaly. Whereas satellites are tracked almost down to the horizon in the west, no satellites are observed below 20° elevation in the east, see Fig. 4.9a. A first anomaly occurs in summer 1997 and recurs annually with increasing amplitude till 2002. In 2003, the station does not show any anomalous behavior anymore. A possible explanation might be an obstruction of the horizon or a signal distortion (Hartinger and Brunner, 1998) by vegetation (foliage plants) which was possibly removed in 2003 (a photo of unknown date shows several bushes close to the antenna that is only mounted a few decimeters above the ground). The coordinate time series do not show any anomalous behavior.

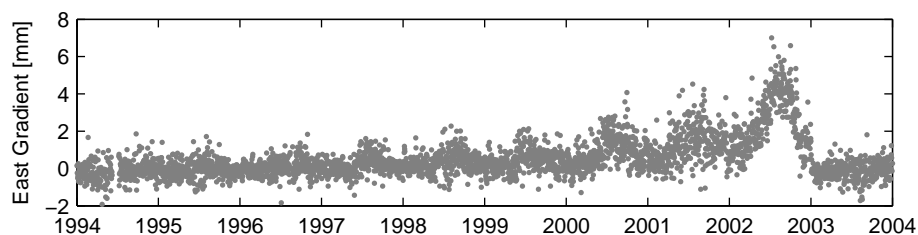


Fig. 4.8: East-west component of the troposphere gradient for North Liberty (USA). The large anomaly in summer 2002 is probably caused by an asymmetric tracking, see Fig. 4.9.

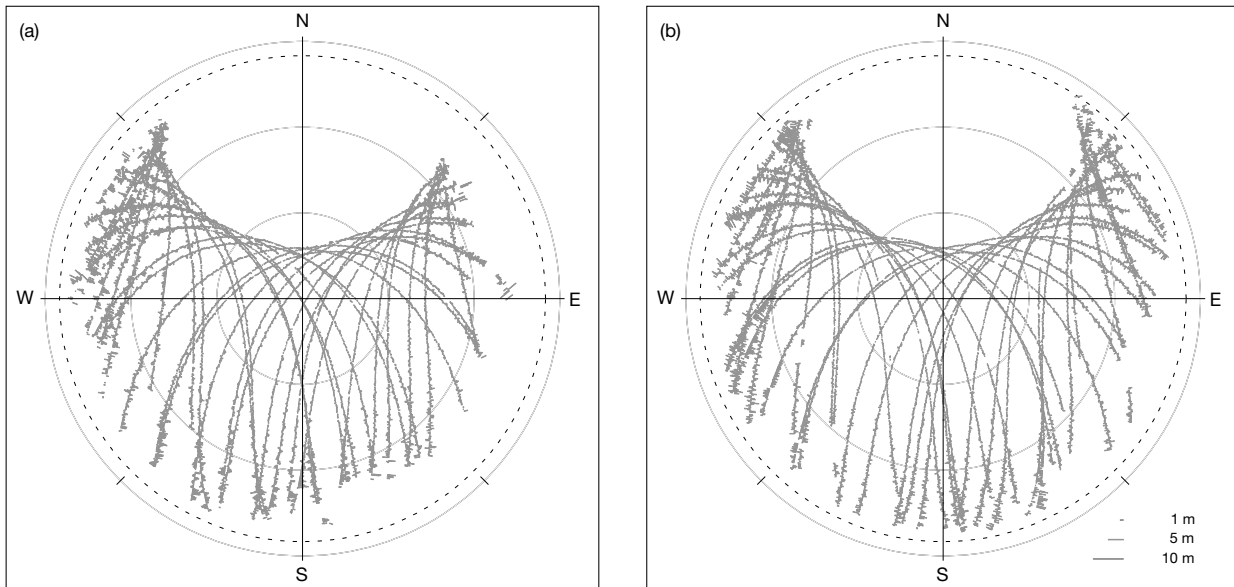


Fig. 4.9: Skyplots for North Liberty: (a) during the asymmetric anomaly (29 July 2002); (b) after the asymmetric tracking (29 July 2003). The length of the lines perpendicular to the satellite tracks indicates the code multipath on L_1 .

ROGUE L_2 Tracking Problem

ROGUE receivers (e.g., SNR-8000, SNR-12 RM) with a firmware version prior to 3.2.32.11 and a certain configuration suffer from a degraded tracking performance on L_2 in periods with high ionospheric activity (see IGSMails 2071, 2190 and 3758). Especially observations at low elevations are affected. As the ionosphere is generally more active in the equatorial region than in higher latitudes, in particular receivers close to the equator suffer from this receiver-specific tracking problem. Fig. 4.10 shows the coordinate time series (north component) for the tracking station at Fortaleza (Brazil, $\varphi = 3.9^\circ\text{S}$) operating a ROGUE SNR-8000 receiver with firmware version 3.2.32.1. In addition, the observation rate (number of recorded observations divided by the number of theoretically possible observations at the location of the tracking site) and the total electron content (also estimated in the reprocessing) are shown. A high anti-correlation between these two signals is obvious. During the ionospheric maximum at the end of 2001 the observation rate of the receiver in Fortaleza is not better than 30 to 50%. After a firmware update in 2002 the tracking performance clearly improves. The non-linearity of the station coordinate's north component might also be related to this problem. *Tregoning et al.* (2004) reported similar effects for the height component of several stations of a regional network in Australia, although the firmware version numbers are messed in that paper.

Altogether 53 receivers of the reprocessing network are affected by the ROGUE L_2 tracking problem. It took till mid of 2003 (more than one year after the release of IGSMail 3758 announcing this problem!) until all receivers had been updated or replaced. Fortunately, not all ROGUE receivers showed such a bad performance as the one at Fortaleza. Most of these receivers were replaced between 1999 and 2001.

Environmental Effects

Stations in higher latitudes sometimes show anomalies during the winter, which are probably caused by snow and ice covering the antennas and radomes, respectively (*Jaldehyag et al.*, 1996; *Kaniuth et al.*, 2005; *Poutanen et al.*, 2005). But also other environmental effects affecting the antenna can bias the estimated site positions. Only a few examples are mentioned here:

- One example for snow-induced effects is the site Yakutsk (Russia) where snow on the antenna biases the coordinate estimates by several centimeters (IGSSTATION 352 and 365). As soon as this problem had been recognized, the station operators started to remove the snow from the antenna (e.g., IGSSTATION 1317).

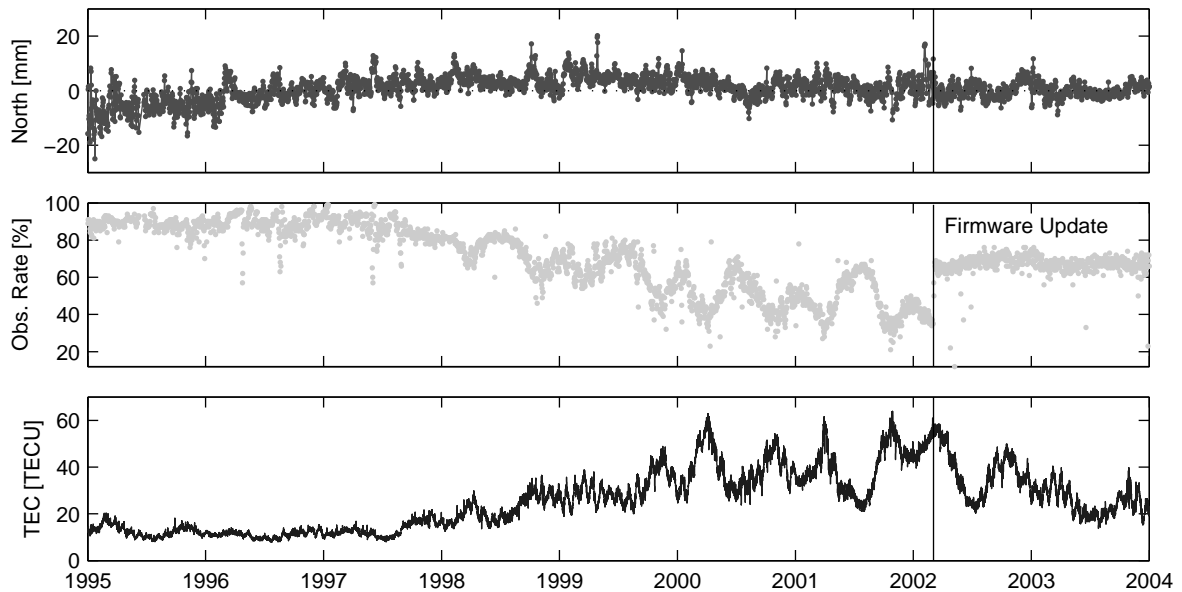


Fig. 4.10: Coordinate time series (north component) and observation rate for Fortaleza (Brazil). In addition, the total electron content estimated from the reprocessing is shown. The firmware update solving the ROGUE L_2 tracking problem is indicated by a vertical line.

- But also for a site in Germany, namely Wettzell, several anomalies due to snow obstructions could be detected. The correlation with the height of the snow cover on the antenna was confirmed by a webcam installed near the antenna (*Rothacher et al., 2005*).
- The antenna in Bogota (Colombia), which is mounted very close to the ground on a concrete pad is flooded periodically (*Kaniuth and Häfele, 2002*). This effect biases the estimates of the vertical component by up to 12 cm before 2000 and up to 8 cm after 2002 (no data available in-between).
- A piece of rock obstructed the antenna in Whitehorse (Canada) between 5 and 13 August 2002 (IGSMAIL 4046) resulting in outliers of up to 7 cm in the horizontal components and up to 13 cm in the station height.

4.2.2. Discontinuities

Compared to other space geodetic techniques, GPS time series suffer from a comparatively large number of discontinuities. Tab. 4.3 lists the reasons for altogether 125 discontinuities detected in the reprocessed time series of station coordinates. The major part is related to equipment changes, but for quite a large part of the discontinuities the reasons are unknown. Two lists of discontinuities of the IGS stations are maintained by NRCAN⁴: the file CONFIRMED.snrx contains a list of confirmed discontinuities seen by several ACs, whereas PROBABLE.snrx lists probable discontinuities seen by only one AC. As a certain part of these discontinuities might have been introduced by model or processing changes of the individual ACs that should not show up in a reprocessed solution, the reprocessed station coordinate time series were properly inspected for discontinuities from scratch. Some of the discontinuities contained in PROBABLE.snrx could be confirmed, some others and even some contained in the list CONFIRMED.snrx are not visible in the reprocessed time series (indicating that these discontinuities might be induced by model changes or changes in the contributions of the ACs to the combined solution) and even new discontinuities could be detected. A detailed list of all discontinuities in the reprocessed time series is given in Tab. C.1 in the appendix.

The most obvious cause for the discontinuities listed in Tab. 4.3 are earthquakes that usually introduce coordinate *and* velocity discontinuities. All stations of the reprocessing network affected by earthquakes during the reprocessing period are listed in detail in Tab. 5.5: altogether 18 stations are affected by displacements due to 11 different earthquakes. However, many more discontinuities are caused by changes of the station equipment. Altogether 66 discontinuities due to equipment changes are visible in the coordinate time series, most of them caused by changes of the antenna/radome combination particularly affecting the

⁴<ftp://macs.geod.nrcan.gc.ca/pub/requests/sinex/discontinuities/>

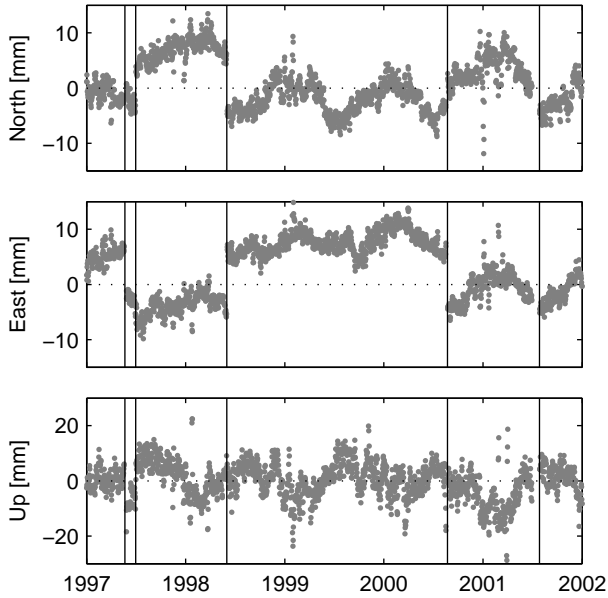


Fig. 4.11: Station coordinate time series for Westford (USA). Antenna replacements affecting the continuity of the time series are indicated by vertical lines.

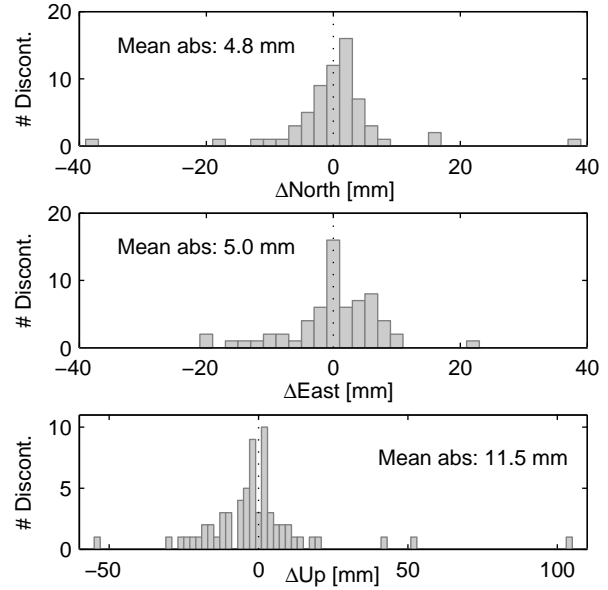


Fig. 4.12: Histograms of station coordinate discontinuities due to equipment changes. The numbers labeled with *Mean abs* refer to the mean of the absolute values of the displacements.

station height. The effects of radomes are discussed by *Kaniuth and Huber (2003)*, *Ray et al. (2007)* and within Sec. 9.2.2. As an example for antenna-induced discontinuities, the effects of frequent antenna changes at Westford (the antenna is casually hit and destroyed by lightning) are shown in Fig. 4.11. Although all spare antennas are of the same type (Dorne Margolin), five discontinuities are visible. Some of them only affect one coordinate component, others all of them.

The reasons for altogether 36 out of 125 discontinuities are unknown. Possible explanations are:

- Firmware updates
- Changed receiver settings, e.g., receiver elevation cut-off angle
- Undocumented equipment changes
- Equipment malfunctions
- Obstructions of the sky
- Changes in the vicinity of the antenna affecting the multipath environment
- Human errors (concerning, e.g., radome information or antenna height).

The histograms in Fig. 4.12 illustrate the size of the discontinuities due to equipment changes. The largest horizontal discontinuity has an absolute value of 45 mm, the vertical discontinuities range from -54 to $+104$ mm. The largest displacement due to an earthquake occurs for the site Arequipa with $\Delta N = -28.7$ cm, $\Delta E = -42.0$ cm and $\Delta U = -3.0$ cm.

Discontinuity type	Number of discontinuities
Antenna/radome change	34
Receiver change	5
Antenna/radome and receiver change	27
Earthquakes	18
Other	5
Unknown	36

Tab. 4.3: Discontinuities in the reprocessed coordinate time series.

As already mentioned above, one has to distinguish between position and velocity discontinuities. For equipment changes, it is a reasonable assumption that only the station position but not the station velocity is affected by the equipment change. For discontinuities of unknown origin, the same assumption is made. In the reference frame solutions, the velocities are forced to be equal before and after such discontinuities by applying constraints on the velocity estimates. For discontinuities due to earthquakes, the velocity after the earthquake usually differs from the velocity before the earthquake (post-seismic reaction). The question whether (and when) the velocity returns to the value from before the earthquake is difficult to answer and has to be decided separately for each station.

4.3. Other Systematic Effects

4.3.1. Correlations with teqc Parameters

Several sites show correlations of outliers or periodic signals in the station coordinate time series with parameters computed by `teqc`, namely the number of cycle slips and the code multipath on L_1 and L_2 . This does not necessarily mean that these parameters directly affect the coordinate time series, but it could indicate that some unknown systematic effects might be the origin of these signals. Like for outliers and discontinuities, a proper detection of these artifacts is essential in order to avoid misinterpretations.

Cycle Slips

In the last few months of its tracking history, the site WETT (operated at the geodetic observatory Wettzell, Germany) showed an anomalous behavior, see Fig. 4.13. All three coordinate components show outliers of up to 6 cm. The anomalies of the horizontal coordinate components are also reflected in the troposphere gradients: the north-south gradient shows a larger scatter, whereas in the east-west gradient a broad peak is visible at the end of 1996. In the `ZWD` residual time series (offset, trend, annual and semi-annual signals removed) no anomalies are visible. The reason for WETT's behavior is unknown, but during the same period, the site suffers from an increased number of cycle slips. As the site WTZR (operated at a distance of only about 3 m away WETT) does not show such a behavior, the problem seems to be related to the equipment of the site WETT. Therefore, WETT data after 4 October 1996 was excluded from reprocessing run M3.

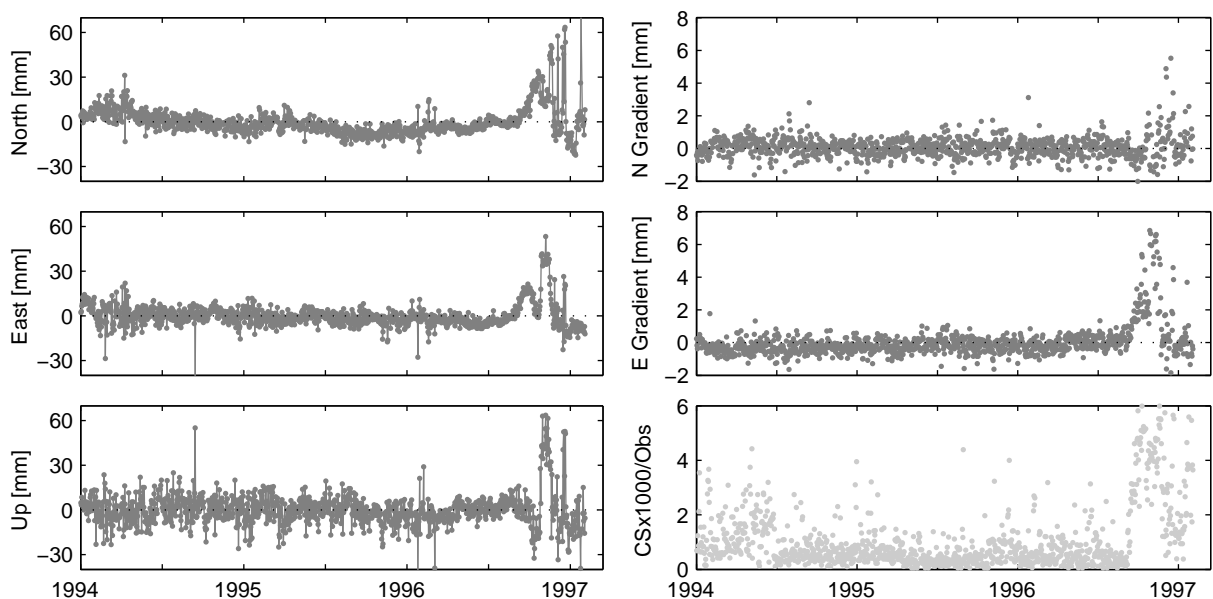


Fig. 4.13: Anomalous behavior of the site WETT. The time series of reprocessing run M1 is shown, since observation data after 4 October 1996 was excluded from run M3. `CSx1000/Obs` stands for the inverted number of observations per cycle slip multiplied by 1000.

Multipath

Periodic signals in the code multipath MP1 and MP2 (Eq. 4.1) that are correlated with certain coordinate components are visible for a number of stations. In particular, this effect becomes evident when it appears or vanishes after an equipment change. Only two examples are shown here.

GLSV Like many other stations, the GLSV site in Kiev (Ukraine) shows a clear seasonal signal in the up component (Fig. 4.14). This signal with an amplitude of 7.0 mm correlates well with the code multipath on L_2 computed by `teqc`. In addition, a local peak at the beginning of 2003 can be identified in both series. However, the parameter estimation step determining the coordinate time series shown in Fig. 4.14 is based on phase observations only (code observations are only used for the Melbourne-Wübbena ambiguity resolution). Therefore, the code multipath cannot be directly responsible for variations in the station height. These variations are probably related to instrumental or environmental effects that affect both, the code multipath and the station height, in a similar way. However, the real reason for the variations is unknown.

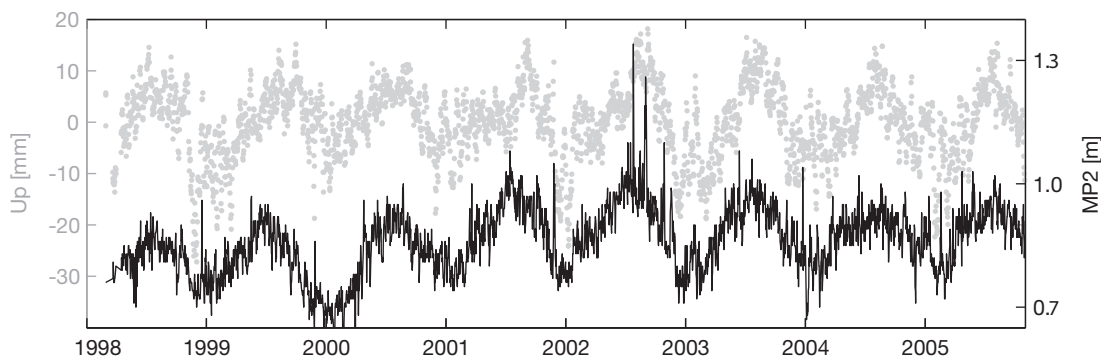


Fig. 4.14: Time series of the GLSV station height (Up) and MP2 computed by `teqc`.

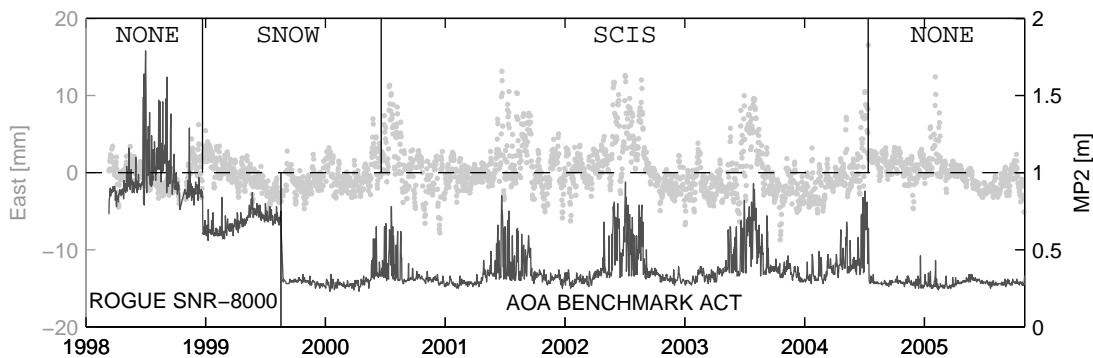


Fig. 4.15: Time series of the east component and MP2 computed by `teqc` for TRO1. Radome changes are indicated by vertical lines in the upper part of the plot, the receiver change by a vertical line in the lower part. The MP2 reduction in August 1999 coincides with the receiver change from a ROGUE SNR-8000 to an AOA BENCHMARK ACT.

TRO1 The site TRO1 at Tromsø (Norway) shows a seasonal, anomalous behavior of the east component between 2000 and 2004: in summertime the scatter of the time series is increased and the coordinate estimates are biased by several millimeters. This phenomenon is correlated with an anomalous behavior of the code multipath on L_2 : MP2 computed by `teqc` is increased by a factor of up to two, and the anomaly only occurs between 2000 and 2004. This is the time period when the TRO1 antenna was covered with a SCIS radome and the receiver type AOA BENCHMARK ACT was in use. In summer 1999, the antenna was covered by a SNOW radome, and the receiver type was a ROGUE SNR-8000 (receiver change in August 1999) not showing any anomalous behavior. The SCIS radome was removed in July 2004 shortly after the summer anomaly started in that particular year. Without a radome, the anomaly neither occurred in the

remaining months of the summer of 2004 nor in 2005. The coordinate residuals before 2000 do also not show any anomalous behavior although increased MP2 values are present in summer 1998.

As a second GPS site (TROM) is available at the Tromsø station, the corresponding time series can be compared with TRO1. TROM is located at a distance of 51 m from TRO1 and does not show a comparable behavior. The outliers in the beginning of 2005 are present in both, the TROM and TRO1 time series and could be related to snow coverage of the antennas. As TROM is not covered by a radome, it is reasonable to assume that this effect is indeed induced by the radome coverage of TRO1 in combination with the AOA BENCHMARK ACT receiver. However, the true reason for this effect remains unknown. A possible explanation might be the condensation of water within the radome.

4.3.2. Orientation of the Orbital Planes w.r.t. the Sun

The orientation of the orbital plane w.r.t. the Sun (see Fig. 2.6) introduces artifacts due to orbit modeling deficiencies into several other parameters. According to *Montenbruck and Gill (2000)* the precession of the ascending node $\dot{\Omega}$ of a satellite (assuming a circular orbit, $e=0$) is given by

$$\dot{\Omega} = -3\pi \frac{J_2}{T} \left(\frac{R_e}{a} \right)^2 \cdot \cos i \quad (4.3)$$

with the revolution period T , the semi-major axis a , the inclination i , the Earth radius R_e and the oblateness of the Earth J_2 . Inserting the corresponding values of the GPS satellites results in a rate of $\dot{\Omega}_{GPS} = -14.1^\circ/y$. Due to this precession of the right ascension of the ascending node, the time period T_R between the same orientation of the orbital planes w.r.t. the Sun is smaller than one year:

$$T_R = \frac{2\pi}{2\pi y^{-1} - \dot{\Omega}_{GPS}} \approx 351.5 \text{ d} \quad (4.4)$$

Assuming a mean Sun (i.e., the Sun moves around the equator with constant speed), the constellation of the six orbital planes has the same orientation w.r.t. the Sun already after one sixth of this period (and its integer multiples), although the individual orbital planes are exchanged. The main period of $T_R=351.5$ days and its integer fractions T_R/n , $n=2,\dots,6$ are clearly visible in the spectra of several parameters and their corresponding formal errors. A similar effect is caused by the TOPEX/Poseidon satellite ($T_R \approx 117$ d) in DORIS (Doppler Orbitography and Radiopositioning Integrated by Satellite) solutions. It is visible in the geocenter estimates (*Feissel-Vernier et al., 2006*), the ERPs (*Gambis, 2006*) and the station coordinates (*Le Bail, 2006*). *Ray et al. (2008)* described this effect for the station coordinate time series of the weekly IGS solutions.

As an example, Fig. 4.16 shows typical spectra of the direct radiation pressure coefficients for a Block IIA (SVN 25) and a Block IIR satellite (SVN 43). Due to gaps in the RPR parameter time series, the Lomb-Scargle algorithm (*Press and Rybicki, 1989*) has been used to compute these spectra. Pronounced peaks can be found at $T_R/2$ and $T_R/4$ for both satellites, whereas a clear peak at $T_R/6$ is only visible for SVN 25 and a peak at T_R only for SVN 43. Besides the RPR parameters, also parameters closely linked (or correlated) to the satellite orbits are sensitive to this effect. Such parameters are, e.g., LOD, nutation rates (for more details see Sec. 8.3) and satellite antenna offsets. The LOD formal error time series and its spectrum are shown in Fig. 4.17. Besides the improvement with time, a periodic pattern can be seen in the formal errors. The corresponding spectrum reveals a significant peak at $T_R/6$ and another smaller, but also sharp peak at $T_R/12$.

As another example, the spectra of the satellite antenna offset time series for SVN 37 are shown in Fig. 4.18. These offsets were estimated from data of reprocessing run M1, for more details see *Schmid et al. (2007)*. The horizontal offsets show clear peaks at the periods mentioned above. For the z -offsets the peaks are not as sharp as for the horizontal offsets, but most periods are also present in the z -offset spectrum. The presence of such signals, even in completely and homogeneously reprocessed time series, indicates deficiencies in the orbit modeling. *Urschl et al. (2008)* showed that the application of an improved a priori RPR model can reduce similar systematic effects in SLR residuals of the GPS satellites SVN 35 and 36. Further studies of these effects and the development of more sophisticated orbit models will remain an important task for the future that is, however, beyond the scope of this thesis.

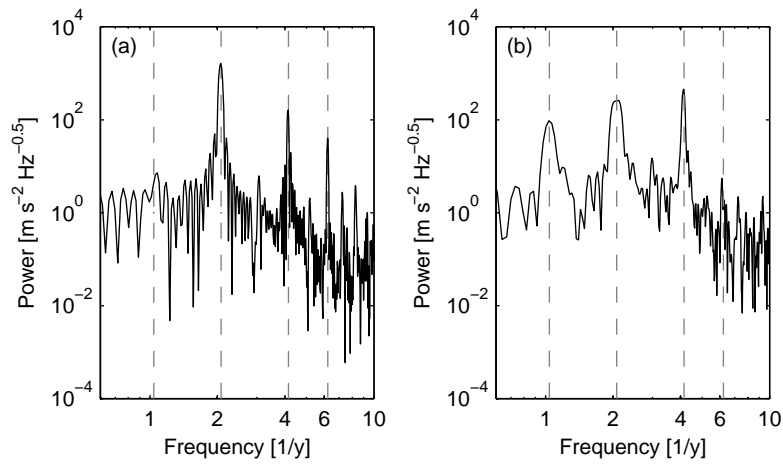


Fig. 4.16: Power spectra of the direct radiation pressure coefficients for: (a) [SVN 25](#) (Block IIA); (b) [SVN 43](#) (Block IIR). The periods T_R , $T_R/2$, $T_R/4$ and $T_R/6$ are indicated by dashed lines.

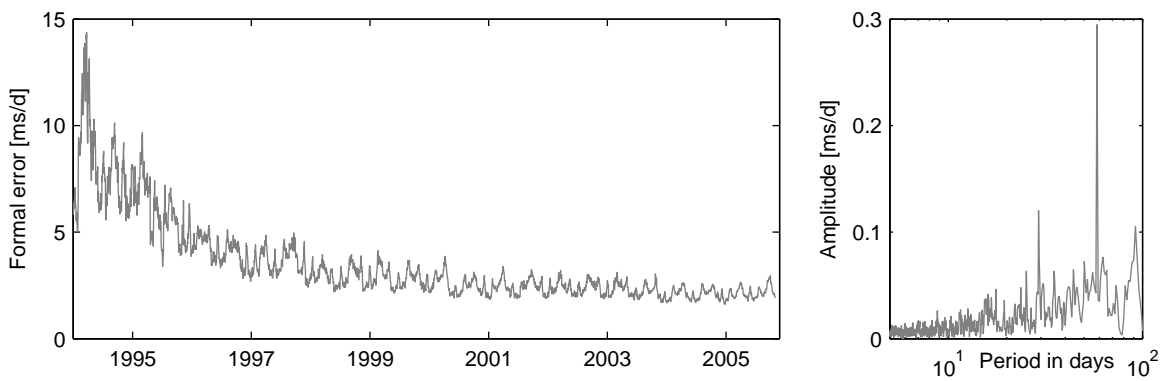


Fig. 4.17: Formal errors of the [LOD](#) estimates of the 3-day solution (24 hours parameter spacing) and their amplitude spectrum. The largest peak corresponds to $T_R/6$, the second largest one to $T_R/12$.

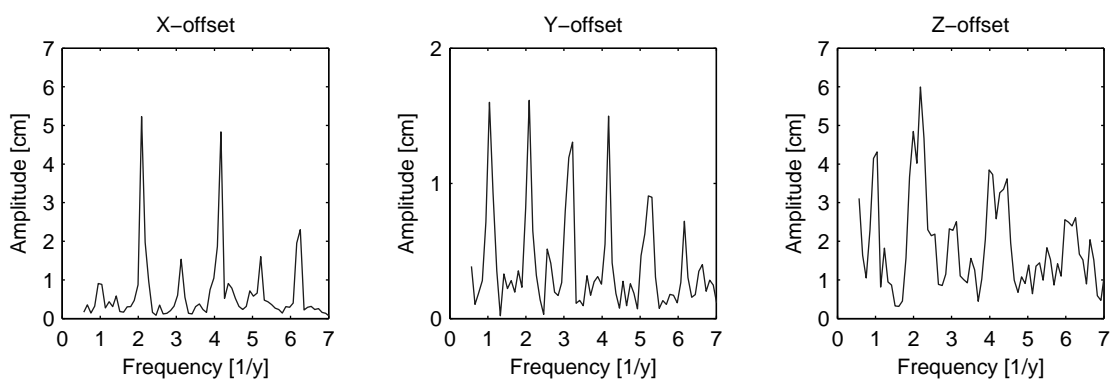


Fig. 4.18: Amplitude spectra of the satellite antenna offset estimates for [SVN 37](#) (Block IIA).

Part II.
Reprocessing Results

5. Station Coordinates and Velocities

The determination of precise station coordinates is the most common application of the GPS. The permanent stations of the IGS and regional networks like EUREF play an important role for the realization of the ITRS and its densification. Long time series of GPS-derived NEQs can be used to derive a GPS-only Terrestrial Reference Frame (TRF). *Heflin et al. (2002)* compare such a TRF based on the JPL solution with the ITRF, whereas *Ray et al. (2004)* describe the IGS implementation of ITRF2000, namely IGB00. As already mentioned in the introduction, *Nikolaidis (2002)* conducted a GPS reprocessing to primarily study geodetic and seismic deformations.

This section gives an internal quality assessment (evaluated by repeatabilities and GPS/GPS co-locations) of the station coordinates and velocities determined within the reprocessing. The normal equations covering the whole time period of the reprocessing are accumulated to compute a TRF solution that is compared to IGB00 and provides the basis for the computation of station coordinate and origin of the tracking network time series. Finally, several examples of station coordinate time series are discussed and compared to the ITRF2005 residual time series.

5.1. Coordinate Repeatabilities

The repeatabilities of seven single coordinate solutions, used for the weekly solutions, compared to the weekly solutions are shown in Fig. 5.1 for a part of the reprocessing time series and the original CODE series. Before April 1996, no corresponding repeatability values for the CODE series are available. Two changes are striking in the CODE series: at the beginning of 1998 the reference frame used for datum definition was changed from ITRF94 to ITRF96 and the number of datum stations grew from 13 to 47 (*Kouba et al., 1998b*). Starting with the same date, station displacement due to ocean loading is corrected for. Both changes cause an improvement of the repeatability by a factor of about two. At the beginning of

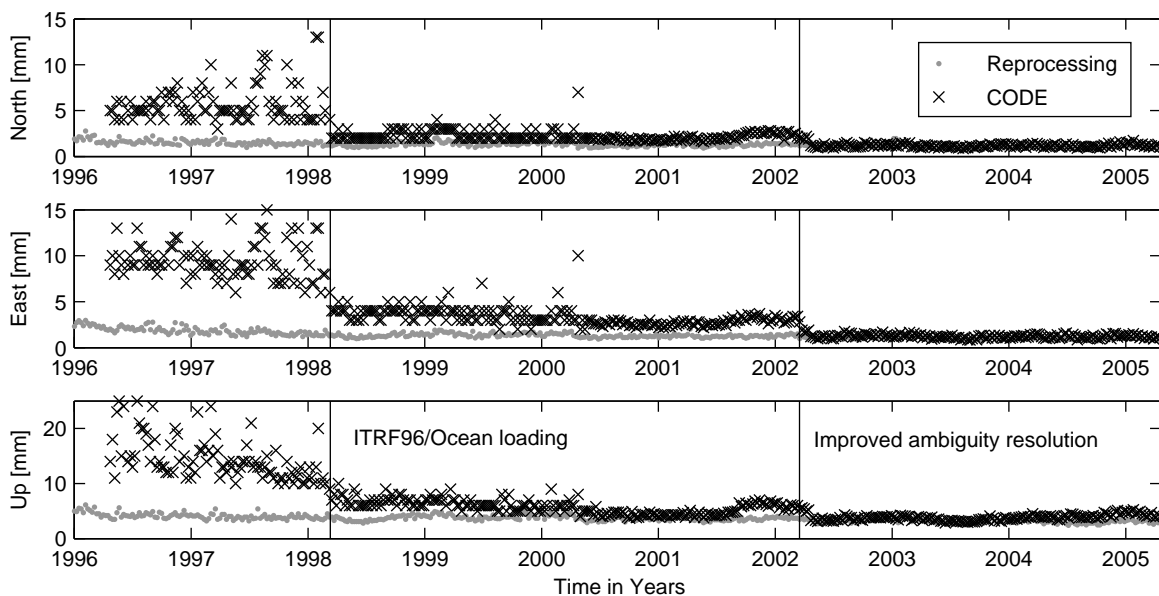


Fig. 5.1: Repeatability of the weekly station coordinates: CODE IGS routine solution and reprocessed solution. The two most important improvements in the CODE processing strategy are indicated by vertical lines.

Station			Sol.	Obs.	North		East		Up	
					STD [mm]	Cor.	STD [mm]	Cor.	STD [mm]	Cor.
Hartebeesthoek	HRAO	HARK	1d	848	2.63	0.9920	4.70	0.9824	6.46	0.8799
			3d	858	2.44	0.9904	4.62	0.9813	5.14	0.8659
Miami	MIA1	AOML	1d	187	1.16	0.9976	1.20	0.9861	5.87	0.9344
			3d	188	1.12	0.9962	1.18	0.9694	3.49	0.9676
Ny Ålesund	NYAL	NYA1	1d	2611	2.61	0.9986	1.60	0.9978	2.78	0.9948
			3d	2671	2.60	0.9986	1.63	0.9976	2.32	0.9961
Thule	THU1	THU3	1d	270	3.21	0.9312	2.33	0.9797	77.43	0.2604
			3d	370	2.90	0.8537	2.57	0.9644	11.97	0.8498
Tromsø	TROM	TRO1	1d	2387	4.02	0.9937	5.43	0.9873	5.97	0.9493
			3d	2452	3.72	0.9946	5.20	0.9882	4.08	0.9679
Wettzell	WETT	WTZR	1d	262	5.08	0.9274	7.47	0.8787	3.41	0.9720
			3d	266	5.05	0.8870	7.50	0.8516	2.39	0.9748
Yakutsk	YAKZ	YAKT	1d	109	5.16	0.8940	2.58	0.9665	10.33	0.8154
			3d	113	4.31	0.8205	2.07	0.9531	4.34	0.9256
Yarragadee	YARR	YAR2	1d	865	0.55	0.9999	0.52	0.9999	2.98	0.9551
			3d	939	1.10	0.9998	0.63	0.9999	2.27	0.9575
Mean STD			1d		3.05		3.23		14.40	
			3d		2.91		3.18		4.50	
Median STD			1d		2.92		2.46		5.92	
			3d		2.75		2.32		3.78	

Tab. 5.1: Coordinate comparisons for GPS-GPS co-locations: **STD** and correlation (*Cor.*) of the 1-day and the 3-day solutions. Larger **STD** values of the 3-day solution are marked in gray. The mean **STD** of the 1-day up component when excluding Thule is 5.40 mm.

2002 an improved ambiguity resolution strategy was implemented at the **CODE** analysis center. It is the same strategy that is also used for reprocessing, see Sec. 3.2.1. The effects on the coordinate repeatability are clearly visible: in particular the east-west component benefits from the improved ambiguity resolution. After this change the repeatabilities of the **CODE** and the reprocessed solution are on almost the same level. The reason for the slightly degraded repeatability in the height component of the **CODE** series at the end of 2001 until the beginning of 2002 is unknown. The mean repeatabilities for the reprocessed solution are 1.5 mm, 1.9 mm and 3.9 mm for the north, east and up component with median values of 1.3 mm, 1.3 mm and 3.7 mm, respectively.

5.2. GPS-GPS Co-locations

Tab. 5.1 compares the 1-day and 3-day station coordinates of stations equipped with more than one receiver. These so-called **GPS-GPS** co-locations allow for an assessment of the internal consistency of the reprocessed station coordinate time series. One combination at Hartebeesthoek, South Africa (HRAO and HART) is excluded as these sites only have 54 days of common observations and also a discontinuity of several decimeters affects the site HART, see Tab. C.1. Unfortunately, there are only two stations running a longer time period in parallel: Ny Ålesund and Tromsø, both located in Norway.

The number of solutions contributing to the comparison is not the same for the 1-day and the 3-day solution as, e.g., one isolated observation day contributes to three consecutive 3-day solutions but only to a single 1-day solution. The bigger the difference in the number of solutions the larger is the number of isolated days (e.g., Thule). The 3-day solutions in general show lower **STD** values for all three coordinate components and larger correlations for the height component due to the higher stability of the 3-day orbital arcs. However, for a few stations some 3-day **STD** values are larger than the 1-day **STD**. The largest difference occurs for the **STD** of the north component of Yarragadee with a factor of two. The reason for this behavior is unknown, the differences for the other stations are much smaller. For the horizontal components there are only small differences between the **STD** values of the 1-day and the 3-day solution. On the other hand, the correlations of the 3-day solutions are in general smaller than those of the 1-day solutions for the horizontal

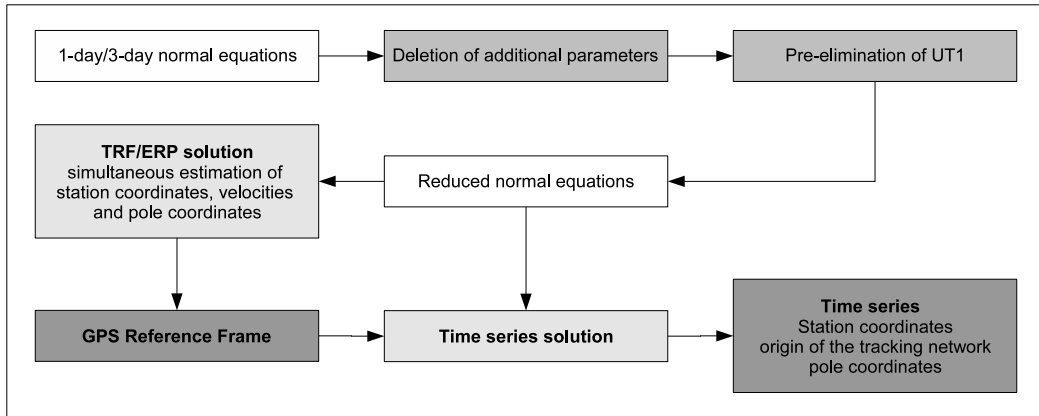


Fig. 5.2: Flow chart of the reference frame and time series solution.

components. This effect might be explained by systematic errors, e.g., artifacts in the network origin estimates (Sec. 4.3.2 and 5.4.1), that are more pronounced for the less stable 1-day solutions compared to the 3-day solutions. For the vertical component the correlations are larger for the 3-day solutions for all stations except for Hartebeesthoek. The **STD** of the height component is a factor of 2–3 worse than that of the horizontal components due to the observation geometry and the correlations of the station height with other parameters like the troposphere zenith delays and the clock parameters (Rothacher, 2002).

Several of the larger **STD** values can be explained by systematic effects. The huge **STD** of the up component of Thule is related to a degraded tracking performance of the THU1 site (observation rate of about 65% only) after an outage in the middle of 2001 resulting in quite noisy coordinate time series. As this problem persisted until the end of the operation of THU1 (beginning of 2003) and THU3 tracking only started in September 2001, the whole comparisons of Thule are affected by this problem. The bad agreement of Wettzell in the horizontal components is caused by the anomalous behavior of the WETT site, see Sec. 4.2.1 (a major part but not the whole period with problems was excluded in run M3). Finally, Yakutsk is affected by snow-induced effects, see Sec. 4.2.1. When excluding these problematic stations, the **STD** of the horizontal components is on the level of 1–5 mm and the vertical component is worse by a factor of two.

5.3. Reference Frame Solution

A reference frame solution has been computed starting with the 3-day **NEQs** for the time interval between 1 January 1994 and 30 October 2005 (4321 days), see Fig. 5.2. Reference frames computed from 1-day **NEQs** with different troposphere modeling as well as different phase center models following the same processing scheme as for the 3-day solutions are compared in Sec. 6.3.1 and 9.2.1. In a first step, the satellite antenna **PCV** and **UT1** parameters (only **UT1** for the 1-day **NEQs**) were pre-eliminated. The time resolution of the pole coordinates was changed from two hours to one day. A subset of 63 stable IGb00 stations (no discontinuities during the time period covered by the **TRF** solution, see Tab. A.1 and Fig. A.1) was used for the datum definition: a **NNR** condition for station coordinates and velocities w.r.t. IGb00. The scale of the **TRF** is defined by the speed of light and the antenna phase center model as this model is highly correlated with the scale parameter, see Sec. 2.4.2. The **TRF** origin is defined by the satellite orbits referring to the Earth’s center of mass.

Station positions and velocities as well as the pole coordinates were estimated simultaneously in one program run to guarantee full consistency between the **TRF** and the polar motion estimates. **UT1** was not included in this solution as satellite techniques are not able to determine **UT1** in an absolute sense (the first **UT1** parameter in the 1-day, 3-day and weekly solution is fixed to its a priori value) and due to limited memory resources. The discontinuities listed in Tab. C.1 have been considered for the **TRF** solution, i.e. independent coordinate sets have been estimated before and after the discontinuities. As earthquakes in general change the station velocity, an independent new velocity was set up after earthquakes. For discontinuities due to equipment changes or unknown reasons, only a new coordinate set was estimated, the velocities before and after the discontinuity were constrained to be equal. No constraints have been applied for the velocities of co-located **GPS** sites. The reference frame obtained from the solution described above was used for datum

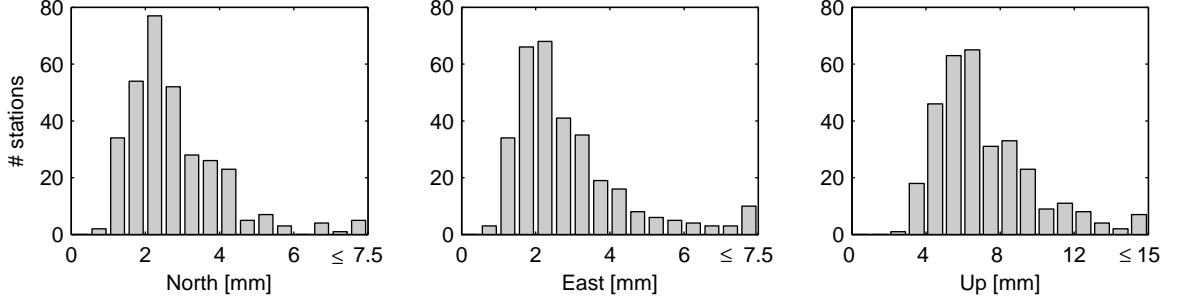


Fig. 5.3: Station coordinate repeatabilities of the reference frame solution.

T_x [mm]	T_y [mm]	T_z [mm]	α [mas]	β [mas]	γ [mas]	s [ppb]
\dot{T}_x [mm/y]	\dot{T}_y [mm/y]	\dot{T}_z [mm/y]	$\dot{\alpha}$ [mas/y]	$\dot{\beta}$ [mas/y]	$\dot{\gamma}$ [mas/y]	\dot{s} [ppb/y]
-4.2 ± 0.4	9.6 ± 0.4	-4.6 ± 0.4	-0.187 ± 0.032	-0.011 ± 0.033	0.081 ± 0.036	-0.17 ± 0.07
0.4 ± 0.4	1.1 ± 0.4	-1.8 ± 0.4	-0.026 ± 0.032	0.018 ± 0.033	0.003 ± 0.036	0.07 ± 0.07

Tab. 5.2: Transformation parameters of the reprocessed reference frame w.r.t. IGB00 obtained from a 14-parameter similarity transformation of the datum stations.

definition in the time series solution based on the reduced normal equations saved after the pre-elimination step mentioned above. As the origin of the tracking network was estimated in this solution, a **NNR/NNT** condition had to be applied.

The repeatabilities of the individual solutions contributing to the combined **TRF** solution allow for an assessment of the scatter of the residual signals w.r.t. the linear model of the **TRF** solution. The residual signals consist of systematic and random errors as well as true geophysical signals, e.g. loading effects. A histogram of the repeatabilities of the **TRF** solution is shown in Fig. 5.3. If a station is splitted into two or more independent coordinate sets (see Sec. 4.2.2) the sub-intervals of this station are treated as two or more independent stations. The mean repeatabilities are 2.8 mm for the north, 2.9 mm for the east and 7.2 mm for the up component with corresponding median values of 2.5 mm, 2.4 mm and 6.4 mm, respectively.

The coordinates \mathbf{x}_i and velocities $\dot{\mathbf{x}}_i$ of a certain **TRF** can be transformed to another **TRF** defined by $\tilde{\mathbf{x}}_i$ and $\dot{\tilde{\mathbf{x}}}_i$ with a 14-parameter similarity transformation. Based on the quantities already described for the 7-parameter similarity transformation (Eq. 2.17), the velocities $\dot{\mathbf{x}}_i = [\dot{x}_i, \dot{y}_i, \dot{z}_i]^T$ and $\dot{\tilde{\mathbf{x}}}_i = [\dot{\tilde{x}}_i, \dot{\tilde{y}}_i, \dot{\tilde{z}}_i]^T$ and the velocity transformation parameters $\dot{\mathbf{T}} = [\dot{T}_x, \dot{T}_y, \dot{T}_z, \dot{\alpha}, \dot{\beta}, \dot{\gamma}, \dot{s}]^T$, the 14-parameter similarity transformation is defined by

$$\begin{bmatrix} \tilde{\mathbf{x}}_i \\ \dot{\tilde{\mathbf{x}}}_i \end{bmatrix} = \begin{bmatrix} \mathbf{x}_i \\ \dot{\mathbf{x}}_i \end{bmatrix} + \begin{bmatrix} \mathbf{B}_i & 0 \\ 0 & \mathbf{B}_i \end{bmatrix} \begin{bmatrix} \mathbf{T} \\ \dot{\mathbf{T}} \end{bmatrix}. \quad (5.1)$$

The transformation parameters between the **TRF** from reprocessed 3-day solutions and IGB00 are given in Tab. 5.2. The mean residuals of this 14-parameter transformation are 3.0 mm, 1.3 mm and 6.7 mm for the coordinate north, east and up component and 0.7 mm/y, 0.6 mm/y and 2.0 mm/y for the velocities, respectively. All translation parameters are significant, although they are below one centimeter. The different stations used for datum definition of IGB00 and the reprocessed **TRF** and their inhomogeneous distribution might explain that shifts. Significant rotations appear for the x - and z -axis, whereas all rotation rates are insignificant. The very small scale offset as well as scale drift could be achieved by the application of an absolute antenna phase center model that was aligned to IGB00. Therefore, an alignment to the **ITRF** scale (determined by **SLR** and **VLBI** for **ITRF2000**) like it is done for the **IGS** weekly solutions (Ferland et al., 2000) is not necessary anymore. More details on different phase center models and their influence on the reference frame will be given in Sec. 9.

To test the stability of the **NNR** datum, three **TRF** solutions with a reduced number of about 20 datum stations (instead of 63, see above) have been computed. As far as possible, the datum stations of each subset are equally well distributed. Tab. 5.3 lists means of the absolute values of the rotation and rotation rate differences of these three **TRF**s amongst each other and w.r.t. the **TRF** solution computed with all datum stations. Rotations and rotation rates have been estimated as part of a 14-parameter similarity

Axis	Reduced/Full		Reduced/Reduced	
	Rotation	Rotation rate	Rotation	Rotation rate
	[mas]	[mas/y]	[mas]	[mas/y]
X	0.039	0.017	0.061	0.026
Y	0.053	0.011	0.081	0.003
Z	0.032	0.014	0.057	0.023

Tab. 5.3: Stability of the **NNR** datum: mean of the absolute values for rotations and rotation rates for three **TRF** solution with reduced number of datum stations w.r.t. a **TRF** solution with full number of datum stations (*Reduced/Full*) and of the **TRF** solution with reduced number of datum stations amongst each other (*Reduced/Reduced*).

transformation. However, all translations, their rates as well as the scale and the scale rate are zero as these quantities are determined by the observations and do not depend on the datum definition.

As expected, the intercomparison of the **TRFs** with a reduced number of datum stations shows a larger scatter compared to the comparison with the **TRF** with the full number of datum stations. The mean instability error derived from the intercomparison of the reduced **TRFs** is 0.017 mas/y. *Ray et al. (2004)* estimated an instability error of 0.020 mas/y for IGB00 solutions based on 25 stations. Compared to the stability of the reprocessed **TRF**, this value is slightly worse although the station number is larger by 5 stations. Based on the stability of solutions with 50 datum stations, *Ray et al. (2004)* concluded that the instability error of a **TRF** based on n datum stations can be deduced from the error estimates of a **TRF** with a smaller number of datum stations n_0 . That extrapolation with the factor $\frac{n_0}{n}$ gives a mean instability error of 0.006 mas/y for the reprocessed **TRF**. This error is only slightly worse compared to the IGB00 value of 0.005 mas/y. In addition, one has to consider that the number of datum stations is about one third larger for IGB00 (99 datum stations) compared to the reprocessed **TRF** (63 datum stations).

Velocities of GPS-GPS Co-locations The station velocities of co-located **GPS** sites with at least one year of observations are given in Tab. 5.4. Goldstone has been excluded due to a coordinate and velocity discontinuity caused by an earthquake. TLSE and TRO1 are affected by coordinate discontinuities due to equipment changes. However, the velocities of these sites have been constrained to be identical before and after the discontinuity as already mentioned above. The horizontal velocities in general agree within one millimeter per year. Several discrepancies can be explained by individual station problems, see footnotes of Tab. 5.4. For the vertical velocities, differences of more than 2 mm/y occur for more than half of the stations. The different sampling of periodic signals in the height component that are not considered by the linear model of the **TRF** solution might explain that effect to some extent. Ny Ålesund, O’Higgins, Thule and Tromsø are located in postglacial rebound regions responsible for the large positive vertical velocities. However, the vertical velocity of OHI2 is unreasonably large and seems to be affected by accumulation of snow on the antenna/radome.

Ny Ålesund and Tromsø are the only stations where both sites have observation periods longer than 8 years. Whereas the velocities of Ny Ålesund agree well below 1 mm/y, the north velocities of Tromsø differ by 1.1 mm/y and the east velocities even by 2.3 mm/y. At two stations, namely Tidbinbilla and Yarragadee (YAR1 and YAR2) two receivers are operated at the same antenna with an antenna splitter. These sites were treated completely independently, i.e. no constraints on the velocities have been applied. Whereas for Yarragadee the horizontal velocities are in almost perfect agreement, the north velocity of Tidbinbilla differs by 3.5 mm/y. For both sites, the vertical velocities differ by more than 5 mm/y. However, one has to be aware that there is no temporal overlap for these stations. For Tidbinbilla, the TIDB height component shows a higher noise compared to TID2 whereas TID2 shows a pronounced annual signal. These effects might explain the largest differences in the vertical velocity of all co-locations to some extent.

For several of the stations without known problems, the horizontal velocities agree within a few tenth of a mm/y and the vertical velocities within 1 mm/y. These numbers provide a realistic measure for the accuracy of the estimated velocities (the mean formal errors of 0.08, 0.07 and 0.11 mm/y for the north, east and up velocities are by far too optimistic). On the other hand, in particular the vertical velocities can show discrepancies larger than 5 mm/y for stations with few or even no overlap in the time series. Seasonal signals in the height component, data gaps or a true velocity change are possible explanations for that.

Station	Site	# days	Observation period		North [mm/y]	East [mm/y]	Up [mm/y]
Easter Island	EISL	3181	3 May 1994	29 Jan 2005	-5.7	67.5	-0.9
	ISPA ^a	609	14 Feb 2004	30 Oct 2005	-5.0	66.6	2.2
Galapagos	GALA ^b	2095	3 Feb 1996	9 Nov 2002	12.0	50.6	-1.7
	GLPS	975	7 Jan 2003	25 Oct 2005	9.9	49.8	-1.3
Hartebeesthoek	HART ^c	899	1 Jan 1994	25 May 1997	19.6	16.4	-5.9
	HARK	1097	13 Jun 1997	7 Aug 2000	18.5	20.9	-1.8
	HRAO	2880	27 Sep 1996	30 Oct 2005	17.3	17.7	1.0
Miami	MIA1	963	17 Sep 1995	31 May 1998	3.7	-12.7	-3.3
	AOML	2300	20 Nov 1997	4 Apr 2004	2.8	-10.6	0.6
Noto	NOTO	1707	21 Oct 1995	6 Sep 2000	19.1	21.6	-1.9
	NOT1	1865	15 Sep 2000	30 Oct 2005	19.9	20.9	-0.3
Ny Ålesund	NYAL	4042	2 Jan 1994	30 Oct 2005	14.2	10.2	7.6
	NYA1	2739	12 Mar 1998	30 Oct 2005	14.9	9.9	7.9
O'Higgins	OHIG	1797	11 Mar 1995	19 Feb 2002	10.8	13.7	4.5
	OHI2 ^d	1226	15 Feb 2002	30 Oct 2005	10.4	13.9	7.9
Taejon	TAEJ	1216	20 Nov 1995	17 Mar 1999	-12.7	28.4	-1.9
	DAEJ	2345	19 Mar 1999	30 Oct 2005	-12.2	26.6	0.6
Thule	THU1	2396	2 May 1995	12 Jan 2003	4.2	-22.4	2.9
	THU3	1513	26 Aug 2001	30 Oct 2005	4.8	-22.8	2.8
Tidbinbilla	TIDB	1395	1 Jan 1994	31 Oct 1997	58.7	18.6	-7.1
	TID2	2781	1 Nov 1997	30 Oct 2005	55.2	18.7	1.5
Toulouse	TOUL	1356	24 Feb 1997	3 Jan 2001	16.7	18.9	-1.0
	TLSE	1754	5 Jan 2001	30 Oct 2005	16.0	19.0	-0.1
Tromsø	TROM	3590	1 Jan 1994	30 Oct 2005	15.3	14.8	2.0
	TRO1	2762	12 Mar 1998	30 Oct 2005	16.4	17.1	2.6
Wettzell	WETT ^e	1007	1 Jan 1994	3 Oct 1996	18.1	24.2	-0.7
	WTZR	3573	10 Jan 1996	30 Oct 2005	15.6	20.1	-0.5
Yakutsk	YAKZ ^f	1288	15 Nov 1997	21 Jun 2001	-7.5	19.8	1.1
	YAKT ^g	1670	24 Jul 2000	30 Oct 2005	-13.7	20.2	3.5
Yarragadee	YARR	966	11 Jun 2002	30 Oct 2005	57.0	39.5	1.8
	YAR1	2642	1 Jan 1994	31 May 2001	57.4	39.7	-2.0
	YAR2	1602	1 Jun 2001	30 Oct 2005	57.4	39.6	3.8

^a observation period of only 20 months might be too short for a reliable velocity determination of the height component

^b noisy data before receiver change in January 2000

^c noisy data before receiver change in March 1996

^d snow-induced effects in the height component

^e tracking problem, see Sec. 4.3

^f annual signal of unknown origin in the north component

^g snow-induced effects in all three coordinate components, see Sec. 4.2.1

Tab. 5.4: Velocity estimates for co-located GPS sites. Sites with less than one year of observations have been excluded (HOB1/HOB2, MASP/MAS1, MCM1/MCM4, PAMA/TAHI/THTI). In addition, Goldstone (GOLD/GOL2) has been excluded due to an earthquake. Horizontal velocities differing by more than 1 mm/y and vertical velocities differing by more than 2 mm/y are given in gray.

5.4. Time Series Solutions

The TRF described in the previous section provides the basis for the time series solution: based on the reduced daily NEQs, station coordinate and origin of the tracking network time series are generated. All coordinate time series described so far in Sec. 4.2 were affected by systematic effects and artifacts. However, despite these effects, the reprocessed time series show a large improvement concerning homogeneity compared to inhomogeneous operational series. Time series of the origin of the tracking network and scale as well as some coordinate time series will be shown. In addition, the benefits of the reprocessed series will be demonstrated by comparisons with the ITRF2005 residual time series.

5.4.1. Origin of the Tracking Network and Scale

Whereas the origin of the tracking network was estimated simultaneously with station positions and ERPs in the time series solution, the scale time series has been determined a posteriori as part of a 7-parameter similarity transformation between the daily station positions and the TRF solution. These time series of the origin of the tracking network and the scale are given in Fig. 5.4. Due to the sparse tracking network, the scale time series as well as the origin time series show a larger scatter in the first two years. The STD of the origin estimates is 7.0 mm for the X-component, 7.6 mm for the Y-component and 15.2 mm for the Z-component. This is an improvement by a factor of three for the X- and Y-component and a factor of almost four for the Z-component compared to the values reported by *Heflin et al. (2002)*.

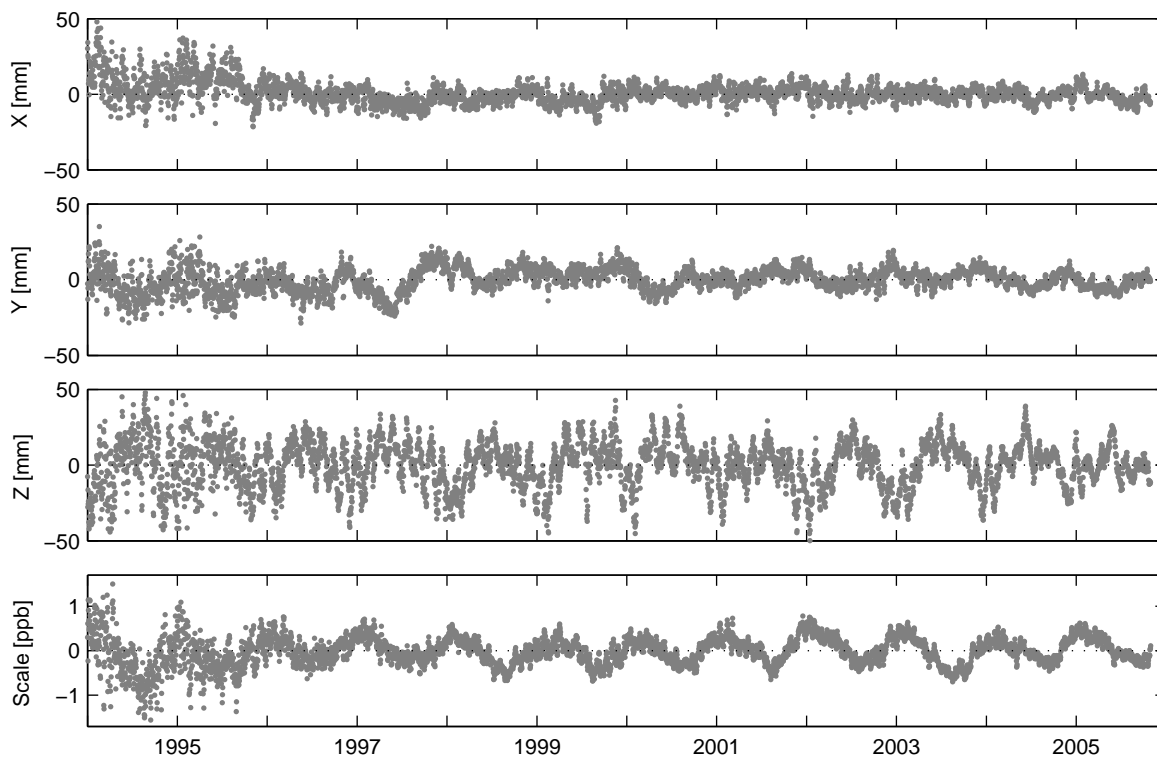


Fig. 5.4: Origin of the tracking network and scale time series. The scale was estimated as part of a 7-parameter similarity transformation of all stations w.r.t. the reference frame solution. Note the homogeneity of the time series compared to the operational CODE series shown in Fig. 1.3.

The simultaneous estimation of offset, drift, annual and semi-annual signals resulted in annual amplitudes of 2.1 ± 0.1 mm, 5.1 ± 0.1 mm and 11.6 ± 0.3 mm for the X-, Y-, and Z-component, respectively. Although the absolute values of these amplitudes are smaller by a factor of 1.5–2 compared to the GPS-derived amplitudes reported by *Heflin et al. (2002)* and *Altamimi et al. (2005b)*, they still exceed the variations observed by SLR or predicted by geophysical models (*Feissel-Vernier et al., 2006*). In particular the Z-component seems to be dominated by systematic errors. Due to the limited length of the time series, it is not possible to determine whether the long-period signal in the Z-component is indeed of annual nature or whether its period is 351.5 days. The latter period is an artifact introduced by the changing orientation of the orbital planes

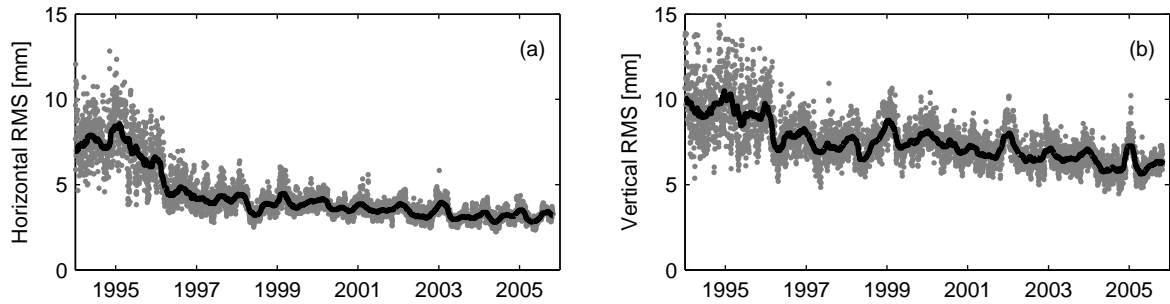


Fig. 5.5: RMS of daily 7-parameter similarity transformations between the time series solution and the reference frame solution: (a) horizontal component; (b) vertical component. Stations exceeding the outlier limit of 20 mm for the north and east component and 50 mm for the height component have been excluded from the transformation. The solid line indicates a 100-day median.

w.r.t. the Sun, see [Hugentobler et al. \(2005b\)](#) and Sec. 4.3.2. In addition, a short-period signal of about 50 days could also be detected in the Z-component ([Flohner, 2008](#)). Other systematic effects are related to the inhomogeneous station distribution as regards northern and southern hemisphere. [Lavallée et al. \(2006\)](#) showed that the additional estimation of surface load coefficients results in more consistent geocenter estimates compared to the simple approach applied here (“network shift approach”). A TRF computed from the reprocessed solution considering surface load is described in detail by [Rülke et al. \(2008\)](#).

Due to the application of satellite-specific antenna z -offsets, no satellite constellation-related effects can be seen in the scale time series (see Sec. 9.2.1). The amplitude of the annual signal in the scale time series is 0.32 ± 0.01 ppb. This value is in good agreement with the amplitude of 0.3 ppb reported by [Heflin et al. \(2002\)](#) from the JPL GPS solutions. On the other hand, this amplitude is smaller by 45% compared to the scale amplitude of 0.56 ± 0.03 ppb determined by [Tesmer et al. \(2007\)](#) from 13 years of VLBI observations. The small number of VLBI telescopes and their inhomogeneous distribution might explain that effect as the scale parameter is related to a common-mode motion of the station heights. With less stations compared to GPS and stations that are in addition concentrated in certain areas of the world (in particular Europe and North America), the VLBI network shows a more pronounced common-mode motion due to, e.g., geographically correlated loading effects resulting in a higher scale amplitude.

The RMS values of the 7-parameter similarity transformations between the daily time series solutions and the reference frame solution are given in Fig. 5.5. The mean RMS values of the horizontal and vertical coordinate components are 4.4 and 7.5 mm with corresponding median values of 3.8 and 7.3 mm. In the first two years, both, the horizontal and the vertical component show larger values as well as an increased scatter due to the small number of tracking stations.

5.4.2. Station Coordinate Time Series

Earthquakes

All sites of the reprocessing network affected by earthquakes are listed in Tab. 5.5. Due to its magnitude of 9.0, the Sumatra earthquake even affected stations far away (up to 2900 km) from the epicenter (located off the west coast of northern Sumatra, Indonesia). In contrast to the analyses of a regional network by [Kaniuth \(2005\)](#), DGAR shows a displacement due to this earthquake. The horizontal displacements reported by [Kaniuth \(2005\)](#) differ by up to 2.0 cm from the results in Tab. 5.5. On the other hand, the horizontal displacements derived from the IGS products by [Kouba \(2005a\)](#) agree with the reprocessing at least within 3 mm. Due to these differences, it seems to be reasonable to assume that the results of the global network (based on a stable reference frame represented by a set of globally distributed stations) are more reliable than those of a regional network where no guarantee can be given that all datum stations are not affected by the earthquake.

The time series of the station with the largest displacement due to an earthquake, namely Arequipa, is shown in Fig. 5.6. As the epicenter was located only about 200 km away, the GPS site experienced a large horizontal displacement of about 50 cm. During the first week after this earthquake, the postseismic displacement was 1.6 cm for the north and 1.9 cm for the east component. A second earthquake that affected

Date Magnitude	Region Reference(s)	Site	ΔN [cm]	ΔE [cm]	ΔU [cm]
17 Aug 1999 7.6	Turkey <i>Ergintav et al. (2002)</i>	ANKR	0.4	-0.9	1.0
16 Oct 1999 7.2	Southern California <i>Owen et al. (2002)</i>	GOL2 JPLM SIO3	-0.1 0.0 0.4	-0.8 -0.3 0.2	0.0 -0.4 -0.7
12 Nov 1999 7.2	Turkey <i>Daniel et al. (2006)</i>	ANKR	-0.1	-0.4	0.6
18 Jun 2000 7.6	South Indian Ocean	COCO	-0.4	2.9	0.4
21 Jun 2000 6.4	Iceland <i>Árnadóttir et al. (2001)</i>	REYK	-0.1	-0.7	-1.2
23 Jun 2001 8.4	Near Coast of Peru <i>Kaniuth et al. (2002)</i>	AREQ	-28.7	-42.0	-3.0
26 Apr 2002 7.1	Mariana Islands	GUAM	-2.0	0.7	-1.1
03 Nov 2002 7.9	Central Alaska <i>Hreinsdóttir et al. (2003)</i>	FAIR	-5.0	2.5	1.7
25 Sep 2003 8.3	Hokkaido, Japan Region <i>Miyazaki et al. (2004)</i>	YSSK	-1.0	0.1	-0.1
23 Dec 2004 8.1	North of Macquarie Island	HOB2 MAC1	-0.1 -2.3	0.4 -1.2	0.0 -0.2
26 Dec 2004 9.0	Off the West Coast of Northern Sumatra <i>Kaniuth (2005), Kouba (2005a)</i>	DGAR IISC KUNM NTUS PIMO	0.7 0.2 -0.5 0.7 0.3	0.5 1.7 -0.5 -1.9 -0.6	0.2 0.0 0.4 -1.3 -0.8

Tab. 5.5: List of earthquakes affecting stations of the reprocessing network and corresponding discontinuities derived from the 3-day solution. The magnitude information was provided by the U.S. Geological Survey (http://neic.usgs.gov/neis/eq_depot/).

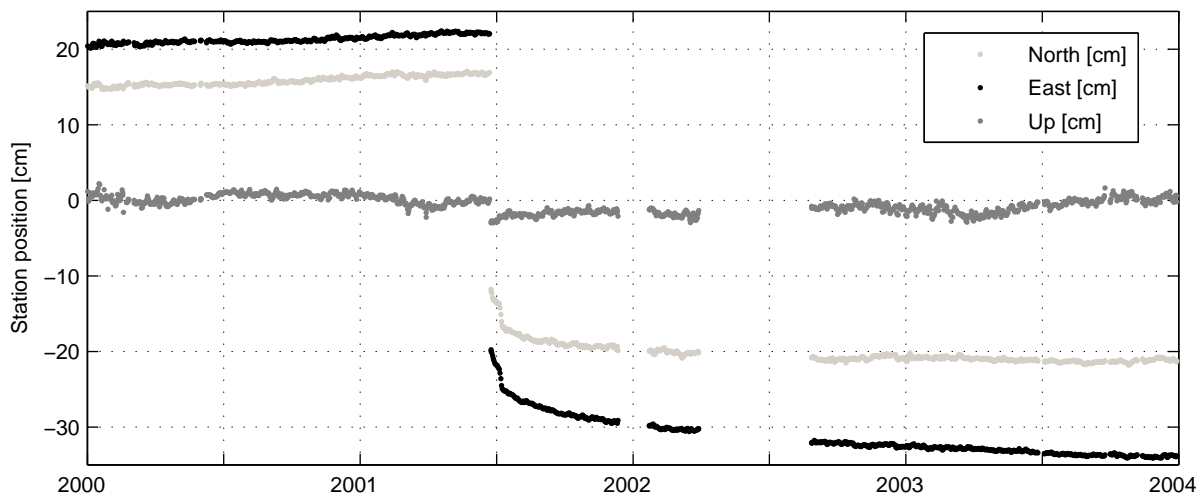


Fig. 5.6: Coordinate time series for Areqipa (Peru). The first earthquake with a magnitude of 8.4 took place on 23 June 2001. The second earthquake with a magnitude of 7.6 on 7 July 2001 can only be seen in the horizontal coordinate components.

Arequipa on 7 July 2001 has not been considered as discontinuity due to its vicinity to the first earthquake on 23 June 2001 and the rapidly changing station velocity during the postseismic reaction. After the data gap from end of 2002 till beginning of 2003, the horizontal movement seems to be linear again although significantly differing from the velocity before the earthquake.

Episodic Tremor and Slip

The coordinate time series for Albert Head (ALBH) located in western Canada in the northern Cascadia subduction zone is shown in Fig. 5.7. It was derived from a special 3-day solution where the reference frame stations were constrained with 0.1 mm to their a priori values. The RMS is 1.3 mm for the north and 5.2 mm for the up component (after correcting for the discontinuity described later). In the east component one can see a phenomenon called Episodic Tremor and Slip (ETS, *Rogers and Dragert, 2003; Szeliga et al., 2004*). Each 13–16 months the station is shifted westwards by a slip event accompanied by seismic activity (tremor). Eight ETS events can clearly be seen in the period between January 1996 and October 2005 shown in Fig. 5.7. Due to the homogeneity of the reprocessed time series this geophysical phenomenon is even visible in a global GPS solution which has higher noise in the coordinate estimates than solutions from a local or regional network. Moreover, a jump caused by an equipment change can be seen in the time series: on 5 September 2003 the antenna was changed to another AOAD/M.T and the radome was changed from EMRA (so called EMR clear spherical acrylic dome) to SCIS (so called SCIGN short antenna dome) resulting in a discontinuity of several millimeters in the east and 12 mm in the up component.

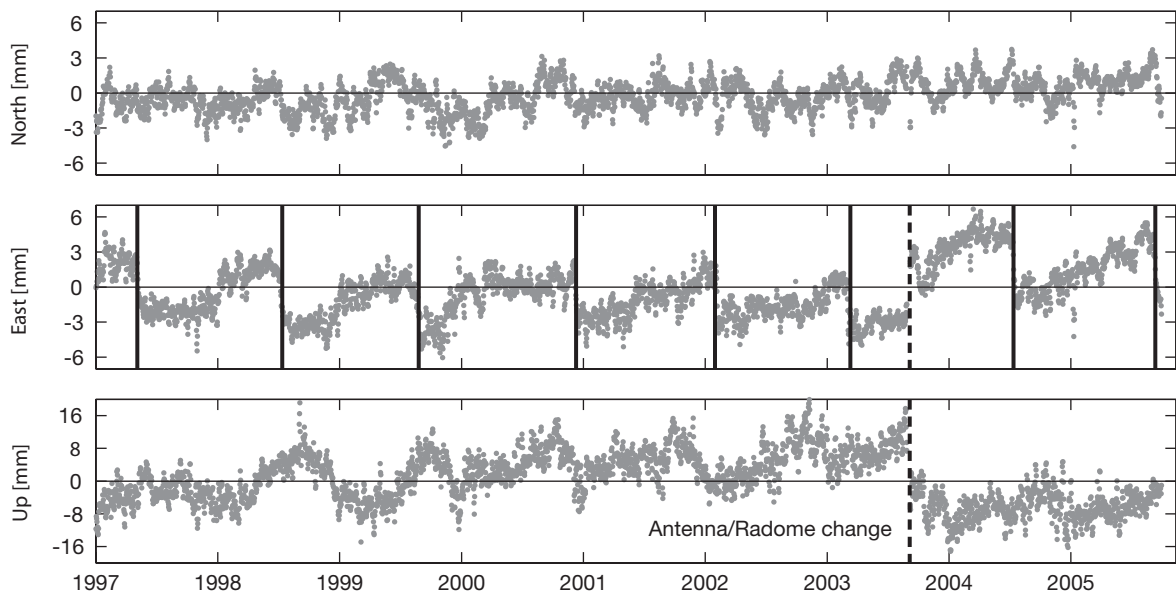


Fig. 5.7: Coordinate time series for Albert Head (Canada). Episodic tremor and slip events in the east component are indicated by solid lines, the antenna/radome change in September 2003 (only affecting the east and up component) by a dashed line.

Comparison with ITRF Residual Time Series

Fig. 5.8 shows the station coordinate residual time series for the reprocessed solution and ITRF2005¹ (*Altamimi et al., 2007*) for two selected stations, namely Santiago (Chile) and Taejon (Korea). The reprocessed series has a daily time resolution whereas the ITRF2005 solution is based on weekly combined IGS SINEX files. Therefore, the scatter of the reprocessed solution is in general higher. For Santiago, the ITRF2005 series shows a discontinuity of 2 cm in the height component in mid of 1996 due to an antenna and receiver change. In the homogeneously reprocessed series, this discontinuity is not visible anymore. This fact indicates that the discontinuity was introduced by changes in the analysis strategy or in the contribution of different ACs to the combined IGS solution. The second discontinuity introduced for ITRF2005

¹available at http://itrf.eng.ign.fr/ITRF_solutions/2005/doc/GPS_residuals.zip

does not suit to the corresponding residual time series at all: discontinuities in the height component can be seen at the beginning of 1998 and at the end of 1999 but not in November 1998, where a discontinuity was introduced. The reprocessed series show some kind of local maximum at the end of 1998 but no discontinuity can be seen.

For Taejon the horizontal components of both series agree quite well except for some outliers in the *ITRF* series. However, the height component of the *ITRF* series shows a clear negative trend before the data gap in the end of 1997. At the beginning of this gap, a position discontinuity was set up in the *ITRF* series, whereas the velocities before and after the discontinuity were forced to be identical. However, as the residuals before the discontinuity show a clear trend, this assumption seems to be erroneous. As the reprocessed height residuals do neither show a discontinuity nor any drift, the strange behavior of the *ITRF* series seems to be related to the inhomogeneous input data of *ITRF*2005. These two examples emphasize the importance of fully reprocessed *GPS* data as input for future *ITRF* computations.

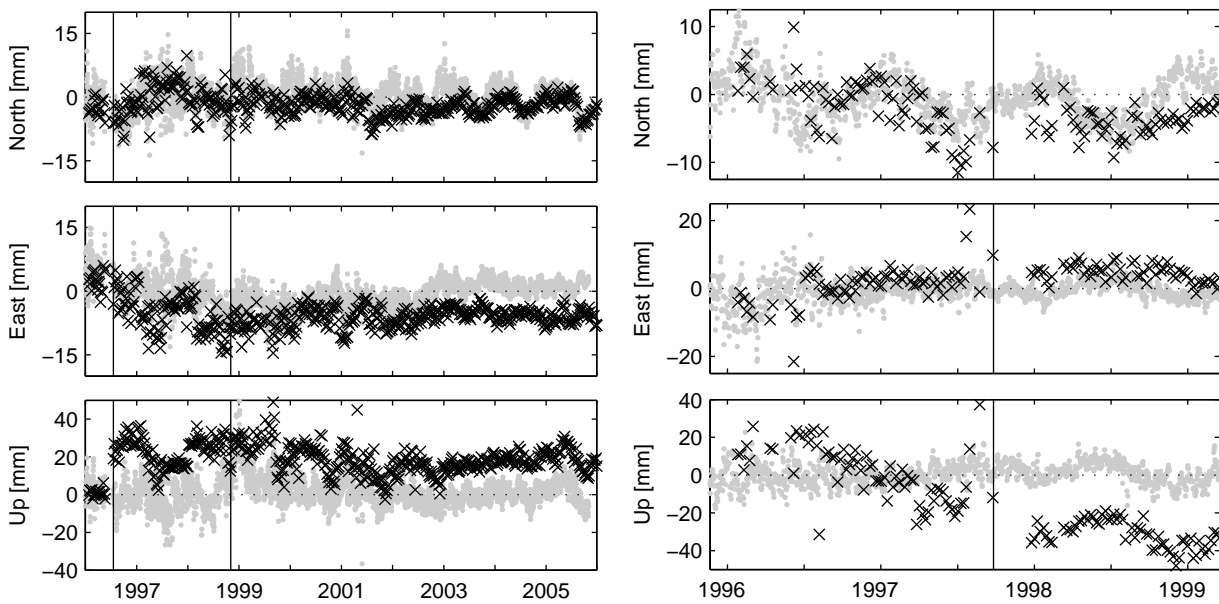


Fig. 5.8: Station coordinate residual time series from *ITRF*2005 (black crosses) and the reprocessing (gray dots). Discontinuities accounted for in the *ITRF* solution are indicated by vertical lines. Santiago (Chile) is shown on the left hand side, Taejon (Korea) on the right hand side.

6. Troposphere Parameters

For the validation of the troposphere parameters (troposphere zenith delays and gradients), comparisons with other **GPS** solutions as well as other techniques can be used. As for the station coordinates, **GPS-GPS** co-locations serve as a quality indicator for the internal consistency of the **GPS**-derived troposphere parameters. Co-locations with other space-geodetic techniques that are able to determine troposphere parameters, like the **VLBI**, allow an independent validation of the **GPS**-derived results as well. The signals of these different techniques pass identical parts of the atmosphere. Therefore, the estimated tropospheric zenith delays should be the same except for the part that is related to the height differences between the different antennas and systematic errors of both techniques. Several authors performed such inter-comparisons (e.g., *Pacione et al., 2002*; *Snajdrova et al., 2005*; *Krügel et al., 2007*), although the number of long-term studies is limited (e.g., *Gradinarsky et al., 2002*; *Haas et al., 2003*; *Negusini and Tomasi, 2005*; *Heinkelmann et al., 2007*). A major disadvantage of these long-term studies is the inhomogeneity of the **GPS** series used. E.g., the reference frame-dependent drift behavior of the **IGS** combined troposphere parameters will be revealed by comparisons with the reprocessed series.

To study the effects of different troposphere modeling approaches in more detail, **GPS** and **VLBI** solutions with different mapping functions and different hydrostatic a priori delays have been computed. These solutions are listed in Tab. 6.1. As not all solutions listed in Tab. 6.1 cover the complete time interval of the reprocessing, inter-comparisons of these solutions will be limited to the time interval 1 January 1994 till 31 December 2004. Like for **IMF** (see Sec. 3.1), the **VMF1** coefficients and the **ECMWF** hydrostatic a priori delays were interpolated from 6-hourly grids provided by TU Vienna. In Sec. 6.1, the solution **NMF** will be used for comparisons with the **IGS ZTD** product. In general, the comparisons of the troposphere zenith delays in Sec. 6.1 and the troposphere gradients in Sec. 6.2 focus on solution **IMF** as this mapping function was also used for the generation of the default 1-day solutions and the multi-day solutions (see Sec. 3.1). Finally, Sec. 6.3 intercompares all solutions listed in Tab. 6.1 as regards troposphere parameters and station coordinates.

Solution	hydrostatic a priori delay	hydrostatic MF	wet MF
NMF	Berg/Saastamoinen	hydrostatic NMF	wet NMF
GMF	Berg/Saastamoinen	hydrostatic GMF	wet GMF
IMF	Berg/Saastamoinen	hydrostatic IMF	wet NMF
VMF1	Berg/Saastamoinen	hydrostatic VMF1	wet VMF1
VMF1 ECMWF	ECMWF	hydrostatic VMF1	wet VMF1

Tab. 6.1: 1-day solutions with different troposphere mapping functions and hydrostatic a priori delays.

6.1. Troposphere Zenith Delays

6.1.1. Comparisons with IGS Troposphere Parameters

From 1997 to 2006 the **IGS** provided a combined troposphere product (*Gendt, 1996*), namely the zenith total delay computed as a weighted mean of the different **AC** solutions. Up to seven **ACs** contributed to the **IGS** final troposphere product using six different software packages (the near real-time **ZTD** product will not be considered here). The **ZTD** contributions were combined in a non-rigorous way independently from the station positions used, not considering inconsistencies introduced by changes in the reference frame as well as all model changes (e.g., cut-off angle and mapping function).

Fig. 6.1 reveals these inconsistencies by comparing the **IGS ZTD** with the reprocessed **GPS** solution for Algonquin Park (Canada). As most **IGS ACs** use the Niell mapping function, for the comparisons with the **IGS** combined troposphere parameters solution **NMF** was used. A systematic bias of about 7 mm can be

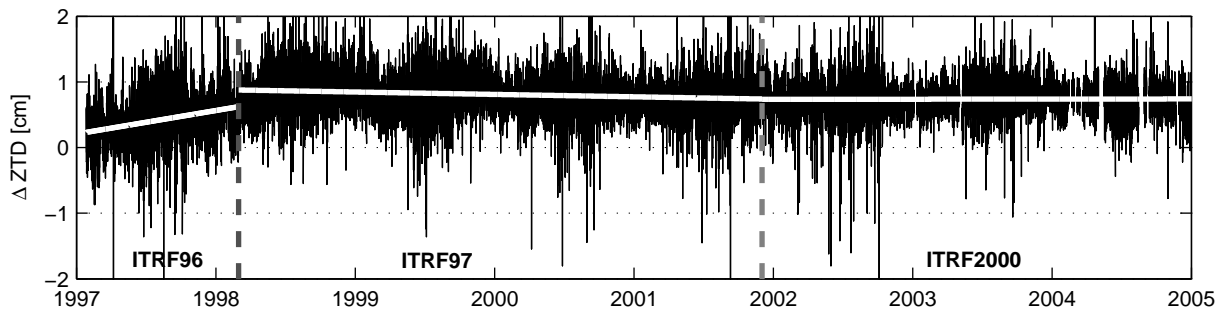


Fig. 6.1: Differences between IGS and reprocessed troposphere zenith delays for Algonquin Park (ALGO). The different drift behavior of the three time periods coincides very well with the different reference frame realizations (marked by dashed vertical lines): ITRF96: +3.6 mm/y, ITRF97: -0.4 mm/y, ITRF2000: 0.0 mm/y.

seen between both solutions which is probably due to different models for the phase centers of receiver and satellite antennas that will be discussed in more detail in Sec. 9.1. Besides, the varying drift behavior of the ZTD difference obviously coincides with the different reference frames used for datum definition by the IGS: ITRF96 (Boucher *et al.*, 1998), ITRF97 (Boucher *et al.*, 1999) and ITRF2000 (Altamimi *et al.*, 2002). As long as ITRF2000 is used within both, the IGS and the reprocessing, the drift of the difference between both solutions is zero as to be expected. In the time interval, when ITRF97 was used for the IGS solution, the drift is -0.4 mm/y, with ITRF96 it is even +3.6 mm/y. The interpretability of such inhomogeneous time series for long-term climatological studies is questionable. Amongst others due to these problems, the creation of the combined IGS troposphere product was stopped after the switch to ITRF2005 in November 2006 (IGSMail 5505).

6.1.2. GPS-GPS Co-locations

Troposphere estimates of co-located GPS stations can be used to evaluate the internal consistency of these parameters as the difference in the zenith delays should be dominated by a constant bias depending on the height difference between both stations. Fig. 6.2 shows the ZTD differences between the two sites NYAL and NYA1 operated at Ny-Ålesund (Norway) for the IGS combined troposphere product and the reprocessed solution. The IGS difference clearly contains an annual signal with an initial amplitude of 2.5 ± 0.1 mm before 2003. The amplitude of the signal decreases in 2003 and the signal vanishes in 2004. This signal is probably induced by the contribution of different ACs to the combined solutions of the two stations: NYAL data is analyzed by ESOC (continuously till January 2004, later only occasionally), JPL (till March 2004), NOAA (till December 2004), NRCAN, and SIO; NYA1 data by CODE, GFZ, JPL and SIO for the time period considered in Fig. 6.2. The periodic signal vanishes as soon as the configuration of the ACs contributing to the combined solution of NYAL changes (beginning of 2004). However, the systematic shifts in 2005 cannot be attributed to a change in the contributions of the ACs, their origin is unknown. According to Dong *et al.* (2002) systematic errors in the different software packages and processing strategies are a major reason for such seasonal signals. The IGS solution for the two sites at Tromsø contains a similar periodic signal whereas the other GPS-GPS co-locations listed in Tab. 6.2 do not show such a signal.

Drift, RMS (after removing offset and drift) and correlation coefficients between the ZTDs of co-located GPS sites for the IGS and the reprocessed solution are displayed in Tab. 6.2. While the differences in correlation are rather small, the improvement of the reprocessed solution w.r.t. the IGS solution is quite evident as regards drift and RMS. The drift of the ZTD difference (physically/theoretically expected to be zero) is smaller by a factor of at least two for most stations of the reprocessed solution. Only for Tromsø the drift is the same, whereas the RMS for the reprocessed solution is smaller by a factor of 2.5. The results for Yakutsk (YAKZ/YAKT: very high drift for IGS, RMS is worse for reprocessed solution) and the reprocessed solution for Hartebeesthoek (HRAO/HART) have to be handled with care as the number of ZTD parameters contributing to the comparison of these stations is small.

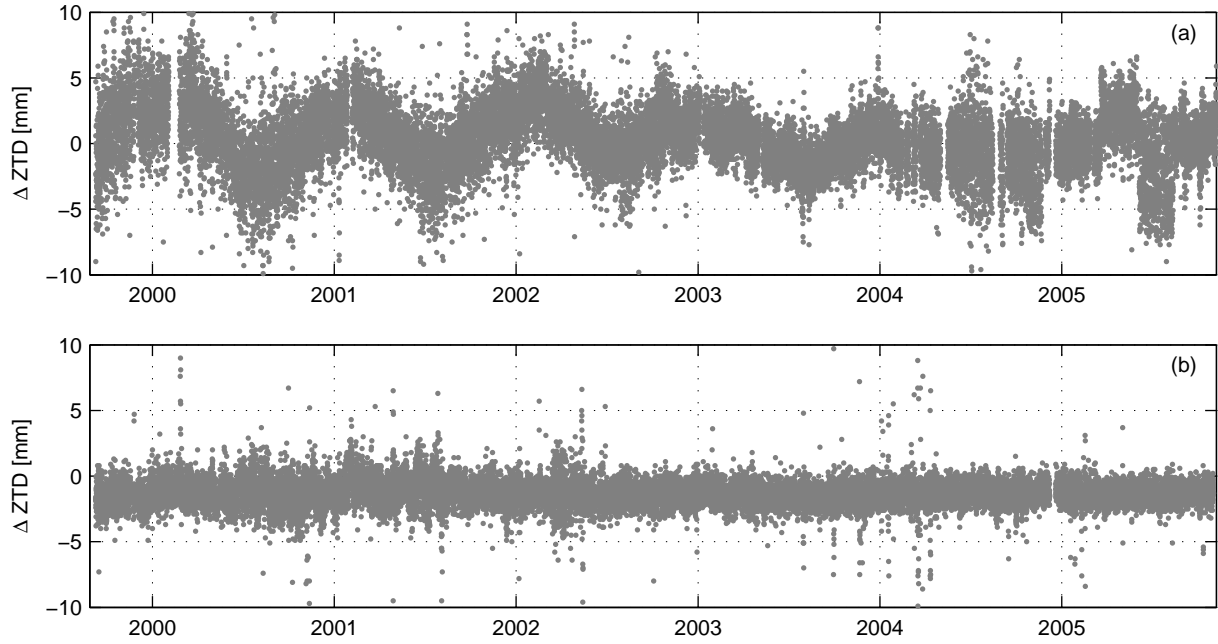


Fig. 6.2: Zenith total delay differences for the [GPS-GPS](#) co-location Ny-Ålesund (NYAL and NYA1): (a) [IGS](#) troposphere parameters; (b) reprocessed troposphere parameters.

Site 1	Site 2	# Parameters		Drift [mm/y]		RMS [mm]		Correlation coefficient	
		IGS	Repro	IGS	Repro	IGS	Repro	IGS	Repro
HRAO	HARK	4,118	9,808	0.9	-0.1	6.5	4.5	0.993	0.997
HRAO	HART	5,150	620	2.0	-0.2	5.7	2.8	0.994	0.998
NYAL	NYA1	27,685	30,931	-0.6	-0.2	5.0	1.3	0.992	0.999
TROM	TRO1	22,886	28,403	0.3	0.3	6.3	2.0	0.993	0.999
YARR	YAR2	3,503	10,210	-1.2	0.1	4.7	2.3	0.990	0.998
YAKZ	YAKT	816	1,270	6.8	0.1	3.0	3.5	0.997	0.996

Tab. 6.2: Drift, [RMS](#) and correlation coefficient for [GPS-GPS](#) co-locations: [IGS](#) troposphere parameters and [ZTDs](#) of solution NMF.

6.1.3. GPS-VLBI Co-locations

Amongst other parameters like station coordinates and [EOPs](#), observations of extragalactic radio sources (quasars) with [VLBI](#) telescopes provide the possibility to determine troposphere zenith delays and gradients. For more details on the [VLBI](#) observation technique see, e.g., [Sovers et al. \(1998\)](#). Geodetic [VLBI](#) sessions are scheduled by the International [VLBI](#) Service for Geodesy and Astrometry ([IVS](#), [Schlüter et al., 2002](#)) on a regular basis and the observations are provided by the [IVS DCs](#). In the following, co-located stations (see [Tab. 6.4](#)) of the [VLBI](#) solution DGFI05R03 computed by Deutsches Geodätisches Forschungsinstitut ([DGFI](#)) with the [OCCAM](#) ([Titov et al., 2004](#)) software will be used for inter-technique comparisons with the reprocessed M3 [GPS](#) 1-day solutions. Earlier comparisons with the M1 solution are described in [Steigenberger et al. \(2007\)](#). A critical issue when comparing common parameters from [GPS](#) and [VLBI](#) are systematic effects between the two techniques and the corresponding software packages. In the framework of recent combination studies using [GPS](#) and [VLBI](#) data collected during the CONT02 campaign ([Krügel et al., 2004](#); [Thaller et al., 2006](#)), an intensive homogenization of the two software packages (Bernese and [OCCAM](#)) concerning modeling (solid Earth tides, pole tide, ocean loading, high-frequency [ERP](#) model, nutation and precession model, troposphere a priori model and mapping functions) and parameterization (constant offsets for station coordinates, continuous piecewise linear functions for troposphere zenith delays and [ERPs](#)) has been performed. This is essential in order to avoid misinterpretations due to differences in modeling and parameterization.

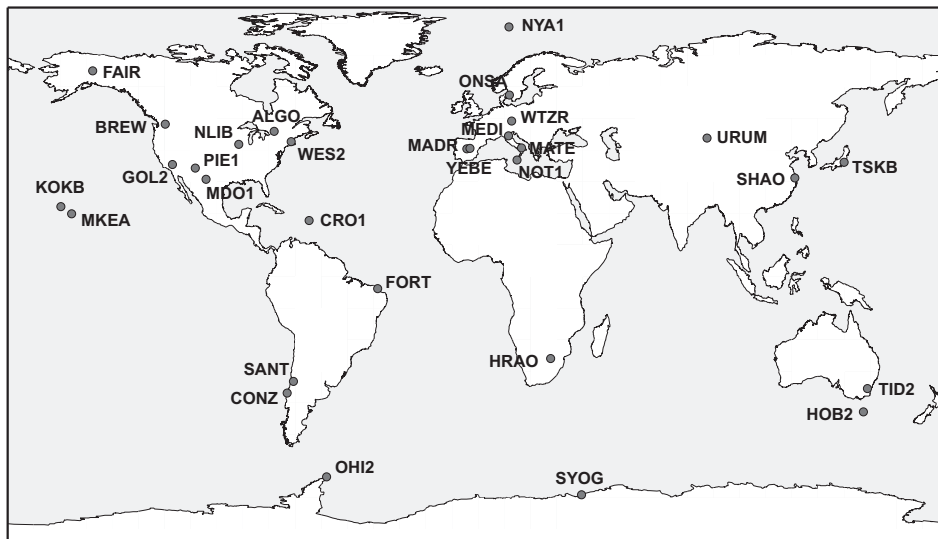


Fig. 6.3: Map of co-located **GPS** and **VLBI** stations. If more than one **GPS** site is located at a station, only the name of the primary **GPS** site is given (all sites belonging to one station are listed in Tab. 6.4).

Altogether five different **VLBI** solutions with the mapping functions and hydrostatic a priori delays according to Tab. 6.1 were computed from data of 49 telescopes (4 to 20 per session) from 2760 24-hour sessions between 4 January 1984 and 30 December 2005 using OCCAM 6.1 and DOGS-CS (Angermann et al., 2004). The terrestrial and the Celestial Reference Frame (CRF) as well as the ERPs were estimated simultaneously to guarantee full consistency within the **VLBI** solution (Tesmer et al., 2004). An elevation cut-off angle of 5° and a refined stochastic model that mainly consists of an elevation-dependent weighting (Tesmer and Kutterer, 2004) were applied. The unknown parameters were estimated with a least-squares adjustment using the Gauß-Markoff model. Important characteristics of the **GPS** and the **VLBI** solution are summarized in Tab. 6.3.

Altogether 39 **GPS** sites are located in the vicinity of 30 **VLBI** stations, see Fig. 6.3. When excluding the co-location with the largest distance between the **GPS** and the **VLBI** reference point (Urumqi with a height difference of 1174 m and a horizontal distance of more than 50 km), the height differences vary from 1.5 m to 400 m and the horizontal distances from 26 m to 8 km with median values of 9 m and 87 m, respectively. The co-located **GPS** and **VLBI** stations are listed in Tab. 6.4, together with the corresponding observation periods, the horizontal distances and the height differences.

As the temporal resolution of the **GPS** troposphere zenith delay parameters is 2 hours, whereas it is 1 hour for **VLBI**, the **GPS** values are interpolated linearly to compare the results of both techniques. Outliers have been removed from the reprocessed series using different criteria: **GPS** parameters with a formal error exceeding the threefold mean formal error (3σ) of the whole time series of each station were excluded. In case of **VLBI**, only parameters determined by at least three observations were used. The number of troposphere parameters excluded due to these criteria are on average 6.9% for **VLBI** (for those stations considered for further comparisons, see below and Tab. 6.5; 8.5% for all stations) and 0.9% for **GPS**.

	GPS	VLBI
Software	Bernese 5.0	OCCAM 6.1, DOGS-CS
Data	4322 1-day solutions (1994–2005)	2760 24-hour sessions (1980–2005)
Number of stations	202 (40–160 per day)	49 (3–20 per session)
Datum	NNR w.r.t. IGb00	NNR/NTT w.r.t. ITRF2000
Solution type	global solution including station coordinates, orbits and ERPs	simultaneous estimation of TRF , CRF and ERPs
Troposphere zenith delays	2-hour resolution	1-hour resolution

Tab. 6.3: Important characteristics of the **GPS** and **VLBI** solutions.

Name	VLBI				GPS				Distance [m]	Height diff. [m]	$b_{\text{saast, wet}}$ [mm]
	Station	Observation period		# ZWD Par.	Station	Observation period		# ZWD Par.			
Algonquin	ALGOPARK	13 May 1994	23 Dec 2005	12,250	ALGO	1 Jan 1994	1 Nov 2005	51,458	111	23.0991	1.99
Brewster	BR-VLBA	14 Jan 1994	29 Sep 2005	2,458	BREW	20 Sep 2001	1 Nov 2005	16,502	58	11.8821	0.99
Concepcion	TIGOCONC	13 May 2002	10 Jun 2005	6,392	CONZ	20 Jun 2002	14 May 2005	11,738	120	-9.7671	-0.87
Sant Croix	SC-VLBA	14 Jan 1994	29 Sep 2005	2,335	CRO1	13 Oct 1995	1 Nov 2005	39,464	81	16.9366	1.85
Fairbanks	GILCREEK	4 Jan 1994	28 Dec 2005	23,739	FAIR	1 Jan 1994	1 Nov 2005	49,736	93	13.0526	1.00
Fortaleza	FORTLEZA	4 Jan 1994	30 Dec 2005	16,925	FORT	1 Jan 1994	1 Nov 2005	42,680	53	3.6000	0.38
Goldstone	DSS15	26 Aug 1994	29 Jun 2005	691	GOLD	1 Jan 1994	31 Dec 1995	8,033	411	-13.5000	-0.53
					GOL2	1 Jan 1996	5 Jan 2005	38,554	411	-13.5000	-0.53
Hartebeesthoek	HARTRAO	17 Jan 1994	20 Dec 2005	9,949	HART	1 Jan 1994	11 Jun 1997	12,620	2261	-129.9000	-3.01
					HARK	13 Jun 1997	7 Aug 2000	10,564	2261	-129.9000	-3.01
					HRAO	27 Sep 1996	1 Nov 2005	33,985	164	1.5173	0.04
Hobart	HOBART26	14 Jan 1994	15 Dec 2005	4,952	HOB1	1 Jan 1994	7 Aug 1994	2,602	60	8.5000	0.85
					HOB2	30 Nov 1995	1 Nov 2005	38,103	193	24.0000	2.43
Kokee Park	KOKEE	4 Jan 1994	30 Dec 2005	23,694	KOKE	1 Jan 1994	1 Nov 2005	47,743	46	9.2360	0.30
Madrid	DSS65	27 Apr 1994	15 Dec 2004	1,344	MADR	1 Jan 1994	1 Nov 2005	34,335	265	4.3818	0.20
Matera	MATERA	7 Jan 1994	28 Dec 2005	8,145	MATE	1 Jan 1994	1 Nov 2005	49,876	57	7.7189	0.48
McDonald	FD-VLBA	12 Jan 1994	29 Sep 2005	2,481	MDO1	1 Jan 2004	1 Nov 2005	50,530	8408	-403.6246	-6.79
Medicina	MEDICINA	27 Apr 1994	30 Dec 2005	4,528	MEDI	4 Mar 1996	1 Nov 2005	40,310	60	17.1283	1.73
Mauna Kea	MK-VLBA	14 Jan 1994	29 Sep 2005	2,456	MKEA	27 Sep 1996	1 Nov 2005	38,169	87	8.3493	0.02
North Liberty	NL-VLBA	14 Jan 1994	29 Sep 2005	2,323	NLIB	1 Jan 1994	1 Nov 2005	49,530	66	15.2355	1.31
Noto	NOTO	31 Aug 1994	23 Mar 2005	1,608	NOTO	21 Oct 1995	6 Sep 2000	22,088	68	17.0146	1.58
					NOT1	15 Sep 2000	1 Nov 2005	19,969	70	16.9000	1.59
Ny-Ålesund	NYALES20	4 Oct 1994	30 Dec 2005	15,127	NYAL	2 Jan 1994	1 Nov 2005	46,453	112	3.6442	0.36
					NYA1	12 Mar 1998	1 Nov 2005	31,548	106	3.1030	0.30
O'Higgins	OHIGGINS	16 Feb 1994	2 Feb 2005	756	OHIG	11 Mar 1995	19 Feb 2002	20,327	51	9.2853	0.96
					OHT2	15 Feb 2002	1 Nov 2005	13,842	26	7.5000	0.77
Onsala	ONSA60	12 Jan 1994	15 Nov 2005	5,760	ONSA	1 Jan 1994	1 Nov 2005	50,525	78	12.7151	1.29
Pie Town	PIETOWN	14 Jan 1994	29 Sep 2005	2,245	PIE1	1 Jan 2004	1 Nov 2005	50,630	59	16.9594	0.16
Santiago	SANTIA12	16 Feb 1994	22 Nov 1996	927	SANT	1 Jan 1994	1 Nov 2005	47,197	133	-7.2443	-0.37
Sheshan	SESHAN25	16 Mar 1994	7 Dec 2005	2,646	SHAO	20 Jan 1995	1 Nov 2005	36,594	92	7.3000	0.76
Syowa	SYOWA	8 Nov 1999	9 Dec 2004	280	SYOG	13 Mar 1995	1 Nov 2005	41,574	124	-1.1059	-0.11
Tidbinbilla	DSS45	27 Jan 1994	9 Jun 2004	1,070	TIDB	1 Jan 1994	31 Oct 1997	33,253	226	9.0227	0.49
					TID2	1 Nov 1997	1 Nov 2005	16,496	226	9.0227	0.49
Tsukuba	TSUKUB32	7 Oct 1998	21 Dec 2005	4,413	TSKB	1 Jan 1994	1 Nov 2005	51,071	47	17.4000	1.72
Urumqi	URUMQI	20 Aug 1997	21 Dec 2005	996	URUM	1 Nov 1998	9 Oct 2005	26,860	50 km	1174.4000	30.25
Westford	WESTFORD	12 Jan 1994	29 Sep 2005	13,314	WES2	1 Jan 1994	1 Nov 2005	48,432	58	1.7359	0.17
Wettzell	WETTZELL	4 Jan 1994	30 Dec 2005	28,026	WETT	1 Jan 1994	3 Oct 1996	11,891	150	3.1000	0.17
					WTZR	10 Jan 1996	1 Nov 2005	42,297	139	3.0950	0.17
Yebees	YEBES	3 Nov 1996	16 Jul 2003	715	YEBE	30 Sep 2000	1 Nov 2005	21,868	106	7.1214	0.28

Tab. 6.4: Co-located **GPS** and **VLBI** stations: observation statistics, horizontal distance and height difference (VLBI – GPS) between the antennas. Height differences with full resolution were obtained from local ties, the others were computed from coordinate differences. The theoretical bias $b_{\text{saast, wet}}$ in the troposphere parameters is computed from the wet part of the Saastamoinen model applying a standard atmosphere.

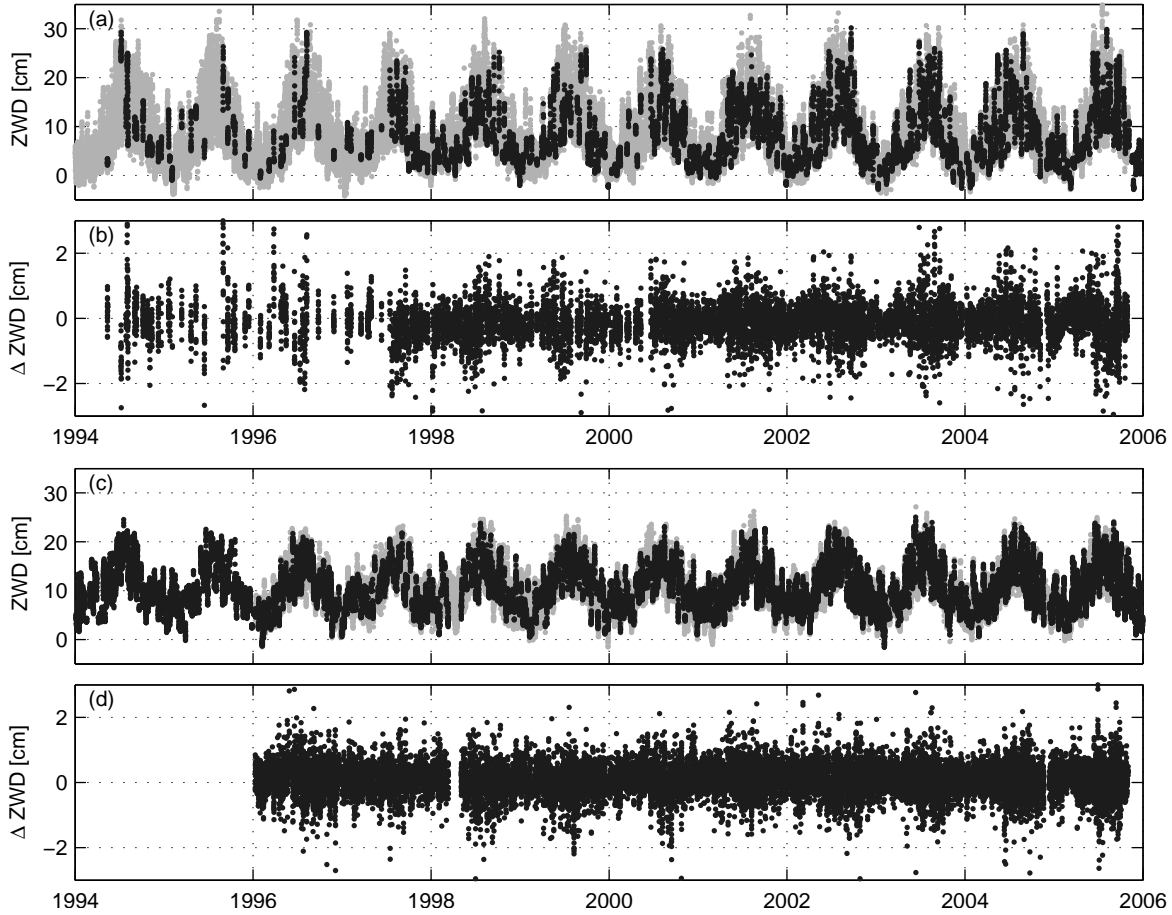


Fig. 6.4: Troposphere zenith wet delays determined by GPS (gray) and VLBI (black) and the difference between the two techniques: (a) ZWD Algonquin Park, correlation: 0.995; (b) ZWD difference Algonquin Park, RMS: 6.0 mm; (c) ZWD Wettzell, correlation: 0.994; (d) ZWD difference Wettzell, RMS: 4.6 mm.

The VLBI and GPS ZWD estimates as well as their differences for Algonquin Park and Wettzell (mid-latitude stations), Ny-Ålesund (GPS site NYAL, high northern latitude) and Fortaleza (southern hemisphere, near the equator) are plotted in Fig. 6.4 and 6.5. These stations have been selected as they have long and almost complete GPS time series and their VLBI telescopes participated in a comparatively large number of VLBI sessions. However, the VLBI observations are sparser before 1998, in particular for Algonquin Park and Ny-Ålesund. The ZWD differences of Algonquin Park and Wettzell show a seasonal pattern: in summertime, when the water content of the atmosphere as well as the variability of the atmosphere are larger, the ZWD difference also shows more scatter. For Ny-Ålesund, the estimated ZWD is periodically below zero. This effect is related to too large a priori delays for stations in higher latitudes. As the hydrostatic a priori delay computed from a standard atmosphere might be even larger than the true total delay, the estimated wet delay has a negative sign to compensate for the deficiencies of the standard atmosphere. As Ny-Ålesund is located in the high northern latitude, the water vapor content and also its variability is smaller than for stations in the mid-latitudes. This fact is reflected in the ZWD difference which does not show a clear seasonal pattern as for Algonquin Park and Wettzell. Fortaleza shows the largest ZWD values of the four stations and also the largest scatter of the ZWD difference due to its location in the tropics.

6.1.4. GPS-VLBI Troposphere Biases

The height difference between the GPS and VLBI reference points introduces a bias between the GPS- and VLBI-derived troposphere zenith delays due to the effect of the atmosphere between the reference points. For the computation of the height difference, it is important to use the height of the GPS antenna phase center (reference point for troposphere parameters), not the height of the marker (reference point for station coordinates). This difference is equivalent to the sum of the antenna height and the up-component of the

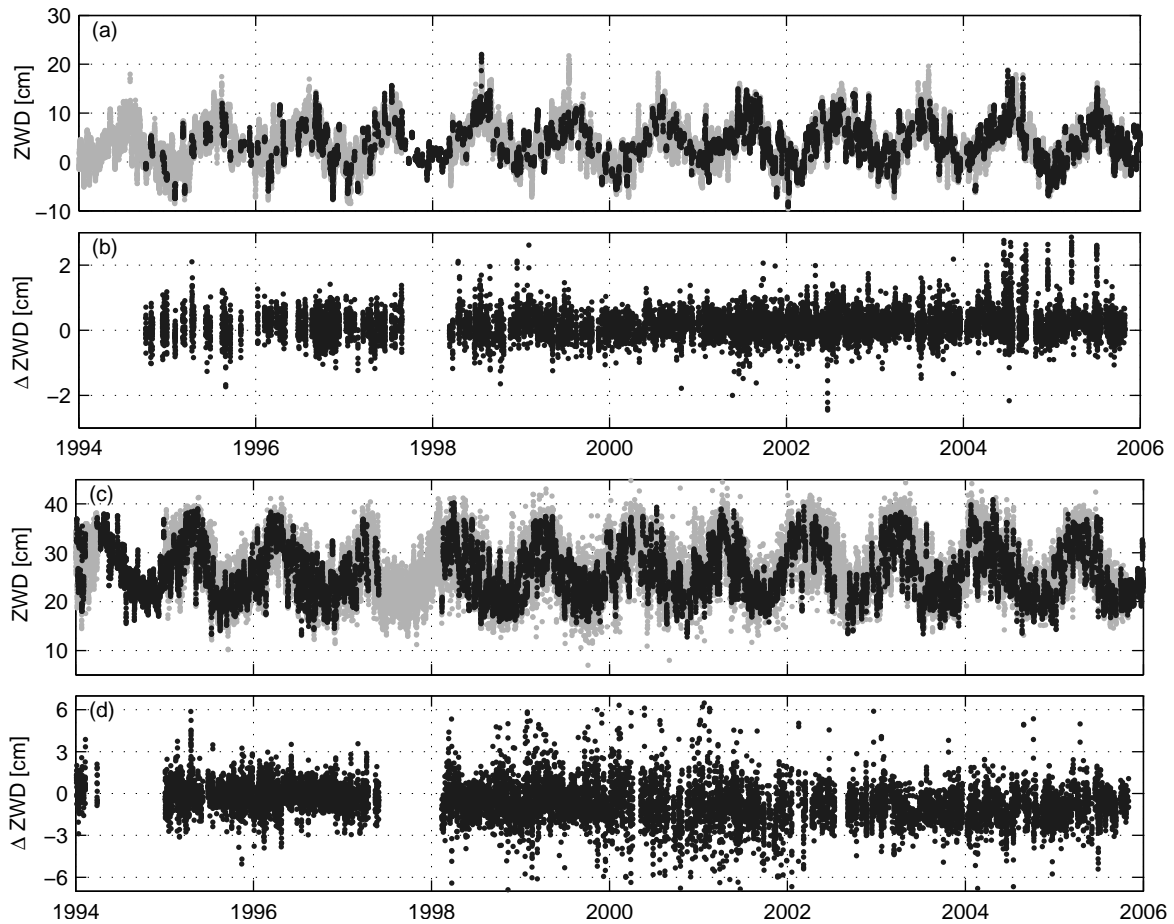


Fig. 6.5: Troposphere zenith wet delays determined by **GPS** (gray) and **VLBI** (black) and the difference between the two techniques: (a) **ZWD** Ny-Ålesund, correlation: 0.995 ; (b) **ZWD** difference Ny-Ålesund, **RMS**: 4.1 mm; (c) **ZWD** Fortaleza, correlation: 0.963; (d) **ZWD** difference Fortaleza, **RMS**: 13.9 mm.

PCO. For most **GPS** stations, this distinction is not necessary as the antenna height is very small or even zero. However, for the sites **HARK**, **HART**, **NYAL** and **ONSA** the antenna height ranges from 1 to 10 m and has to be considered. For **VLBI** the reference point for the troposphere parameters is the same as for the station coordinates, namely the intersection of the telescope axes.

The constant a priori delays for the **GPS** and **VLBI** analysis are computed with the hydrostatic *Saastamoinen* (1973) model (Eq. 2.25). As continuous and reliable pressure observations are not available for all **GPS** stations, Eq. 2.26a is applied for the computation of the pressure. Therefore, these a priori delays only depend on the station height and are time-independent. When comparing **GPS**- and **VLBI**-derived **ZWD**s, only the wet part of the theoretical bias due to the height difference is relevant as the hydrostatic part is accounted for by different a priori delays for **GPS** and **VLBI**. The wet bias can optionally be corrected with the wet part of the *Saastamoinen* (1973) model computed with input from

- the standard atmosphere given in Eqs. 2.26b and 2.26c (one single correction per station for the whole time period, see last column of Tab. 6.4)
- temperature and water vapor values derived from **ECMWF** data and provided in the site-specific **VMF1** files for the **VLBI** stations (correction time series with 6-hour resolution)
- temperature and humidity recorded near the **GPS** or **VLBI** sites (the conversion from humidity to water vapor is given in Eq. 2.27, resolution depending on the sampling of the meteorological sensors).

Due to sometimes inhomogeneous recordings of the meteorological sensors and problems with data availability, the last method will not be considered here. The raw (uncorrected) **GPS-VLBI** biases and the biases corrected with the other two methods are shown in Fig. 6.6. However, it is difficult to assess which correction method is better as the true biases are unknown. It is only a vague hope that the biases should be zero as both, **GPS** and **VLBI**, are affected by systematic errors. On the other hand, it is a reasonable

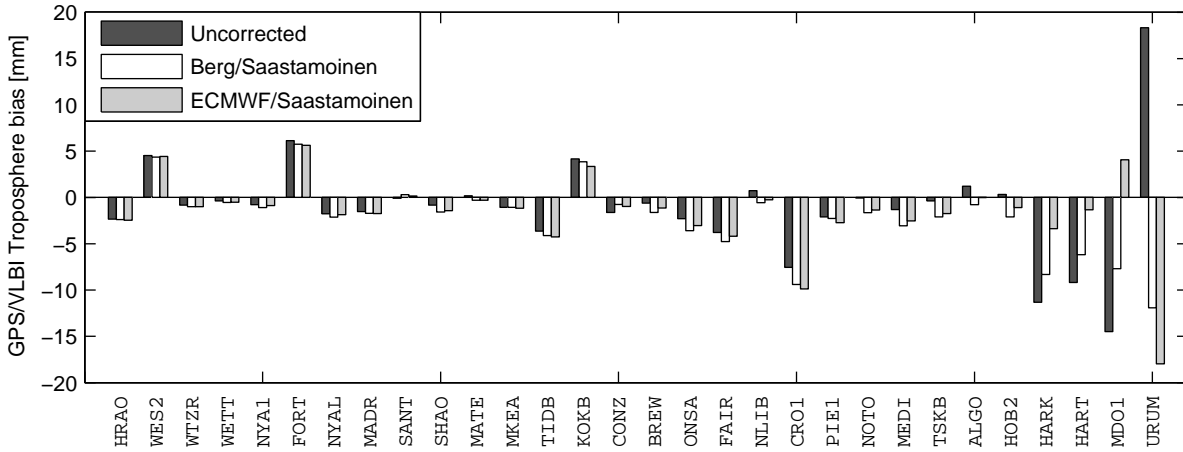


Fig. 6.6: Mean [GPS-VLBI](#) troposphere [ZWD](#) biases: uncorrected biases, biases corrected with Saastamoinen delays computed from the standard atmosphere of [Berg \(1948\)](#) and from [ECMWF](#). The stations are ordered by the absolute value of the [GPS-VLBI](#) height difference (smallest height difference on the left hand side).

assumption that the corrected biases should get smaller for large height differences if one applies the more sophisticated correction model: for large height differences, the bias is dominated by the tropospheric effect. Systematic errors have a less important impact compared to smaller height differences. For HARK, HART and MDO1 the [ECMWF](#) bias corrections result in biases whose absolute values are smaller by a factor of about three compared to the raw biases. However, the [ECMWF](#)-corrected bias of MDO1 has a different sign than the raw bias and the bias corrected with the standard atmosphere. For the standard atmosphere, the reduction of the biases is smaller than 50%. For URUM the raw and the [ECMWF](#)-corrected biases have the same order of magnitude (about 2 cm) but opposite sign whereas the bias corrected for with the standard atmosphere is smaller by about one third. In general, the scatter of the [GPS-VLBI ZWD](#) difference time series is slightly increased (not shown here) when applying the [ECMWF](#) corrections. As the results of the correction methods described above are not satisfying (and in the case of the [ECMWF](#) corrections introduce additional noise), no wet corrections for the height difference will be applied in the following (as mentioned above, the hydrostatic effect is already accounted for by different a priori delays). Therefore, stations with height differences larger than 25 meters (i.e., HARK, HART, MDO1 and URUM) will be excluded from the following [GPS-VLBI](#) comparisons.

The biases for all other [GPS-VLBI](#) co-locations (except for occasionally observing [VLBI](#) stations with less than 500 estimated troposphere parameters during the time periods where corresponding [GPS](#) parameters

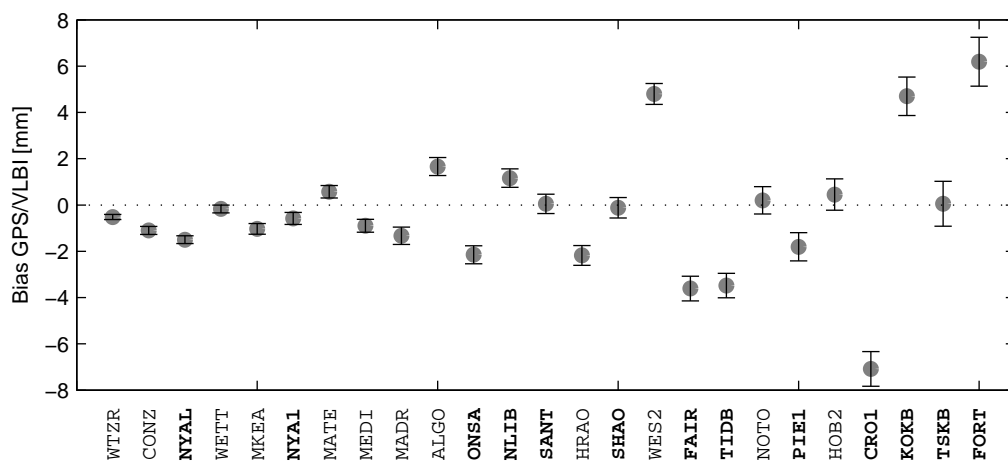


Fig. 6.7: Mean [GPS-VLBI](#) troposphere [ZWD](#) biases. The error bars represent the [WRMS](#) of monthly mean biases. The stations are ordered by the size of these [WRMS](#) values. [GPS](#) sites permanently or partly equipped with a radome are given in bold. In Onsala and Westford, the [VLBI](#) telescope is covered by a radome.

Site	# ZWD Par.	Bias [mm]		RMS [mm]		Correlation	
		NMF	IMF	NMF	IMF	NMF	IMF
ALGO	9,998	+1.25	+1.66	5.90	5.91	0.9949	0.9949
CONZ	2,936	-1.42	-1.10	7.83	7.77	0.9757	0.9760
CRO1	1,504	-7.43	-7.08	12.10	12.12	0.9700	0.9699
FAIR	19,915	-3.76	-3.61	5.67	5.66	0.9935	0.9936
FORT	11,037	+6.29	+6.19	13.33	13.33	0.9655	0.9657
HOB2	2,709	-0.02	+0.45	8.34	8.41	0.9775	0.9773
HRAO	5,494	-2.23	-2.18	7.83	7.76	0.9883	0.9885
KOKB	18,431	+4.49	+4.70	10.65	10.68	0.9624	0.9620
MADR	792	-1.63	-1.33	7.61	7.62	0.9778	0.9777
MATE	7,137	-0.13	+0.57	6.62	6.58	0.9879	0.9881
MEDI	3,425	-1.36	-0.90	6.02	5.99	0.9929	0.9930
MKEA	1,147	-1.24	-1.03	5.96	5.98	0.9084	0.9078
NLIB	2,092	+0.82	+1.16	8.00	7.95	0.9927	0.9928
NOTO	888	-0.63	+0.20	8.00	7.92	0.9840	0.9844
NYAL	11,677	-1.71	-1.50	4.06	4.04	0.9952	0.9954
NYA1	9,265	-0.71	-0.58	4.00	3.98	0.9952	0.9954
ONSA	4,708	-2.34	-2.15	5.27	5.22	0.9935	0.9938
PIE1	2,026	-2.04	-1.81	5.95	5.89	0.9906	0.9908
SANT	659	-0.21	+0.05	9.45	9.41	0.9416	0.9414
SHAO	1,433	-0.39	-0.12	7.17	7.11	0.9964	0.9965
TIDB	553	-4.11	-3.48	9.07	8.96	0.9769	0.9774
TSKB	3,002	-0.46	+0.05	7.96	7.78	0.9961	0.9962
WES2	10,508	+4.04	+4.80	6.80	6.70	0.9951	0.9952
WETT	5,855	-0.61	-0.17	6.35	6.27	0.9906	0.9909
WTZR	18,539	-0.78	-0.52	4.67	4.64	0.9943	0.9945

Tab. 6.5: Comparison of [GPS](#) and [VLBI ZWD](#) estimates for the time interval 1 January 1994 till 31 December 2004. [GPS ZWD](#) estimates have been interpolated to 1-hourly values. The number of troposphere parameters refers to solution NMF (small differences to the number of troposphere parameters of solution IMF can occur due to the outlier detection).

are available) are given in Fig. 6.7. As a measure for the stability of the biases, the error bars represent the [WRMS](#) of monthly mean biases (weighted with the number of observations). In general, the biases between both techniques are on the level of a few millimeters. They reveal a quite good agreement of both techniques and confirm the level of agreement that could be expected from analyzing the [GPS-GPS](#) co-locations (see Sec. 6.1.2). The stations with the smallest [WRMS](#) values also show the smallest absolute values of the [ZWD](#) bias. For Tsukuba, the bias is almost zero whereas the [WRMS](#) is 1.0 mm. This is probably a result of the extreme weather conditions at this site. The other sites with [WRMS](#) values larger than 0.7 mm (CRO1, KOKB and FORT) are all located quite close to the equator where the variability of the troposphere is larger. Except for the largest [WRMS](#) values, these stations also show the largest absolute values of the [ZWD](#) biases. The fact that all three stations are equipped with a radome might contribute to these large bias values.

[Pacione et al. \(2002\)](#) reported biases between [GPS](#) and [VLBI ZTDs](#) of 10 to 15 mm. A major part of these larger biases is probably attributed to systematic differences in modeling and parameterization between the two software packages GIPSY-OASIS II ([GPS](#)) and CALC/SOLVE ([VLBI](#)) used in this study. [Heinkelmann et al. \(2007\)](#) derived mean biases between the [IVS ZTD](#) product and the [IGS ZTD](#) product. These biases range from 3 to 12 mm. By carefully harmonizing the [GPS](#) and [VLBI](#) software packages and fully reprocessing the [GPS](#) and [VLBI](#) solutions, a much better level of consistency for the biases shown in Fig. 6.7 can be achieved than in the two studies mentioned above. The important effects of different modeling of the antenna phase center on the troposphere biases will be discussed in Sec. 9.2.3.

The [RMS](#) of the [ZWD](#) differences (after removing offset and trend), their bias and the correlation coefficients between the [GPS](#) and [VLBI](#) time series for the solutions NMF and IMF are listed in Tab. 6.5. For convenience, only the abbreviations of the [GPS](#) sites are given. The difference between solution NMF and IMF as regards the biases is smaller than 1 mm for all stations and exceeds 0.5 mm for only four stations (TIDB,

Stat.	ALGO		NYA1		NYAL		WTZR	
	#ZWD Par.	Drift [mm/y]	#ZWD Par.	Drift [mm/y]	#ZWD Par.	Drift [mm/y]	#ZWD Par.	Drift [mm/y]
GPS _a	51,277	0.33 ± 0.06	31,508	0.02 ± 0.05	46,063	0.19 ± 0.03	42,151	0.29 ± 0.05
VLBI _a	11,503	0.14 ± 0.14	14,444	0.17 ± 0.05	14,444	0.17 ± 0.05	25,827	-0.11 ± 0.05
GPS _i	5,603	0.19 ± 0.21	5,354	-0.70 ± 0.14	6,527	-0.13 ± 0.08	10,431	0.54 ± 0.10
VLBI _i		0.22 ± 0.21		-0.70 ± 0.14		0.04 ± 0.08		0.45 ± 0.10
GPS _a	51,277	0.36 ± 0.06	31,508	0.00 ± 0.05	46,063	0.24 ± 0.02	42,151	0.31 ± 0.05
VLBI _a	11,503	0.23 ± 0.14	14,444	0.11 ± 0.05	14,444	0.11 ± 0.05	25,827	-0.03 ± 0.05
GPS _i	5,603	0.23 ± 0.21	5,354	-0.55 ± 0.12	6,527	-0.23 ± 0.08	10,431	0.58 ± 0.10
VLBI _i		0.25 ± 0.21		-0.55 ± 0.13		-0.06 ± 0.08		0.49 ± 0.10

Tab. 6.6: Long-term trends estimated from 2-hourly GPS- and 1-hourly VLBI-derived ZWD values: For the upper part of the table offset, drift and annual signal were estimated; for the lower part of the table a semi-annual signal was estimated in addition. The index *a* denotes that all epochs of the GPS and VLBI time series were used for the adjustment, the index *i* means that only identical epochs were used.

NOTO, MATE and WES2). For two of these stations (NOTO and TIDB) the fact that they only have a quite small number of common observations might be an explanation for the larger differences. Therefore, it can be concluded that the mapping function has no significant influence on the GPS-VLBI troposphere bias.

The RMS values are in general on the level of 5 to 8 mm. All stations with RMS values exceeding 10 mm are located close to the equator (CRO1, FORT, KOKB). Probably, the higher variability of the troposphere in the tropics is responsible for this effect. The differences of the RMS values of solution NMF and IMF are smaller than one tenth of a millimeter. The mean RMS values of 7.38 mm for solution NMF and 7.34 mm for solution IMF do not differ significantly. The correlation coefficients between the GPS and VLBI time series are larger than 0.9 for all stations and larger than 0.96 for all stations except for MKEA and SANT. The differences of the correlation coefficients computed from solutions NMF and IMF are smaller than 0.006 for all stations. In conclusion it must be stated that the mapping function (not shown here for solutions GMF and VMF1) has no significant influence on the differences between GPS- and VLBI-derived troposphere parameters, neither on the bias, nor on the RMS, nor on the correlation coefficient. However, it is important that the same mapping function is used for the GPS and VLBI solutions and that the mapping function is computed in the same way. That was done for the GPS and VLBI solutions used here: although a site-specific version of the IMF (and the VMF1, too) is available for the VLBI stations, the grid-version was used for the GPS and the VLBI solutions to guarantee full consistency. However, the differences between these two different versions of the VMF1 are in general small, see Kouba (2008).

6.1.5. Long-term Trends

As the homogeneously reprocessed GPS and VLBI long-time series show a high level of consistency, it is of special interest to study the long-term behavior of both series in more detail. A possible positive trend in the ZWD might indicate an increase of the water vapor and would be interesting for climatological studies. Therefore, several authors tried to estimate long-term trends from troposphere zenith delays determined by space geodetic techniques (e.g., Boehm *et al.*, 2003; Gradinarsky *et al.*, 2002; Haas *et al.*, 2003; Heinkelmann *et al.*, 2007). As only the ZWD of solution VMF1 ECMWF could directly be converted to water vapor (the hydrostatic part is already accounted for by the ECMWF a priori delays), this solution will be used for the determination of long-term trends.

Unfortunately, only a few of the co-located GPS and VLBI stations have suitable data (frequent observations covering a time span of several years) to determine a reliable long-term trend in the estimated ZWDs. The number of stations of interest further decreases when excluding GPS sites with discontinuities due to equipment changes or tracking problems (see Sect. 4.2). Offset, drift, amplitude and phase of an annual signal were estimated simultaneously in a least-squares adjustment for the stations Algonquin Park, Ny-Ålesund and Wetzell (see upper part of Tab. 6.6). The drifts derived from all observations of the GPS and VLBI time series often differ significantly from each other, as well as the two GPS-derived values for Ny-

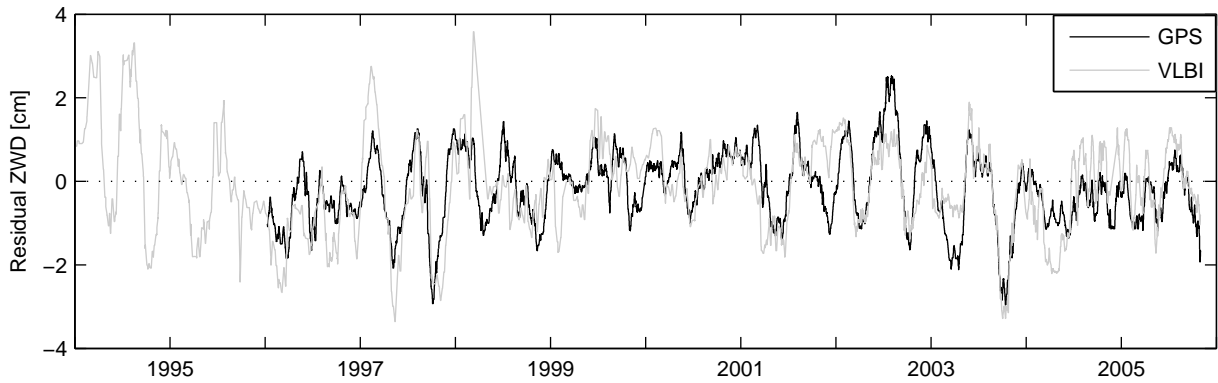


Fig. 6.8: **GPS** and **VLBI ZWD** residual time series (smoothed with a 30-day median filter) for Wettzell after removing offset, trend and annual signal.

Ålesund. *Haas et al. (2003)* pointed out that the different sampling is a critical issue for the determination of trends in long time series of troposphere delays.

Limiting the time series to epochs with common estimates for both techniques increased the similarity of all trends to the 95% confidence level except for NYAL. Also, the size of the drift significantly changes when using the identical sampling. For ALGO, the estimated rates for identical observations are between the **GPS** and **VLBI** rates for all observations, but for NYA1 and WTZR, the values for identical observations are completely different compared to those using all observations. This clear dependence on the sampling indicates that the series contain signals that are neither of linear nor of sinusoidal annual nature.

Fig. 6.8 illustrates the **GPS** and **VLBI ZWD** residuals (smoothed with a 30-day median filter) for Wettzell (**GPS** site WTZR only) after removing offset, trend and the annual signal. An irregular semi-annual signal with changing amplitude can be detected. The residuals of the other stations show comparable properties. It is worthwhile to mention that the semi-annual signal does not have a physical meaning: it simply accounts for deviations of the annual signal from a sinusoidal shape. If a semi-annual signal is estimated in addition, the periodical fraction from the residual signal is removed. However, this does not significantly decrease the dependence on the sampling (see lower part of Tab. 6.6). When using a simple model for the drift determination as described above, a maximum level of agreement between two different techniques can only be achieved if the individual time series are limited to identical epochs.

A drift estimation with different time windows allows for a realistic assessment of the stability of the estimated long-term trends. Fig. 6.9 shows the long-term trend estimates from solution VMF1 ECMWF for the three sites at Ny-Ålesund. The drift values given on the y -axis were determined from the time interval

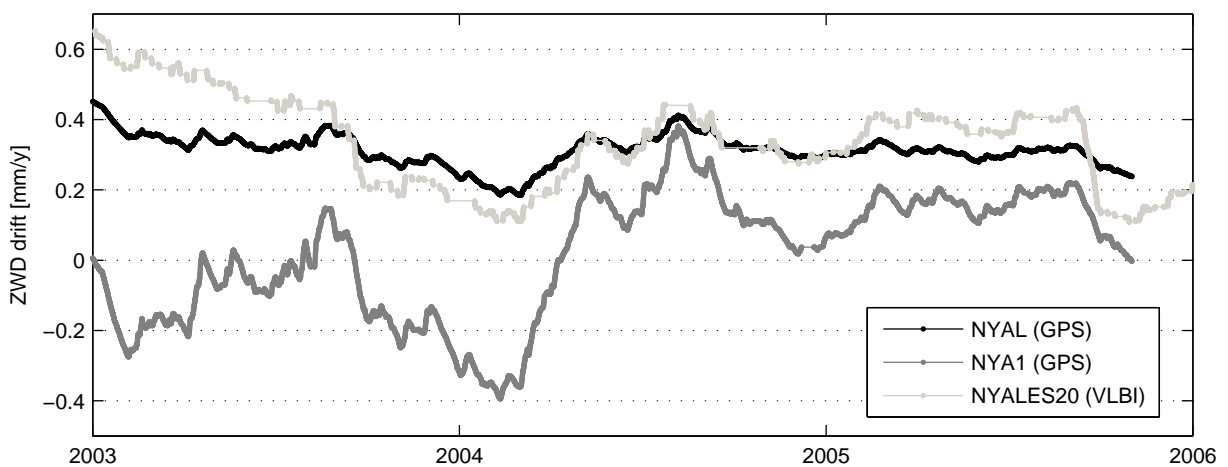


Fig. 6.9: Variations in **ZWD** drift determination due to different time windows for Ny-Ålesund. The drift estimates given on the y -axes are based on the time interval between the first parameter of each site and the date given on the x -axis.

from the first parameter of each time series (2 January 1994 for NYAL, 12 March 1998 for NYA1, 4 October 1994 for NYALES20) until the epoch given on the x -axis. The expression *drift variation* will be used in the following for the difference between the maximum and the minimum drift. It is clear that the shortest time series, namely NYA1, shows the largest drift variation of about 0.8 mm/y. The longest and densest time series (NYAL) shows with 0.3 mm/y the smallest variation in the long-term trends. Although the VLBI time series of NYALES20 is almost as long as the time series of NYAL, the variation in the estimated drifts is with 0.5 mm/y larger than for NYAL due to the sparser sampling, in particular in the early years, see Fig. 6.5. Several features are visible in the curves of all three sites, e.g. the local maximum in summer 2004 and a decay in fall 2005. As this decay coincides with the CONT05 campaign, the decay is in particular pronounced in the VLBI series as 16 days of continuous observations have a comparatively large influence on the sparse VLBI time series compared to the denser GPS time series.

To get a more detailed impression of the stability of the GPS-derived long-term trends, a similar investigation has been performed for all GPS stations with more than 43,800 ZWD parameters (corresponding to 10 years of continuous observation). Long-term trends have been estimated for all time intervals covering more than 39,420 ZWD parameters (corresponding to 9 years of continuous observation). The minimum and maximum long-term trends per station are shown in Fig. 6.10. The stations are ordered by the length of their ZWD time series. It is obvious that there is no systematic relationship between the length of the time series and the drift variation. The difference between the maxima and minima ranges from 0.14 mm/y (CAS1) to 1.04 mm/y (NLIB). It is not astonishing that the station with the smallest drift variation is located in Antarctica. In this region, the humidity is in general very low and the variability of the troposphere small. Also the second Antarctic station McMurdo (MCM4) has a quite small drift variation of 0.16 mm/y. All eight stations with drift variations larger than 0.5 mm/y are located in Europe or Northern America. However, an assessment of this fact is difficult as three-quarter of the stations shown in Fig. 6.10 are located in this area, too (the installation of GPS permanent stations in the mid of the nineties, which is a basic prerequisite for the long time series considered here, was focussed on Europe and North America).

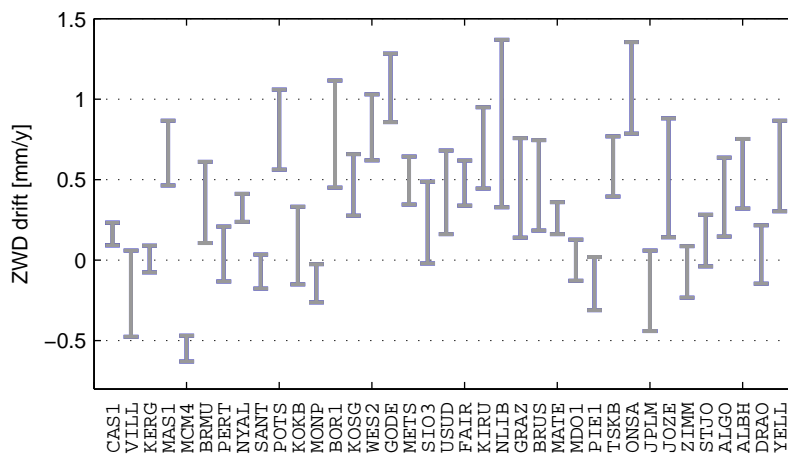


Fig. 6.10: Variations in ZWD drift determination due to different time windows. The stations are ordered by the length of their time series (longest time series on the right hand side). The mean drift variation is 0.42 mm/y.

The drift variations described above exceed the formal errors of the drift estimates for all GPS epochs (GPS_a) given in Tab. 6.6 by far. The mean formal error for the drift estimates of the 37 stations shown in Fig. 6.10 is 0.05 mm/y (minimum of 0.01 mm/y for MCM4, maximum of 0.08 mm/y for BRMU and GODE). Due to the huge number of (pseudo-) observations for the drift estimation, the formal errors are by far too optimistic. Therefore, the mean drift variation of 0.4 mm/y derived from drift estimations with different time windows seems to be a more realistic measure for the precision of GPS-derived ZWD long-term trends. However, one has to be aware of systematic effects correlated with a ZWD drift, in particular a drift in the terrestrial scale. The impact of different antenna phase center models on the terrestrial scale is discussed in Sec. 9.2.1. E.g., the scale rate difference of 0.34 ppb/y between solutions IGS01 and IGS05 (see Tab. 9.2, caused by deficiencies of the IGS01 model) induces ZWD drift differences of up to 0.5 mm/y (not shown here). This example clearly demonstrates the necessity of a full reprocessing with up-to-date models as a precondition for the determination of long-term trends.

As shown above, the estimation of trends from the long-time **ZWD** series is quite sensitive to different sampling and different time windows. The **ZWD** residuals contain irregular signals that cannot be modeled with the simple approach of estimating offset, drift, annual and semi-annual signal. Therefore, the trends of the troposphere **ZWDs** have to be interpreted with care, especially when thinking of climatological or global change phenomena.

6.2. Troposphere Gradients

6.2.1. GPS-GPS Co-locations

Offset, **RMS** (after removing offset and trend) and correlation coefficients between troposphere gradients of **GPS-GPS** co-locations at one station, derived from the reprocessed 1-day solution, are listed in Tab. 6.7. In addition to the stations in Tab. 6.2, the stations in Miami (AOML and MIA1) and two co-locations where **IGS** troposphere parameters are not available for both stations (Thule and Wettzell) are included. In general, the correlation of the troposphere gradients is worse than that of the zenith delays: this can be explained by a much smaller and less pronounced periodic signal in the troposphere gradients. However, if a co-located pair of sites shows particularly large **RMS** values and low correlations, this generally indicates a problem at one of the sites, like the tracking problems of WETT at Wettzell already mentioned in Sec. 4.2.1.

Earlier comparisons (*Steigenberger et al., 2007*) showed a correlation below 0.3 between the two **GPS** sites WETT and WTZR for both, the east-west and the north-south gradients. In the last few months of its operation time (before it was switched off in February 1997) this receiver showed a curious behavior: all coordinate components were biased up to 5 cm. Therefore, WETT observation data after October 1996 has been excluded from the processing run M3. The discrepancies between the WETT and WTZR gradients are now smaller but these two sites are still worse than the other sites in Tab. 6.7. The site THU1 at Thule (Greenland) also shows a degraded performance resulting in high **RMS** values and small correlations for the respective gradients (accompanied by a small number of common parameters for the two sites). The reasons for the large biases between the sites at Miami Beach are unknown.

Station	Site 1	Site 2	# Par.	North-South Gradients			East-West Gradients		
				Offset [mm]	RMS [mm]	Corr.	Offset [mm]	RMS [mm]	Corr.
Hartebeesthoek	HRAO	HARK	834	0.04	0.27	0.857	-0.12	0.33	0.803
Hartebeesthoek	HRAO	HART	49	0.15	0.18	0.921	0.18	0.20	0.898
Miami Beach	MIA1	AOML	179	0.58	0.26	0.887	0.39	0.26	0.858
Ny-Ålesund	NYAL	NYA1	2552	0.09	0.05	0.974	0.04	0.05	0.975
Thule	THU1	THU3	169	-0.06	0.61	0.359	-0.33	0.55	0.435
Tromsø	TROM	TRO1	2349	0.07	0.14	0.854	0.06	0.08	0.935
Yarragadee	YARR	YAR2	847	-0.06	0.13	0.925	0.06	0.13	0.907
Yakutsk	YAKZ	YAKT	105	0.08	0.15	0.887	-0.08	0.12	0.917
Wettzell	WETT	WTZR	257	0.24	0.30	0.724	0.10	0.40	0.481

Tab. 6.7: Comparison of troposphere gradients for co-located **GPS** sites.

6.2.2. Gradient Time Series

The gradient time series of all stations with more than 2 years of observations were analyzed by simultaneously estimating drift, offset, annual and semi-annual terms. The mean gradients (offsets) ordered by the latitude of the stations are shown in Fig. 6.11. The north-south gradients show a significant latitude-dependence: most of them are positive in the southern hemisphere and negative in the northern hemisphere. This systematic effect is caused by the temperature difference between the poles and the equator whose sign does not show a seasonal dependence (*Chen and Herring, 1997*). The east-west gradients are generally

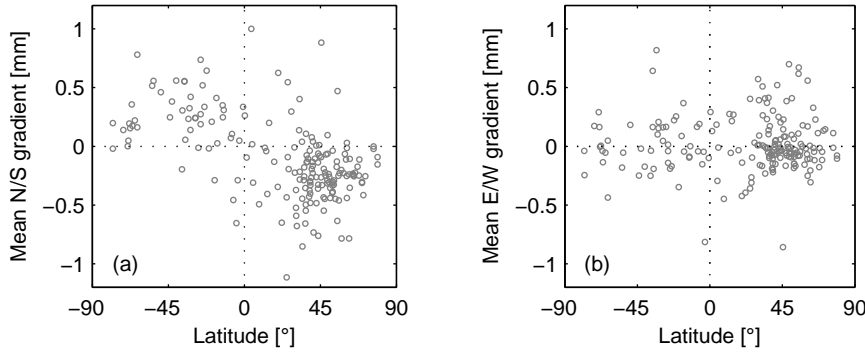


Fig. 6.11: Mean troposphere gradients of solution IMF: (a) north-south gradients; (b) east-west gradients.

smaller (mean absolute value of 0.17 mm compared to 0.30 mm for the north-south gradients), a fact already known from the studies of *Meindl et al. (2004)*. This effect might be explained by the general east-west motion of weather systems that average the individual east-west gradient time series to a value closer to zero than for the north-south gradients. No latitude-dependent systematics is visible for the east-west gradients and no longitude-dependent systematics for both types of gradients (not shown here).

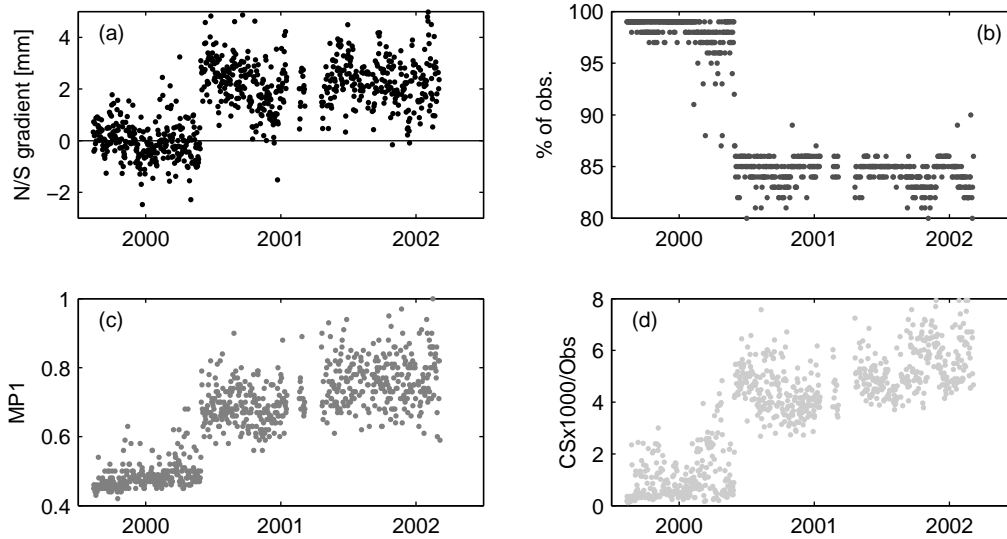


Fig. 6.12: Time series of the Maldives GPS station: (a) N/S troposphere gradient; (b) observation rate; (c) multipath on L1; (d) number of cycle slips.

The mean gradients of some stations are biased by systematic effects as already shown in Sec. 4.2.1 for North Liberty. Another example is the Maldives station which has the largest north-south gradient of 1.00 mm. The gradient time series shows a clear discontinuity in mid of 2000, see Fig. 6.12a. This discontinuity coincides with a reduced observation rate, an increased code multipath as well as an increased number of cycle slips computed with *teqc* and a discontinuity of unknown origin in the coordinate time series ($\Delta N = 41.1$ mm, $\Delta E = 1.1$ mm, $\Delta U = 35.3$ mm), see Tab. C.1. The mean north-south troposphere gradient before 28 May 2001 is -0.10 mm, afterwards it is $+2.35$ mm. Thus, the large gradient value is most likely related to a tracking problem of this station. The station with the largest absolute value for the east-west gradient (Venice, -0.86 mm) is affected by a discontinuity due to an antenna change. On the other hand, there are also physical explanations for large gradient values. E.g., Santiago has, with 0.82 mm, the second largest east-west gradient. This station is located in the Central Valley of Chile, about 80 km inland of the coast and very close to the Andes. Maritime air can stream into the Central Valley through valleys like those of the Mapocho and Maule river beds (*Miller, 1976*). This wet air from the west and the dry air above the Andes in the east might be a reasonable explanation for the large troposphere gradient that is also seen by VLBI (*Steigenberger et al., 2007*). Santiago is also the station with the largest annual amplitude of 0.65 mm in the east gradient (isolated circle at -33° latitude in Fig. 6.13b).

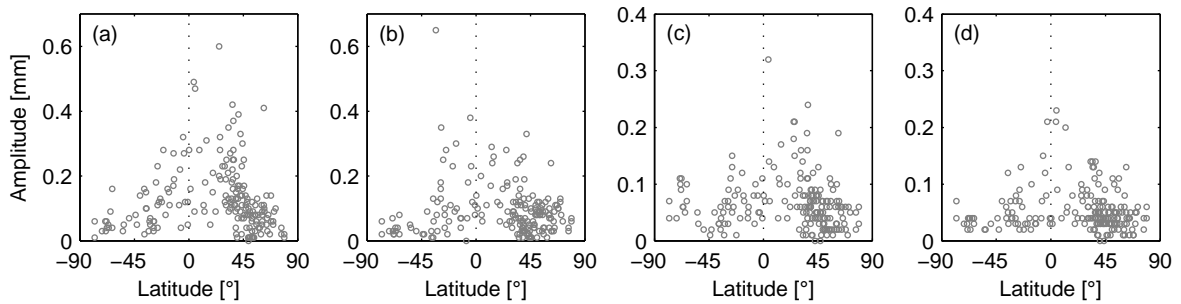


Fig. 6.13: Periodic signals in the troposphere gradients: (a) annual amplitude north-south gradients; (b) annual amplitude east-west gradient; (c) semi-annual amplitude north-south gradient; (d) semi-annual amplitude east-west gradient. Note the different scale of the y -axis for the annual and semi-annual amplitudes.

The amplitudes of the annual and semi-annual signals in the troposphere gradients for all stations are displayed in Fig. 6.13. In general the amplitudes are smaller for higher latitudes due to the lower seasonal variability of the troposphere in these regions. The mean amplitudes of the north-south gradients ($A_{N/S,a} = 0.13$ mm, $A_{N/S,sa} = 0.07$ mm) are larger by about 40% compared to the east-west gradient amplitudes ($A_{E/W,a} = 0.09$ mm, $A_{E/W,sa} = 0.05$ mm). This effect can be explained by the global seasonal cycle in temperature and water vapor that depends on the latitude. Longitude-dependent variations are driven by local and regional effects resulting in a smaller mean amplitude of the E/W gradients compared to the N/S gradients.

Tsukuba (located in Japan, i.e., in the Asian monsoon region) is an example for a station with a quite clear periodic signal in the north-south gradient, see Fig. 6.14. The amplitude of the annual signal is 0.42 mm, the amplitude of the semi-annual signal 0.18 mm. The north-south gradient time series shows clear maxima in summertime and minima in wintertime. This effect could be related to a wind called Oroshi blowing southwards from Mount Tsukuba (located north of the city of Tsukuba) only in wintertime ([Larsen and Hansen, 2004](#)). This wind brings dry and cold air to the city of Tsukuba and results in a small north-south troposphere gradient. During summer, the weather in the city is in general hot and humid resulting in a quite large troposphere gradient w.r.t. Mount Tsukuba. The phase of the annual signal of the north-south troposphere gradient determined by the Tsukuba VLBI site is in good agreement with the GPS results although the amplitude is slightly larger ([Steigenberger et al., 2007](#)).

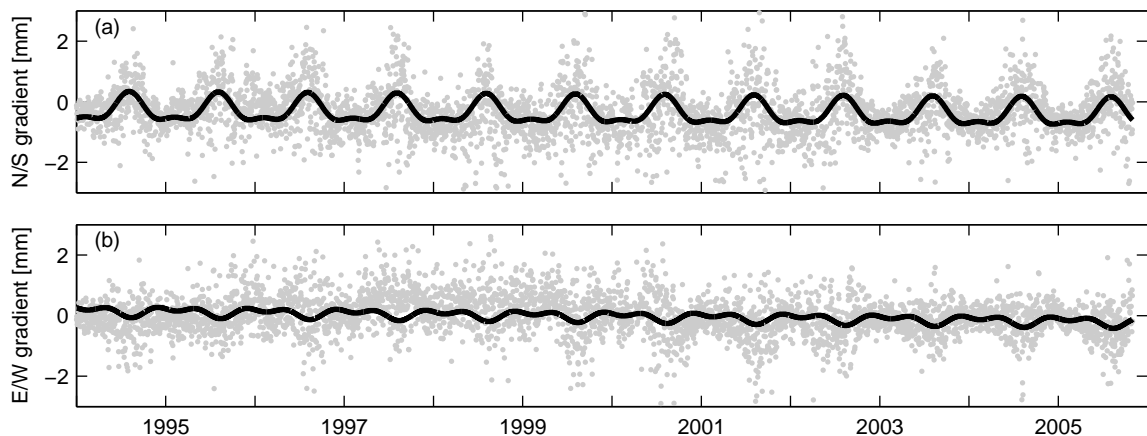


Fig. 6.14: Troposphere gradients for Tsukuba: (a) north-south gradient; (b) east-west gradient.

6.3. Impact of different Troposphere Modeling

Due to the correlations of the troposphere zenith delays with the station height and the troposphere gradients with the horizontal station coordinates, changes in the troposphere modeling do not only affect the troposphere parameters themselves but also the station coordinates. However, the effect on station heights is much larger than that on the horizontal coordinate components. Therefore, the comparisons in this section will be limited to station heights and zenith delays computed with different mapping functions and hydrostatic a priori delays listed in Tab. 6.1. *Vey et al. (2006)* compared NMF and IMF for a limited data set of the reprocessing, whereas *Tesmer et al. (2007)* investigated the impact of different mapping functions on 20 years of VLBI data. The impact of different a priori ZHDs was already studied by *Tesmer et al. (2006)* for 20 years of VLBI data and by *Tregoning and Herring (2006)* for one year of GPS data.

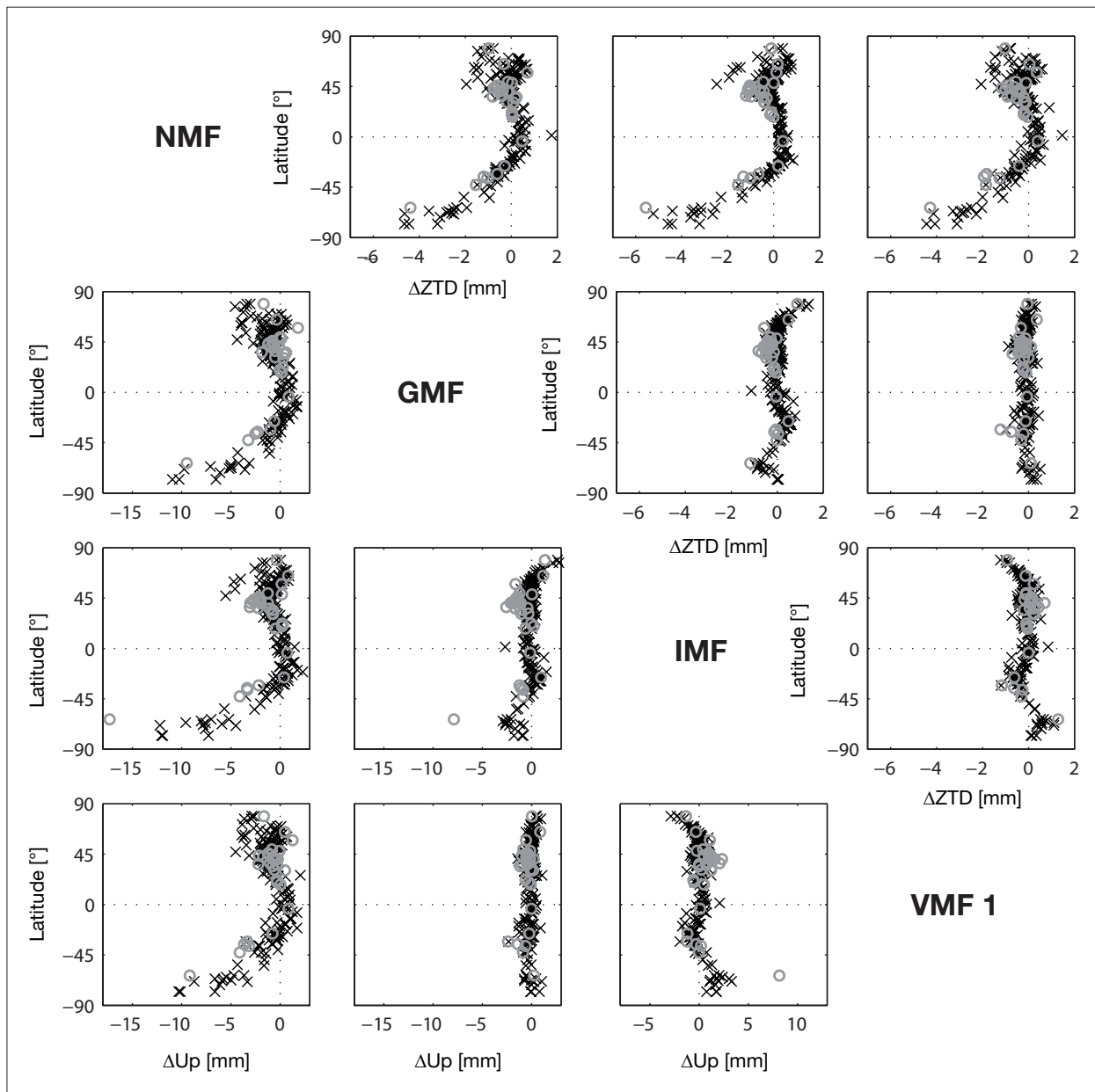


Fig. 6.15: Effect of different troposphere mapping functions on GPS- and VLBI-derived station heights and troposphere zenith total delays: the differences refer to the solution IDs given on the diagonal (e.g., the lowest plot on the left hand side shows the coordinate differences between solutions NMF and VMF1). GPS-derived differences are indicated by black crosses, VLBI-derived differences by gray circles.

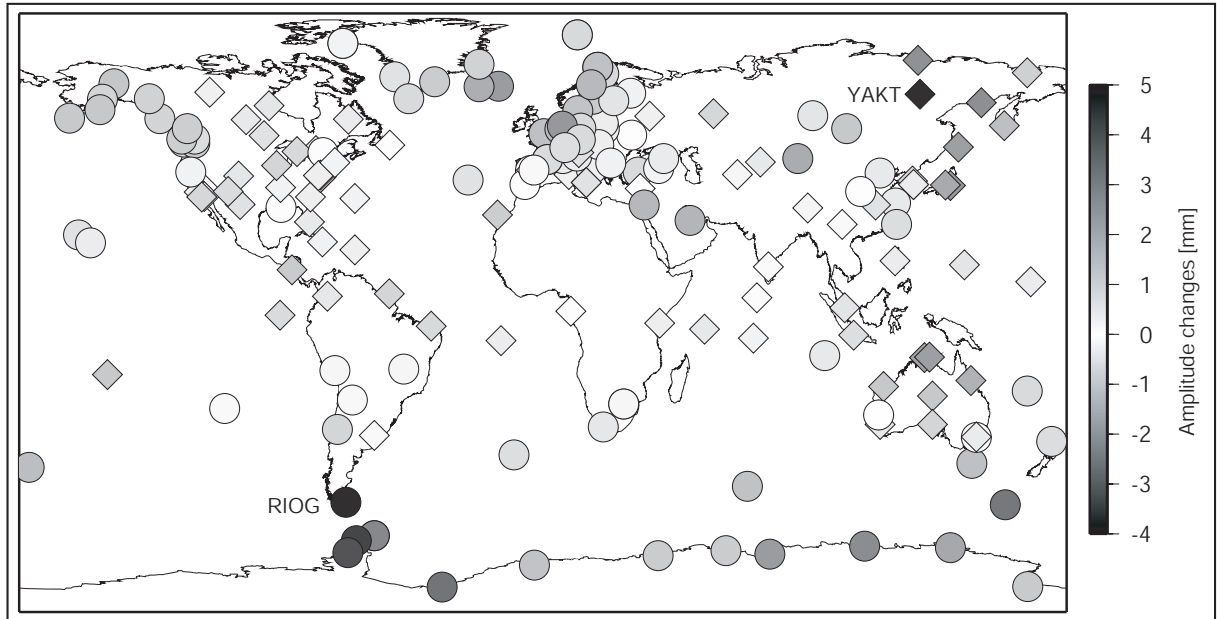


Fig. 6.16: Amplitude differences of annual signals in the station height between solutions NMF and VMF1. Positive amplitude changes are indicated by circles, negative amplitude changes by diamonds. Stations with less than 1000 observation days have been excluded. The hydrostatic mapping functions for the stations with the largest amplitude change, Yakutsk (YAKT) and Rio Grande (RIOG) are shown in Fig. 6.17.

6.3.1. Mapping Functions

The mapping functions applied for the solutions discussed in this section and the major deficiencies of the NMF have already been discussed in Sec. 2.5.1. Fig. 6.15 shows the mean differences of the station heights (lower triangle of the figure) and the troposphere ZTDs (upper triangle of the figure) between solutions NMF, GMF, IMF and VMF1 for both, GPS and VLBI solutions. All comparisons with the solution NMF (station coordinates as well as ZTDs) show a clear latitude-dependent systematic pattern due to the deficiencies of the NMF. In particular the height differences of up to more than 1 cm and the ZTD differences of up to 6 mm in Antarctica are striking. But also in the northern hemisphere a slightly latitude-dependent pattern is visible. As this systematic effect is visible for both, the GPS and the VLBI solutions, it is obvious that this behavior is related to the mapping function.

The solution IMF also shows a slight latitude-dependent systematics compared to GMF and VMF1 although this effect is much smaller than for the NMF. The southernmost VLBI station O'Higgins shows large station height differences for all comparisons with solution IMF. As this effect is not visible for the corresponding GPS station, it could be explained to some extent by the isolated location of this station w.r.t. the other VLBI stations and the small number of only 32 sessions resulting in a STD of 3.8 cm for the height component.

On the other hand, there is no systematic pattern visible in the comparisons of solutions GMF and VMF1. This is what we would have expected, as the GMF and the VMF1 were generated in a consistent way (Boehm *et al.*, 2006a). None of the comparisons shows a longitude dependence. Therefore, these results are not shown here. As different mapping functions mainly affect the height component, the horizontal position differences are much smaller. For GPS, the means of the absolute values of the position differences range from 0.2 mm (IMF/VMF1) to 0.7 mm (NMF/GMF) for the north component and from 0.1 mm (IMF/VMF1) to 0.4 mm (NMF/IMF) for the east component.

As VMF1 is the most sophisticated mapping function whereas NMF is still widely used within the geodetic community, further comparisons will be limited to solutions NMF and VMF1. The different mapping functions do not only affect the mean values of the station heights and troposphere zenith delays but also their seasonal behavior. Fig. 6.16 displays the amplitude differences of annual signals in the station height for solutions NMF and VMF1 for all GPS stations with more than 1000 days of observations. The largest positive amplitude changes (amplitudes of solution NMF are larger than those of VMF1) of up to 5 mm occur in Tierra del Fuego and the Antarctic Peninsula. The VMF1 amplitudes are larger by up to 4 mm for

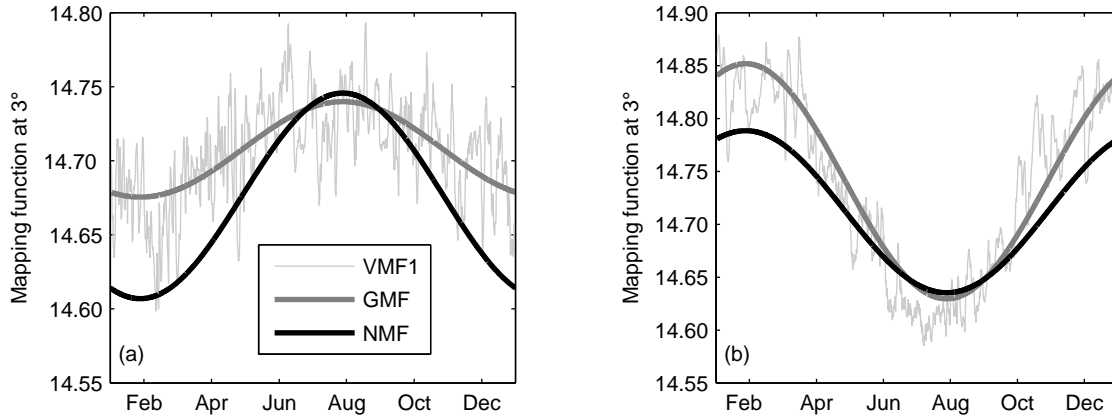


Fig. 6.17: Hydrostatic mapping functions at an elevation of 3° for the year 2005: (a) Rio Grande (Argentina) and (b) Yakutsk (Russia).

the east of Russia, Japan and northern Australia. This highly geographically correlated effect has its origin in the different behavior of the hydrostatic mapping functions. The hydrostatic **NMF**, **GMF** and **VMF1** for the two stations with the largest amplitude changes are shown in Fig. 6.17. It is obvious that the changes in the station height amplitudes are related to the annual behavior of the different mapping functions.

For Rio Grande (Argentina, Fig. 6.17a) the station height amplitude is larger by 4.8 mm for solution NMF compared to solution VMF1. The amplitude of the hydrostatic **NMF** at 3° elevation is with $A_{\text{NMF}} = 0.070$ more than two times larger than the amplitudes of **GMF** or **VMF1** ($A_{\text{GMF}} = A_{\text{VMF1}} = 0.032$) introducing an artificial signal in the height component. For Yakutsk (Russia, Fig. 6.17b), the situation is vice versa: the station height amplitude of solution NMF is 3.8 mm smaller than that of solution VMF1. Accordingly, the annual amplitude of the **NMF** ($A_{\text{NMF}} = 0.077$) is about one third smaller than the amplitudes of **GMF** ($A_{\text{GMF}} = 0.111$) and **VMF1** ($A_{\text{VMF1}} = 0.114$). In general, the station height amplitudes are not smaller for solution VMF1 compared to solution NMF. For 102 stations the VMF1 amplitudes are smaller, for 82 stations the NMF amplitudes are smaller. As the mean **STD** of the height time series after removing the annual signals is smaller for solution VMF1 (8.26 mm) compared to solution NMF (8.55 mm), *Boehm et al. (2007a)* concluded that **VMF1** reveals geophysical signals (e.g., loading effects) as well as signals due to systematic errors (e.g., multipath) more clearly.

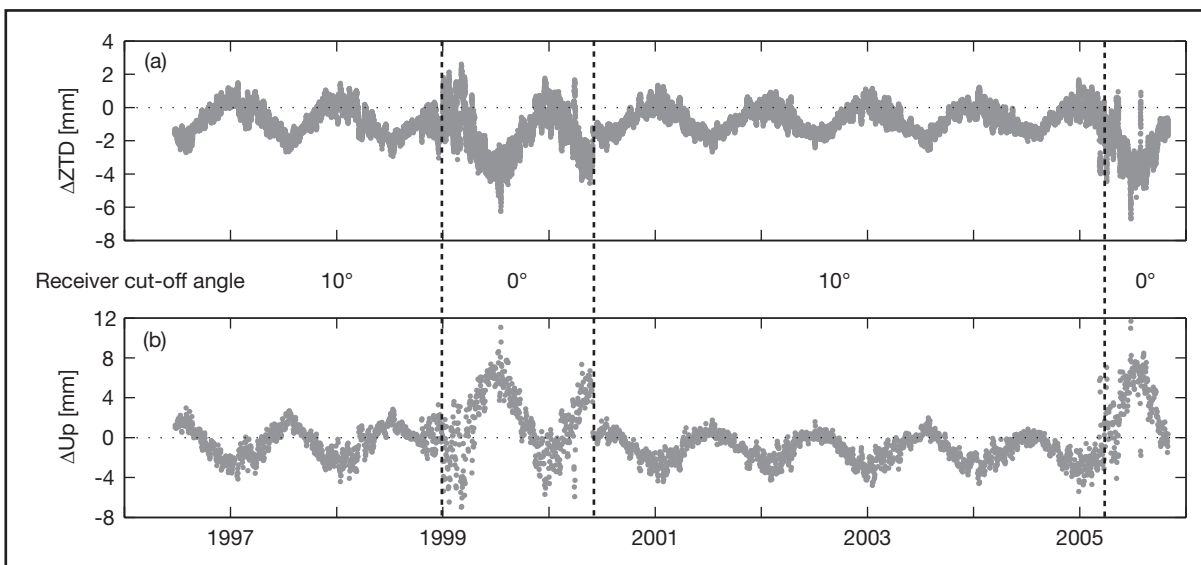


Fig. 6.18: Differences between solution NMF and VMF1 for Bahrain: (a) zenith total delay; (b) station height. The **ZTD** and station height amplitudes are larger for solution NMF compared to solution VMF1. Changes in the receiver cut-off angle are indicated by vertical lines.

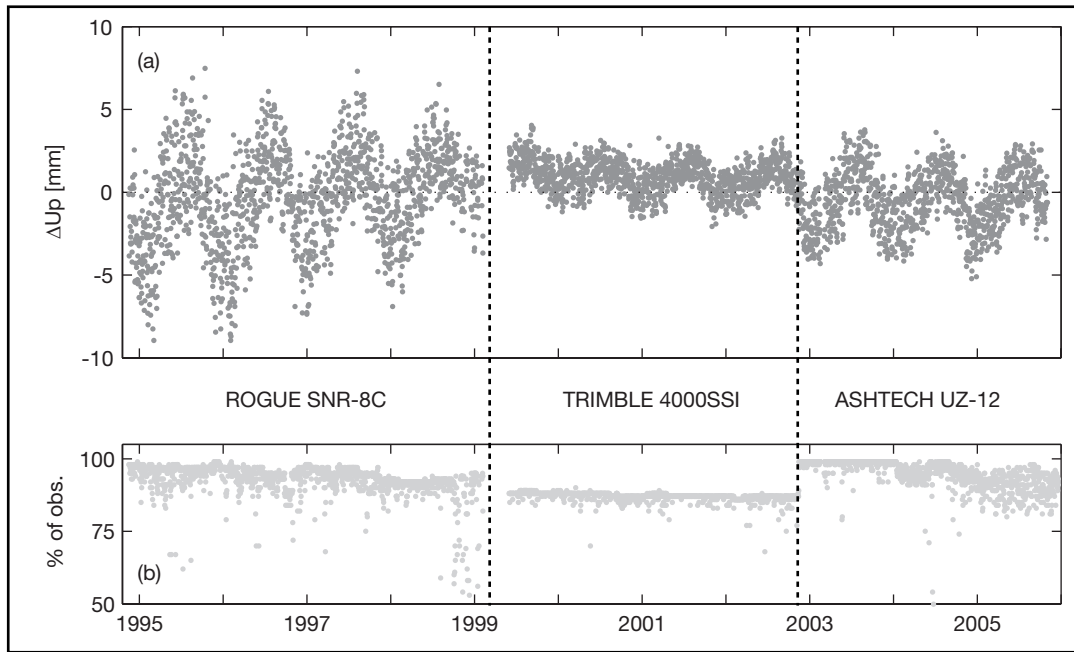


Fig. 6.19: Differences between solution NMF and VMF1 for Kerguelen Island: (a) station height differences; (b) observation rate. Changes in the receiver type are indicated by vertical lines.

The time series of the station height differences and the [ZTD](#) differences between solution NMF and VMF1 for Bahrain are given in Fig. 6.18. Despite the seasonal signal already described above, another feature in the time series is striking: the annual amplitude of the [ZTD](#) difference as well as the station height difference is about two times larger between 1999 and mid of 2000 as well as starting with 2005. This effect is related to undocumented changes in the receiver cut-off angle. These changes have been detected by analyzing the observation statistics derived with [teqc](#). Although the observations at low elevations are down-weighted, these observations have a significant influence on the parameter estimation as they are especially important for the decorrelation of the station heights and the zenith delays and in particular contribute to the determination of the troposphere gradients, see Eq. 2.32. In addition, differences between the various mapping functions are largest at low elevations. As the software cut-off angle applied by the [IGS ACs](#) has been changed several times (e.g., two times for the [CODE AC](#), see Tab. 1.2) it is clear that similar effects are present in the operational series of the [ACs](#) for *all* stations.

A similar behavior coincides for several stations with changes in the tracking performance of the receiver (due to firmware updates or receiver changes) as in particular observations at low elevations are affected by an improved or degraded tracking. As an example, Fig. 6.19 demonstrates this effect for Kerguelen Island: the three time periods with different receivers can clearly be distinguished in the station height difference between solutions NMF and VMF1 (Fig. 6.19a) as well as in the observation rate computed by [teqc](#) (Fig. 6.19b). The tracking performance of the ROGUE SNR-8C receiver decreased until the replacement of the receiver in April 1999. Therefore, also the amplitude of the station height difference decreased. During the time period when the site is equipped with a Trimble 4000SSI receiver, the station height difference as well as the tracking performance is smallest. At the beginning of its operation, the Ashtech μZ receiver provides the highest observation rate, the reasons for the decrease in 2005 are unknown. However, the amplitude of the station height differences is smaller than during the time period with the ROGUE receiver. This effect can be explained by the observation distribution which is also influenced by a receiver cut-off angle differing from zero. For the ROGUE receiver, on average 6.8% of the total number of observations are tracked between 0 and 10° elevation, whereas only 0.2% for the Trimble receiver and 0.1% for the Ashtech receiver. Although no information is given in the station log, the observation distribution (also derived with [teqc](#), not shown here) is a clear indicator that the hardware cut-off angle of the Trimble and the Ashtech receiver was set to 10°. Therefore, the station height differences are smaller for the Trimble and the Ashtech receiver compared to the ROGUE receiver. In general the scatter of the station height differences increases when the receiver cut-off angle is lowered or the tracking performance increases. It is clear that these inhomogeneities related to the observation data cannot be overcome by a reprocessing and limit the stability of the estimated long time series.

Solution	NMF	IMF	GMF	VMF1
Scale offset [ppb]	0.41 ± 0.06	0.20 ± 0.07	0.22 ± 0.06	0.20 ± 0.07
Scale amplitude all stations [ppb]	0.37 ± 0.01	0.32 ± 0.01	0.34 ± 0.01	0.34 ± 0.01
Scale amplitude datum stations [ppb]	0.25 ± 0.01	0.15 ± 0.01	0.19 ± 0.01	0.18 ± 0.01

Tab. 6.8: Scale offset of **TRF**s computed with **NMF**, **IMF**, **GMF** and **VMF1** w.r.t. IGB00 and annual scale amplitudes of the corresponding time series. The scale offset (referred to 1 January 2000) was estimated as part of a 14-parameter similarity transformation of the datum stations of the corresponding **TRF**s.

As the mapping function significantly affects the estimation of station heights also the scale of the whole tracking network is affected: the mean scale offsets w.r.t. IGB00 of the **TRF**s determined from the **NEQ**s based on the four different mapping functions (according to the strategy described in Sec. 5.3) are listed in the first line of Tab. 6.8. The lower part contains annual scale amplitudes of the corresponding time series solutions. The different order of magnitude of the formal errors can be explained by the different number of observations as well as parameters: For the scale offset, number of stations times six (three positions and velocities per station) observations are used to estimate 14 transformation parameters. For the scale amplitude, 4018 daily scale values are used to estimate amplitude and phase of an annual signal resulting in much smaller formal errors compared to the scale offset. The scale offset of the **NMF TRF** differs from the other **TRF** solutions by about 0.20 ppb and is two times larger than that of the **IMF**, **GMF** and **VMF1 TRF**s. Due to the different seasonal behavior of the mapping functions already described above also the scale time series are affected. Like for the scale offset, the scale amplitudes of solutions **IMF**, **GMF** and **VMF1** are quite similar, the **NMF** amplitude is slightly larger (scale is determined from all stations). The differences get larger if only the datum stations are used for the generation of the scale time series: the annual scale amplitude of solution **NMF** is almost 40% larger compared to solution **VMF1**. However, the magnitude of the scale amplitude is reduced for all solutions. This effect is probably related to the fact that primarily stable stations with small annual amplitudes in the station height have been selected as datum stations.

Solutions	Component	NMF	IMF	GMF	VMF1
Weekly 2004	North [mm]	1.61	1.62	1.61	1.61
	East [mm]	1.64	1.65	1.64	1.64
	Up [mm]	5.35	5.26	5.36	5.16
TRF	North [mm]	3.68	3.72	3.70	3.70
	East [mm]	4.25	4.26	4.25	4.25
	Up [mm]	9.46	9.37	9.36	9.18

Tab. 6.9: Upper part: Mean coordinate repeatabilities of combined weekly solutions for 2004 based on 1-day **NEQ**s. Lower part: Mean coordinate repeatabilities of **TRF** solutions.

The upper part of Tab. 6.9 lists the mean repeatabilities of weekly solutions computed from 1-day **NEQ**s in 2004. The repeatabilities of the horizontal coordinate components do not differ significantly and also the largest difference for the height repeatability is only 0.2 mm. However, the repeatabilities of the empirical mapping functions **NMF** and **GMF** are worst as only mean annual variations of the atmosphere are modeled. Variations on shorter time scales are neglected. The height repeatability is smaller by 1/10 mm for solution **IMF** and another 1/10 mm for solution **VMF1**. These mapping functions are based on 6-hourly data from numerical weather models that also consider short-term variations of the atmosphere resulting in a slightly improved height repeatability. The repeatabilities of the **TRF** solutions given in the lower part of Tab. 6.9 are a factor of roughly two larger than the weekly repeatabilities as seasonal signals are not accounted for in the linear **TRF** model. Like for the weekly solutions, the horizontal repeatabilities do not differ significantly. The differences in the vertical component are slightly larger, the height repeatability of solution **VMF1** is about 0.3 mm smaller compared to solution **NMF**. Whereas the general behavior of the mapping functions as regards the repeatability agrees with the **VLBI** results of *Tesmer et al. (2007)*, the differences of the repeatabilities in Tab. 6.9 are slightly smaller.

The examples discussed above clearly demonstrate the importance of up-to-date mapping functions (like **IMF** and **VMF1**) for a proper interpretation of **GPS**-derived station height time series. Another important issue that also affects the station height time series, namely the hydrostatic a priori delays, will be discussed in the next section.

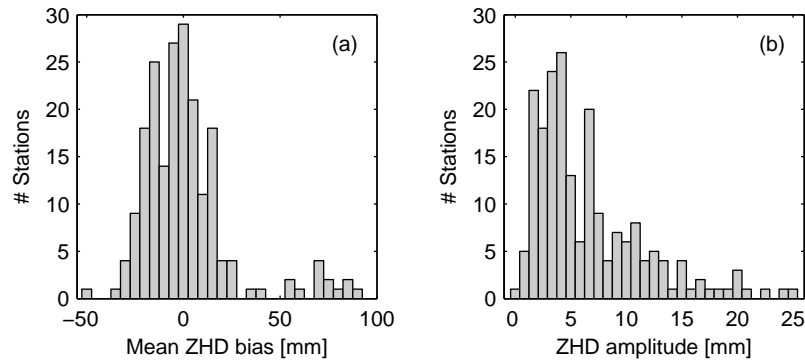


Fig. 6.20: Histograms of hydrostatic ECMWF zenith delays: (a) mean biases w.r.t. the Berg/Saastamoinen model; (b) annual amplitudes.

6.3.2. Hydrostatic a Priori Delays

Whereas solutions NMF, IMF, GMF and VMF1 applied constant a priori ZHDs computed with the Berg/Saastamoinen model (Eqs. 2.25 and 2.26a), the a priori ZHDs of solution VMF1 ECMWF are based on numerical weather model data, see Sec. 2.5.1. The mean biases of the hydrostatic ECMWF zenith delays compared to the Berg/Saastamoinen model are shown in Fig. 6.20a. In particular stations in Antarctica show mean biases between 5 and 10 cm due to the deficiencies of the simple standard atmosphere. The maximum biases in this region can reach up to 18 cm. The ECMWF ZHDs have annual amplitudes of up to 25 mm, see Fig. 6.20b. However, 80% of the ZHD amplitudes are smaller than 10 mm and 52% are smaller than 5 mm. Amplitudes larger than 15 mm in particular occur in the east of Russia and China, in Greenland and Alaska. These seasonal as well as the short-term variations (see Fig. 2.3) are ignored when applying the time-independent Berg/Saastamoinen model.

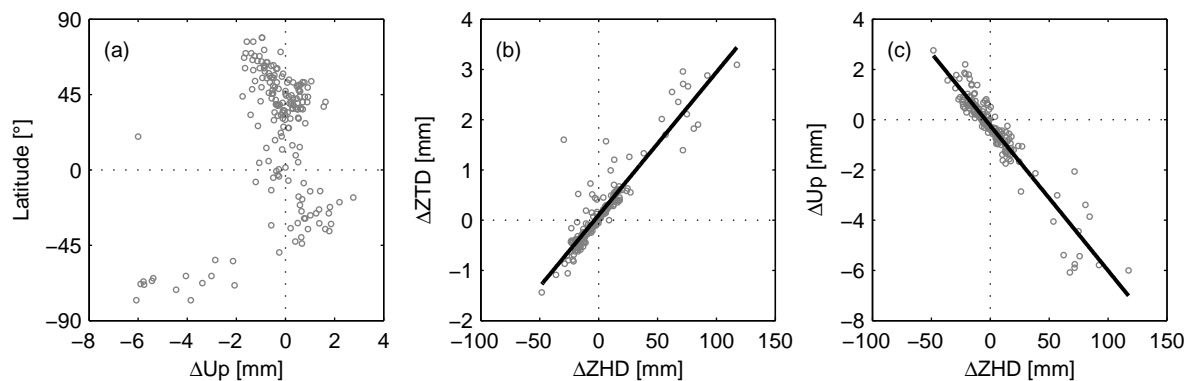


Fig. 6.21: Interaction between troposphere zenith delays and station heights. Differences between solutions VMF1 and VMF1 ECMWF: (a) station height changes; (b) ZHD changes vs. ZTD changes, regression coefficient $+0.028$; (c) ZHD changes vs. station height changes, regression coefficient -0.058 .

Like for the different mapping functions, the largest mean station height differences of up to 6 mm occur in Antarctica, see Fig. 6.21a. However, an isolated station at 20° latitude also shows a height change of about -6 mm. This behavior of Mauna Kea can be explained by the huge height difference of more than 3 km between the ECMWF DEM and the actual station height: the extrapolation applied (Eq. 2.28) is only valid for small height differences. For most of the other stations the changes are related to the deficiencies of the standard atmosphere applied for solution VMF1. The changes of the hydrostatic delay are primarily absorbed by the estimated ZWD. However, due to differences of the hydrostatic and the wet mapping functions, also the ZTD is affected by the different a priori delays, see Fig. 6.21b. The mean changes in the ZTD range from about -1.5 to $+3.0$ mm. The dependence of the ZTD changes on the ZHD changes seems to be quite linear with a regression coefficient of $+0.0028 \pm 0.003$. The sign of this regression coefficient is positive as the wet compared to the hydrostatic mapping function is steeper. The observed distance between receiver and satellite does not depend on the troposphere modeling (the different a priori delays and mapping functions only change the discrimination between troposphere delay and station height).

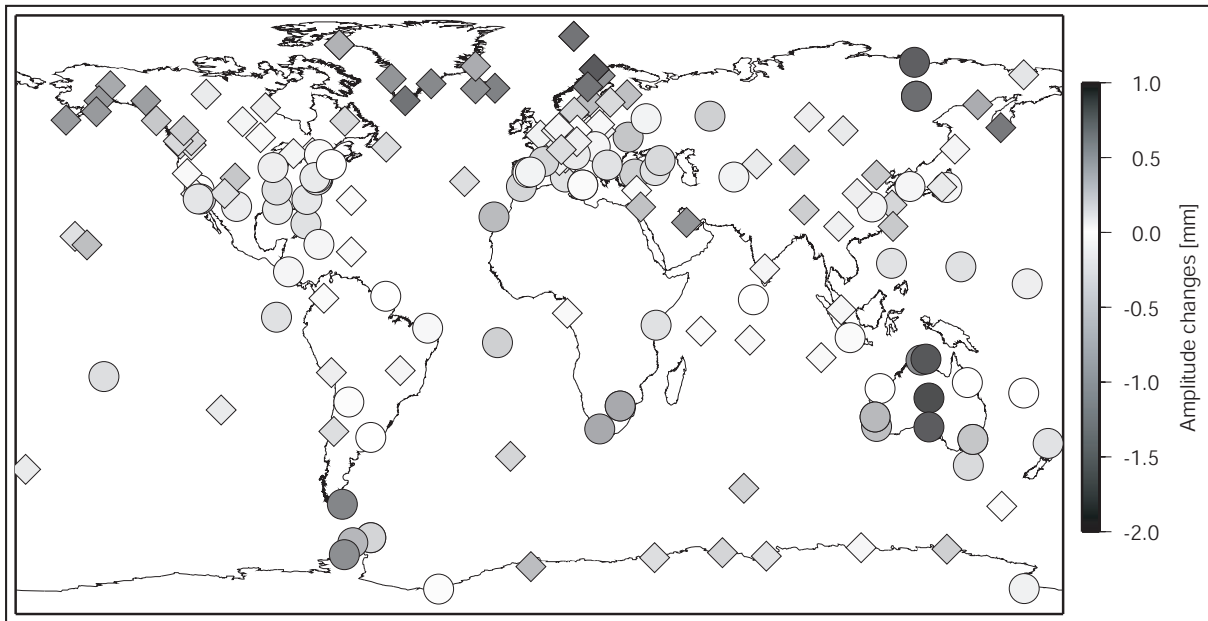


Fig. 6.22: Amplitude differences of annual signals in the station height between solutions VMF1 and VMF1 ECMWF. Positive amplitude changes are indicated by circles, negative amplitude changes by diamonds. Stations with less than 1000 observation days have been excluded.

Therefore, *ZHD* changes and station height changes have a negative regression coefficient of -0.058 ± 0.006 (see Fig. 6.21c). *Tregoning and Herring (2006)* reported a regression coefficient of -0.083 when applying the Global Pressure and Temperature (*GPT*) model (computed from 3 years of *ECMWF* data, *Boehm et al., 2007b*) for the computation of the a priori *ZHD*. Possible explanations for this difference might be the different cut-off angle (7° vs. 3°), the different weights for the elevation-dependent weighting, the shorter time period (1 year vs. 11 years), the application of atmospheric loading (not applied for solutions VMF1 and VMF1 ECMWF) and of course differences between the *GPT*-derived *ZHDs* and the *ECMWF ZHDs*.

Due to their seasonal variations, the a priori *ZHDs* also affect the annual amplitude of the station heights. The amplitude differences between solution VMF1 and VMF1 ECMWF are shown in Fig. 6.22. The largest positive amplitude changes (amplitude of solution VMF1 is larger than the amplitude of solution VMF1 ECMWF) of up to 1 mm occur in Australia, northern Russia, Terra del Fuego and the Antarctic Peninsula. The annual amplitudes are amplified by the *ECMWF ZHDs* in Alaska, Greenland and northern Scandinavia.

7. Satellite Orbits

As already mentioned in Sec. 1.1, the major task of the IGS in the early years was the improvement of the orbit quality. This quality could be improved from about 20 cm in 1994 to less than 5 cm nowadays, see Fig. 1.2. The majority of the AC submissions even agree within 2 cm with the combined IGS orbit (Gendt and Kouba, 2008). This chapter discusses the consistency of the reprocessed orbits and compares them with the CODE orbits and the combined IGS final orbits. Finally, residuals computed from SLR normal points provide an independent validation of the orbits computed from GPS microwave observations.

7.1. Formal Accuracy

One indicator for the formal accuracy of satellite orbits is given in the header of the SP3c¹ orbit files. This so-called SP3 accuracy code n allows for a weighting of the individual satellites and stands for a formal position accuracy of $\pm 2^n$ mm. In contrast to the combined IGS orbits, where the accuracy codes are derived from the RMS values of the different AC orbits contributing to the combination, the corresponding accuracy codes in the Bernese GPS software are derived from the formal errors of the argument of latitude. The SP3 accuracy codes of the reprocessed 1-day orbits are shown in Fig. 7.1. In 1994 and 1995 the accuracy is significantly worse what is also shown by internal consistency tests, see Sec. 7.2. For most satellites, the accuracy codes are worse by a factor of 2–3 during the very first weeks after the launch. A limiting factor for the accuracy of the orbit determination immediately after the launch is the small number of tracking stations recording observations of new satellites. E.g., only receivers with an all-in-view option are able to track satellites that are set unhealthy in the almanac what is usual for all satellites before the official commissioning. But even if a satellite is set healthy, it usually takes several days until all receivers actually track this satellite. Another effect degrading the orbit accuracy during the first weeks after the launch are unmodeled accelerations due to outgasing (Springer, 2000). The mean SP3 accuracy code of all 1-day orbits is 3.18 (corresponding to 9.1 mm), the mean values of the preliminary and final 3-day orbits are 1.59 (corresponding to 2.5 mm) and 1.60 (corresponding to 2.6 mm), respectively. These numbers confirm the assumption that the 3-day arcs are more stable than the 1-day orbits. However, as shown in the next section, these accuracies are far too optimistic.

¹Format description available at <http://igsb.jpl.nasa.gov/igsb/data/format/sp3c.txt>

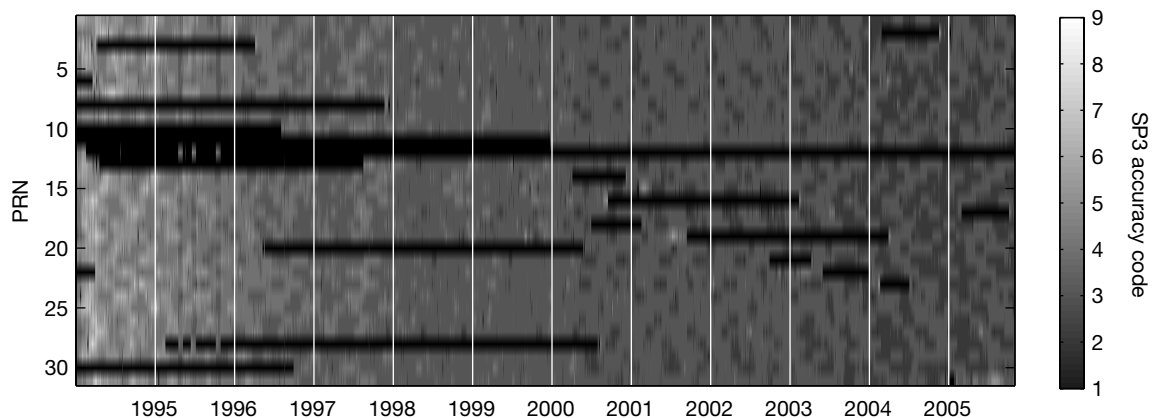


Fig. 7.1: SP3 accuracy codes of the 1-day orbits. Periods with unoccupied PRNs are given in black.

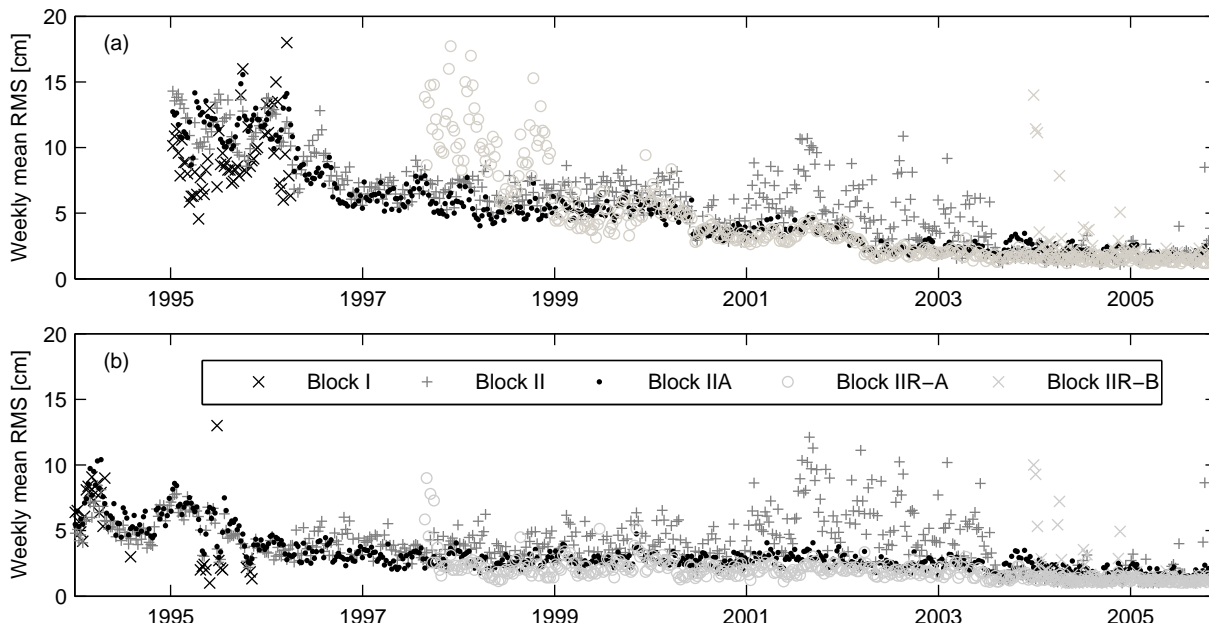


Fig. 7.2: Mean weekly RMS values of 3-day orbit fits through 1-day orbits for the different types of GPS satellites: (a) CODE final orbits (RMS values only available starting with GPS week 782); (b) reprocessed orbits.

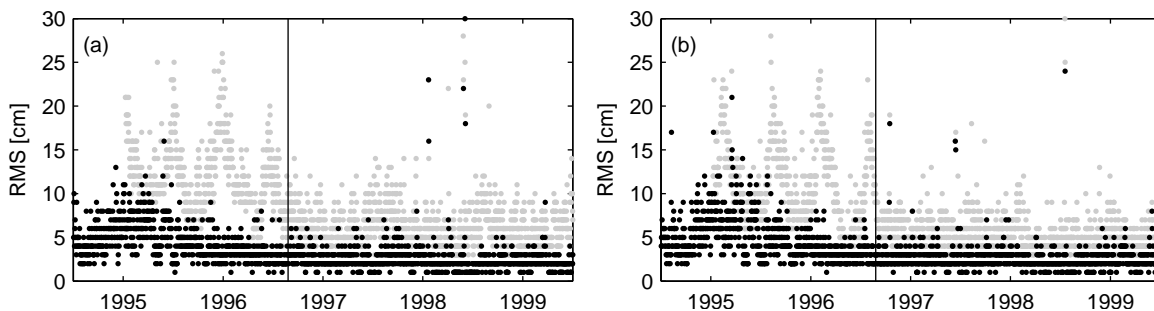


Fig. 7.3: RMS values of 3-day orbit fits through 1-day CODE (gray) and reprocessed (black) orbits for (a) SVN 17 (PRN 17) and (b) SVN 21 (PRN 21). The CODE orbit fits show a periodic signal before changing the orbit modeling in August 1996 (indicated by a vertical line). The maxima of this periodic signal coincide with the zero-crossings of the β_0 angle.

7.2. Internal Consistency

To quantify the internal consistency of the satellite orbits, 3-day orbit arcs were fitted through 3 consecutive 1-day orbits. The mean RMS of the 3-day arc w.r.t. the three 1-day arcs serves as a quality indicator. Weekly means of these RMS values for the different satellite blocks are shown in Fig. 7.2. The increased RMS values for the Block II satellites between 2001 and 2003 that are present in both the CODE and the reprocessed series are probably related to the aging of these satellites (problems with momentum wheels or the attitude control in general). The situation improves in mid 2003 when the attitude control system of two of these problematic Block II satellites (SVN 15 and 17) was changed, see Tab. 4.2. In 1995, the RMS values could be reduced by a factor of about two by reprocessing the orbits. Between 1996 and 2000, the RMS values of the CODE orbits are generally above the 5 cm level whereas the reprocessed orbits are on a level below 5 cm. A clear improvement of the CODE orbits can be seen in June 2000 when the pseudo-stochastic pulses were changed (see Tab. 1.2). After switching to an improved ambiguity resolution strategy in March 2002 (see Tab. 1.2 and Sec. 5.1), the internal consistency of the CODE and the reprocessed orbits is on almost the same level of 1–2.5 cm.

Satellite Block	Δx [m]	Δy [m]	Δz [m]
I	0.210	0.000	0.854
II/IIA	0.279	0.000	1.023
IIR-A/B	0.000	0.000	0.000

Tab. 7.1: IGS01 block-specific satellite antenna phase center offsets used by the IGS ACs until November 2006 (available at ftp://igsceb.jpl.nasa.gov/igsceb/station/general/igs_01.atx). No distinction is made between Block IIR-A and IIR-B satellites.

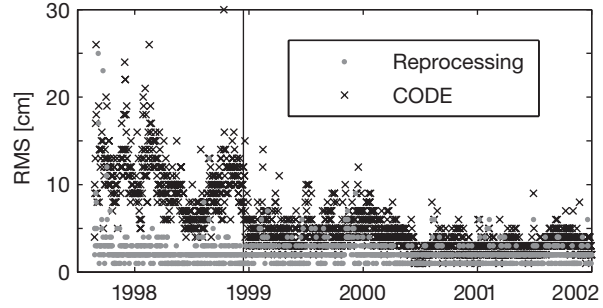


Fig. 7.4: RMS values of 3-day orbit fits through 1-day orbits for SVN 43 (PRN 13). The change of the z -offset in the CODE solution is indicated by a vertical line.

Time series of two individual satellites, namely SVN 17 and SVN 21, are shown in Fig. 7.3. At the beginning, the CODE orbit fits show a periodic signal whose maxima coincide with the zero-crossings of the β_0 angle (not shown here). After changing the orbit modeling (see Tab. 1.2) in August 1996 this periodic signal vanishes and the orbit quality improves. However, the CODE orbit fits are still worse by a factor of about two for the time period shown in Fig. 7.3, probably due to a less sophisticated modeling of the pseudo-stochastic pulses. Besides the general improvement in the early years, in particular the improvement for the Block IIR-A satellites (actually only one satellite for more than two years) in Fig. 7.2 is striking. SVN 43 (PRN 13) was the first Block IIR-A satellite in orbit and therefore, its vertical antenna offset was unknown. The IGS ACs used the offset of the Block II/IIA satellites (1.023 m, see Tab. 7.1) instead. This assumption led to large and varying RMS values for the orbit fits (see Fig. 7.4) indicating that this offset was not appropriate. Offset estimates by CODE, GFZ and JPL showed that the z -offset seemed to differ significantly from the value of the Block II/IIA satellites. Therefore, a z -offset value of 0.000 m was adopted by the IGS on 29 November 1998 (Kouba and Mireault, 1999). By changing the offset, the orbit quality could be significantly improved and also the large variations disappeared. In the reprocessed time series, the RMS values for SVN 43 are almost constant for the whole time period. The larger values at the beginning are probably due to the fact that shortly after the launch the satellite was tracked by a small number of stations only.

Tab. 7.2 lists yearly mean RMS values of the orbit fits for all individual satellites from 1995 till 2004. The year 1994 is not shown as no corresponding CODE values are available for that year, and the year 2005 is not shown as it is not completely covered by the reprocessing. SVN 10 was excluded from the reprocessing for several periods in 1995 as well as SVN 28 starting with November 1995, as the number of stations tracking the two satellites was very small and the resulting orbit quality quite bad. In the early years, the consistency of the orbits of most satellites could be improved by a factor of more than two. As expected, the differences get smaller with time due to improvements in the CODE processing strategy.

For several satellites with modeling problems, the RMS values of the reprocessed orbits are worse by several mm up to about 16 cm (SVN 21). On the other hand, well-behaving satellites generally also show improvements in the recent years except for a few satellites, where the RMS values of the reprocessed orbits are merely worse on the 1-mm level (e.g., SVN 35 and 36). Even in 2004, in general, the reprocessed orbits show smaller RMS values than the CODE orbits although the processing strategy of both solutions is very similar. This effect can probably be attributed to the application of an absolute antenna phase center model for receiver and satellite antennas for the reprocessed solution (CODE used the relative model for receiver antennas until 4 November 2006 like the other IGS ACs) resulting in a better internal consistency of the orbits, see Sec. 9.2.4. This is particularly evident for the Block IIR-B satellites: the RMS values of the satellites belonging to this block (SVN 47, 59, 60 and 61) are smaller by 3–9 mm in the reprocessed solution. For the other satellite blocks, the differences are generally on the level of a few millimeters.

As already mentioned in Sec. 4.1, several Block II/IIA satellites suffer from RW problems resulting in thruster firings. These satellites, namely SVN 14, 15, 16, 18, 19, 20, 21, 24 and 29, are given in italic in Tab. 7.2. The deficiencies as regards the attitude control system result in a degraded accuracy in both, the reprocessed and the CODE orbits. As an example for a satellite with a RW failure, Fig. 7.5 shows the orbit fits for SVN 15. According to Tab. 4.2, RW1 was disabled in April 1999 and re-enabled on 28 June 1999 when RW2 failed. Starting with that time, huge RMS values of the orbit fits of up to 4 m (in particular during the eclipse periods) can be observed as momentum has to be dumped with thrusters, see Sec. 4.1.

SVN	PRN	Block	1995	1996	1997	1998	1999	2000	2001	2002	2003	2004
10	12	I	8.9	11.1	–	–	–	–	–	–	–	–
			3.6	–	–	–	–	–	–	–	–	–
13	2	II	12.8	8.7	5.6	5.2	6.1	3.6	8.5	10.0	4.8	1.7
			5.1	2.9	2.6	2.5	3.8	2.2	8.2	13.1	4.8	1.6
14	14	II	<i>10.5</i>	<i>13.7</i>	<i>18.5</i>	<i>44.6</i>	<i>39.7</i>	<i>54.9</i>	–	–	–	–
			<i>4.9</i>	<i>8.9</i>	<i>16.9</i>	<i>44.1</i>	<i>40.2</i>	<i>56.8</i>	–	–	–	–
15	15	II	11.5	8.8	6.7	6.1	<i>12.2</i>	<i>15.2</i>	<i>13.9</i>	5.0	3.4	1.8
			5.0	3.1	3.0	2.5	<i>9.9</i>	<i>15.4</i>	<i>16.4</i>	7.9	5.0	1.5
16	16	II	11.3	<i>16.7</i>	<i>20.3</i>	<i>23.6</i>	<i>24.1</i>	<i>26.0</i>	–	–	–	–
			5.3	<i>12.5</i>	<i>17.7</i>	<i>21.9</i>	<i>21.8</i>	<i>27.1</i>	–	–	–	–
17	17	II	12.7	9.4	6.4	6.3	5.9	5.2	<i>30.6</i>	<i>6.3</i>	<i>7.4</i>	1.6
			5.0	3.0	2.6	2.5	2.3	3.0	<i>35.2</i>	<i>17.3</i>	<i>10.8</i>	1.5
18	18	II	10.3	<i>10.9</i>	<i>11.4</i>	<i>13.1</i>	<i>12.1</i>	<i>13.7</i>	–	–	–	–
			4.7	<i>6.3</i>	<i>8.1</i>	<i>10.9</i>	<i>9.9</i>	<i>12.1</i>	–	–	–	–
19	19	II	12.1	<i>14.0</i>	<i>13.1</i>	<i>13.9</i>	<i>14.5</i>	<i>12.0</i>	<i>13.9</i>	–	–	–
			5.0	<i>10.4</i>	<i>10.6</i>	<i>12.3</i>	<i>11.6</i>	<i>10.9</i>	<i>13.9</i>	–	–	–
20	20	II	<i>11.8</i>	<i>9.9</i>	–	–	–	–	–	–	–	–
			<i>4.5</i>	<i>3.2</i>	–	–	–	–	–	–	–	–
21	21	II	11.3	9.2	5.8	5.1	4.9	4.0	<i>28.9</i>	<i>25.3</i>	–	–
			5.4	3.2	2.7	2.3	2.5	2.5	<i>36.7</i>	<i>41.1</i>	–	–
22	22	IIA	12.9	8.7	6.3	5.3	5.2	3.7	3.3	2.3	2.4	–
			5.7	3.3	2.7	2.4	2.5	2.2	2.4	2.3	2.8	–
23	23	IIA	20.6	19.6	19.7	23.1	27.4	31.9	26.8	4.2	11.9	3.0
			18.1	17.7	18.3	21.7	26.1	31.4	27.7	4.3	12.3	2.1
24	24	IIA	14.0	8.8	5.6	18.2	<i>18.2</i>	<i>13.1</i>	<i>11.3</i>	<i>11.5</i>	8.5	<i>10.1</i>
			5.3	3.0	2.6	16.5	<i>16.0</i>	<i>12.7</i>	<i>11.7</i>	<i>15.1</i>	8.5	<i>11.1</i>
25	25	IIA	11.9	7.8	5.9	4.9	4.9	3.8	3.0	2.2	2.1	1.6
			5.7	3.1	2.7	2.3	2.4	2.2	2.2	2.1	2.0	1.4
26	26	IIA	10.6	7.9	6.1	5.3	5.0	3.8	3.5	2.3	1.9	1.6
			5.4	3.1	2.6	2.2	2.5	2.1	2.6	2.3	2.0	1.5
27	27	IIA	10.8	7.3	5.8	5.0	4.9	3.3	2.8	2.2	1.8	1.7
			4.6	3.0	2.5	2.2	2.5	2.0	2.1	2.0	1.8	1.5
28	28	IIA	12.2	9.4	16.0	–	–	–	–	–	–	–
			4.3	–	–	–	–	–	–	–	–	–
29	29	IIA	9.2	8.0	6.8	5.6	5.2	4.7	4.0	<i>10.9</i>	<i>11.8</i>	<i>19.1</i>
			4.6	3.4	3.8	3.1	3.2	3.6	3.6	<i>12.0</i>	<i>12.3</i>	<i>20.7</i>
30	30	IIA	–	10.4	6.3	4.6	4.7	3.5	2.8	2.1	1.8	1.5
			–	8.3	3.2	2.2	2.3	2.0	2.3	2.2	1.9	1.5
31	31	IIA	12.7	9.3	6.4	5.2	5.9	4.2	3.3	2.1	1.7	2.1
			5.1	3.2	2.5	2.3	2.6	2.4	2.2	2.0	1.7	1.5
32	1	IIA	11.2	8.5	5.9	4.8	5.2	4.3	3.1	2.3	2.0	1.7
			5.6	3.3	2.5	2.2	2.4	2.1	2.1	2.1	1.8	1.4
33	3	IIA	–	9.8	5.9	5.0	4.9	3.7	3.4	2.4	1.9	1.9
			–	5.5	2.6	2.1	2.9	2.3	2.6	2.4	2.1	1.7
34	4	IIA	12.2	8.8	6.1	5.7	5.6	3.6	3.1	2.2	1.9	1.6
			5.2	3.0	2.6	2.4	2.4	2.0	2.0	1.9	1.7	1.5
35	5	IIA	10.9	7.5	5.4	4.4	4.5	3.5	2.9	2.3	2.0	1.9
			4.4	2.7	2.3	2.2	2.2	2.1	2.3	2.4	2.1	1.7
36	6	IIA	12.3	8.7	5.4	4.7	4.7	3.4	3.3	2.1	1.8	1.7
			4.9	2.8	2.5	2.1	2.3	1.9	2.3	2.2	2.0	1.7
37	7	IIA	14.4	10.5	5.8	5.1	5.7	4.1	3.3	2.3	1.9	2.4
			5.2	3.0	2.5	2.2	2.6	2.2	2.5	2.1	1.9	2.2
38	8	IIA	–	–	8.2	6.0	4.6	3.3	3.0	2.3	2.0	1.9
			–	–	6.5	3.3	2.5	2.1	2.3	2.2	1.9	1.7
39	9	IIA	11.0	7.1	5.8	4.8	4.8	3.5	3.1	2.2	1.8	1.7
			5.0	2.8	2.4	2.2	2.3	2.1	2.3	2.2	1.9	1.6

SVN	PRN	Block	1995	1996	1997	1998	1999	2000	2001	2002	2003	2004
40	10	IIR-A	–	8.7	6.5	5.3	4.8	3.5	3.2	2.2	1.8	1.5
			–	5.2	3.3	2.2	2.3	2.0	2.2	2.1	1.8	1.4
41	14	IIR-A	–	–	–	–	–	3.8	3.5	2.4	1.8	1.8
			–	–	–	–	–	3.1	2.3	2.1	1.6	1.3
43	13	IIR-A	–	–	13.8	10.0	4.9	3.6	3.2	2.1	1.8	1.5
			–	–	4.5	2.4	2.4	1.7	1.9	1.8	1.5	1.3
44	28	IIR-A	–	–	–	–	–	3.5	3.1	2.3	1.6	1.5
			–	–	–	–	–	2.3	2.0	2.0	1.7	1.4
45	21	IIR-A	–	–	–	–	–	–	–	–	2.2	1.3
			–	–	–	–	–	–	–	–	2.0	1.3
46	11	IIR-A	–	–	–	–	–	4.9	3.5	2.2	1.9	1.7
			–	–	–	–	–	2.2	2.0	1.9	1.8	1.4
47	22	IIR-B	–	–	–	–	–	–	–	–	–	2.5
			–	–	–	–	–	–	–	–	–	1.6
51	20	IIR-A	–	–	–	–	–	3.8	3.4	2.2	1.8	1.5
			–	–	–	–	–	2.0	1.8	1.8	1.6	1.2
54	18	IIR-A	–	–	–	–	–	–	4.2	2.5	1.8	1.4
			–	–	–	–	–	–	2.7	2.3	1.8	1.3
56	16	IIR-A	–	–	–	–	–	–	–	–	2.4	1.5
			–	–	–	–	–	–	–	–	2.2	1.2
59	19	IIR-B	–	–	–	–	–	–	–	–	–	2.3
			–	–	–	–	–	–	–	–	–	1.8
60	23	IIR-B	–	–	–	–	–	–	–	–	–	2.8
			–	–	–	–	–	–	–	–	–	2.0
61	2	IIR-B	–	–	–	–	–	–	–	–	–	4.9
			–	–	–	–	–	–	–	–	–	4.6

Tab. 7.2: Yearly mean RMS values [cm] of 3-day orbit fits through three consecutive 1-day orbits. The first line for each satellite contains the CODE values, the second one the reprocessing results. Huge RMS values exceeding 100 cm have been excluded. In case the RMS of the reprocessed series is larger than the CODE RMS, values are given in gray. Time periods of satellites affected by RW problems are given in *italic*.

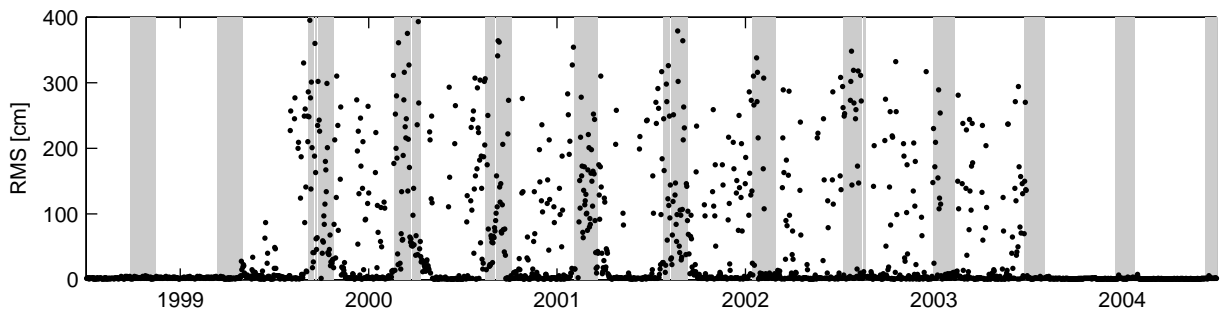


Fig. 7.5: Attitude control problems during the eclipse season: RMS of 3-day orbit fits through 1-day orbits for SVN 15 (PRN 15). Eclipse periods are shaded.

The situation improves dramatically in 2003 when this satellite was put into AMMM mode 5: the mean orbit fit RMS of 63 cm (computed from all orbit fit values) after the RW failure could be reduced to 1.9 cm by AMMM mode 5.

For SVN 23 only a slight improvement of a few millimeters can be achieved, even in the early years, due to the modeling problems caused by manually pitching the solar panels till January 2002. Fig. 7.6 shows the orbit fits as well as the direct radiation pressure estimates for this satellite. Two of the four operation modes described in Sec. 4.1 can be clearly identified in both time series: The smallest RMS values (mean RMS of 5.8 cm) occur in the hold mode (light gray) when the panels are not moved, the largest (mean RMS of 51 cm) in the scissor mode (dark gray) when the position of the panels is rapidly swapped once per day. The intermediate slew mode (mean RMS of 22 cm) and the hyper slew mode (mean RMS of 19 cm) cannot be distinguished in Fig. 7.6. Both modes result in an increased scatter of the orbit fits and a similar pattern in the direct radiation pressure. The time periods with $|\beta_0| > 45^\circ$ get shorter and shorter with time due to

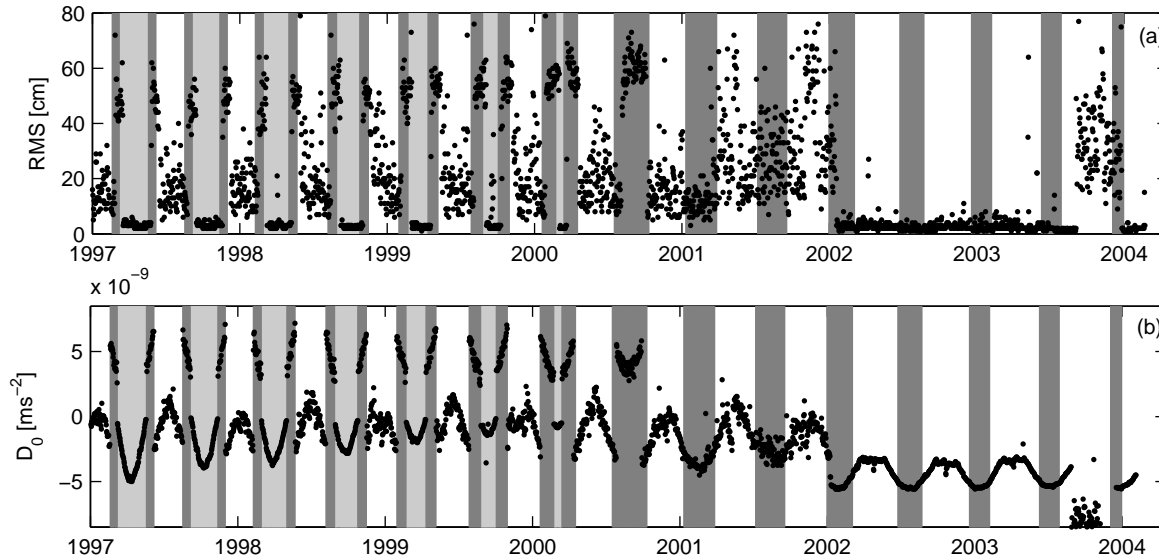


Fig. 7.6: Modeling problems of SVN 23 (PRN 23): (a) RMS of 3-day orbit fits through 1-day orbits; (b) direct radiation pressure. Time periods with $|\beta_0| > 45^\circ$ (hold mode during four season operation) are given in light gray, periods with $30^\circ < |\beta_0| < 45^\circ$ (scissor mode during four season operation) are given in dark gray.

the decreasing maximum β_0 angle for that particular satellite. Starting with the second eclipse season in 2000, the absolute value of β_0 does not exceed 45° anymore. Therefore, the satellite is not put into the hold mode anymore.

At the end of 2000, the four season mode was obviously deactivated as the characteristic pattern in the direct RPR parameter vanishes. Compared to previous years, the pattern in the orbit fits is quite homogeneous although the RMS values are quite large (mean RMS of 29 cm). The orbit fits improve by a factor of ten to a mean value of 2.9 cm in the years 2002 and 2003 after an automated mechanism for pitching the solar panels was implemented, see Sec. 4.1. The reason for the different behavior at the end of 2003 (resulting in increased RMS values with a mean of 35 cm as well as in negatively biased D_0 estimates with an increased scatter) is unknown.

7.3. Intra-Technique Comparisons

For external validation, the final 3-day orbits have been compared with the combined IGS orbits and the CODE orbits (not shown here) by a 7-parameter similarity transformation. The first reprocessing run showed several huge outliers in the transformation parameters within the early years. A closer look revealed that these outliers were related to satellites only tracked by a few stations resulting in a very small number of observations (sometimes below 100 per satellite). Due to small formal errors, these satellites had not been detected as bad satellites. To avoid such badly determined satellite orbits, a minimum number of 1000 observations was introduced as additional quality measure.

The reference frame changes present in the IGS orbits are clearly visible in the transformation parameters, see Fig. 7.7 and Tab. 7.3. The largest rotations as well as rotation rates show up for ITRF92 and ITRF93. Whereas for ITRF93 till ITRF2000 the NNR-NUVEL1A model (DeMets et al., 1994) was used for the realization of the NNR datum, NNR-NUVEL1 (Argus and Gordon, 1991) was used for ITRF92 (Boucher et al., 1993). ITRF93 is slightly rotated w.r.t. NNR-NUVEL1A as the time evolution of the ERPs estimated in the solutions contributing to ITRF93 does not follow the NNR-NUVEL1A model (Boucher et al., 1994). The absence of clear translation discontinuities has two different reasons: (1) For ITRF94, ITRF96 and ITRF97 a continuity condition for the origin has been applied (McCarthy and Petit, 2004). (2) The impact of a shift in the reference frame on the center of mass determined by the GPS orbits is smaller by a factor of 5–10 than the shift itself (Ferland et al., 2005). The scale offset does not significantly differ for ITRF92 till ITRF97, but is larger by almost a factor of two for ITRF2000. In addition, the scatter of the scale gets significantly smaller in mid 2003. The reason for this effect is unknown. The general scale difference

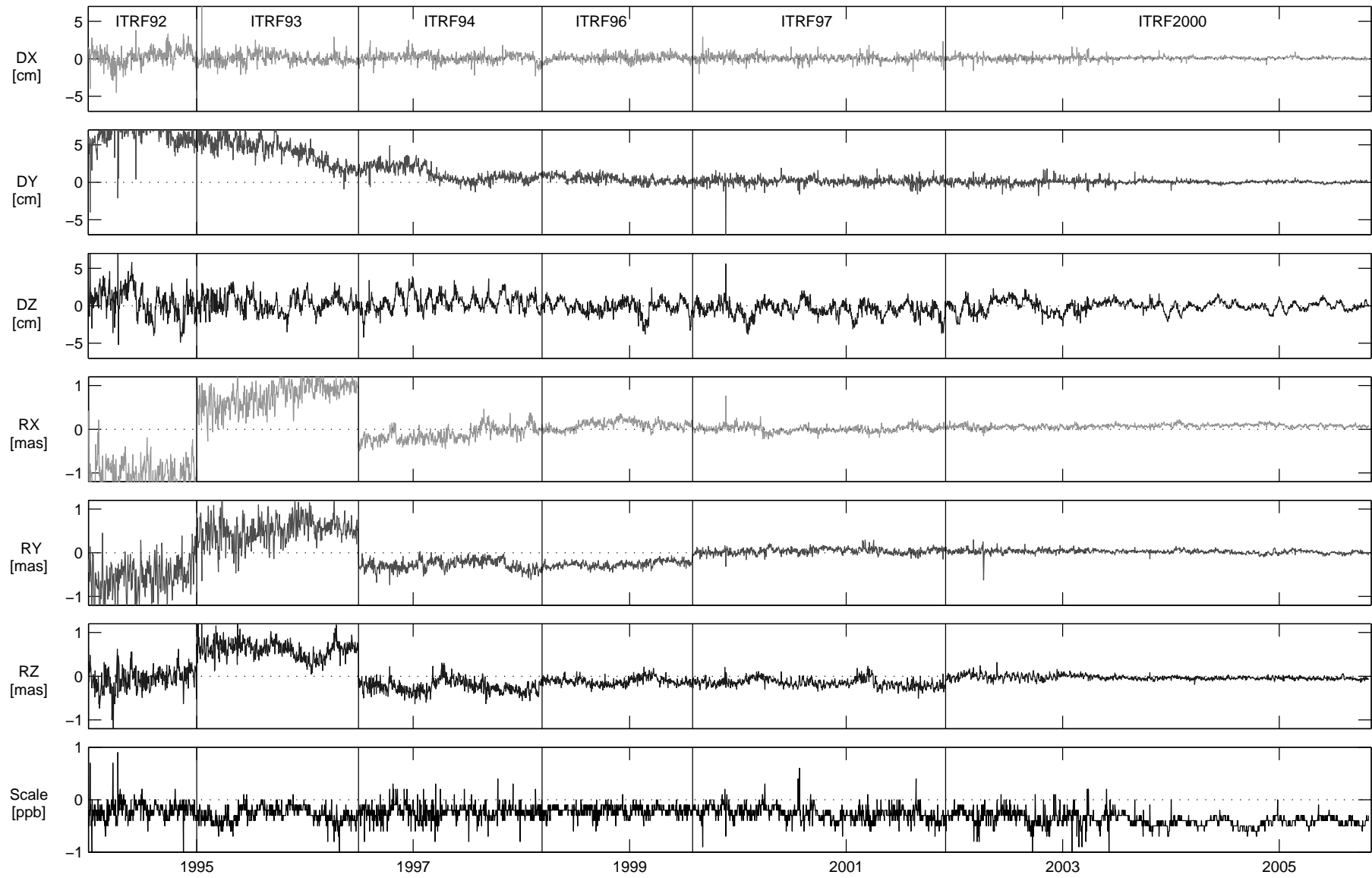


Fig. 7.7: Transformation parameters from daily 7-parameter similarity transformations between the combined IGS orbits and the reprocessed final 3-day orbits.

Transformation parameter	Epoch	ITRF92 1994.50	ITRF93 1995.75	ITRF94 1997.34	ITRF96 1998.89	ITRF97 2000.75	ITRF2000 2003.88
Translation X	[mm]	3.0	0.6	1.3	1.1	1.2	1.0
Translation rate X	[mm/y]	10.1	-1.1	-1.3	1.9	-0.1	0.0
Translation Y	[mm]	65.3	41.9	11.2	4.2	1.4	0.4
Translation rate Y	[mm/y]	-0.7	-30.3	-13.1	-6.4	-0.2	-0.1
Translation Z	[mm]	5.0	3.1	5.3	-1.5	-5.1	-0.5
Translation rate Z	[mm/y]	-28.1	-0.7	2.6	-2.6	-1.7	0.2
Rotation X	[mas]	-1.04	0.78	-0.11	0.10	0.00	0.07
Rotation rate X	[mas/y]	0.04	0.38	0.20	0.07	0.00	0.01
Rotation Y	[mas]	-0.54	0.51	-0.28	-0.26	0.04	0.03
Rotation rate Y	[mas/y]	0.43	0.18	0.00	0.09	0.01	-0.01
Rotation Z	[mas]	-0.06	0.61	-0.24	-0.11	-0.15	-0.03
Rotation rate Z	[mas/y]	0.27	-0.11	-0.04	0.01	-0.05	-0.01
Scale	[ppb]	-0.20	-0.29	-0.23	-0.21	-0.26	-0.39
Scale rate	[ppb/y]	0.04	0.00	0.00	0.01	-0.07	-0.04

Tab. 7.3: Transformation parameters between the IGS orbits and the reprocessed orbits for periods when different reference frames were used for the IGS solution. The epoch for the offset parameters is the middle of the time interval in which the reference frame was used by the IGS.

is probably related to the different models and software packages used by the IGS ACs. Even after transforming IGS final orbits given in ITRF97 to ITRF2000 with the transformation parameters provided by the IGS, *Kierulf et al. (2008)* report station height discontinuities of 6–10 mm due to the reference frame change. These discontinuities emphasize the importance of homogeneously reprocessed satellite orbits given in a unique reference frame for long-term studies of station positions.

The RMS of daily 7-parameter similarity transformations between the IGS orbits and the reprocessed 3-day orbits is shown in Fig. 7.8. In the first year, the RMS is on a level of 10–15 cm. In the following years, the RMS steadily decreases, reaches a level of about 2 cm in 2003 and is thereby on the same level as the RMS of the ACs with the smallest RMS values (*Gendt and Kouba, 2008*).

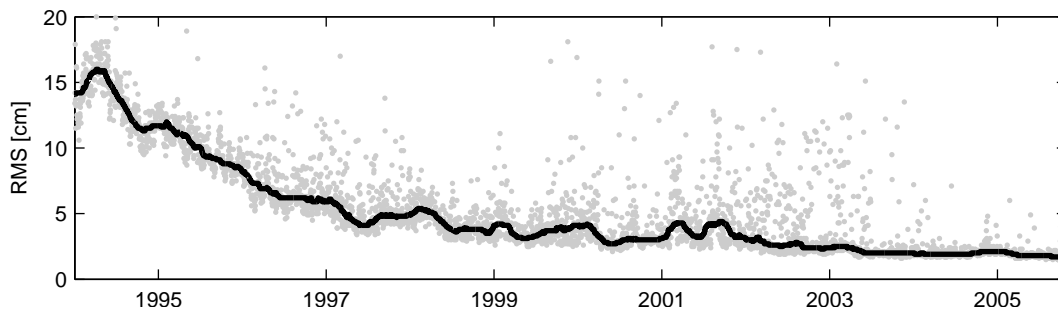


Fig. 7.8: RMS of 7-parameter similarity transformations between the IGS final orbits and the reprocessed orbits. The solid line represents a 100-day median.

7.4. Validation with Satellite Laser Ranging

As two of the GPS satellites (SVN 35 and 36) are equipped with Laser Retroreflector Arrays (LRAs), these satellites can be tracked with SLR. Thus, the satellite orbits computed from the GPS microwave observations can be validated by an independent (optical) technique. First results of the SLR tracking of GPS satellites are given in *Degnan and Pavlis (1994)*, *Pavlis (1996)*, *Zhu et al. (1997)* and *Springer (2000)*, more recent results can be found in *Appleby and Otsubo (2005)* and *Urschl et al. (2005, 2007, 2008)*.

The quantity Δt_R^S measured by SLR is the light travel time of a short laser pulse from the telescope to the LRA onboard the satellite and back to the telescope:

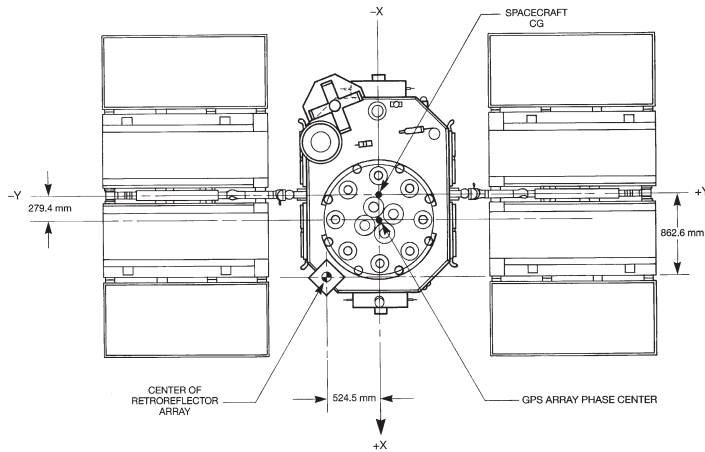


Fig. 7.9: Location of the LRA onboard the GPS satellites (Pavlis, 1996).



Fig. 7.10: LRA used onboard SVN 35 and 36 (Degnan and Pavlis, 1994).

SVN	X [mm]	Y [mm]	Z [mm]
35	862.6	-524.5	669.5
36	862.6	-524.5	671.7

Tab. 7.4: GPS laser retroreflector offsets provided by the ILRS.

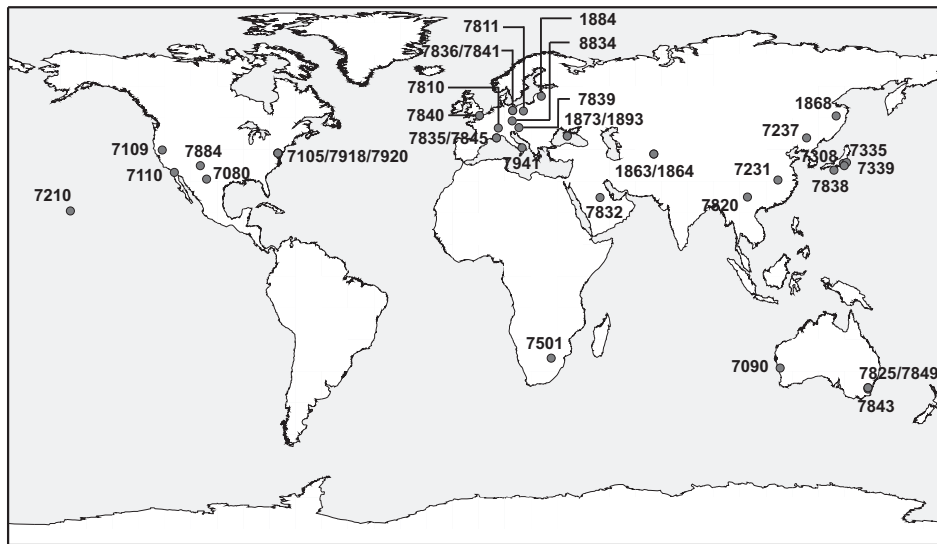


Fig. 7.11: SLR stations that tracked the GPS satellites SVN 35 and 36 between January 1994 and October 2005. Stations that were not used, as they are not included in ITRF2005 (Evpatoria, Urumqi, Tanegashima and TIGO Wettzell), are not shown. The stations are labeled with their CDP number, the station names are given in Tab. 7.5.

$$\Delta t_R^S = \frac{2}{c} (\rho_R^S + \Delta \rho_{trp} + \Delta \rho_{rel}) + \frac{1}{c} \Delta \rho_{sys} + \epsilon_R^S \quad (7.1)$$

with

ρ_R^S	geometric distance between the telescope and the satellite at the time of reflection at the satellite
$\Delta \rho_{trp}$	tropospheric delay
$\Delta \rho_{rel}$	relativistic effects
$\Delta \rho_{sys}$	signal delay in the laser system
ϵ_R^S	measurement error
c	speed of light.

General details on the SLR technique can be found in, e.g., Degnan (1993) or Schillak (2004), whereas Degnan and Pavlis (1994) focus on the SLR tracking of GPS satellites. The absolute accuracy of up-to-date SLR systems is below one centimeter (Pearlman et al., 2007). In the following, range residuals, i.e., differences between the SLR range and the range computed from GPS-derived orbits, will be used for comparisons (no parameters are estimated). Due to the high altitude of the GPS satellites, these range residuals are approximately equivalent to the radial orbit accuracy.

The location of the **LRA** onboard the **GPS** satellites is shown in Fig. 7.9. Due to the small size of this **LRA** (see Fig. 7.10; the 32 individual retroreflectors cover an area of $23.9 \times 19.4 \text{ cm}^2$) and the high altitude of the **GPS** satellites, only powerful laser ranging systems are able to track **GPS** satellites, in particular during daytime. The tracking activities of the **SLR** stations are coordinated by the International Laser Ranging Service (**ILRS**, *Pearlman et al.*, 2002). Although the two **GPS** satellites have the lowest tracking priority of the missions supported by the **ILRS** at the moment², these satellites are tracked on a regular basis complemented by dedicated campaigns like the **CSTG GPS** Laser Tracking Campaign (*Degnan*, 1997) in fall 1996. Between 3000 and 8000 **SLR** normal points per year are available. The **DCs** of the **ILRS** provide these normal points computed from about 5 minutes of individual **SLR** range observations.

The **SLR** stations tracking **GPS** satellites between January 1994 and October 2005 are shown in Fig. 7.11. Altogether 37 telescopes located at 30 stations observed the **GPS** satellites **SVN** 35 and 36 during this time period. **SLR** stations not included in the **ITRF2005** (1867, 7355, 7358 and 7594) have not been used and are not shown in Fig. 7.11. For the computation of the laser residuals, the coordinates of the **SLR** stations have been fixed to the rescaled version of **ITRF2005**³. This version is consistent with the scale determined by **SLR**, whereas the scale of the original **ITRF2005** (determined by **VLBI**) significantly differs from the **SLR** scale (*Altamimi et al.*, 2007). The reflector offsets provided by the **ILRS**⁴ (see Tab. 7.4) have been applied. In contrast to **GPS**, the tropospheric delay of the optic **SLR** measurements can be modeled with sufficient accuracy. Therefore, the estimation of troposphere parameters is not necessary. The model of *Marini* (1972) together with the meteorological observations at the **SLR** sites have been applied to correct for the tropospheric delay of the **SLR** observations. As the Bernese **GPS** Software was used for the computation of the **SLR** residuals, full consistency of the applied models (e.g., solid Earth tides and ocean loading) is guaranteed.

More than 67,000 **SLR** normal points of the time period from January 1994 till October 2005 were used to compute the residuals of the microwave-derived **GPS** satellite orbits. The number of normal points is a bit smaller for **SVN** 36 as this satellite was only launched in March 1994. Thus, its laser tracking did not start before April 1994 (the laser tracking of **SVN** 35 started in October 1993) and, besides, it had a lower tracking priority. Outliers exceeding an absolute value of 0.5 m or the 5-fold mean **STD** of each station have been excluded. 1.7 and 1.4% of the normal points met these criteria for the reprocessed orbits of **SVN** 35 and 36, respectively. The number of observations, the mean biases and the **STDs** of all **SLR** stations shown in Fig. 7.11 are given in Tab. 7.5, separately for **SVN** 35 and 36. The well-known systematic bias of about several centimeters (e.g., *Urschl et al.*, 2008) between the optic technique **SLR** and the microwave technique **GPS** can also be seen in the reprocessed orbits. As the sign of this bias is negative, the distance measured by **SLR** is shorter than that derived from the **GPS** observations. The origin of this bias is still unknown. However, *Ziebart et al.* (2007) showed that the bias can be reduced by a factor of almost two if Earth radiation pressure and antenna thrust are taken into account in the force model. In addition, *Ziebart et al.* (2007) claim that a shim was used to mount the **LRA** to the satellite. This shim correction of +11 mm for **SVN** 35 and +13 mm for **SVN** 36 (erroneously denoted as **SVN** 39 by *Ziebart et al.*, 2007) was apparently not taken into account for the **LRA** offsets published by the **ILRS**. It reduces the absolute values of the negative biases in Tab. 7.5 and 7.6 by the corresponding values.

The station-specific mean **STDs** vary between 5 mm and 28 cm. However, the smallest and largest **STDs** occur for stations with only few observations. In general, stations with large **STDs** also show large differences between the station-specific bias and the mean bias. This indicates that the **ITRF2005** coordinates of these stations might be inaccurate. For stations with more than 500 normal points, the **STDs** range from 16 mm to 13 cm with a weighted mean value of 33.0 mm. This value is in good agreement with the weighted mean **STD** for **SVN** 35 and 36 of 33.2 mm.

Mean biases and **STDs** for **IGS**, **CODE** and reprocessed orbits are given in Tab. 7.6. When comparing the numbers in this table, it is worthwhile to mention that the **IGS** orbits are a combined product of several **ACs** which is assumed to be more accurate, whereas the **CODE** and the reprocessed orbits were generated by a single **AC**. As the residual time series of all orbits shows a general improvement at the beginning of 1998 (see Fig. 7.13), bias and **STD** for a limited time interval covering January 1998 till October 2005 are also given in Tab. 7.6. The upper part of the table considers all normal points available, whereas observations of eclipsing satellites have been excluded for the results in the lower part. *Springer* (2000) showed that the residuals during the eclipse phase itself and the time period until the reestablishment of the nominal

²http://ilrs.gsfc.nasa.gov/satellite_missions/priorities/

³http://itrf.ensg.ign.fr/ITRF_solutions/2005/ITRF2005_SLR.php

⁴http://ilrs.gsfc.nasa.gov/satellite_missions/center_of_mass/

CDP No.	Domes No.	Station	SVN 35			SVN 36		
			# NPs	Mean [mm]	STD [mm]	# NPs	Mean [mm]	STD [mm]
1863	12340S001	Maidanak	–	–	–	3	–117.6	16.5
7335	21701M002	Kashima	4	–25.4	7.1	–	–	–
7811	12205S001	Borowiec	5	–75.1	32.4	–	–	–
1873	12337S003	Simeiz	–	–	–	6	118.5	88.9
7231	21602S004	Wuhan	10	–25.7	19.5	5	–52.7	54.1
7920	40451M117	Greenbelt	–	–	–	18	34.5	110.0
7109	40433M002	Quincy	29	–55.6	12.6	11	–52.3	5.1
7501	30302M003	Hartebeesthoek	10	–22.7	8.4	31	–31.3	11.5
1868	12341S001	Komsomolsk	8	34.6	275.2	40	–119.1	156.9
1893	12337S006	Katsively	50	–97.7	53.1	10	–142.4	67.6
7838	21726S001	Simosato	27	–40.6	29.2	35	–64.1	51.1
7237	21611S001	Changchun	58	–31.8	23.0	8	–60.1	55.9
7841	14106S011	Potsdam	31	–29.5	8.8	42	–45.2	12.7
7339	21740M001	Tateyama	39	–35.5	15.8	38	–50.5	21.8
7308	21704S002	Tokyo	114	–61.6	11.7	–	–	–
7836	14106S009	Potsdam	119	–45.8	17.9	6	60.5	160.1
7835	10002S001	Grasse	78	–54.3	17.5	61	–58.8	16.8
7820	21609S002	Kunming	68	–50.7	24.1	164	–53.8	106.8
7918	40451M120	Greenbelt	111	–72.1	71.9	156	–74.9	28.4
7941	12734S008	Matera (MLRO)	145	–37.7	10.0	161	–31.5	30.0
7849	50119S001	Mount Stromlo	233	–41.4	14.0	297	–26.5	24.8
7884	40429S001	Albuquerque	414	–72.0	23.1	182	–79.9	25.7
7105	40451M105	Greenbelt	331	–58.1	28.5	346	–57.8	44.0
1884	12302S002	Riga	548	–43.6	56.4	191	–12.3	74.5
7825	50119S003	Mount Stromlo	494	–26.1	24.3	353	–34.0	30.0
1864	12340S002	Maidanak	605	–146.5	127.5	250	–59.0	80.8
7843	50103S007	Orroral	972	–35.7	45.4	829	–53.3	57.3
7810	14001S007	Zimmerwald	1023	–36.0	15.7	824	–42.5	23.3
7080	40442M006	McDonald	1495	–70.6	40.5	1485	–74.7	36.0
7845	10002S002	Grasse (LLR)	2251	–48.5	17.8	2003	–54.4	26.5
7840 ^c	13212S001	Herstmonceux	2645	–41.6	17.6	2342	–52.2	25.2
8834	14201S018	Wettzell (WLRS)	3121	–21.7	41.9	1930	–38.2	47.3
7110	40497M001	Monument Peak	2940	–57.9	28.2	2559	–74.5	41.7
7832	20101S001	Riyadh	3045	–37.0	20.2	2906	–39.1	22.9
7839 ^b	11001S002	Graz	3280	–41.7	16.0	3259	–44.0	21.2
7210 ^a	40445M001	Haleakala	4229	–46.0	48.0	3121	–56.3	55.8
7090	50107M001	Yarragadee	7961	–50.2	28.2	6105	–61.2	35.7
Total number, weighted mean and STD			36,493	–46.8	31.0	29,777	–53.9	36.0

^a discontinuity on 20 January 1994

^b discontinuity on 19 September 1996

^c discontinuity on 19 March 2001

Tab. 7.5: Station-specific SLR range residuals for the final 3-day orbits of SVN 35 and 36 for the time span January 1994 till October 2005. The stations are sorted by the total number of NPs.

Orbits	Data	SVN 35				SVN 36			
		full		limited		full		limited	
		Bias	STD	Bias	STD	Bias	STD	Bias	STD
IGS	all	-42.5	39.2	-37.1	23.0	-36.2	40.7	-35.6	29.8
CODE	all	-51.5	41.8	-45.3	25.2	-52.3	44.4	-49.7	31.7
Reprocessing	all	-46.8	31.0	-46.1	22.3	-53.9	36.0	-53.4	29.0
IGS	non-eclipsing	-41.8	35.7	-37.0	21.8	-35.4	35.2	-34.8	26.7
CODE	non-eclipsing	-50.6	38.1	-45.1	24.0	-51.0	38.4	-49.0	29.0
Reprocessing	non-eclipsing	-46.2	27.6	-46.0	21.0	-53.1	30.9	-52.8	26.2

Tab. 7.6: Mean offset and **STD** of **SLR** range residuals in millimeters for **GPS**-derived satellite orbits of **SVN 35** and **36** determined by the **IGS**, **CODE** and the reprocessing. The values for two different time intervals are given: *full* stands for the time interval from January 1994 till October 2005, *limited* for the time interval from January 1998 till October 2005.

attitude (see Sec. 2.6.2) are significantly increased due to deviations from the nominal attitude and the comparatively big distance of more than 1 m between the rotation axis and the **LRA**, see Fig. 7.9 and Tab. 7.4. As the number of normal points during eclipses is quite small (1.8% for **SVN 35** and 2.9% for **SVN 36**), the **STDs** only decrease by a few millimeters when excluding these data. By reprocessing the **GPS** orbits, the mean **STD** for the full time interval could be reduced by about 1 cm compared to the **CODE** orbits and by 4–8 mm compared to the **IGS** orbits. The **STDs** for the reduced time interval are almost identical for the **IGS** and the reprocessed orbits, and only a few millimeters larger for the **CODE** orbits. For the **IGS** and **CODE** orbits, the biases of **SVN 35** differ by up to 6 mm between the full and the limited time interval. Due to their homogeneity, no such large differences can be seen for the biases of the reprocessed orbits. For **SVN 36**, only the biases of the **CODE** orbits computed from all normal points differ by more than one millimeter between the full and the limited time interval.

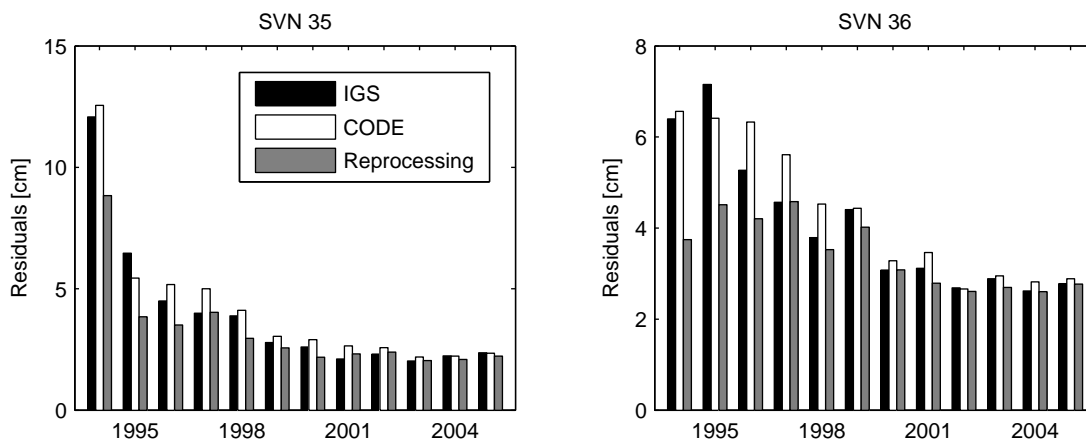


Fig. 7.12: Yearly mean **SLR** range residuals for **IGS**, **CODE** and reprocessed orbits of **SVN 35** and **36**. Note the different scales of the *y*-axes.

To get a more detailed impression of the improvement of the **STD** with time, Fig. 7.12 shows yearly mean standard deviations for **SVN 35** and **36**. In 1994 and 1995, the mean **STD** of the reprocessed orbits is 30–40% smaller than the **STD** of the **IGS** and **CODE** orbits. The increased **STD** values of **SVN 35** in 1994 (compared to **SVN 36**, see Fig. 7.12) can be explained by particularly large residuals of up to 50 cm at the beginning of 1994 (before the launch of **SVN 36** in March 1994, see Fig. 7.13). In the following years, the **STD** differences get smaller, in particular between the **IGS** orbits and the reprocessed orbits. Starting with 2002, the **STD** of all three orbit solutions is almost on the same level. These results indicate that a significant improvement of the orbit quality can be achieved by a complete reprocessing of the data from 1994 till 1997. On the other hand, the orbit quality – as evaluated by **SLR** – can only be slightly improved after 2000. However, one has to be aware that the laser residuals do not only reflect the **GPS** orbit accuracy but also errors in the laser ranging technology. Therefore, the improvements described above during the early years might be too pessimistic as the **SLR** technology has also been improved during the time period considered.

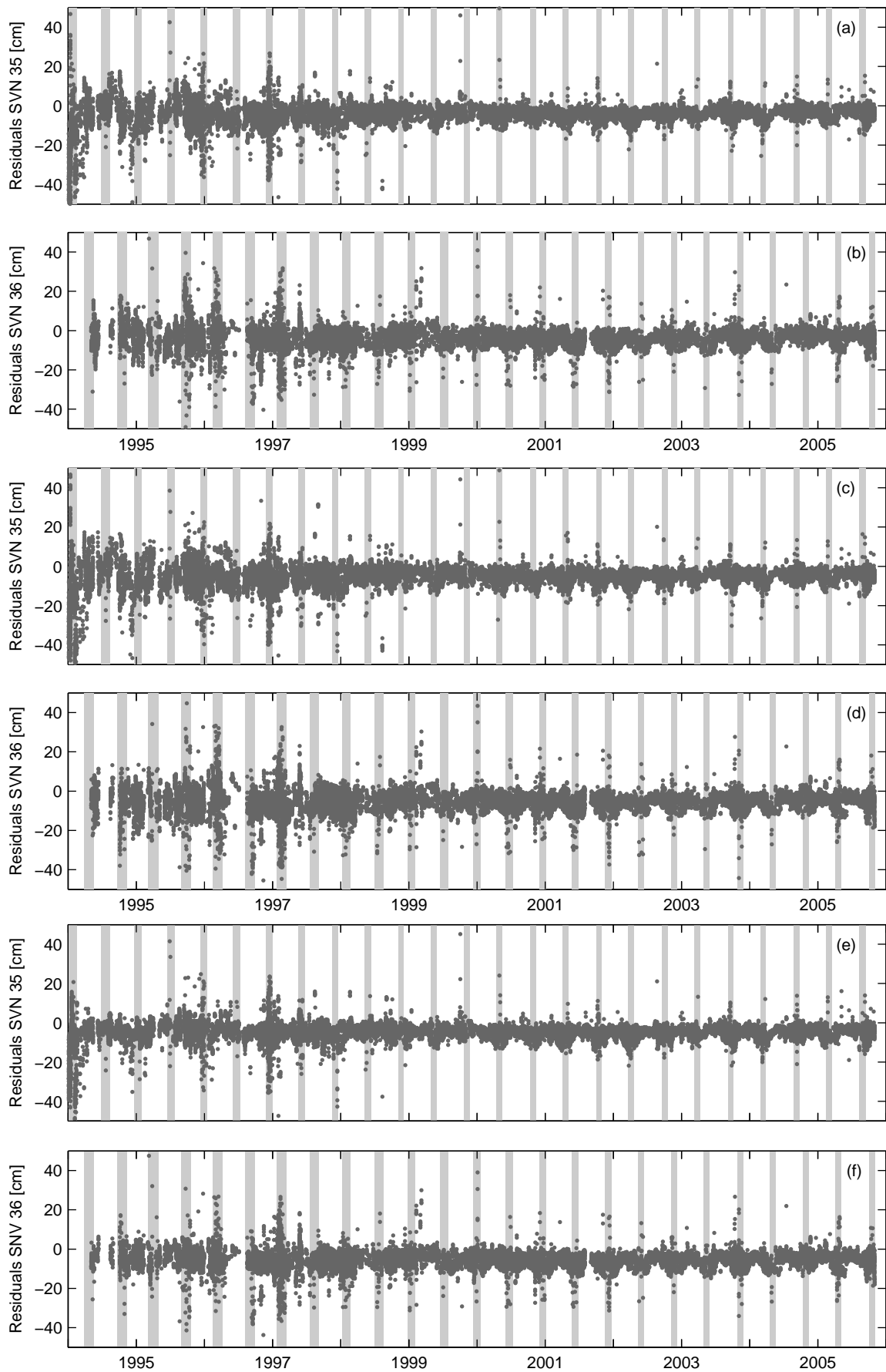


Fig. 7.13: SLR residual time series for SVN 35 and 36: (a,b) IGS, (c,d) CODE and (e,f) reprocessed orbits. Eclipse periods are shaded.

Due to the large scatter of the IGS orbit residuals in the first years (see Fig. 7.13), only the limited time interval (1998–2005) will be considered for the comparison of the biases. Whereas the biases of the CODE and the reprocessed orbits do not significantly differ, the bias of the IGS orbits is smaller by about 1.5 cm. This effect can be explained by the different orbit scales of the IGS ACs differing by up to ± 0.5 ppb from the combined IGS orbit scale (*Gendt and Kouba, 2008*). A clear systematic pattern in the vicinity of the eclipse periods can be seen in the time series of the laser residuals plotted in Fig. 7.13. To some extent, this effect can be explained by deficiencies of the ROCK a priori RPR model (*Fliegel et al., 1992*) that have already been described by *Urschl et al. (2008)*: the residuals show a clear dependence on the position of the satellite within the orbital plane. This effect can be reduced by applying a more sophisticated a priori RPR model (*Urschl et al., 2007*). This indicates that the systematic pattern in the SLR range residuals is most likely caused by deficiencies of the dynamic orbit modeling of the GPS satellites and emphasizes the importance of an independent validation of the orbits determined from GPS observations.

8. Earth Orientation Parameters

Besides variations with annual and Chandler period, variations in Earth's rotation are primarily caused by tidal effects and mass redistributions within the system Earth (e.g., [Lambeck, 1988](#)). A major part of the latter can be expressed as angular momentum of the oceans and the atmosphere. Assuming that the angular momentum of the solid Earth and the oceans is conserved (i.e., neglecting external torques and exchange of angular momentum with, e.g., the atmosphere), changes in the ocean tidal angular momentum induce changes in the angular momentum of the solid Earth. These changes cause variations in the rotation of the solid Earth, e.g., observable by space geodetic techniques as [LOD](#). Due to the irregular distribution of the oceans, the oceans can also influence the non-axial components of the Earth's rotation, i.e., polar motion ([Gross, 1993](#)). The Effective Angular Momentum Functions ([EAMFs](#)) χ_1 and χ_2 for polar motion and χ_3 for [LOD](#) are given by (e.g., [Gross et al., 2003, 2004](#))

$$\chi_1 = \frac{1.61}{\Omega_e (C - A)} \left[\Delta h_1 + \frac{\Omega_e \Delta I_{13}}{1.44} \right] \quad (8.1a)$$

$$\chi_2 = \frac{1.61}{\Omega_e (C - A)} \left[\Delta h_2 + \frac{\Omega_e \Delta I_{23}}{1.44} \right] \quad (8.1b)$$

$$\chi_3 = \frac{1}{\Omega_e C_m} [\Delta h_3 + 0.756 \cdot \Omega_e \Delta I_{33}] \quad (8.1c)$$

with

Ω_e	mean angular velocity of the Earth
A	equatorial moment of inertia of the entire Earth
C	polar moment of inertia of the entire Earth
C_m	polar moment of inertia of the Earth's crust and mantle
$\Delta h_1, \Delta h_2, \Delta h_3$	relative angular momentum changes
$\Delta I_{13}, \Delta I_{23}, \Delta I_{33}$	changes in the indicated elements of the Earth's inertia tensor.

The relative angular momentum changes are caused by motions in the atmosphere and the oceans (e.g., ocean currents), the changes in the Earth's inertia tensor by, e.g., the ocean tidal sea level height changes. The [EAMFs](#) are related to polar motion and [LOD](#) by

$$\chi_1 = x_p + \frac{\dot{y}_p}{\sigma_0} \quad (8.2a)$$

$$\chi_2 = -y_p + \frac{\dot{x}_p}{\sigma_0} \quad (8.2b)$$

$$\chi_3 = \text{LOD} \cdot \frac{1}{86400 \text{ s}} \quad (8.2c)$$

with

$$\sigma_0 = \frac{C - A}{A} \Omega_e \left(1 - \frac{k}{k_s} \right) \quad (8.3)$$

and

k	Love number
k_s	secular Love number, see Dickman (2003) .

In this chapter, the [ERPs](#) with daily resolution are compared with other [ERP](#) series and validated with geophysical angular momentum series. The subdaily [ERPs](#) are analyzed in the spectral domain and by estimating the ocean tidal amplitudes. Subdaily [ERPs](#) determined by [VLBI](#) allow for an independent

validation and a combination with the GPS estimates. Finally, the GPS-derived nutation rates provide the input for the estimation of a nutation model limited to short-period variations.

8.1. Earth Rotation Parameters with Daily Resolution

The ERPs of the 3-day and the weekly solutions with 24-hour parameter spacing will be compared with other ERP series determined from GPS, SLR and VLBI observations as well as combined series. Similar comparisons with operational series have been performed by, e.g., *Mireault and Kouba (1999)* and *Vennebusch et al. (2007)*. Geophysical angular momentum series provide an independent validation of polar motion (e.g., *Gross et al., 2003; Kouba, 2005b*) and LOD (e.g., *Gross et al., 2004; Kouba and Vondrak, 2005*) determined by space geodetic techniques.

8.1.1. Comparisons with Other Series

Polar Motion Tab. 8.1 lists polar motion differences between the reprocessed weekly solutions and ERP series provided by the IAG services (IGS, ILRS, IVS) as well as selected individual ACs. Offset, drift and RMS have been estimated in a weighted least squares adjustment. All series were provided by the IERS EOP Product Center¹ except for the IGS series², the IVS series³ and SPACE2006⁴. Whereas the SLR and VLBI solutions are completely reprocessed, the GPS solutions are based on operational analysis. At the beginning, the IGS series contains ERPs from weekly combinations on the result level applying the weights of the orbit combination. These values have been aligned to ITRF2000. Starting with 27 February 2000, the ERPs of the weekly SINEX combination are given. The original IERS C04 series is a non-rigorous combination of ERP time series determined by the space geodetic techniques Doppler Orbitography and Radiopositioning Integrated by Satellite (DORIS), GPS, SLR and VLBI (*Gambis, 2004*). As this solution has several deficiencies, a new solution called C04 05 was generated based on the ITRF2005 ERPs (*Bizouard and Gambis, 2007*). Time periods before and after the time interval covered by ITRF2005 were aligned to this reference frame. The combined SPACE2006 series (*Gross, 2007*) in addition includes Lunar Laser Ranging (LLR) observations and is composed of other ERP input time series. Tab. 8.1a covers the full time interval of the reprocessing, Tab. 8.1b only starts in December 2001, when the IGS switched to ITRF2000 to account for reference frame effects and improvements in the processing strategy of the ACs. Epochs of series given at midnight (C04, C04 05, IAA) have been linearly interpolated to noon.

Fig. 8.1 demonstrates the impact of different reference frames on the polar motion time series. The CODE solution extracted from the operational weekly solutions is shown in Figs. 8.1a and 8.1b. Discontinuities of up to 1.8 mas appear when the TRF was changed. The discontinuities at the beginning are not visible in Figs. 8.1c and 8.1d showing the comparison with the current CODE ERP time series. This series is splitted in two parts: before December 2001 the series was reprocessed on the normal equation level applying ITRF97 for datum definition, starting with December 2001 the operational weekly solutions applying ITRF2000 are given. As the processing strategies of the CODE AC and the reprocessing are quite similar, the differences still present in the early years of Figs. 8.1c and 8.1d can be primarily attributed to the benefits of the reprocessed series (homogeneity and improved modeling for the whole time period), to some smaller extent to the differences between ITRF97 and ITRF2000.

The comparison of the reprocessed y-pole series with the original C04 series in Fig. 8.2b shows the well known offset (*Altamimi et al., 2005a*) of about 140 μas for the full time interval and even 300 μas for the limited time interval, see Tab. 8.1a and 8.1b. This effect is attributed to inconsistencies between C04 and the ITRF. This offset as well as the y-pole drift gets significantly smaller for the C04 05 series. The residual RMS of the C04 polar motion series is only slightly above its internal precision of 100 μas given by *Gambis (2004)*. The scatter in the differences of the reprocessed series and C04 05 decreases dramatically in February 2000 when GPS-derived ERPs are included for the generation of the ITRF2005 ERP series demonstrating the importance of the highly accurate GPS observations for this series. This fact is also reflected in the SPACE2006 series: it has a smaller residual RMS (25% for x-pole, 17% for y-pole) compared to the C04 series for the full time interval. The better agreement of SPACE2006 with the reprocessed series in the early

¹<http://hpiers.obspm.fr/eop-pc/>

²<ftp://cddis.gsfc.nasa.gov/gps/products/igs00p02.erp.Z>

³<http://vlbi.geod.uni-bonn.de/IVS-AC/>

⁴<ftp://euler.jpl.nasa.gov/keof/combinations/2006/>

Series	Type	Epochs	X-Pole			Y-Pole		
			Offset [μ as]	Drift [μ as/y]	RMS [μ as]	Offset [μ as]	Drift [μ as/y]	RMS [μ as]
C04	combined	4328	35	-1	109	-135	-41	102
C04 05	combined	4328	-12	-12	107	41	-12	104
SPACE2006	combined	4328	-2	-15	80	49	-13	87
IGS	GPS combined	3411	-10	-12	67	-4	-20	79
CODE	GPS	4328	57	-22	126	-23	-3	114
ILRS	SLR combined	1889	-97	7	240	-59	-10	236
IAA	SLR	4328	-6	12	190	-56	-33	187
IVS	VLBI combined	1549	-24	-11	137	25	-4	126
GSFC	VLBI	1643	-50	5	140	-147	-22	139

(a) Full time interval: 26 December 1993 till 30 October 2005 (GPS week 729 – 1332).

Series	Type	Epochs	X-Pole			Y-Pole		
			Offset [μ as]	Drift [μ as/y]	RMS [μ as]	Offset [μ as]	Drift [μ as/y]	RMS [μ as]
C04	combined	1430	36	27	59	-297	-25	55
C04 05	combined	1430	-62	-7	46	1	-7	47
SPACE2006	combined	1430	-64	-6	34	-3	-2	34
IGS	GPS combined	1430	-38	1	37	-48	0	34
CODE	GPS	1430	-35	-8	41	-28	4	43
ILRS	SLR combined	1430	-96	12	254	-68	-8	250
IAA	SLR	1430	51	1	179	-193	-3	173
IVS	VLBI combined	513	-74	-4	96	6	-13	92
GSFC	VLBI	572	-39	-5	105	-213	-23	81

(b) Limited interval: 2 December 2001 (switch to ITRF2000 within the IGS) till 30 October 2005 (GPS week 1143 – 1332).

Tab. 8.1: Comparison of polar motion from the reprocessed weekly solution with inter-technique and intra-technique combined series as well as individual GPS, SLR and VLBI AC solutions. The solutions of the official services and the ACs with the longest time series are given. The offsets refer to the middle of the time interval considered for comparison.

years is probably attributed to the inclusion of the JPL GPS series before the start of the IGS series. On the other hand, the residual RMS for the limited time interval is smaller by about 25% compared to the C04 series. The offsets and drifts of SPACE2006 are comparable to C04 05 for both, the full and the limited time interval. It is obvious from Figs. 8.2a to 8.2d as well as from the numbers given in Tab. 8.1a and 8.1b that SPACE2006 shows a better agreement in general with the reprocessed series than C04 05. However, the y-pole comparison of SPACE2006 plotted in Fig. 8.2d still shows a discontinuity in June 1996 when IGS changed the reference frame from ITRF93 to ITRF94, although different offsets for the input series have been estimated within the generation of SPACE2006.

As to be expected, the differences compared to the GPS series (IGS and CODE) are the smallest of all comparisons. The IGS series performs best as it was aligned to ITRF2000 and data with the largest differences (before mid of 1996) is missing in this series. At the change from ITRF97 to ITRF2000 in December 2001, no abrupt change in the differences to the IGS series can be seen due to the reference frame alignment, see Figs. 8.2c and 8.2d. On the other hand, the differences to the CODE series shown in Figs. 8.1c and 8.1d get significantly smaller at that date, as ITRF97 was used before (see above). The large RMS improvement in the recent years can also be seen in Tab. 8.1: the IGS RMS is smaller by almost 50%, whereas the CODE RMS even improves by a factor of about three when comparing Tab. 8.1a with Tab. 8.1b. A level of 26 μ as for the IGS and 41 μ as for the CODE series is reached in the most recent year. The larger discrepancies in the early years reflect the increased noise of all GPS solutions due to a smaller number of stations on the one hand and the benefits of the reprocessing on the other hand. The outlier of about 700 μ as in the x-pole of the IGS series is related to a processing problem. This particular week has been replaced in the IGS ERP series that is aligned to ITRF2005 (igs00p03.erp). However, the igs00p02.erp series has been used here due to the reference frame consistency with the reprocessed weekly solutions.

The residual **RMS** of the **SLR** solutions compared to the combined and **GPS**-only solutions is worse by a factor of almost two for the full time interval and even a factor of up to seven for the limited time interval. As the **ILRS** series only starts in August 2000, the **IAA SLR** solution is shown in Figs. 8.2g and 8.2h. The quite large drift in the *y*-pole of $-33 \mu\text{as}/\text{y}$ (indicating differences in the **GPS** and **SLR** velocity fields) is even evident in Fig. 8.2h. The scatter of the polar motion differences is quite homogeneous for the whole time period. Therefore, **SLR** is the only technique, where the **RMS** does not significantly decrease when the time interval of the comparison is limited (for the **ILRS** series the **RMS** is even slightly larger for the limited time interval). This indicates that the **SLR ERP** accuracy is clearly worse than the accuracy of **GPS**, as the improvements of the latter in the recent years do not result in a decreased scatter of the **GPS/SLR ERP** differences. The **SLR ERP** accuracy of $250 \mu\text{as}$ given by *Pavlis (2005)* is in good agreement with the **RMS** values of the **GPS/SLR** differences given in Tab. 8.1. In addition, the **RMS** of the **IAA** individual **AC** solution is smaller than the **RMS** of the combined **ILRS** solution. Neither **GPS** (**CODE** and **IGS**) nor **VLBI** (**GSFC** and **IVS**) solutions show such a strange behavior.

For both **VLBI** solutions, outliers exceeding the threefold mean formal error have been excluded in an iterative procedure. These outliers of up to 15 mas for the **GSFC** solution and 4 mas for the **IVS** combined solution are usually related to weak sessions (in particular regional sessions) that do not allow for a reliable estimation of **ERPs**. The **RMS** values of the **VLBI** solutions are a factor of about 2–3 worse compared to the **GPS** solutions but still a factor of about two better than **SLR**. Although not clearly visible in Figs. 8.2i and 8.2j, the **RMS** of the limited compared to the full time interval is smaller by about one third for the **IVS** series. For the **GSFC** series, the **RMS** reduction is more pronounced for the *y*-pole (42%) than for the *x*-pole (25%). According to *Schlüter and Behrend (2007)*, the accuracy of the *y*-pole estimates was worse by a factor of two compared to the *x*-pole estimates in 2002, whereas the accuracy of both pole components is on the same level at the present time.

Length of Day As **GPS** is not able to determine **UT1** in an absolute sense, **LOD** comparisons are given in Tab. 8.2. Combined **IGS LOD** values are only available starting with 23 February 1997. Therefore, the number of epochs differs from the **IGS** polar motion comparison in Tab. 8.1a. The comparisons with the combined series are quite homogeneous, the residual **RMS** of the full time interval does not differ significantly from the **RMS** of the limited time interval. Therefore, only the C04 05 series is shown in Fig. 8.3a. On the other hand, large differences are visible in the comparison with **CODE** in the early years, see Fig. 8.3b. The clear improvement at the end of 1996 in Fig. 8.3b is attributed to changed constraints on the **RPR**

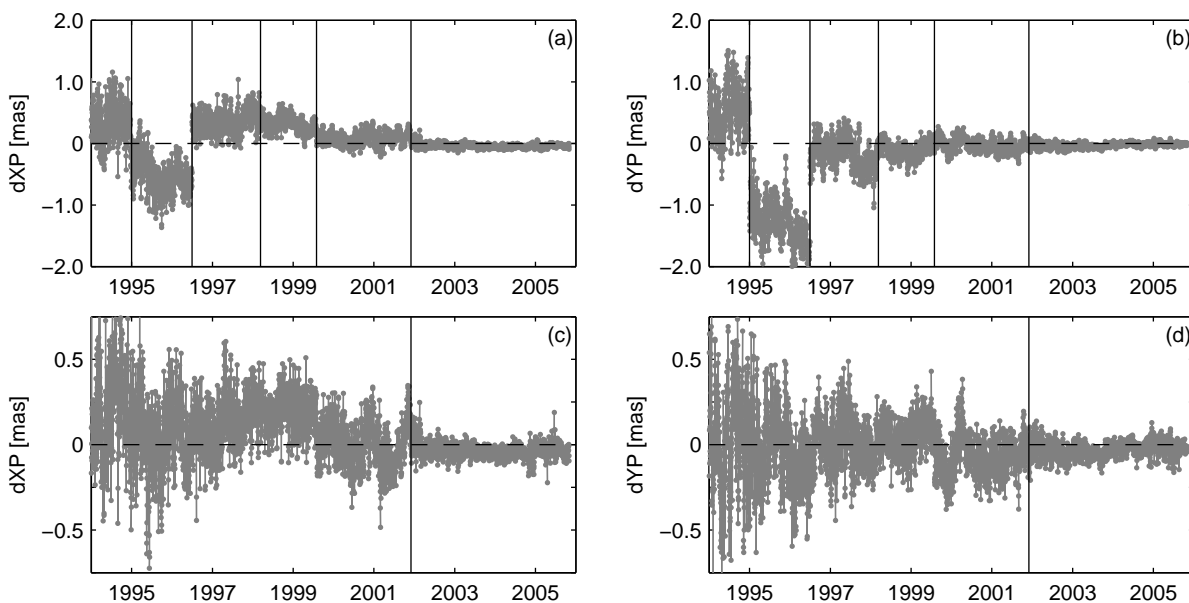


Fig. 8.1: Polar motion differences to **CODE**: (a,b) operational weekly solutions, reference frame changes are indicated by vertical lines; (c,d) partly reprocessed series, the transition from the reprocessed part based on **ITRF97** to the operational part based on **ITRF2000** is indicated by a vertical line. Note the different scale of the *y*-axis.

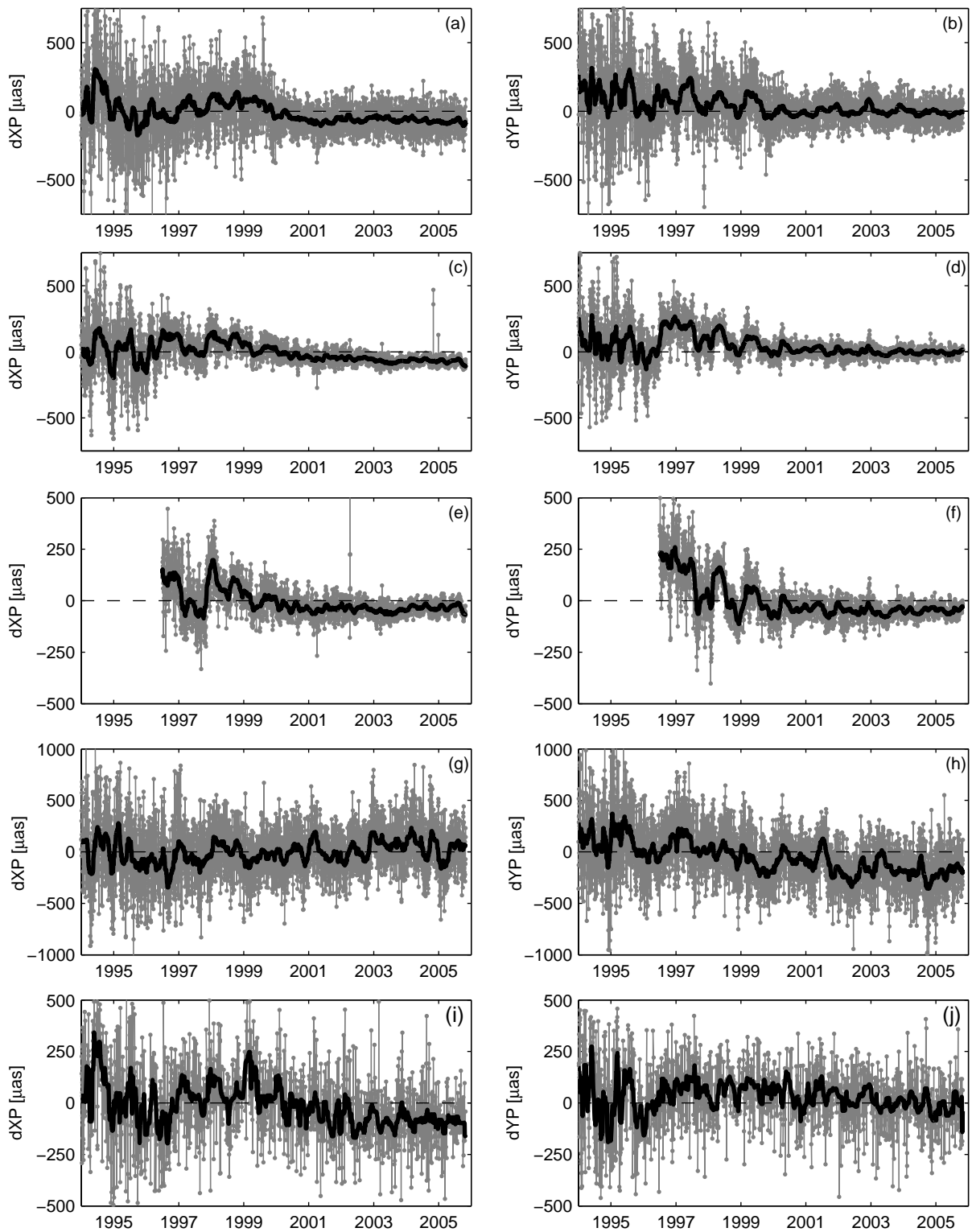


Fig. 8.2: Polar motion differences of the reprocessed weekly solution w.r.t. (a,b) **IERS C04 05** combined inter-technique solution; (c,d) **SPACE2006** combined inter-technique solution; (e,f) **IGS** combined **GPS** solution; (g,h) **IAA SLR AC** solution; (i,j) **IVS** combined **VLBI** solution. Note the different scale of the y -axis. The solid line represents a 50-day median.

Series	Type	Epochs	Offset [$\mu\text{s}/\text{d}$]	RMS [$\mu\text{s}/\text{d}$]	Epochs	Offset [$\mu\text{s}/\text{d}$]	RMS [$\mu\text{s}/\text{d}$]
C04	combined	4328	-13	25	1430	-10	26
C04 05	combined	4328	-14	16	1430	-11	15
SPACE2006	combined	4328	-13	19	1430	-11	19
IGS	GPS combined	3192	-12	17	1430	-11	16
CODE	GPS	4328	-4	17	1430	1	9
ILRS	SLR combined	1889	-8	64	1430	-6	66
IAA	SLR	4328	-12	21	1430	-7	21
IVS	VLBI combined	1461	-15	19	523	-12	18
DGFI	VLBI	1474	-11	21	520	-8	19

Tab. 8.2: Comparison of LOD for the full time interval 26 December 1993 till 30 October 2005 (left) and the time interval 2 December 2001 till 30 October 2005 (right). The offsets are given at the middle of the time interval considered for comparison.

parameters and another improvement at the beginning of 2001 is due to the setup of pseudo-stochastic pulses at the day boundaries, see Tab. 1.2.

For some time periods in Figs. 8.3a and 8.3b, a pronounced semi-annual signal can be seen in the median time series. In the CODE series an annual signal can be seen at the beginning. As this signal disappears after changes in the orbit modeling and the amplitude of the semi-annual signal at least gets smaller, it is reasonable to assume that the origin of these signals is related to differences in the orbit modeling. A spectral analysis of the LOD difference time series reveals significant peaks at $T_R/6$ and $T_R/12$ that are related to the orientation of the orbital planes w.r.t. the Sun, see Sec. 4.3.2. These periods are also present in the spectrum of the LOD formal errors, see Fig. 4.17. A peak at 14.2 days is only present in the IGS comparison. *Gendt and Kouba (2008)* reported a peak at this particular period in the comparison of the CODE and SIO LOD series with the combined IGS series. They concluded that this peak is probably introduced by differences in the O_1 term of the subdaily ERP model (14.2 days are the beat period of the O_1 period and 24 hours).

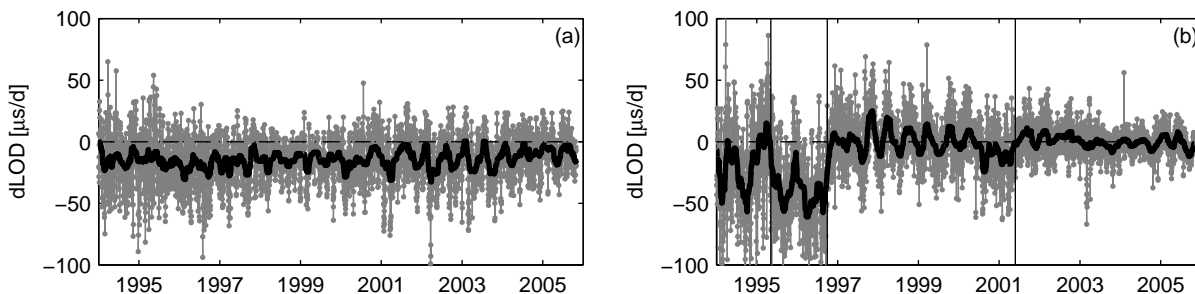


Fig. 8.3: LOD differences of the reprocessed weekly solution w.r.t. (a) IERS C04 05 combined inter-technique solution; (b) CODE GPS solution. The most important changes in the CODE orbit modeling according to Tab. 1.2 are indicated by vertical lines. The solid line represents a 50-day median.

All series show a negative offset for the full time interval. For the limited time interval, this offset gets smaller but still exceeds $-10 \mu\text{s}/\text{d}$ for the IGS and the combined series. However, this bias is well within the range of LOD biases of the IGS ACs compared to the combined IGS series. As there is almost no bias w.r.t. the CODE series, this effect seems to be related to modeling differences between series computed with the Bernese GPS Software and series generated with other software packages. As LOD is related to the change of the right ascension of the ascending node (see Eq. 2.65), a systematic effect related to the coefficient C_{20} of the gravity field used for orbit integration could introduce such an effect, e.g. the handling of the permanent tide. However, a thorough inspection of the source code could not identify any coding errors in the software.

Like for polar motion, the residual RMS of ILRS series is worse than that of the IAA AC solution but for LOD even by a factor of three. However, the GPS/SLR residual RMS values are in good agreement with the SLR LOD accuracy of $62 \mu\text{s}/\text{d}$ given by *Pavlis (2005)*. As LOD is not included in the GSFC ERP series,

the **DGFI** series has been used as an example for an individual **VLBI AC** solution. Both, the **DGFI** as well as the combined **IVS** solution, show **RMS** values that are on the level of the **IAA SLR** solution.

8.1.2. Comparisons with Angular Momentum Time Series

Non-tidal changes in the Earth's rotation are primarily driven by interactions of the atmosphere and the ocean with the Earth. These interactions are expressed as angular momenta, namely the Atmospheric Angular Momentum (**AAM**) and the Oceanic Angular Momentum (**OAM**). The biggest part of the non-tidal variations of the Earth's rotation is attributed to changes in the zonal winds caused by seasonal changes in the land-ocean temperature difference and in the pole-to-equator temperature gradient. Comparisons and analysis of geodetic **EAMFs** (computed from **ERPs** estimated from space geodetic observations) with geophysical **EAMFs** (computed from numerical weather and ocean models) have been performed by numerous authors, e.g., *Ponte and Ali* (2002); *Kouba and Vondrak* (2005); *Kouba* (2005b); *Ray et al.* (2005). However, the comparisons with angular momentum time series will only be used as a validation tool for the reprocessed **ERP** series in this section. Further analyses and a geophysical interpretation are beyond the scope of this thesis.

AAM series computed from the National Centers for Environmental Prediction (**NCEP**) reanalysis data with a resolution of six hours are provided by the **IERS** Special Bureau for the Atmosphere⁵ (*Salstein et al.*, 1993). The **AAM** series assuming an inverted barometer effect of the oceans w.r.t. the surface pressure variations was used here to be consistent with the **OAM** series. **OAM** series derived from the **ECCO**⁶ ocean model with a resolution of six hours are provided by the **IERS** Special Bureau for the Oceans⁷ (*Gross et al.*, 2005). For a comparison with geodetic excitation functions computed from **ERPs** estimated with 24 hours resolution, these 6-hourly geophysical **EAMFs** have to be smoothed to daily values. As the polar motion estimates of the **IGS ACs** refer to 12:00 **UT**, this epoch was used for the comparisons with the geophysical **EAMFs**. The algorithm proposed by *Kouba and Vondrak* (2005) was applied to get the smoothed geophysical **EAMFs** χ_{SMT} at 12:00 **UT**:

$$\chi_{SMT} = \frac{1}{4} \left(\frac{1}{2} \chi_{0:00 \text{ UT}} + \chi_{6:00 \text{ UT}} + \chi_{12:00 \text{ UT}} + \chi_{18:00 \text{ UT}} + \frac{1}{2} \chi_{24:00 \text{ UT}} \right). \quad (8.4)$$

Polar Motion

The polar motion and polar motion rate estimates can be converted to excitation functions with Eqs. 8.2a and 8.2b. Tab. 8.3 lists correlation coefficients between polar motion excitation functions computed from space geodetic **ERP** time series and excitation functions based on geophysical models. The upper part considers only **ERP** time series covering the time period January 1994 till October 2005, namely the reprocessed series, the operational **CODE** series and the multi-technique combined **SPACE2006** series. The **C04** series has been excluded as no polar motion rates are given. Except for $\chi_{1,OAM}$, the correlations of the reprocessed **ERP** time series are larger compared to the operational **CODE** series. On the other hand, the **SPACE2006** series shows in general higher correlations than the reprocessed series demonstrating the benefits of a multi-technique combination.

The correlation coefficients in the lower part of Tab. 8.3 were computed from a limited time interval starting with 1 January 1999 (polar motion rates are available for all **ERP** series starting with that date). In addition to the **ERP** series already mentioned above, most **IGS ACs** as well as the combined **IGS** series are included. The correlations of the reprocessed series are in general larger compared to the other **GPS** series except for $\chi_{2,AAM}$ from **CODE** and **SIO**. As for the full time period, **SPACE2006** shows the largest correlations. For all series, the **AAM** and **AAM+OAM** correlations in χ_2 are in general larger due to the more pronounced annual signal in this component compared to χ_1 .

To study the short-term agreement of the geodetic and geophysical **EAMFs** in more detail, the mean correlation coefficients of sliding time windows of 10, 15 and 30 days are listed in Tab. 8.4. As already mentioned by *Kouba and Vondrak* (2005), the correlation of one single of those time windows is rather insignificant due to the very short data span. However, as the mean correlation coefficients in Tab. 8.4

⁵<http://www.aer.com/scienceResearch/diag/sb.html>

⁶<http://www.ecco-group.org>

⁷http://euler.jpl.nasa.gov/sbo_data.html

Sol.	Epochs	Correlation χ_1			Correlation χ_2		
		AAM	OAM	AAM+OAM	AAM	OAM	AAM + OAM
Reproc.	4321	0.57634	0.43688	0.75320	0.72738	0.34792	0.87404
CODE	4321	0.54739	0.44580	0.73520	0.72582	0.34165	0.86897
SPACE2006	4321	0.58224	0.44974	0.76626	0.74083	0.34038	0.88215
Reproc.	2495	0.60978	0.47438	0.79218	0.72629	0.35014	0.89032
CODE	2495	0.59870	0.47083	0.78081	0.72789	0.34768	0.89031
ESOC	2495	0.48151	0.38367	0.63103	0.68161	0.32881	0.83567
GFZ	2495	0.58744	0.47114	0.77174	0.71516	0.34314	0.87567
JPL	2495	0.49739	0.34541	0.62064	0.64566	0.29760	0.78319
NRCan	2495	0.43799	0.38305	0.59488	0.65086	0.30163	0.79048
SIO	2495	0.60229	0.46599	0.78079	0.73250	0.33675	0.88799
IGS	2495	0.60427	0.47035	0.78509	0.72562	0.34556	0.88690
SPACE2006	2495	0.60901	0.47744	0.79334	0.73356	0.34147	0.89184

Tab. 8.3: Correlation coefficients between geodetic and geophysical excitation functions. The upper part covers the time period 1 January 1994 till 31 October 2005. The lower part is limited to 1 January 1999 till 31 October 2005.

Sol.	Epochs	Correlation 10 d		Correlation 15 d		Correlation 30 d	
		χ_1	χ_2	χ_1	χ_2	χ_1	χ_2
Reproc.	4321	0.76309	0.81973	0.79220	0.84021	0.81747	0.86528
CODE	4321	0.75121	0.81252	0.78572	0.83520	0.81546	0.85993
SPACE2006	4321	0.77286	0.82613	0.80874	0.84622	0.83992	0.87231
Reproc.	2495	0.78059	0.84415	0.80940	0.85890	0.83504	0.87759
CODE	2495	0.76498	0.83539	0.79640	0.85246	0.82535	0.87364
ESOC	2495	0.66362	0.76405	0.69883	0.78774	0.72970	0.81441
GFZ	2495	0.73617	0.81889	0.77099	0.83769	0.80185	0.85886
JPL	2495	0.64375	0.74152	0.67936	0.76794	0.71063	0.79490
NRCan	2495	0.59461	0.73425	0.62718	0.76016	0.65645	0.78666
SIO	2495	0.75552	0.84162	0.79099	0.85731	0.82307	0.87633
IGS	2495	0.76716	0.83890	0.79870	0.85488	0.82629	0.87359
SPACE2006	2495	0.77496	0.84072	0.81058	0.85641	0.83977	0.87711

Tab. 8.4: Short-term comparison of geodetic polar motion excitation functions with AAM and OAM. Mean correlation coefficients from sliding time windows for the time period 1 January 1994 till 31 October 2005 (upper part) and 1 January 1999 till 31 October 2005 (lower part) are given.

represent the average of a huge number of individual correlation coefficients, they can be considered precise and reliable. As for Tab. 8.3, the upper part covers the full time interval of the reprocessing whereas the lower part is limited to 1 January 1999 till 31 October 2005. The correlations increase with increasing window length (as the impact of the noise compared to the signal decreases) and the χ_2 correlation coefficients are again larger compared to χ_1 . For the full time interval SPACE2006 performs best and the reprocessed series has larger correlation coefficients for all time windows compared to the operational CODE series. For the limited time interval, the reprocessed series has the largest correlation coefficients of all GPS-only series, for some single values they are even larger than those of the multi-technique combined SPACE2006 series. The ESOC, JPL and NRCan series show quite bad correlations compared to the reprocessed and the other IGS AC series. For ESOC and NRCan, increased residuals in 1999 and 2000 are responsible for the degraded performance of these ERP series whereas the JPL series in general has lower correlation coefficients for the whole time interval.

Length of Day The LOD estimates from the 3-day solution with daily resolution, reduced for the tidal part according to the IERS 2003 conventions, and the AAM and OAM series described above and converted to equivalent LOD units according to Eq. 8.1c are shown in Fig. 8.4. It is obvious that AAM is the major source of LOD variations whereas the influence of OAM is quite small, but still significant as will be shown below. The GPS-derived LOD in addition includes long-term signals caused by tidal friction, motions in

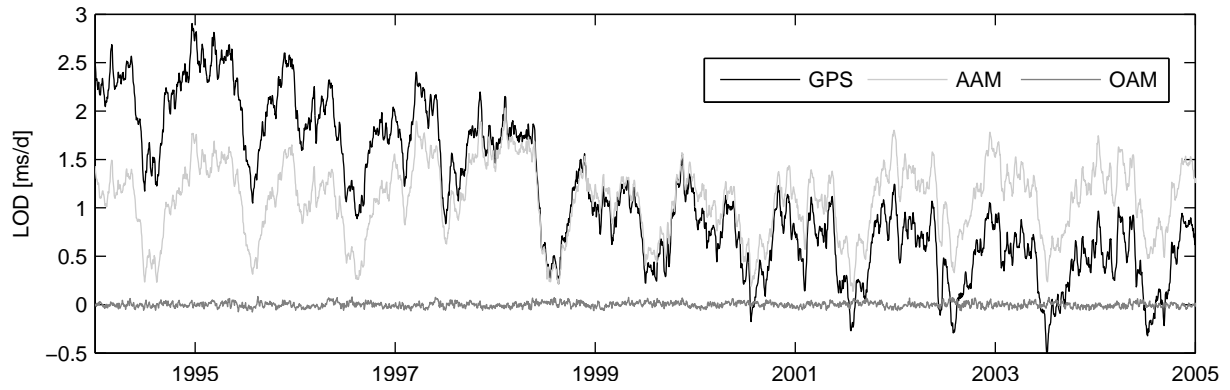


Fig. 8.4: GPS-derived LOD, z-component of the atmospheric angular momentum (sum of pressure and wind terms) and the oceanic angular momentum expressed in equivalent LOD units. A mean value of 130 ms/d has been removed from the AAM series.

the Earth's liquid core and slow climatic variations (*Torge, 2001*). For the comparisons given below, this signal was removed by fitting a polynomial of that degree that minimizes the residuals.

The upper part of Tab. 8.5 shows the correlation coefficients and the residual RMS of the geodetic LOD compared to the geophysical LOD from AAM and AAM + OAM for the time interval 1 January 1994 till 31 December 2004. Besides the reprocessed series, only the CODE, the C04 and the SPACE2006 series are available for that full time interval. Although the differences of the three series in the correlation coefficient as well as the residual RMS are small (only a few $\mu\text{s/d}$), the reprocessed solution shows the best agreement with the angular momentum series. The residual RMS can be reduced by about 10% when considering the OAM in addition to the AAM.

Sol.	Epochs	Polynomial degree	Correlation		Residual RMS	
			AAM	AAM + OAM	AAM [ms/d]	AAM + OAM [ms/d]
Reproc.	4017	7	0.98317	0.98730	0.071	0.063
C04	4017	9	0.98138	0.98553	0.074	0.066
C04 05	4017	9	0.98159	0.98580	0.074	0.066
CODE	4017	8	0.97978	0.98342	0.078	0.071
SPACE2006	4017	9	0.97913	0.98341	0.079	0.071
Reproc.	3106	7	0.98304	0.98671	0.070	0.063
C04	3106	9	0.98133	0.98501	0.073	0.066
C04 05	3106	9	0.98177	0.98540	0.072	0.065
CODE	3106	8	0.97953	0.98253	0.077	0.072
ESOC	3106	3	0.96332	0.96762	0.103	0.097
JPL	3106	3	0.96027	0.96509	0.107	0.100
NRCan	3106	3	0.96074	0.96524	0.107	0.101
SIO	3106	3	0.95433	0.95839	0.115	0.110
SPACE2006	3106	9	0.98171	0.98536	0.072	0.066

Tab. 8.5: Long-term comparisons of geodetic LOD series with AAM and OAM. The upper part covers the time interval 1 January 1994 till 31 December 2004, the lower part 30 June 1996 till 31 December 2004.

In the lower part of Tab. 8.5, the comparison interval starts on 30 June 1996. Most IGS AC ERP solutions are included in addition as they are available at the IERS EOP product center starting with that date. The GFZ series is excluded due to unreasonable LOD values before 1998 and the NOAA series is excluded as no LOD values are available before 2002. Due to its homogeneity, the reprocessed solution shows the highest correlation coefficients as well as the smallest residual RMS values for the full as well as for the limited time interval. The residual RMS of the reprocessed, the CODE and the C04 solution is smaller by one third compared to the other IGS AC solutions. This effect is probably related to a less sophisticated orbit modeling of these ACs in the early years.

Sol.	Epochs	Correlation 10 d		Correlation 15 d		Correlation 30 d	
		AAM	AAM + OAM	AAM	AAM + OAM	AAM	AAM + OAM
Reproc.	4017	0.83686	0.87828	0.87779	0.91081	0.92289	0.94505
C04	4017	0.77642	0.81170	0.83920	0.87032	0.90520	0.92675
C04 05	4017	0.80523	0.84870	0.85598	0.89154	0.91270	0.93565
CODE	4017	0.81062	0.85110	0.86041	0.89337	0.91522	0.93641
SPACE2006	4017	0.81391	0.84848	0.86323	0.89350	0.91626	0.93744
Reproc.	3106	0.83754	0.88081	0.88153	0.91471	0.92622	0.94754
C04	3106	0.76936	0.80713	0.83649	0.86818	0.90589	0.92671
C04 05	3106	0.80858	0.85537	0.86036	0.89664	0.91638	0.93851
CODE	3106	0.81633	0.85969	0.86698	0.90011	0.92072	0.94072
ESOC	3106	0.80727	0.84748	0.85781	0.88823	0.90986	0.92896
JPL	3106	0.75116	0.78938	0.80984	0.84120	0.88040	0.90197
NRCan	3106	0.78544	0.82988	0.83763	0.87264	0.89846	0.91975
SIO	3106	0.75658	0.79069	0.80948	0.83674	0.86838	0.88924
SPACE2006	3106	0.81277	0.85033	0.86462	0.89586	0.91832	0.93854

Tab. 8.6: Short-term comparison of LOD with AAM and OAM. Mean correlation coefficients from sliding time windows for the time period 1 January 1994 till 31 December 2004 (upper part) and 30 June 1996 till 31 December 2004 (lower part) are given.

The mean short-term correlation coefficients for sliding time windows of 10, 15 and 30 days are given in Tab. 8.6. For the 10-day time period, the C04 correlation coefficient is significantly worse than most of the other series. As the correlation improves for 15 days and even more for 30 days, this effect is probably the result of the smoothing applied during the generation of the C04 series (*Gambis, 2004*). It seems, that for the newer C04 05 series, a much softer smoothing has been applied.

8.2. Subdaily Earth Rotation Parameters

Subdaily changes in Earth rotation at diurnal and semidiurnal periods are mainly caused by ocean tidal effects. Smaller effects are attributed to the interaction of the atmosphere with the solid Earth. The amplitudes of the tidal-driven variations in Earth rotation can be determined from ocean tide models based on satellite altimetry (e.g., *Ray et al., 1994*). On the other hand, subdaily ERP models have been determined by various authors from observations of the space-geodetic techniques GPS (*Rothacher et al., 2001*), SLR (*Watkins and Eanes, 1994*) and VLBI (*Chao et al., 1995, 1996; Gipson, 1996; Herring and Dong, 1994*). More recently, *Petrov (2007)* determined an empirical Earth rotation model also including subdaily ERP variations from 23 years of VLBI observations.

In this section, the subdaily ERPs of the reprocessing are analyzed in the spectral domain and by estimating a subdaily ERP model. The benefits of the reprocessing are demonstrated by comparisons with the CODE operational subdaily ERP series. The accuracy of the reprocessed ERP model is evaluated by comparisons with a subdaily ERP model computed from VLBI observations as well as models determined from altimetry. Finally, the GPS subdaily residual signals (after subtracting the estimated ERP model) are analyzed.

As already mentioned in Sec. 3.2.2, subdaily Earth rotation parameters are estimated in a special 3-day solution. The time resolution of these solutions is 2 hours for x-pole, y-pole and LOD. In order to get only the subdaily part of the ERPs, long-term trends (> 1 day) were removed using Bulletin A or the ERPs of the weekly reprocessing solution. In Fig. 8.5 the subdaily part of polar motion and LOD determined by GPS and from the IERS2003 model are shown for the time period of one month. The diurnal and semidiurnal variations as well as a beat period of about 14 days originating from the superposition of different tidal frequencies are clearly visible.

To demonstrate the improvements achieved by the reprocessing, the CODE subdaily ERP time series described by *Rothacher et al. (2001)* is used for comparisons. This data set starts on 2 January 1995 and ends with 17 August 2001. The CODE solution was reprocessed based on normal equations which means that the reference frame is consistent. However, changes in the modeling, in particular in the orbit modeling, are still present. Figure 8.6 shows the formal errors of the two polar motion time series. The CODE series contains several discontinuities due to changes in the orbit modeling (size of the constraints on the pseudo-stochastic

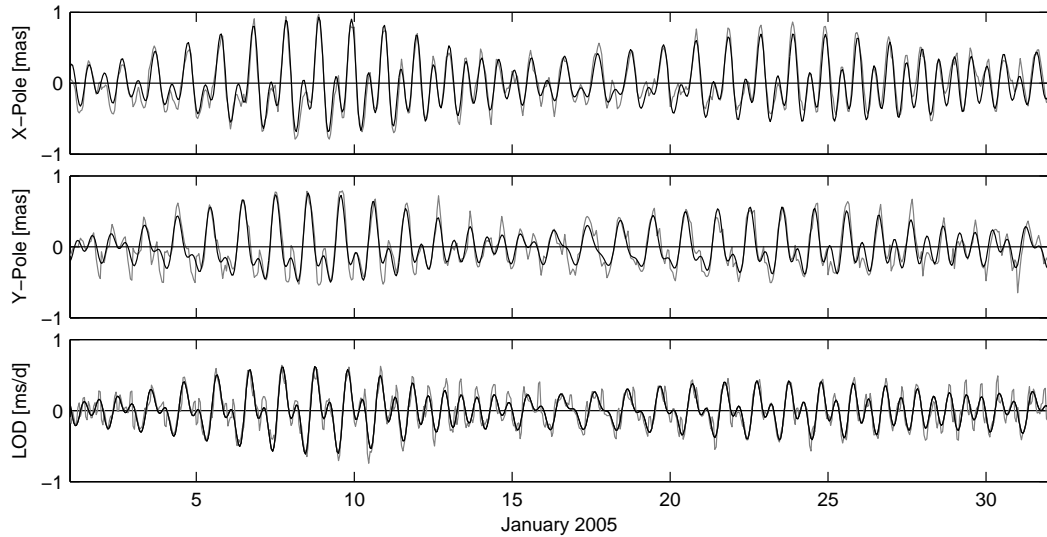


Fig. 8.5: Time series of subdaily polar motion and LOD for January 2005: IERS2003 model (black) and GPS-determined values (gray).

pulses, different number of radiation pressure parameters and constraints on these parameters, see Tab. 1.2) and in other processing parameters indicated by vertical lines. The discontinuities in the reprocessed series are caused by the activation or deactivation of AS, see Tab. 2.2. Even the deactivation of SA on 2 May 2000 can be seen in the reprocessed time series resulting in a slight improvement in the formal errors. The mean formal errors are 37 and 41 μas for the CODE, 22 and 24 μas for the reprocessed x- and y-pole series. The corresponding median of the formal errors are 34 and 38 μas for the CODE, 17 and 19 μas for the reprocessed solution (improvement by exactly a factor of two). The CODE LOD formal errors are unreasonably small at the beginning of the time series and therefore not comparable to the reprocessing results which have a mean formal error of 0.14 ms/d and a median of 0.11 ms/d.

8.2.1. Frequency Analysis

Each periodic function $y(x)$ can be described by an infinite Fourier series

$$y(x) = \frac{a_0}{2} + \sum_{i=1}^{\infty} a_i \cos ix + b_i \sin ix \quad (8.5)$$

with

a_i, b_i cosine and sine coefficients of the Fourier series.

For frequency analysis of time series of limited length, often the Fast Fourier Transform (FFT) is used to determine an also limited set of Fourier coefficients a_i and b_i . An alternative approach is the estimation of Fourier coefficients in a least squares adjustment. Due to the huge number of parameters for the long time series of the reprocessing, only periods within the time interval $[T_1, T_2]$ are estimated (e.g., diurnal or semidiurnal frequency band):

$$y(t) = \sum_{i=n}^m a_i \cos i\omega_0 t + b_i \sin i\omega_0 t \quad \text{with } \omega_0 = \frac{2\pi}{\Delta T + H} \quad \text{and} \quad H = \frac{\Delta T}{N-1} \quad (8.6)$$

n start index $n = \text{FLOOR}\left(\frac{2\pi}{\omega_0 \cdot T_2}\right)$
 m maximum order $m = \text{CEIL}\left(\frac{2\pi}{\omega_0 \cdot T_1}\right)$
 ω_0 basic frequency in radians per time unit
 ΔT length of the time series
 N number of samples.

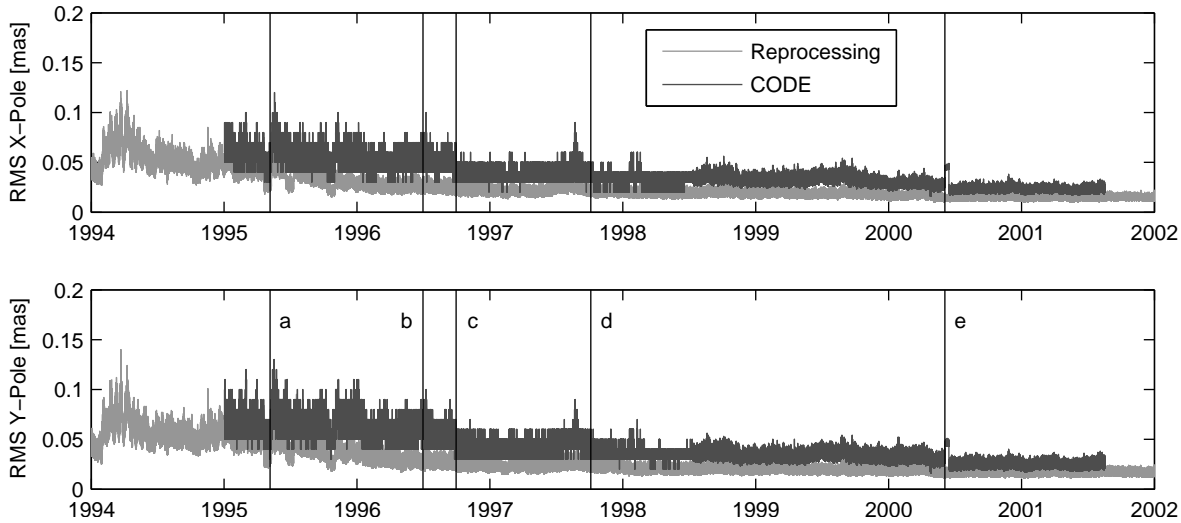


Fig. 8.6: Formal errors of GPS-derived subdaily polar motion: CODE and reprocessing. Important model changes in the CODE series are indicated by vertical lines. a: 2 instead of 6 radiation pressure parameters, no a priori subdaily ERP model instead of RAY96; b: RAY96 subdaily ERP model as a priori; c: 6 instead of 2 radiation pressure parameters; d: elevation cut-off angle lowered from 20° to 10° ; e: fewer pseudo-stochastic pulses. The formal errors of the reprocessed series after 2002 are not shown as they are quite constant.

As the amplitudes $A_i = \sqrt{a_i^2 + b_i^2}$ are determined in a least squares adjustment, the observations y_j can be weighted with their formal errors

$$\sigma_j^2 = \left(\frac{\sigma_m}{\sigma_{y_j}} \right)^2 \quad \text{with the mean formal error } \sigma_m = \frac{\sum_{j=1}^N \sigma_{y_j}}{N} . \quad (8.7)$$

If all observations are weighted with unit weight, the results are completely identical to the FFT but have the advantage that one gets formal errors of the estimated amplitudes. Based on the Fourier coefficients of polar motion (either from a FFT or the LSA FT), pro- and retrograde amplitudes can be determined

$$A_{i,retro} = \sqrt{(0.5(a_{i,xp} + b_{i,yp}))^2 + (0.5(-a_{i,yp} + b_{i,xp}))^2} \quad \text{with } \omega_{i,retro} = (-n - i) \cdot \omega_0 \quad (8.8a)$$

$$A_{i,pro} = \sqrt{(0.5(a_{i,xp} - b_{i,yp}))^2 + (0.5(a_{i,yp} + b_{i,xp}))^2} \quad \text{with } \omega_{i,pro} = (n + i) \cdot \omega_0 . \quad (8.8b)$$

Fig. 8.7 shows the amplitude spectra of diurnal and semidiurnal polar motion for the CODE and the reprocessed time series. As already mentioned in Sec. 3.1, retrograde diurnal terms of polar motion are blocked on the normal equation level. The peaks in the retrograde diurnal polar motion spectrum of the CODE time series are artifacts from the aliasing of errors in the IAU80 nutation model, which was used for this series and whose deficiencies are well known (e.g., *Herring et al., 1986, 1991*). These deficiencies show up in the retrograde diurnal polar motion spectrum due to the correlations with the nutation parameters (*Mendes Cerveira et al., 2007; Thaller et al., 2007*). For the reprocessing the IAU2000A model has been used and the artifacts in this spectrum are much smaller. However, the presence of artifacts even in the reprocessed spectrum could point to deficiencies of the IAU2000A nutation model.

In the reprocessed spectra peaks of smaller tidal constituents are visible, e.g., ν_2 in the semidiurnal retrograde polar motion spectrum. In the semidiurnal prograde polar motion spectrum one can in particular see the reduced noise of periods near 12 hours. The K_2 and S_2 peaks (whose periods are close to the GPS orbit frequency) are much sharper in the reprocessed spectrum, probably due to improvements in orbit modeling. The UT1 spectra shown in Fig. 8.8 were derived from UT1–UTC rates (= –LOD) by multiplying the amplitudes with the factor $\frac{T_i}{2\pi}$ computed from the corresponding periods T_i , see *Rothacher et al. (1999a)*. Again, periods not visible in the CODE spectrum can be seen in the reprocessed spectrum: ν_2 in the semidiurnal, σ and J_1 in the diurnal UT1 spectrum. As the amplitudes of UT1 were computed from the LOD estimates, the formal errors are proportional to the period of the estimated amplitudes.

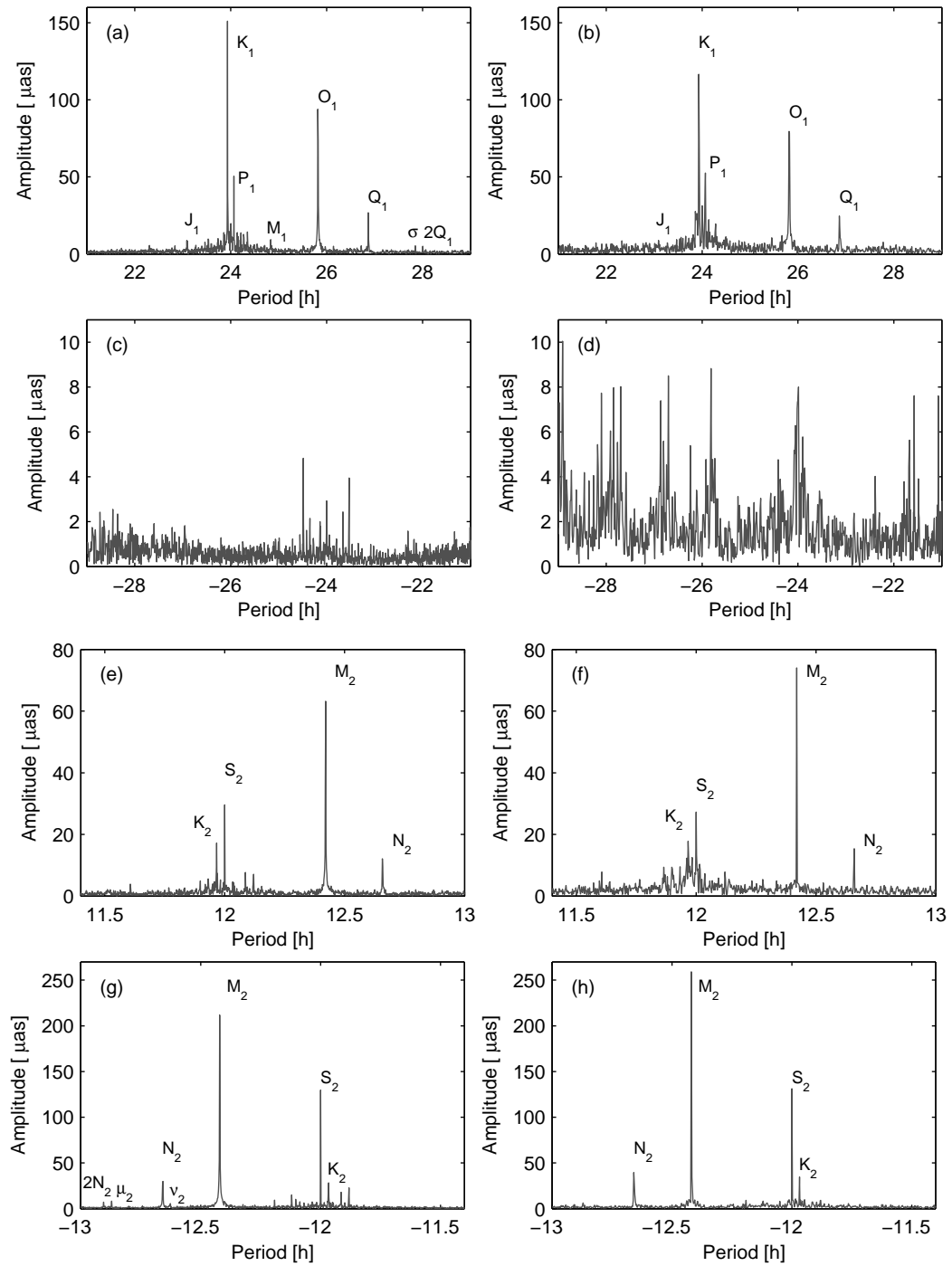


Fig. 8.7: Amplitude spectra of subdaily polar motion and corresponding mean formal amplitude errors $\sigma_{A,m}$: (a,c) diurnal, reprocessed, $\sigma_{A,m} = 1.8 \mu\text{as}$; (b,d) diurnal, CODE, $\sigma_{A,m} = 2.1 \mu\text{as}$; (e,g) semidiurnal, reprocessed, $\sigma_{A,m} = 1.7 \mu\text{as}$; (f,h) semidiurnal, CODE, $\sigma_{A,m} = 1.9 \mu\text{as}$.

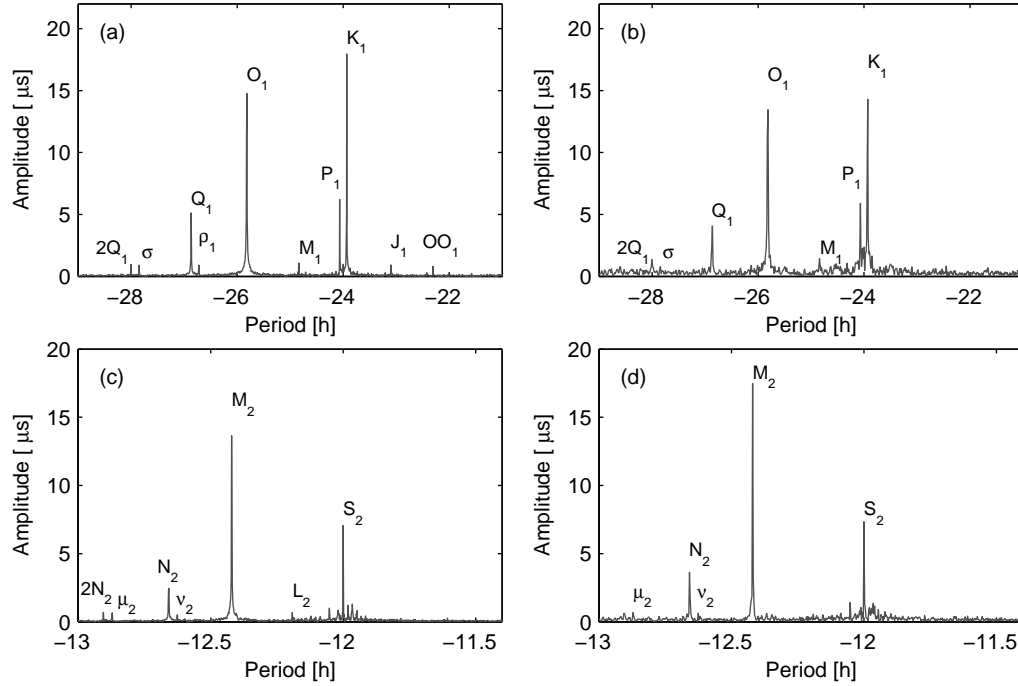


Fig. 8.8: Amplitude spectra of subdaily **UT1** and corresponding mean formal amplitude errors $\sigma_{A,m}$: (a) diurnal, reprocessed, $\sigma_{A,m} = 1.1 \mu\text{s}$; (b) diurnal, **CODE**, $\sigma_{A,m} = 1.6 \mu\text{s}$; (c) semidiurnal, reprocessed, $\sigma_{A,m} = 0.5 \mu\text{s}$; (d) semidiurnal, **CODE**, $\sigma_{A,m} = 0.8 \mu\text{s}$.

8.2.2. Estimation of Subdaily ERP Models

Using the long time series of **ERPs** as pseudo-observations (weighted with their formal errors), subdaily **ERP** models consisting of n ocean tide constituents can be estimated in a least squares adjustment:

$$\Delta X(t) = \sum_{j=1}^n [-p_j^c \cos \psi_j(t) + p_j^s \sin \psi_j(t)] \quad (8.9a)$$

$$\Delta Y(t) = \sum_{j=1}^n [p_j^c \sin \psi_j(t) + p_j^s \cos \psi_j(t)] \quad (8.9b)$$

$$\Delta UT1(t) = \sum_{j=1}^n [u_j^c \cos \psi_j(t) + u_j^s \sin \psi_j(t)] \quad (8.9c)$$

with

$\Delta X(t), \Delta Y(t)$	subdaily tidally driven variations in polar motion
$\Delta UT1(t)$	subdaily tidally driven variations in UT1
p_j^s, p_j^c	sine and cosine coefficients of tidal constituent j for polar motion
u_j^s, u_j^c	sine and cosine coefficients of tidal constituent j for UT1 .

The angle argument $\psi_j(t)$ is calculated from the Doodson number of constituent j and the fundamental arguments of nutation theory, see *McCarthy and Petit (2004)*. The set of estimated tidal amplitudes consists of 57 tidal constituents for polar motion and 41 for **UT1**. It is the same set already used by *Gipson (1996)* and *Rothacher et al. (2001)*. All terms with a magnitude larger than 5 mm in the tidal potential (*Cartwright and Taylor, 1971; Cartwright and Edden, 1973*) are considered. In addition, amplitudes of six smaller terms, whose amplitude should not significantly differ from zero, are estimated to get an impression of the size of errors of the amplitude estimates. Two different models including these tidal amplitudes and applying the same estimation strategy have been estimated: the model TUM05G is based on the reprocessed 3-day solutions, the model CODE01G on the operational **CODE IGS AC** solutions. The following estimation strategy has been used:

	TUM05G	CODE01G
Time interval	1 January 1994 - 29 October 2005	2 January 1995 - 17 August 2001
No. of pseudo-obs.	310,971	174,240
WRMS x-pole rate	3.103 mas/d	4.464 mas/d
WRMS y-pole rate	3.109 mas/d	4.270 mas/d
WRMS UT1–UTC rate	1.0485 ms/d	5.0501 ms/d

(a) Input data and general statistics.

Terms	TUM05G	CODE01G
Diurnal prograde polar motion [μas]	4.2	6.5
Semidiurnal prograde polar motion [μas]	2.7	5.9
Semidiurnal retrograde polar motion [μas]	2.8	3.4
Diurnal retrograde UT1 [μs]	0.38	0.57
Semidiurnal retrograde UT1 [μs]	0.60	0.63

(b) **RMS** differences of estimated subdaily **ERP** models w.r.t. the **IERS2003** model.Tab. 8.7: Subdaily **ERP** models estimated from the reprocessed (TUM05G) and the **CODE** operational (CODE01G) **ERP** series.

- Polar motion rates and **LOD** values as pseudo-observations: [Rothacher \(2002\)](#) and [Steigenberger et al. \(2006\)](#) showed that subdaily **ERP** models estimated from polar motion rates instead of the polar motion values help to reduce systematic effects.
- Weighting of the pseudo-observations with their formal errors.
- Constraints for the side band amplitudes: Although the temporal resolution is very high due to the length of the time series (e.g., 0.00025 d at the diurnal band), this resolution is not high enough to properly solve for the sidebands of the tidal constituents (a time series of at least 18.6 years would be needed to do so). Therefore, the ratio of the sideband amplitudes $a_{j'}$ and the amplitudes of the major tides a_j is constrained to the ratio of the corresponding heights of the tide generating potential $h_{j'}$ and h_j , see [Gipson \(1996\)](#):
$$\frac{a_{j'}}{a_j} = \frac{h_{j'}}{h_j} . \quad (8.10)$$
 a_j stands for the coefficients p_j^s , p_j^c , u_j^s and u_j^c from Eq. 8.9, $a_{j'}$ for the coefficients of the corresponding side band amplitudes.
- Bulletin A as a priori information.

Details on the input data of the models are given in Tab. 8.7a, the **WRMS** values are computed from the full subdaily **ERP** signals after removing long-term trends. The polar motion rate **WRMS** values are smaller by about 30% for the reprocessed solution, emphasizing the benefits of the homogeneous reprocessing. By far too optimistic formal errors in the early years are the explanation for the unreasonably large **WRMS** of the **CODE** **UT1–UTC** rates. Tab. 8.7b shows **RMS** differences of the estimated coefficients of these two models w.r.t. the a priori model **IERS2003**. The total polar motion **RMS** difference of the reprocessed model is with 3.5 μas about 40% smaller than the **RMS** difference of the corresponding **CODE** model (5.7 μas). For **UT1**, the improvement from 0.59 to 0.47 μs is somewhat smaller (20%). The residual amplitudes of the TUM05G model compared to **IERS2003** model are shown in Fig. 8.9. The threefold mean formal errors of the corresponding estimates in each frequency band are indicated by circles. The largest discrepancies for polar motion in the semidiurnal band occur for the tidal constituents that also have the largest amplitudes (K_2 , M_2 , S_2). In the diurnal band, larger discrepancies show up for tides with periods near 24 hours, namely S_1 , K_1 and ψ_1 . Systematic effects due to the 2:1 resonance of the orbit period and the sidereal day might contribute to this effect. Some part of the differences could also be explained by atmospheric tides ([Brzezinski et al., 2002](#)) and non-tidal **AAM** and **OAM**. The **IERS2003** model only contains the effect of ocean tides whereas space geodetic techniques measure the sum of oceanic and atmospheric tides as well as non-tidal effects of the atmosphere and the ocean. The largest amplitudes of atmospheric tides occur for the S_1 and S_2 term, see Tab. 8.11. For **UT1** also the amplitude differences of several smaller terms (namely K_2 , T_2 and μ_2 in the semidiurnal band, OO_1 and J_1 in the diurnal band) clearly exceed the threefold mean formal errors. The largest semidiurnal **UT1** discrepancy between the **GPS**-derived model and the

[IERS2003](#) model based on altimetry occurs for the M_2 semidiurnal tide. A major part of this difference can be attributed to the semidiurnal spin libration that will be discussed below.

The six small tidal constituents, whose amplitudes are expected to be zero, give an impression of the accuracy of the estimated coefficients. The mean amplitudes of 0.71 and 1.38 μs for these estimated semidiurnal and diurnal polar motion terms agree well with the mean formal errors of 0.64 and 1.35 μs . For [UT1](#) the corresponding amplitudes of 0.06 μs for both, the estimated semidiurnal and diurnal [UT1](#) terms, are far below the mean formal errors of 0.15 and 0.30 μs . This indicates that the formal errors for polar motion are realistic and those for [UT1](#) obviously too pessimistic by a factor of $\sim 2-5$.

8.2.3. Comparisons and Combination with VLBI

As already mentioned in the introduction of this section, subdaily [ERPs](#) can also be determined from [VLBI](#) observations. A subdaily [VLBI ERP](#) solution provided by Goddard Space Flight Center ([GSFC](#)) will be used for comparisons and combination with the [GPS](#) solution already described above. The [VLBI](#) solution computed from altogether 3804 24-hour sessions with the [CALC/SOLVE](#) software ([Gordon et al., 2006](#)) covers the time interval April 1980 till June 2007. Polar motion and [UT1](#) were estimated as constant offsets with 1 hour time resolution applying relative constraints of 45 mas/d and 5 ms/d , respectively. The [Gipson \(1996\)](#) subdaily [ERP](#) model was used as a priori model. Nutation was fixed to smoothed estimates from a reference frame solution.

Based on the same set of tidal amplitudes already mentioned above, a subdaily [ERP](#) model has been estimated from this series. In contrast to [GPS](#) where polar motion rates and [LOD](#) have been used as pseudo-observations, polar motion and [UT1](#) have been used for [VLBI](#). [VLBI](#) polar motion or [UT1](#) estimates with formal errors exceeding 5 mas or 0.3 ms , respectively, have been marked as outliers and excluded (2.1% of the total number of 96,413 pseudo-observations for each, x-pole, y-pole and [UT1](#)).

The major tidal amplitudes (namely K_1 , O_1 , P_1 , Q_1 in the diurnal band and M_2 , K_2 , N_2 , S_2 in the semidiurnal band) of this [VLBI](#) model called [GSFC07V](#), the [GPS](#) model [TUM05G](#) described in [Sec. 8.2.2](#)

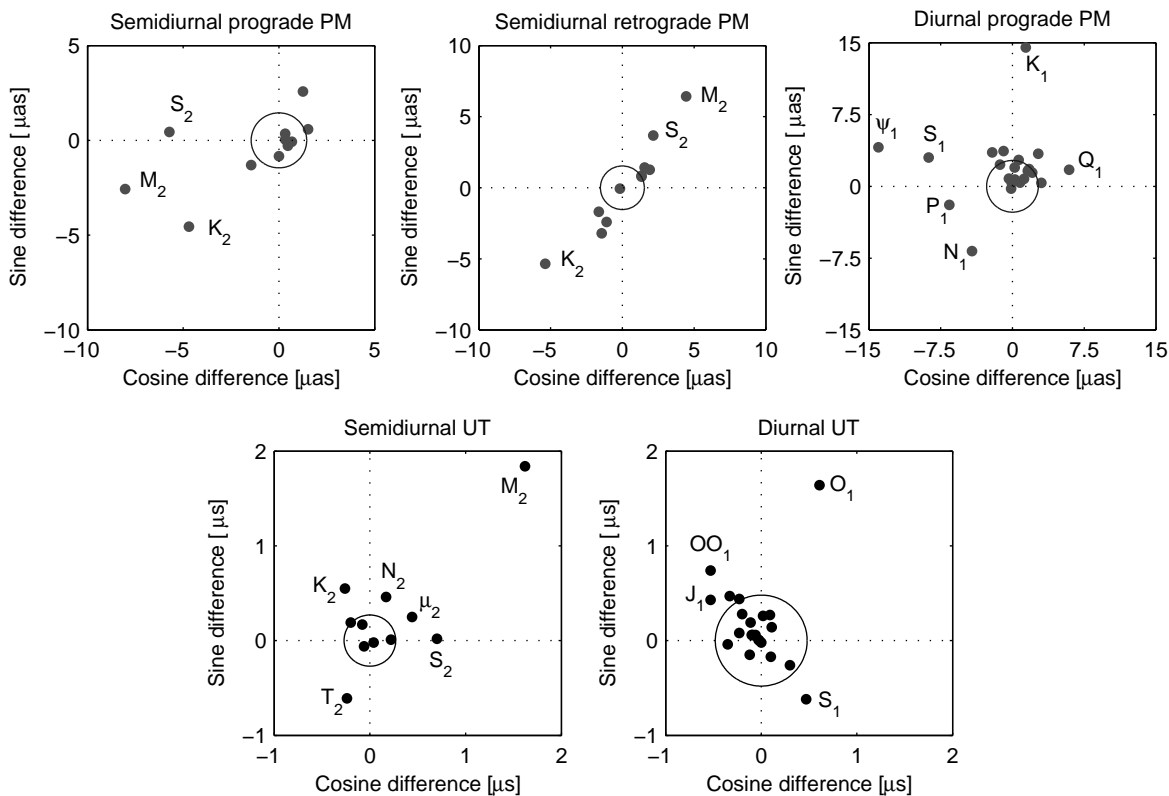


Fig. 8.9: Amplitude residuals of the subdaily [ERP](#) model [TUM05G](#) w.r.t. [IERS2003](#). The circles indicate the 3σ formal errors.

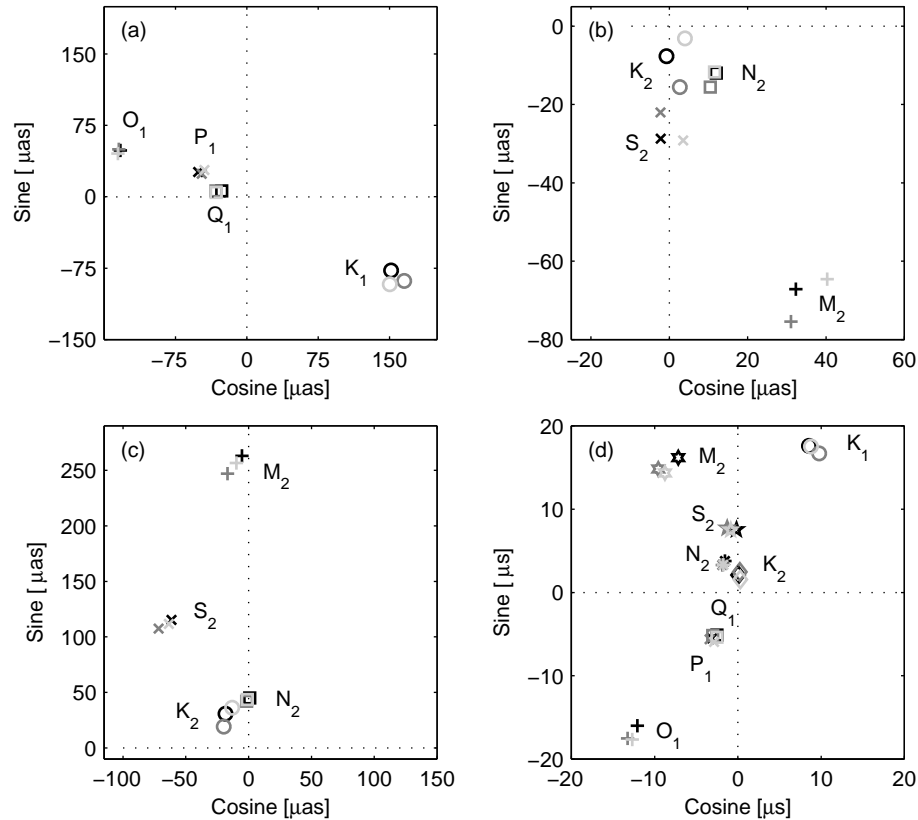


Fig. 8.10: Major tidal amplitudes of TUM05G (light gray), GSFC07V (dark gray) and the IERS2003 model (black): (a) diurnal prograde polar motion; (b) semidiurnal prograde polar motion; (c) semidiurnal retrograde polar motion; (d) diurnal and semidiurnal UT1.

and the IERS2003 model are shown as a phasor diagram in Fig. 8.10. The polar motion amplitudes in general agree on the level of 2–13 μas , the UT1 amplitude differences are between 0.5 and 1.5 μs . However, the maximum polar motion differences can reach up to 19.7 μas (retrograde M_2 differences of GSFC07V and IERS2003) but also the K_1 estimates show differences of up to 17.5 μas . The largest UT1 differences of 2.8 μs for GSFC07V/IERS2003 and 2.5 μs for TUM05G/IERS2003 are present for the M_2 tide. However, a major part of these semidiurnal UT1 differences is related to libration and will be discussed below.

Phasor diagrams of smaller semidiurnal tidal terms of polar motion and UT1 from TUM05G, GSFC07V, and IERS2003 are plotted in Fig. 8.11. The mean threefold formal errors are indicated by circles showing that most terms significantly differ from zero. The sideband terms M_2' and K_2' show in general a good agreement (except for the prograde K_2' tide) due to the quite good agreement of the major tidal amplitudes and the constraining of the sidebands (Eq. 8.10). The largest discrepancies for prograde semidiurnal polar motion (Fig. 8.11a, b, c) of up to 4.5 μas occur for the T_2 term. For retrograde semidiurnal polar motion (Fig. 8.11d, e, f), TUM05G and GSFC07V show discrepancies of 3.5 and 3.7 μas compared to the IERS2003 model for the μ_2 tide, respectively. On the other hand, the μ_2 estimates of TUM05G and GSFC07V differ only by 0.6 μas , whereas the largest differences between TUM05G and GSFC07V occur for L_2 with 2.4 μas . The largest discrepancies of semidiurnal UT1 (Fig. 8.11g, h, i) occur for T_2 when comparing TUM05G to GSFC07V (0.8 μs) and to IERS2003 (0.7 μs). The T_2 differences between GSFC07V and IERS2003 are quite small (0.2 μs) but μ_2 differs by 0.6 μs . The other small semidiurnal tidal constituents differ by 0.2–2.8 μas for polar motion and 0.1–0.5 μs for UT1. A general comparison of all smaller tidal terms is given in Tab. 8.8b.

In contrast to TUM05G, the formal errors of the six small tidal constituents of GSFC07V do not differ for diurnal and semidiurnal amplitudes, neither for polar motion ($\sigma_{PM} = 1.0 \mu\text{as}$) nor for UT1 ($\sigma_{UT1} = 0.26 \mu\text{s}$). This effect can be explained by the different type of pseudo-observations used for the estimation of the subdaily ERP models: TUM05G was determined from polar motion rates and LOD, whereas polar motion and UT1 pseudo-observations were used for GSFC07V. The UT1 mean amplitude of 0.27 μs is in good agreement with the formal error of 0.26 μs . On the other hand, the mean polar motion amplitude of

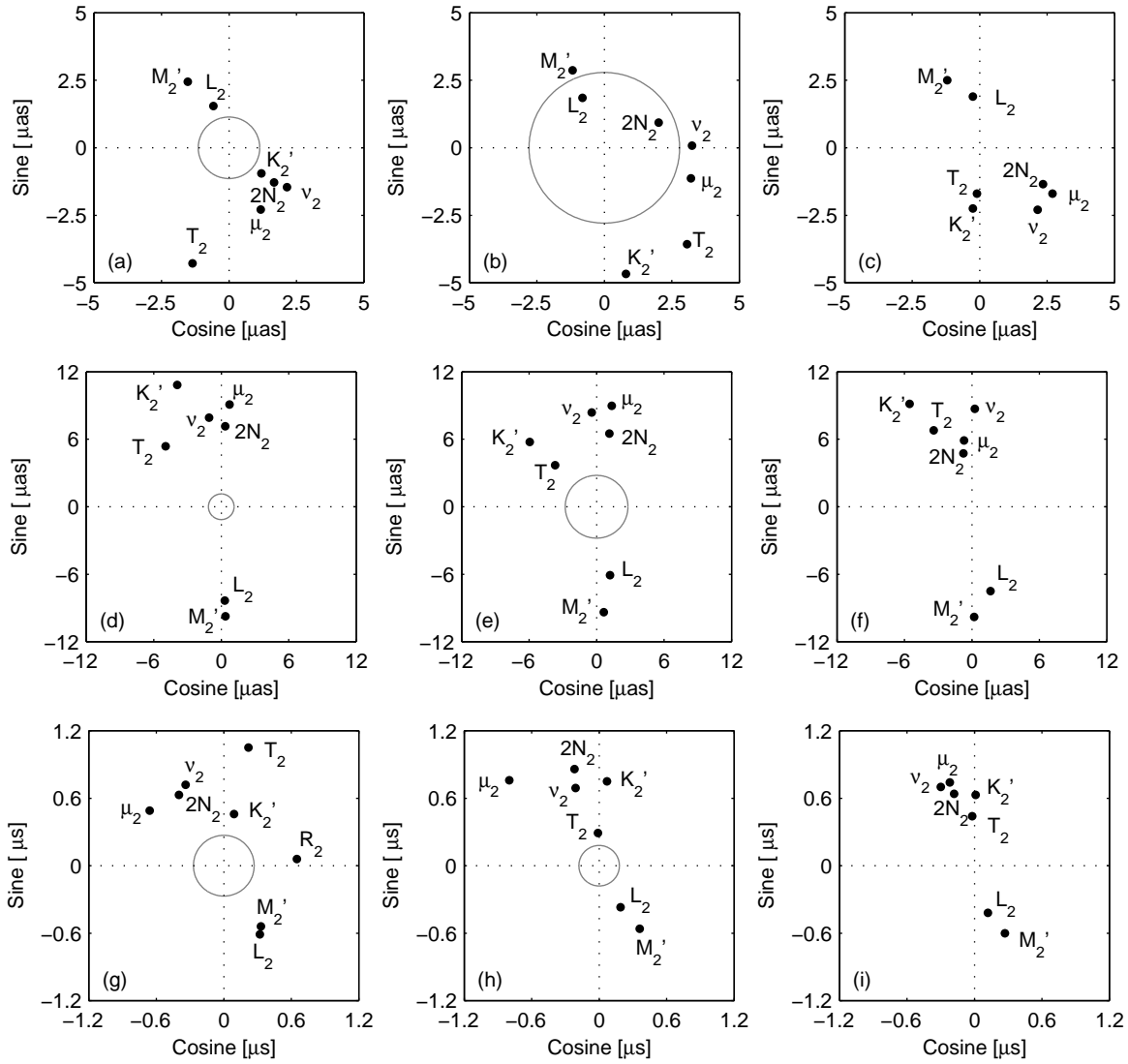


Fig. 8.11: Smaller semidiurnal tidal amplitudes of the [GPS](#) model TUM05G (a,d,g), the [VLBI](#) model GSFC07V (b,e,h) and the [IERS2003](#) model (c,f,i): (a,b,c) prograde polar motion; (d,e,f) retrograde polar motion; (g,h,i) [UT1](#). The circles indicate the threefold mean formal errors of the [GPS](#)- and [VLBI](#)-derived amplitudes.

$2.37 \mu\text{as}$ is larger by a factor of more than two compared to the mean formal error of $1.0 \mu\text{as}$ indicating that the polar motion formal errors are too optimistic.

Libration

In addition to the subdaily variations due to ocean tides discussed above, this section focusses on a direct tidal torque called libration that affects Earth rotation on subdaily timescales. Libration is caused by the tri-axial shape of the Earth (ellipsoid with axis $a \neq b \neq c$), i.e., the deviation of the equator from a circle or the difference $B - A$ in the moments of inertia of the Earth. According to [Groten \(2000\)](#) the difference of the equatorial axis of the Earth is about 70 m. These equatorial bulges cause additional tidal torques ([Chao et al., 1991](#)) affecting the Earth's spin (L_z) and polar motion (L_{xy}):

$$L_z = \frac{3GM(B-A)}{2r^3} \sin^2 \Theta \sin 2(\Lambda - \Lambda_0) \quad (8.11a)$$

$$L_{xy} = -\frac{3iGM(B-A)}{4r^3} \sin 2\Theta e^{-i(\Lambda - 2\Lambda_0)} \quad (8.11b)$$

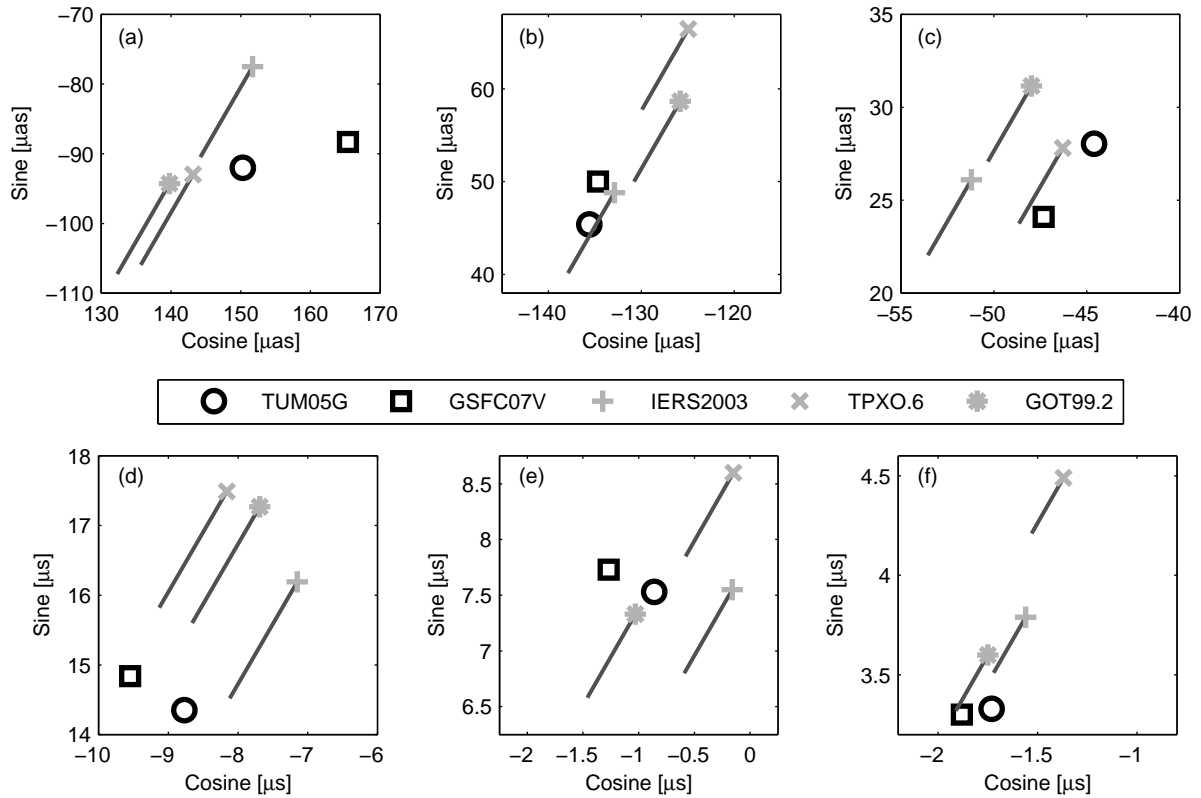


Fig. 8.12: Diurnal prograde polar motion: (a) K_1 tide; (b) O_1 tide; (c) P_1 tide. Semidiurnal $UT1$: (d) M_2 tide; (e) S_2 tide; (f) N_2 tide. The dark gray lines indicate libration according to [Chao et al. \(1991\)](#).

with

GM	gravitational coefficient of the Earth
A, B	moments of inertia of the Earth ($A < B < C$)
r	distance Earth – Sun/Moon
Θ	co-latitude of the sub-solar/lunar point on the Earth
Λ	longitude of the sub-solar/lunar point on the Earth
Λ_0	longitude of the a-axis of the Earth.

These torques result in a semidiurnal spin libration (dependence on 2Λ in Eq. 8.11a) and a prograde diurnal polar motion libration (dependence on $-i\Lambda$ in Eq. 8.11b). Amplitudes of the spin libration are given in [Wünsch \(1991\)](#), whereas polar motion libration is given in Tab. 5.1 of [McCarthy and Petit \(2004\)](#). However, the values published by [Chao et al. \(1991\)](#) will be used here as both, polar motion and spin libration, were computed in a consistent way.

The space geodetic techniques are sensitive to libration affecting the Earth's rotation, whereas it cannot be detected by altimetry (measuring the height of the ocean surface). The largest libration effects occur for prograde polar motion at K_1 , O_1 , P_1 and for $UT1$ at M_2 , S_2 and N_2 (numerical values are given in Tab. 8.11). Fig. 8.12 shows these three largest diurnal prograde polar motion and semidiurnal $UT1$ amplitudes of TUM05G and GSFC07V as well as three subdaily ERP models derived from ocean tide models: the IERS2003 model, TPXO.6 and GOT99.2. GOT99.2 ([Ray, 1999](#)) is primarily based on 6 years of TOPEX/POSEIDON altimeter data. Several hydrodynamic models have been added in shallow and polar seas. TPXO.6 (successor of the model described by [Egbert et al., 1994](#)) is an assimilation model that is based on a numerical hydrodynamic model as well as TOPEX/POSEIDON altimeter data. The libration according to [Chao et al. \(1991\)](#) is indicated by dark gray lines in Fig. 8.12.

For the largest polar motion libration effect, namely for the K_1 tide, with a magnitude of $15 \mu\text{as}$, the differences between TUM05G and IERS2003 get significantly smaller when accounting for libration whereas the differences for GSFC07V get larger. The differences w.r.t. the GPS as well as the VLBI model get larger for TPXO.6 and GOT99.2. These two models corrected for libration show reduced differences to

Model 1	IERS2003	IERS2003	TUM05G
Model 2	TUM05G	GSFC07V	GSFC07V
Prograde diurnal polar motion [μas]	6.3	6.8	6.0
Prograde diurnal polar motion + Libration [μas]	5.3	8.9	–
Prograde semidiurnal polar motion [μas]	4.3	5.1	7.6
Retrograde semidiurnal polar motion [μas]	4.2	9.4	8.4
Diurnal UT1 [μs]	0.66	0.89	0.58
Semidiurnal UT1 [μs]	0.94	1.08	0.49
Semidiurnal UT1 + Libration [μs]	0.41	0.71	–

(a) Major tidal amplitudes as shown in Fig. 8.10.

Model 1	IERS2003	IERS2003	TUM05G
Model 2	TUM05G	GSFC07V	GSFC07V
Prograde diurnal polar motion [μas]	3.5	3.5	3.6
Prograde semidiurnal polar motion [μas]	1.1	1.6	2.0
Retrograde semidiurnal polar motion [μas]	1.6	1.8	2.3
Diurnal UT1 [μs]	0.28	0.43	0.32
Semidiurnal UT1 [μs]	0.25	0.18	0.24

(b) Small tides: all estimated tidal constituents except for that shown in Fig. 8.10.

Tab. 8.8: Mean **RMS** differences of tidal amplitudes. + *Libration* indicates comparisons with the IERS2003 model corrected for prograde diurnal polar motion and semidiurnal spin libration according to *Chao et al. (1991)*.

the space geodetic models for the O_2 tide. On the other hand, the differences get larger for IERS2003 compared to GSFC07V and are almost the same for IERS2003 compared to TUM05G. For the P_1 tide, the libration correction increases the differences to TUM05G, they get smaller for GSFC07V compared to TPXO.6 and GOT99.2 but get larger for IERS2003. The largest semidiurnal spin libration effect occurs for the M_2 tide. A clear reduction of the differences between all ocean tide models and the TUM05G as well as the GSFC07V model can be seen in Fig. 8.12d. For S_2 the situation is less clear: the differences get smaller for TPXO.6, are almost the same for IERS2003 and even get larger for GOT99.2. For N_2 the differences for all combinations between the space geodetic models and the altimetric models get smaller if libration is corrected for.

To quantify the results shown in Figs. 8.10 and 8.12, the mean **RMS** differences between major tidal constituents of the TUM05G, GSFC07V and IERS2003 model are given in Tab. 8.8a. The **RMS** differences to the IERS2003 model corrected for the libration effects given in *Chao et al. (1991)* are indicated by + *Libration*. For semidiurnal **UT1**, the **RMS** differences are reduced by one third for GSFC07V and a factor of more than two for TUM05G when accounting for libration. The fact that the **RMS** differences of both space geodetic techniques to the altimetric model are significantly reduced is a clear indicator that libration is indeed the reason for that.

Due to the longer time span and their homogeneity, the M_2 as well as the N_2 semidiurnal spin libration can be detected in the reprocessed **GPS** and **VLBI** series in contrast to the shorter and inhomogeneous **GPS** and **SLR** time series described by *Rothacher et al. (2001)*. On the other hand, the libration correction only reduces the differences to two of three altimetric models for the S_2 term (Fig. 8.12e). For diurnal prograde polar motion, the situation is not as conclusive as for **UT1**. Whereas the **RMS** differences between TUM05G and IERS2003 improve by 1 μas when accounting for libration, the GSFC07V differences get worse by about 2 μas .

Stability of subdaily ERP Models

To test the stability of the **GPS**- and **VLBI**-derived subdaily **ERP** models, 7 models per technique have been estimated from limited time intervals of the whole series. A large **STD** of an individual coefficient is caused by a bad repeatability/stability indicating that this particular coefficient cannot be well determined. The **GPS** models are based on 6 years of data shifted by one year (time period 1994–2005), the **VLBI** models are based on 11 years of data (accounting for the data gaps between individual **VLBI** sessions) shifted by two

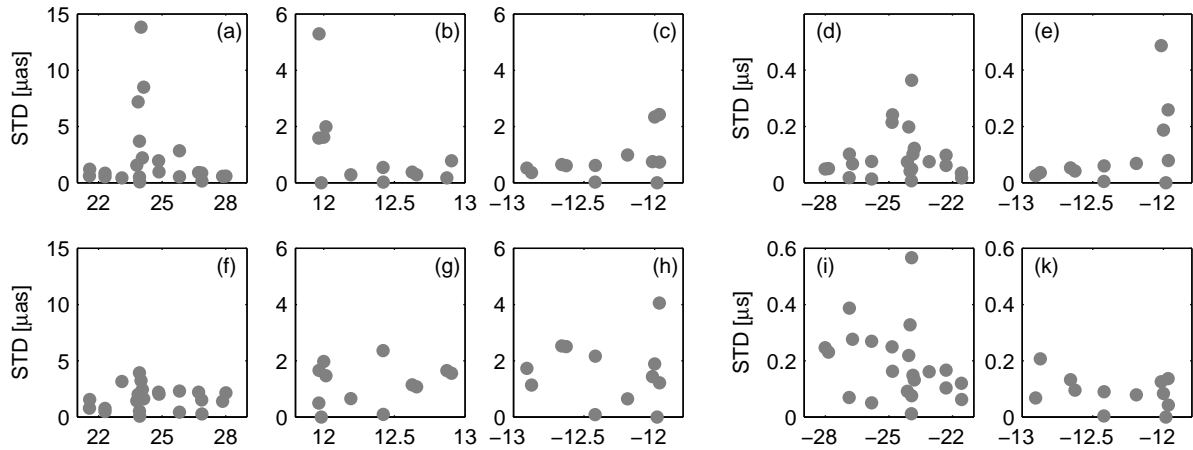


Fig. 8.13: STDs of tidal amplitudes for GPS (a–e) and VLBI (f–k) subdaily ERP models: (a,f) diurnal prograde polar motion; (b,g) semidiurnal prograde polar motion; (c,h) retrograde semidiurnal polar motion; (d,i) diurnal UT1; (e,k) semidiurnal UT1. The periods on the x -axis are given in hours.

years (time period 1984–2006). Fig. 8.13 shows the GPS- and VLBI-derived STD values for semidiurnal and diurnal polar motion and UT1 terms. The STD values very close to zero belong to the constrained sideband terms (Eq. 8.10).

Huge STD values for diurnal prograde polar motion are visible in the GPS models for the S_1 ($13.8 \mu\text{s}$), N_1 ($8.5 \mu\text{s}$) and ψ_1 ($7.2 \mu\text{s}$) terms in Fig. 8.13a. As such large values are not present in the VLBI models (the largest STD in Fig. 8.13f is $3.9 \mu\text{s}$ for K_1), this seems to be a technique-specific effect. Deficiencies in the modeling of the GPS satellite orbits are the most probable explanation. The mean diurnal polar motion STDs are $1.7 \mu\text{s}$ for GSFC07V and $2.3 \mu\text{s}$ for TUM05G. The latter value can be reduced to $1.1 \mu\text{s}$ if the S_1 , N_1 and ψ_1 amplitudes are excluded. Other TUM05G terms with increased STD values are K_2 ($5.3 \mu\text{s}$) for semidiurnal prograde polar motion (Fig. 8.13b), K_1 ($0.36 \mu\text{s}$) for diurnal UT1 (Fig. 8.13d), and T_2 ($0.49 \mu\text{s}$) for semidiurnal UT1 (Fig. 8.13e). The GSFC07V K_2 semidiurnal polar motion ($4.1 \mu\text{s}$, Fig. 8.13h) and the K_1 diurnal UT1 term ($0.57 \mu\text{s}$, Fig. 8.13i) are the only VLBI terms with an increased STD. The mean STD values for semidiurnal polar motion are 1.0 and $1.4 \mu\text{s}$ for GPS and VLBI, respectively. Whereas the GPS-derived STDs of diurnal ($0.11 \mu\text{s}$) and semidiurnal UT1 ($0.09 \mu\text{s}$) are almost on the same level, the GSFC07V semidiurnal STDs ($0.19 \mu\text{s}$) are larger by a factor of two compared to the diurnal STDs ($0.09 \mu\text{s}$).

Comparison of Different Models

Tab. 8.9 compares subdaily polar motion and UT1 amplitudes of the GPS and VLBI models described above with other subdaily ERP models. *Ro01* is the GPS model described by Rothacher et al. (2001) based on about 3 years of GPS data processed by the CODE IGS AC. *Gip99* is an updated version of the VLBI model described by Gipson (1996) consisting of the same set of tidal constituents as *Ro01*, TUM05G and GSFC07V. In addition to models based on space geodetic observations, two models computed from ocean tide models derived from altimetry are included, namely the actual IERS2003 model and its predecessor, the IERS96 model. Only amplitudes present in both models of an individual comparison have been considered. This is the major reason for the small differences between the IERS96 model (12 polar motion and 8 UT1 constituents) and the IERS2003 model (101 polar motion and 71 UT1 constituents). TPX0.6 and GOT99.2 are not included in Tab. 8.9 as only the major tidal constituents shown in Fig. 8.10 are available for those models.

The best agreement is achieved between models based on the same observation technique: the intra-technique comparisons for GPS (*Ro01* and TUM05G) as well as VLBI (*Gip99* and GSFC07V) give both polar motion differences of $3.6 \mu\text{s}$ and UT1 differences of $0.33 \mu\text{s}$ and $0.22 \mu\text{s}$, respectively. Whereas the inter-technique differences are smallest between the latest models TUM05G and GSFC07V, the polar motion differences are smaller by $0.5 \mu\text{s}$ between the older GPS model *Ro01* and the newer VLBI model GSFC07V compared to TUM05G. On the other hand, TUM05G shows the smallest differences of all space geodetic models w.r.t. the altimetric IERS2003 model for polar motion as well as for UT1. The newer models TUM05G and

Model	GPS		VLBI		Altimetry	
	Ro01	TUM05G	Gip99	GSFC07V	IERS96	IERS2003
Ro01		3.6	4.5	3.8	4.9	4.3
TUM05G	3.6		5.3	4.3	5.0	3.5
Gip99	4.5	5.3		3.6	6.8	5.3
GSFC07V	3.8	4.3	3.6		7.2	4.5
IERS96	4.9	5.0	6.8	7.2		0.7
IERS2003	4.3	3.5	5.3	4.5	0.7	

(a) Polar motion differences in μas .

Model	Ro01	TUM05G	Gip99	GSFC07V	IERS96	IERS2003
Ro01		0.33	0.43	0.39	0.81	0.48
TUM05G	0.33		0.43	0.35	0.83	0.47
Gip99	0.43	0.43		0.22	1.06	0.63
GSFC07V	0.39	0.35	0.22		1.01	0.59
IERS96	0.81	0.83	1.06	1.01		0.16
IERS2003	0.48	0.47	0.63	0.59	0.16	

(b) UT1 differences in μs .

Tab. 8.9: RMS differences between different subdaily ERP models.

GSFC07V reduce the polar motion differences to IERS2003 by $0.8 \mu\text{as}$ compared to the older models Ro01 and Gip99. On the other hand, the UT1 improvement is pretty small.

Based on the stability test described in the previous section, one can assume that the precision of the latest single-technique subdaily ERP models is on average on the level of $1-2 \mu\text{as}$ for polar motion and $0.1-0.3 \mu\text{s}$ for UT1. However, as shown above, individual tidal terms in particular affected by systematic errors can differ by up to $14 \mu\text{as}$ for polar motion and $0.5 \mu\text{s}$ for UT1. The accuracy derived from the comparisons of subdaily ERP models determined by different techniques is on the level of $4-7 \mu\text{as}$ for polar motion and $0.3-0.6 \mu\text{s}$ for UT1.

Combined GPS/VLBI Model

As the GPS and VLBI subdaily ERP models discussed above showed a high level of consistency, the combined GPS/VLBI model TUM07C has been computed. Different relative weights (in addition to the weighting with the formal errors) for the GPS and VLBI pseudo-observations have been tested. Empiric weights of 10:1 for VLBI-derived polar motion and GPS-derived polar motion rates and an equal weighting of UT1 and LOD resulted in the smallest differences w.r.t. the reference model IERS2003. The other estimation options were identical to the single-technique models described above.

	TUM05G	GSFC07V	TUM07C
Prograde diurnal polar motion [μas]	4.2	4.3	3.7
Prograde semidiurnal polar motion [μas]	2.7	3.3	2.0
Retrograde semidiurnal polar motion [μas]	2.8	5.8	3.1
Diurnal UT1 [μs]	0.38	0.38	0.44
Semidiurnal UT1 [μs]	0.60	0.67	0.59

Tab. 8.10: Mean RMS differences of the GPS and VLBI single-technique and the combined GPS/VLBI subdaily ERP models w.r.t. the IERS2003 model.

Tab. 8.10 lists the RMS differences of the GPS and VLBI single-technique models TUM05G and GSFC07V and the combined model TUM07C w.r.t. the IERS2003 model. A significant RMS reduction of 15 and 40% could be achieved for diurnal and semidiurnal prograde polar motion, respectively. For retrograde polar motion, the RMS differences of the combined model are slightly worse compared to TUM05G but smaller by a factor of almost two compared to GSFC07V. For UT1, the impact of the combination is smaller: the diurnal RMS differences of the combined model are slightly larger than those of the single-technique

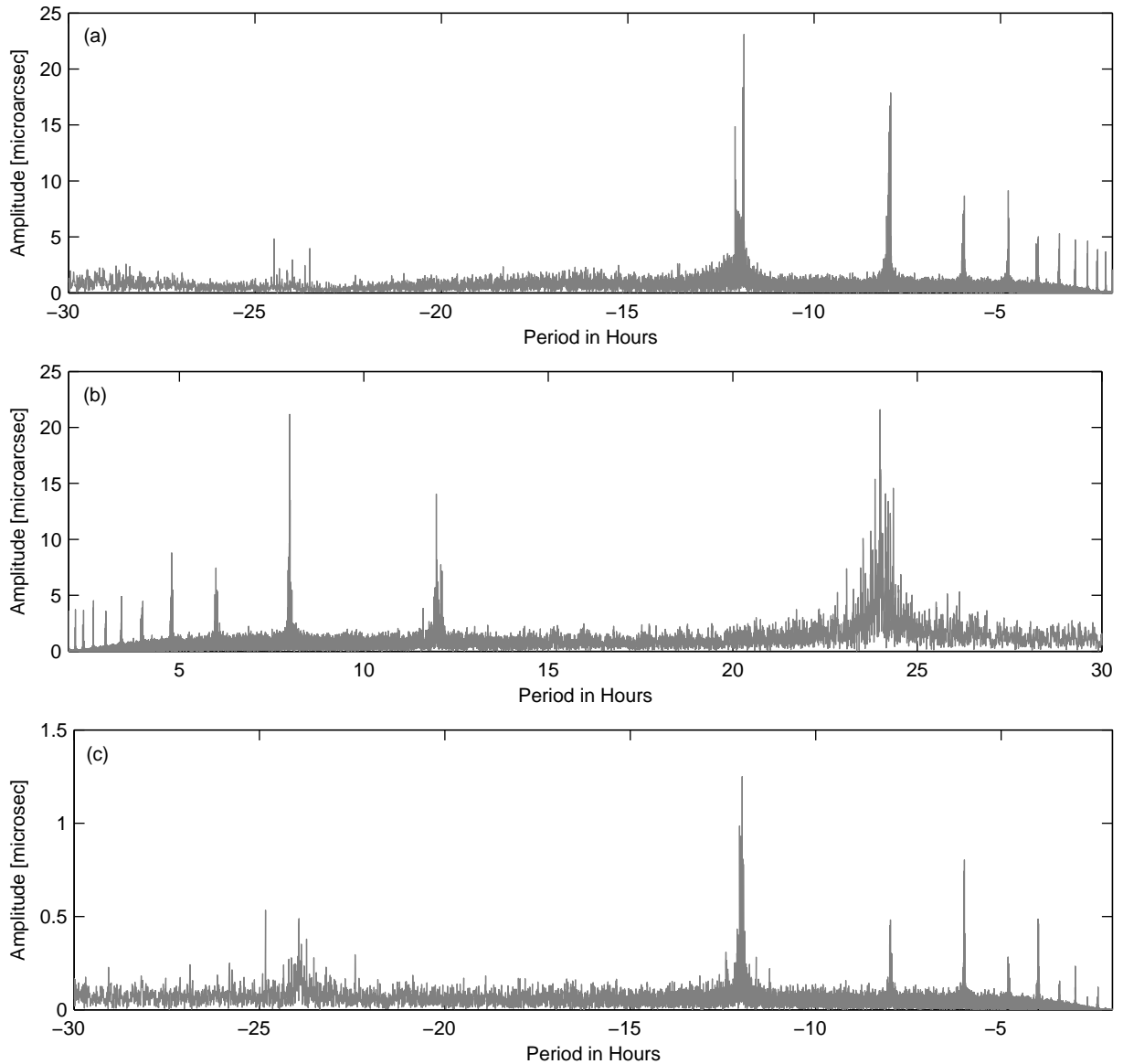


Fig. 8.14: Residual amplitude spectra (TUM05G subdaily ERP model removed) of subdaily (a) retrograde polar motion; (b) prograde polar motion; (c) UT1.

solutions whereas for semidiurnal UT1, the RMS values of the combined model are almost the same as for the GPS-only model. The RMS differences in semidiurnal UT1 can be reduced from 0.59 to 0.31 μs when correcting the IERS2003 model for libration. Due to the increased RMS differences for prograde diurnal polar motion of GSFC07V when accounting for libration (already mentioned above), the RMS differences of the combined model also slightly increase from 3.7 to 4.0 μas when accounting for polar motion libration.

8.2.4. Residual Signals

As already mentioned above, the major part of the variations in subdaily Earth rotation is caused by ocean tides. In the previous sections, the amplitudes at these tidal periods have been determined from GPS and VLBI observations. Therefore, these amplitudes can be removed from the time series of subdaily ERPs to study the remaining residual signals. Fig. 8.14 displays the residual spectra of the GPS polar motion and UT1 time series after subtracting the TUM05G subdaily ERP model. The largest residual amplitudes appear close to 12 and 24 hours. A major part of these amplitudes might be explained by deficiencies in the orbit modeling.

Period [h]	Amplitude PM [μ as]	Amplitude UT1 [μ s]	Comment	Reference
8.0000	0.46(p)/0.57(r)	0.48	S_3 atmospheric tide	<i>Viron et al. (2005)</i>
8.28	0.43(p)/0.30(r)	0.57	M_3 from hydro-dynamic model	<i>Haas and Wünsch (2006)</i>
11.9672	–	0.2	K_2 libration	<i>Chao et al. (1991)</i>
12.0000	2.9	0.5	S_2 atmospheric tide	<i>Brzezinski et al. (2002)</i>
	–	0.9	S_2 libration	<i>Chao et al. (1991)</i>
12.4206	–	1.9	M_2 libration	<i>Chao et al. (1991)</i>
12.6584	–	0.3	N_2 libration	<i>Chao et al. (1991)</i>
14.6	3	–	ξ_2^1 atmospheric normal mode	<i>Brzezinski et al. (2002)</i>
23.0985	0.8	–	J_1 libration	<i>Chao et al. (1991)</i>
23.8693	0.7	–	ψ_1 atmospheric tide	<i>Brzezinski et al. (2002)</i>
23.9345	1.6	–	K_1 atmospheric tide	<i>Brzezinski et al. (2002)</i>
	0.8	–	K_1 atmospheric tide	<i>Brzezinski et al. (2004)</i>
23.9345	15	–	K_1 libration	<i>Chao et al. (1991)</i>
24.0000	7.1	0.5	S_1 atmospheric tide	<i>Brzezinski et al. (2002)</i>
	7.8	–	S_1 atmospheric tide	<i>Brzezinski et al. (2004)</i>
	7.8	–	non-tidal AAM	^a
	17	–	non-tidal OAM	^a
	24.7	0.6	non-tidal angular momentum	<i>Haas and Wünsch (2006)</i>
24.0659	1.3	–	P_1 atmospheric tide	<i>Brzezinski et al. (2002)</i>
	1.2	–	P_1 atmospheric tide	<i>Brzezinski et al. (2004)</i>
	4.7	–	P_1 libration	<i>Chao et al. (1991)</i>
24.8333	0.8	–	M_1 libration	<i>Chao et al. (1991)</i>
25.8193	10	–	O_1 libration	<i>Chao et al. (1991)</i>
26.8684	0.8	–	Q_1 libration	<i>Chao et al. (1991)</i>
28.8	31	–	ψ_1^1 atmospheric normal mode	<i>Brzezinski et al. (2002)</i>

^a http://hpiers.obspm.fr/eop-pc/models/PM/PM_oceanic_nt_hf_tab.html

Tab. 8.11: Subdaily signals in polar motion and **UT1** that are not related to diurnal and semidiurnal ocean tides.

Significant peaks in polar motion as well as in **UT1** also appear around periods $T = \frac{24}{n} h$ with $n = 3, \dots, 11$ with decreasing amplitudes for higher frequencies. These peaks have already been detected in the operational **CODE** series by *Rothacher et al. (2001)*. The homogeneous reprocessing of the **ERP** series discussed here could not remove these peaks. Although there are some geophysical effects causing high-frequency Earth rotation variations (e.g., the M_3 ocean tide and the S_3 atmospheric tide, see Tab. 8.11), the predicted amplitudes are much smaller than the observed. In addition, these effects could only explain the peaks around the 8 h period. Therefore, these high-frequency peaks are assumed to be artifacts. The fact that peaks at the same periods are visible in the formal error spectra (not shown here) supports this assumption.

Tab. 8.11 lists the magnitude of subdaily signals not related to semidiurnal and diurnal ocean tides as given in the literature. As already described above, the largest terms of semi-diurnal spin libration could be detected by comparing the **GPS** and **VLBI** models with altimetric models. For the diurnal polar motion libration, the **GPS** differences get smaller when accounting for libration, whereas the **VLBI** differences get larger. For periods, where several different sources contribute (e.g., S_1 oceanic and atmospheric tides as well as non-tidal **AAM** and **OAM** at 24 hours), **GPS** can only measure the sum of these effects. This fact could explain the S_1 and S_2 differences in Fig. 8.9 to some extent.

Other peaks that could be detected in the subdaily **ERP** spectra are related to atmospheric normal modes. According to *Brzezinski et al. (2002)*, the retrograde ψ_1^1 atmospheric normal mode has an amplitude of 31 μ as (sum of wind and inverted-barometer pressure effect). Although this value is well above the noise level of the reprocessed **ERP** series, no significant peak could be detected at the corresponding period. However, as retrograde diurnal polar motion is blocked (see Sec. 3.1), a major part of the corresponding retrograde amplitude could be suppressed by this constraint (*Thaller et al., 2007*). The much smaller ξ_2^1 atmospheric normal mode is, with an amplitude of 3 μ as, also above the noise level but can be neither seen in the prograde nor in the retrograde spectrum. The M_3 **UT1** amplitude of 0.57 μ s reported by *Haas and Wünsch (2006)* is also clearly above the noise level but cannot be detected in the **UT1** spectrum. The M_3 polar motion peak on the other hand is too small to be seen in the spectra.

Further investigations could benefit from high-resolution long time series of **AAM** and **OAM**. These series can help to verify which signals are technique-specific artifacts or true geophysical signals visible in both, the **GPS**-derived and the angular momentum spectra. However, most of these angular momentum data sets are based on 6-hourly numerical weather model data. Series based on 3-hourly forecast data or with even higher resolution are only available for limited time intervals (e.g., *Salstein et al., 2008*).

8.3. Nutation Parameters

Nutation parameters can only be determined in an absolute sense by **VLBI** and **LLR**. For the theoretical nutation model recommended by the **IERS** conventions (namely, the **IAU2000A** model), **VLBI** was used to determine a set of best fitting Earth parameters (*Mathews et al., 2002*). Nutation models solely based on **VLBI** observations have been determined by, e.g., *Herring et al. (2002)*. On the other hand, the rates of the nutation parameters can be determined by **GPS**, see Sec. 2.7. *Rothacher et al. (1999a)* demonstrated that **GPS**-derived nutation rates can contribute to nutation periods up to 16 days. Fig. 8.15 shows the nutation rates in longitude and obliquity of the special 3-day solution already mentioned in Sec. 3.2.2 for the **CODE** and the reprocessed series. The nutation rates in longitude $\Delta\psi$ are multiplied by $\sin\epsilon_0$ (where ϵ_0 is the mean obliquity of the ecliptic) for better comparability with the nutation rates in obliquity (*Herring et al., 1986*). One nutation rate per 3-day solution (72-hour parameter interval) is estimated, i.e., the parameter at the beginning of the 3-day interval is heavily constrained to its a priori value (**IAU2000A** for the reprocessed series, **IAU80** for the **CODE** series) and the piecewise linear parameter at the end of the interval is estimated freely. Polar motion and **LOD** are estimated with a 24-hour parameter spacing. The behavior of the **CODE** series clearly changes in fall 1996: in addition to the **RPR** parameters D_0 and Y_0 (see Eq. 2.49) also the parameters X_0 , X_C and X_S are estimated starting with that date.

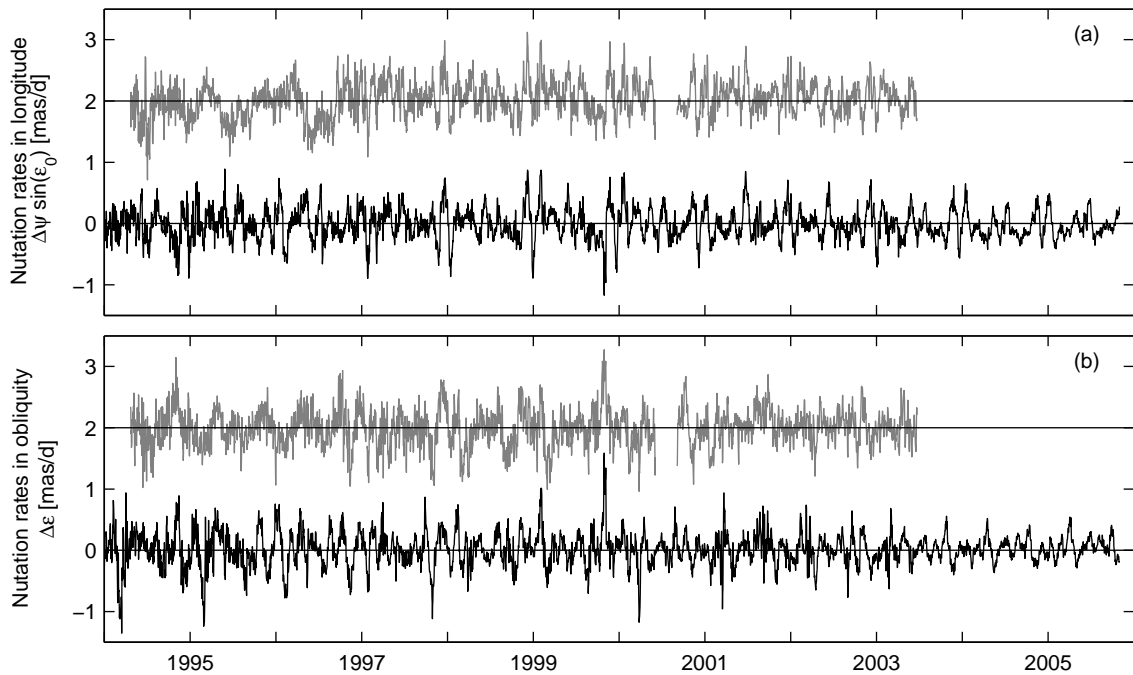


Fig. 8.15: Nutation rates in (a) longitude and (b) obliquity. The operational **CODE** nutation rates are given in gray and shifted by 2 mas/d, the reprocessed series is given in black. In the **CODE** series, about three months in 2000 are missing due to erroneous settings.

The formal errors of the nutation rate estimates are shown in Fig. 8.16. The sparse tracking network in the first two years significantly degrades the quality of the nutation rates from the reprocessed solution. The mean formal errors of this solution are $14.8 \mu\text{as/d}$ for the nutation rates in longitude and $15.4 \mu\text{as/d}$ for obliquity with median values of $12.0 \mu\text{as/d}$ and $12.3 \mu\text{as/d}$, respectively. The decrease of the **CODE** formal errors at the beginning of 1995 is related to the implementation of ambiguity fixing (**QIF** method), see *Rothacher et al. (1999a)*. The change in the set of freely estimated **RPR** parameters in fall 1996 already

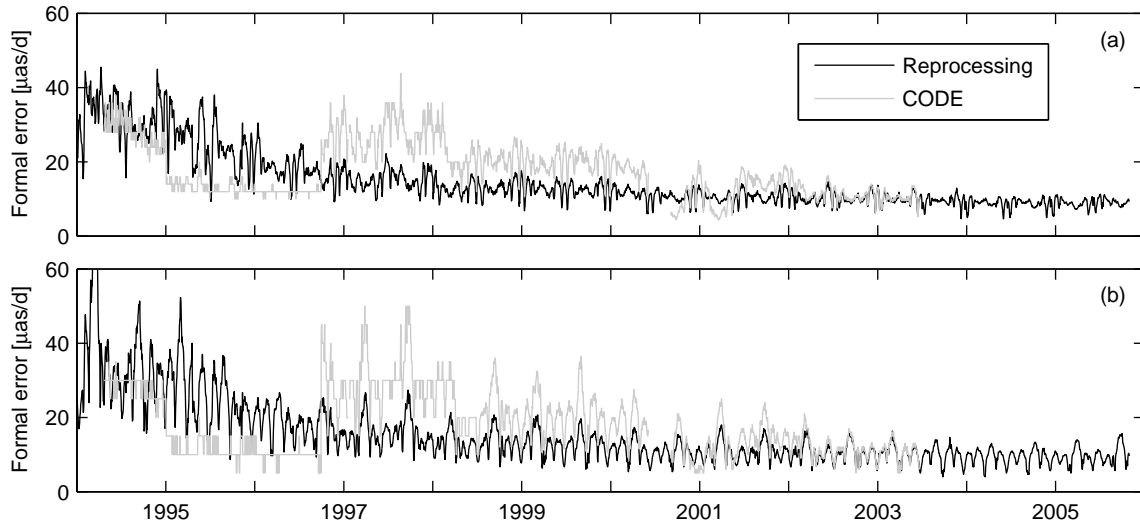


Fig. 8.16: Formal errors of nutation rates in (a) longitude $\Delta\psi \sin \epsilon_0$ and (b) obliquity $\Delta\epsilon$.

mentioned above also affects the formal errors of the **CODE** series: the significant increase of the formal errors of the nutation rates indicates that the nutation parameters and the **RPR** parameters are correlated. Starting with the beginning of 2002, the formal errors of the **CODE** nutation rates are on the level of the reprocessed series and also show the same pattern.

The spectra of the nutation rates shown in Fig. 8.15 are plotted in Fig. 8.17. *Vondrak et al. (2003)* already mentioned systematic errors in the nutation rates with a major period at 58 days. In addition to this period (related to the orientation of the orbital planes w.r.t. the Sun, see Sec. 4.3.2) further peaks at T_R/n , $n=2, \dots, 5$ and 44.3 days can be seen in the spectra of the nutation rates in longitude as well as in obliquity. Due to the close connection of the nutation rates and the orbital elements (see Eq. 2.65), the artifacts from the orbit modeling are also visible in the estimated nutation rates. However, as **GPS** is only able to determine nutation amplitudes for periods up to 16 days, these artifacts will not be discussed in more detail here. The spectra of nutation amplitudes for periods up to 17 days are shown in Fig. 8.18. Like for **UT1** and **LOD** (see Sec. 8.2.1), the nutation spectra have been computed from the nutation rates.

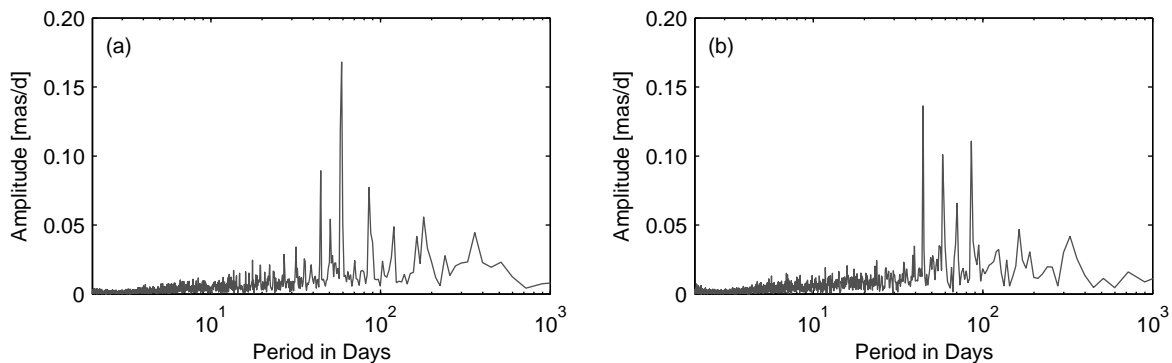


Fig. 8.17: Spectra of nutation rates in (a) longitude $\Delta\psi \sin \epsilon_0$ and (b) obliquity $\Delta\epsilon$.

It is already obvious from Fig. 8.16 that both reprocessed formal error time series show clear but different periodic signals. Fig. 8.19 gives the Continuous Wavelet Transforms (**CWTs**) computed with the Morlet wavelet as well as **FFT** spectra for the time interval January 1996 till October 2005. As for the nutation rates themselves, the periodic signal with the largest amplitude in the formal errors of the $\Delta\epsilon$ nutation rates has a period of 44.3 days whereas the largest peak in the $\Delta\psi$ spectrum occurs at 29.2 days. In particular at shorter periods, the power in the **CWT** decreases with time indicating more stable nutation rate estimates. This effect might be related to changes in the satellite constellation, i.e., the decommissioning of old Block II/IIA satellites and the increasing number of Block IIR satellites (see Fig. 2.2) that are easier to model. Besides the fact that the quality of nutation amplitudes estimated from nutation rates decreases with increasing

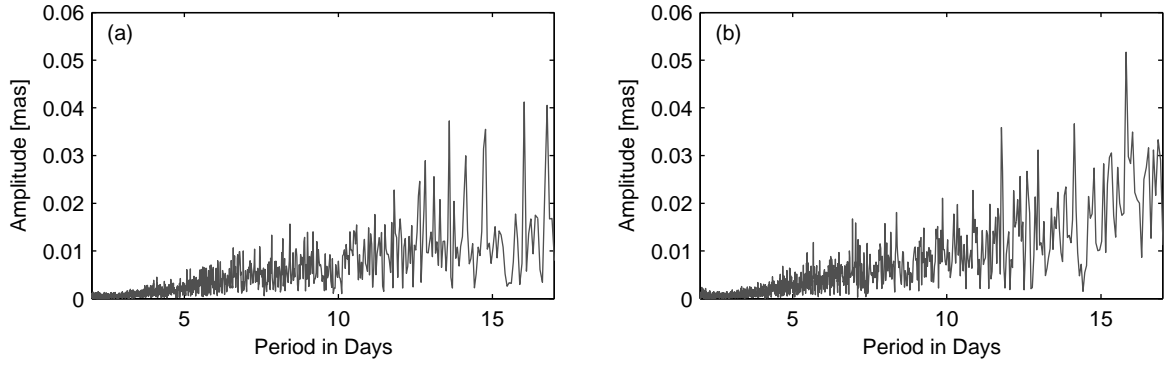


Fig. 8.18: Nutation residual spectra w.r.t. IAU2000A computed from nutation rates in (a) longitude $\Delta\psi \sin \epsilon_0$ and (b) obliquity $\Delta\epsilon$.

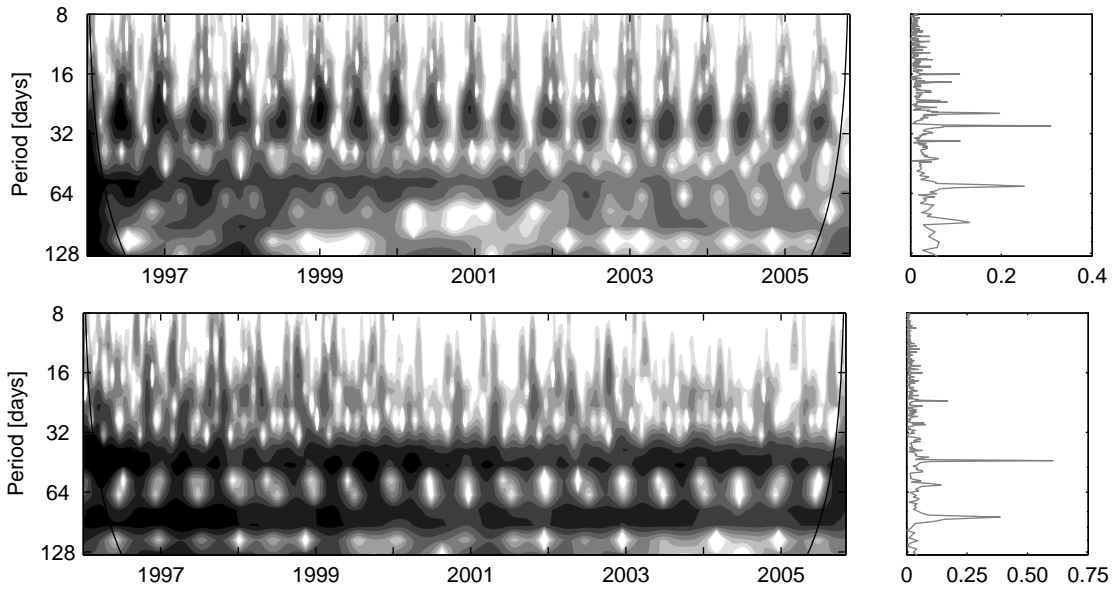


Fig. 8.19: CWT of nutation rate formal errors in longitude (top) and obliquity (bottom). Due to increased formal errors in 1994 and 1995, the time period has been limited to January 1996 till October 2005.

period, it is clear that GPS can only contribute to short period nutation variations due to the systematic effects discussed above.

As for the subdaily ERP models described in Sec. 8.2.2, nutation models can be described by a harmonic expansion of n nutation terms represented by the sine and cosine coefficients $\delta\psi_j^s$, $\delta\epsilon_j^s$ and $\delta\psi_j^c$, $\delta\epsilon_j^c$ of nutation in longitude and obliquity:

$$\delta\Delta\epsilon(t) = \sum_{j=1}^n \delta\epsilon_j^c \cos \theta_j(t) + \delta\epsilon_j^s \sin \theta_j(t) \quad (8.12a)$$

$$\delta\Delta\psi(t) = \sum_{j=1}^n \delta\psi_j^c \cos \theta_j(t) + \delta\psi_j^s \sin \theta_j(t) \quad (8.12b)$$

where θ_j stands for a combination of the five fundamental arguments of lunisolar nutation as given in McCarthy and Petit (2004).

The nutation rates discussed in the previous section have been introduced as pseudo-observations in an unweighted least squares adjustment to solve for these model coefficients. The same set of nutation terms that was used by Rothacher et al. (1999a) was estimated. This set consists of altogether 34 periods between 4 and 16 days. In addition, offset and drift for the nutation rates in longitude and obliquity have been estimated to remove long-term variations resulting in a total number of 140 parameters. Due to the increased formal errors (see Fig. 8.16), data in 1994 has been excluded.

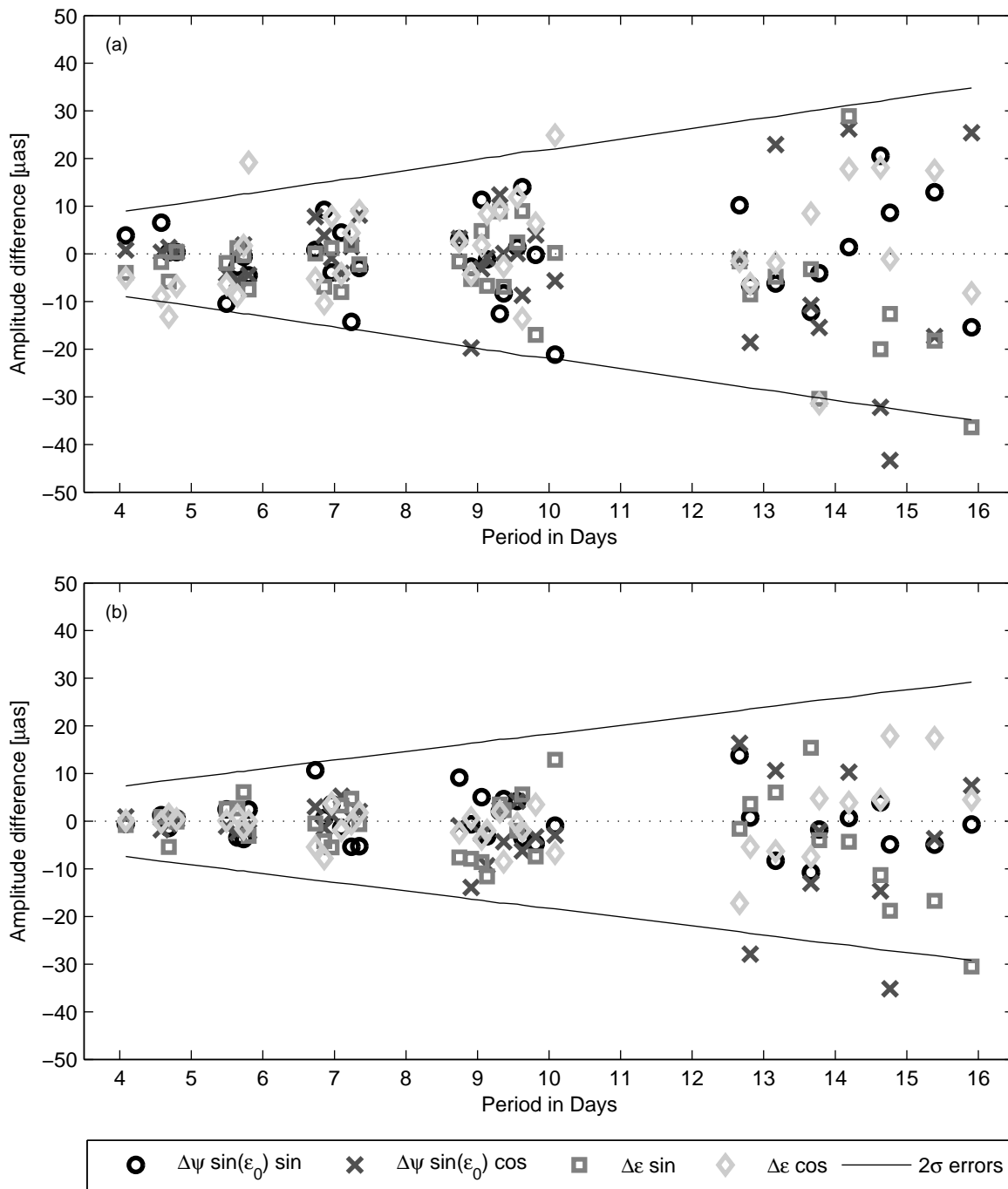


Fig. 8.20: Comparison of nutation amplitudes estimated from GPS-derived nutation rates with the IAU2000A model for (a) COD03N based on the CODE operational series and (b) TUM05N based on the reprocessed series.

Model	Type	$\delta\epsilon^s$	$\delta\epsilon^c$	$\delta\psi^s \cdot \sin \epsilon_0$	$\delta\psi^c \cdot \sin \epsilon_0$	All
		[μas]	[μas]	[μas]	[μas]	
Ro99	mean	16.1	11.0	14.3	14.7	14.0
COD03N		8.0	9.1	7.0	9.3	8.3
TUM05N		6.5	4.3	3.9	6.4	5.3
Ro99	median	16.1	11.0	14.3	14.7	14.0
COD03N		5.0	8.0	5.4	4.3	6.0
TUM05N		4.5	3.0	3.5	3.0	3.6

Tab. 8.12: Absolute coefficient differences of the GPS-derived nutation models Ro99, COD03N, and TUM05N with the IAU2000A model. *Type* indicates whether these differences are *mean* or *median* values of all estimated coefficients. The column *All* stands for the mean/median of all estimated coefficients.

The coefficients of this GPS-derived nutation model TUM05N are listed in Appendix E. The formal errors of the TUM05N coefficients vary between 4 and 15 μas for $\delta\epsilon$ and between 10 and 38 μas for $\delta\psi$ for periods at 4 and 15 days, respectively. Compared to Rothacher et al. (1999a), this is an improvement of almost a factor of two. To demonstrate the benefits of the reprocessed nutation series, the model COD03N based on the operational CODE series shown in Fig. 8.15 (covering the time period from 22 April 1994 till 21 June 2003) has been estimated with the same options as for TUM05N. The COD03N formal coefficient errors range from 5 to 17 μas for $\delta\epsilon$ and from 11 to 44 μas for $\delta\psi$ for periods at 4 and 15 days, respectively.

The differences of COD03N and TUM05N w.r.t. the IAU2000A model are given in Fig. 8.20. The twofold formal errors of the estimates are indicated by solid lines. As the parameter estimation of GPS-derived nutation models is based on nutation rates, the formal errors as well as the differences of the estimated coefficients w.r.t. IAU2000A get larger with increasing period. However, only three coefficients of TUM05N exceed the 2σ limit, all of them at longer periods (12.81, 14.77, and 15.91 days). On the other hand, 10 coefficients of COD03N exceed the 2σ limit (that is slightly larger due to the shorter time period of the input data), some of them also at shorter periods.

The mean as well as the median absolute differences of the COD03N and TUM05N coefficients w.r.t. the IAU2000A model are listed in Tab. 8.12. In addition, the model Ro99 described by Rothacher et al. (1999a) is included. This model was computed from 3.5 years (22 April 1994 till 27 October 1997) of the operational CODE nutation rate series. In particular due to the limited length of the input time series, the small number of stations, and the worse orbit quality in the early years, the differences of Ro99 w.r.t. the IAU2000A model are much larger compared to COD03N and TUM05N. The largest improvement between COD03N and TUM05N of a factor of more than two can be achieved for the $\delta\epsilon^c$ coefficients. For the other coefficients, the improvement ranges from 10 to 44%. Although a significant improvement of the nutation model computed from the reprocessed nutation rate time series compared to the operational CODE series could be achieved, systematic effects are still a problem. As already mentioned in Sec. 4.3.2, a more sophisticated orbit modeling could reduce these systematic effects and contribute to improved GPS-derived nutation models.

9. Antenna Phase Center Models and their Influence on Global GPS Solutions

As already described in Sec. 2.8, the GPS Antenna Phase Center Model (APCM) consists of phase center offsets and phase center variations for receiver and satellite antennas. Due to other larger error sources, receiver antenna PCVs could be neglected in the early years of the IGS. The CODE IGS AC started to apply relative PCVs in June 1996 (see Tab. 1.2). More than a decade later (in November 2006), the IGS switched to an absolute APCM for receiver *and* satellite antennas. This section describes different APCMs and discusses their influence on selected parameters of global GPS solutions. In particular, the benefits of absolute APCMs will be outlined.

9.1. Calibration of Receiver and Satellite Antennas

Phase center offsets and variations for receiver antennas can be retrieved by

- relative field calibrations w.r.t. a reference antenna on short baselines,
- absolute field calibrations using a robot or by
- anechoic chamber measurements (also resulting in absolute calibration values).

For relative field calibrations usually a baseline length of up to about ten meters between the reference antenna and the antenna to be calibrated is used. The National Geodetic Survey (NGS) of the United States has calibrated a large number of antennas¹ applying this method (*Mader, 1999*). The result of this type of calibration is a relative phase center model w.r.t. the reference antenna. The reference antenna of the IGS is the Dorne Margolin T (AOAD/M.T) antenna, implying the arbitrary assumption that the PCVs of this antenna are zero. Due to the higher noise of observations at low elevations, only PCVs down to an elevation of 10° can be determined. The inhomogeneous distribution of observations, multipath and other possible site-dependent effects further decrease the accuracy of this calibration method resulting in a PCV repeatability of a few millimeters. Usually, only PCVs with zenith-dependence (not considering the azimuth-dependence) are determined by the relative field calibration although the azimuth-dependent part could be determined by equally rotating both antennas. When using these relative antenna corrections, the PCVs of the transmitting antennas are ignored. The offsets of the transmitting antennas w.r.t. the center of mass of the satellite are assumed to be equal within the Block I, II/IIA, and IIR satellites (no distinction between Block IIR-A and IIR-B, see Sec. 2.1).

An absolute receiver APCM can be determined by field calibrations using a robot or by anechoic chamber measurements. The robot calibration method has been developed by the University of Hannover and the company Geo++ GmbH (*Menge et al., 1998*): the antenna to be calibrated receives real GPS signals and is mounted on a robot rotating and tilting the antenna. Therefore, this method is capable of determining elevation- and azimuth-dependent PCVs down to 0°. Multipath effects can be eliminated or determined by repeating the calibration after one sidereal day and differencing the observations, by using triple differences or by estimating multipath parameters as stochastic processes. The repeatability of PCVs determined by robot calibrations is 0.3–0.4 mm for elevations above 10° and about 1 mm below 10° (*Wübbena et al., 2000*). The calibration values provided to the IGS are usually type means of several individual antennas. For the chamber calibrations (*Campbell et al., 2004*), multipath effects are minimized by the anechoic environment of the chamber. A directional helix antenna with negligible PCVs transmits a monochromatic carrier wave generated by a frequency synthesizer. This signal is received by the antenna to be calibrated. By comparing the phase of the signals from the transmitter with the signals received by the test antenna with a network analyzer, the PCVs can be determined. Rotating the test antenna around two axes enables the determination of zenith- and azimuth-dependent PCVs. The accuracy of this method is better than 1 mm for elevations

¹<http://www.ngs.noaa.gov/ANTCAL/>

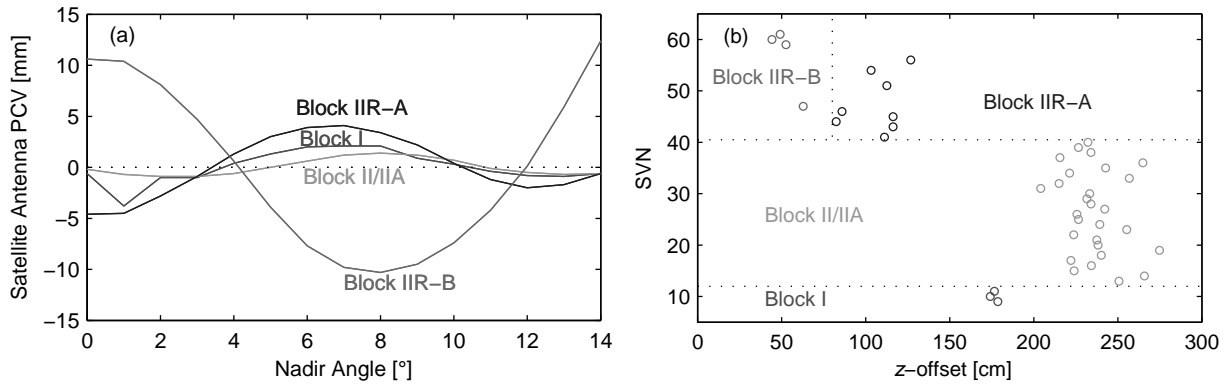


Fig. 9.1: Satellite antenna phase center variations and z -offsets for the ionosphere-free linear combination L_3 used for solution TUM05: (a) block-specific satellite antenna PCVs for Block I, II/IIA, IIR-A and IIR-B satellites; (b) satellite-specific z -offsets.

above 10° and 2 mm below 10° (Zeimetz and Kuhlmann, 2006). The two absolute calibration methods are completely independent from each other and show a good agreement on the level of 1 mm (Görres et al., 2006). If the absolute PCVs of the reference antenna are known, relative APCMs can be converted to absolute APCMs (Schmid et al., 2007).

An initial problem when introducing absolute receiver antenna PCVs in global GPS solutions was a large scale offset w.r.t. the ITRF (Springer, 2000; Rothacher, 2001). This problem could be solved by additionally considering the PCVs of the satellite antennas which are neglected in the relative model. Absolute satellite antenna PCVs and PCOs can be estimated from global GPS data introducing an absolute APCM for the receiver antennas (Schmid and Rothacher, 2003). Due to the high correlations of the PCVs, the PCOs and the terrestrial scale, these parameters cannot be determined simultaneously. Either PCVs or PCOs can be determined in one estimation step in which the terrestrial scale has to be fixed (e.g., with a NNS condition, see Sec. 2.4.2) to a certain reference frame (IGb00 for the satellite APCMs described below). As the PCVs of the individual satellites within one block type are quite similar, block-specific mean values for Block I, II/IIA, IIR-A and IIR-B satellites have been determined. The same PCVs are used for Block IIR-B and IIR-M satellites as the Block IIR-M satellites are equipped with the same antenna panel as the Block IIR-B satellites (the PCVs of the Block IIR-M satellites indeed do not significantly differ from the Block IIR-B satellites). The precision of these block-specific PCVs is on the sub-millimeter level. Differences of the individual satellites within one block type are accounted for by satellite-specific vertical (z -direction) offsets that can be determined with an accuracy of several centimeters. For the horizontal satellite antenna PCOs, the block-specific values provided by the satellite manufacturer (and also used by the IGS, see Tab. 7.1) are used in the absolute models as well as in the relative model.

The satellite antenna PCVs and PCOs used for reprocessing run M3 (that have been estimated from data of run M1) are shown in Fig. 9.1, the numerical values are given in Tab. 3.2 and 3.3. Further details on the estimation of satellite antenna PCVs and PCOs are given in Schmid et al. (2007). In particular the Block IIR-B satellites show large PCVs that significantly differ from those of the Block IIR-A satellites. The differences of the z -offsets within one satellite block reach values of up to 70 cm for the Block II/IIA satellites. The satellite antenna PCVs (Fig. 9.1a) as well as the z -offset differences within one satellite block are ignored when applying the relative APCM. This simplification causes systematic errors that exceed the accuracy of the GPS technique. Zhu et al. (2003) and Ge et al. (2005) analyzed the influence of different satellite antenna offsets on the global scale and could demonstrate systematic effects for the relative APCM due to the change of the satellite constellation. Schmid et al. (2005) and Schmid et al. (2007) showed first results of the influence of an absolute APCM for receivers and satellites on global GPS solutions. Further details on the influence of different APCMs on the reference frame, station coordinate time series, troposphere parameters, satellite orbits and ERPs will be discussed in the next section.

9.2. Effects on Global Solutions

To study the influence of different APCMs on global GPS solutions, altogether six different solutions have been computed (see Tab. 9.1). All the solutions cover the time interval from 1 January 1994 till 31 December

Solution	Type	Receiver Antenna Model			Satellite Antenna Model		
		zen.-dep.	az.-dep.	radomes	zen.-dep.	az.-dep.	sat.-spec.
		PCVs	PCVs		PCVs	PCVs	z-offsets
IGS01	rel.	x	–	–	–	–	–
TUM04	abs.	x	x	–	x	–	–
TUM05	abs.	x	x	–	x	–	x
IGS05	abs.	x	x	x	x	–	x
IGS05woR	abs.	x	x	–	x	–	x
IGS05azi	abs.	x	x	x	x	x	x

Tab. 9.1: Global 1-day solutions applying different **APCMs**. Solution IGS05 is identical to solution IMF in Tab. 6.1.

2004 (altogether 4018 days) and are completely identical except for the **APCM** used. IGS01 is the relative phase center model provided by the **IGS**² that was used by the **IGS ACs** till November 2006 (the block-specific satellite antenna offsets are given in Tab. 7.1). TUM04 is an early **TUM** phase center model based on reprocessing run M0 with block-specific satellite antenna **PCVs** and *z*-offsets. TUM05 additionally takes the *z*-offset differences of the individual satellites into account. It is based on reprocessing run M1, but **IMF** was used instead of **NMF** to generate a consistent satellite **APCM** for reprocessing run M3 also applying **IMF**. TUM05 was also used for the generation of the official **IGS** absolute phase center model called IGS05 which is a combined solution of **TUM** and **GFZ** (*Schmid et al., 2007*). Additionally, in IGS05 the drift of the *z*-offsets (about 2 cm/y, caused by the scale rate of IGB00) is corrected for and all offsets are referred to the epoch 2000.0. The preliminary version *igs_test05*³ that was used for solution IGS05 also includes calibrations for 22 antenna/radome combinations: 10 of them are absolute calibrations by Geo++ GmbH (zenith- and azimuth-dependent), the others converted relative calibrations by **NGS** (zenith-dependent and down to 10° elevation only).

In the more recent versions of IGS05 (*igs05_www.atx*⁴, **www** stands for the **GPS** week of the latest update), the **GPS** satellite antenna **PCVs** and **PCOs** are the same as in *igs_test05.atx*, but more receiver antenna and antenna/radome calibrations, recently launched **GPS** satellites as well as **GLONASS** satellites are included. E.g., *igs05_1365.atx* contains altogether 151 different receiver antennas, 106 without radome (32 of them robot calibrations) and 45 antenna/radome calibrations. Solution IGS05woR is identical to IGS05 except for ignoring the calibrated antenna/radome combinations. For solution IGS05azi also block-specific azimuth-dependent **PCVs** for the satellite antennas determined by *Schmid et al. (2005)* are included. The receiver antenna calibration values for the **TUM** models and the IGS05 models are identical, respectively. However, in contrast to the IGS05 models, the **TUM** models do not comprise antenna/radome calibrations. All the solutions described above are based on the cleaned **SD**-files of the 1-day solutions with fixed ambiguities. The final parameter estimation step (with an identical parameter setup as for the standard 1-day solution) was repeated applying the corresponding **APCM**. After pre-eliminating troposphere and orbit parameters, **NEQs** containing station coordinates and **ERPs** have been saved for the reference frame solutions described in the next section.

9.2.1. Reference Frame

Based on the **NEQs** of the solutions described above, reference frame solutions, coordinate and **ERP** time series covering the time interval from 1 January 1994 till 31 December 2004 (4018 days) have been computed according to the strategy described in Sec. 5.3. Data of IGB00 stations affected by the earthquakes on 23 and 26 December 2004 (DGAR, HOB2, NTUS) was included before, but excluded after the corresponding earthquakes. Thus, the number of stable datum stations (not affected by discontinuities) is 66. Tab. 9.2 compares these reference frames with IGB00. Translations, rotations, scale and the corresponding rates were determined by a 14-parameter similarity transformation (Eq. 5.1) of the datum stations.

The offsets of the translations and the rotations are generally smaller for IGS01, probably due to the fact that IGB00 was computed from solutions that also applied the relative **APCM**. The translations and rotations of the solutions with absolute **APCMs** are very similar except for the *x*-translation and the *z*-rotation of

²ftp://igs.cb.jpl.nasa.gov/igs01/station/general/igs_01.pcv

³ftp://igs.cb.jpl.nasa.gov/igs05/station/general/pcv_proposed/igs_test05.atx

⁴<ftp://igs.cb.jpl.nasa.gov/igs05/station/general/>

Solution	dX	dY	dZ	rX	rY	rZ	Scale
	[mm]	[mm]	[mm]	[mas]	[mas]	[mas]	[ppb]
	dX rate	dY rate	dZ rate	rX rate	rY rate	rZ rate	Scale rate
	[mm/y]	[mm/y]	[mm/y]	[mas/y]	[mas/y]	[mas/y]	[ppb/y]
IGS01	1.2±0.4	6.3±0.4	0.1±0.4	-0.084±0.032	0.026±0.033	0.021±0.036	0.98±0.07
	0.3±0.4	2.8±0.4	-2.8±0.4	-0.058±0.032	0.023±0.033	0.010±0.036	0.34±0.07
TUM04	-2.6±0.4	8.7±0.4	-5.4±0.4	-0.170±0.032	0.011±0.034	0.079±0.036	-0.78±0.07
	0.6±0.4	1.4±0.4	-1.0±0.4	-0.027±0.032	0.015±0.034	0.000±0.036	0.16±0.07
TUM05	-4.1±0.4	9.2±0.4	-5.4±0.4	-0.173±0.032	-0.009±0.033	0.099±0.035	-0.16±0.07
	0.4±0.4	1.4±0.4	-1.8±0.4	-0.033±0.032	0.018±0.033	0.001±0.035	0.08±0.07
IGS05	-4.6±0.4	9.1±0.4	-5.3±0.4	-0.170±0.032	-0.018±0.033	0.106±0.035	0.20±0.07
	0.4±0.4	1.4±0.4	-1.8±0.4	-0.034±0.032	0.017±0.033	0.002±0.035	0.12±0.07
IGS05woR	-3.8±0.4	9.1±0.4	-4.8±0.4	-0.166±0.031	-0.009±0.032	0.095±0.034	0.20±0.06
	0.5±0.4	1.4±0.4	-1.6±0.4	-0.031±0.031	0.017±0.032	0.001±0.034	0.12±0.06
IGS05azi	-4.7±0.4	8.9±0.4	-5.4±0.4	-0.167±0.031	-0.019±0.032	0.104±0.034	0.26±0.07
	0.3±0.4	1.4±0.4	-1.8±0.4	-0.033±0.031	0.017±0.032	0.002±0.034	0.12±0.07

Tab. 9.2: Offsets and rates of the translations, the rotations and the scale of solutions with different **APCMs** w.r.t. IGB00 obtained from a 14-parameter similarity transformation of the corresponding reference frames. The epoch of the offsets is 1 January 2000.

TUM04. Compared to IGS01, the rates of all the transformation parameters (except for the x -translation) are significantly smaller for the **TUM** and IGS05 solutions indicating that the absolute **APCMs** can provide a more stable realization of the terrestrial reference system. The largest differences in the transformation parameters occur for the scale offset and its rate. TUM05 provides the smallest scale offset together with the smallest drift. The scale offset of IGS01 is almost 1 ppb and its rate is 0.34 ppb/y. Compared to IGS01, the scale offset of the absolute **APCM** TUM04 (including block-specific satellite antenna z -offsets) is about 20% smaller and its rate is smaller by a factor of more than two. By additionally taking into account the individual satellite antenna z -offsets within one block type (solutions TUM05 and IGS05), the scale offset can be reduced by a factor of 5 and the corresponding drift by a factor of 3–4. With 0.08 ppb/y, the scale drift of TUM05 is even one third smaller than the drift of IGS05. This is probably due to the fact that for TUM05 the same software was used for the determination of the phase center model and the reference frame. The reduced scale offset and drift w.r.t. IGB00 of the absolute **APCMs** compared to the relative model is the most striking advantage of the absolute models.

As the five **TRFs** computed with absolute **APCMs** only differ slightly from each other, the **TRF** inter-comparison is limited to the solutions IGS01 and IGS05. The coordinate and velocity residuals after a 14-parameter similarity transformation between these two solutions are shown in Fig. 9.2. The horizontal residuals are below 5 mm as regards the coordinates and below 1 mm/y as regards the velocities, the vertical component ranging from -16 to +8 mm and from -2.5 to +2.5 mm/y, respectively. In some areas (e.g., Europe, East and West Coast of the United States) the coordinate and velocity residuals show a regional geographic correlation. In other regions (e.g., Australia) only the coordinate residuals show a geographic correlation whereas the velocity residuals seem to be quite random. The reasons for this behavior are difficult to explain as there are several important differences between IGS01 and IGS05: the consideration of satellite antenna **PCVs**, satellite-specific vertical **PCOs**, azimuth-dependent receiver antenna **PCVs** and radome calibrations. In addition, changes in the antenna configuration of a particular station and the inhomogeneous distribution of stations might affect the residuals.

However, clear correlations of the residuals with the antenna type are not evident. Fig. 9.3 shows the height residuals for datum stations with the same antenna/radome configuration for the three most commonly used antenna types. The height residuals range from -10 to +8 mm indicating that also the station-specific environment of the antenna and not only the antenna type itself influences the station height changes.

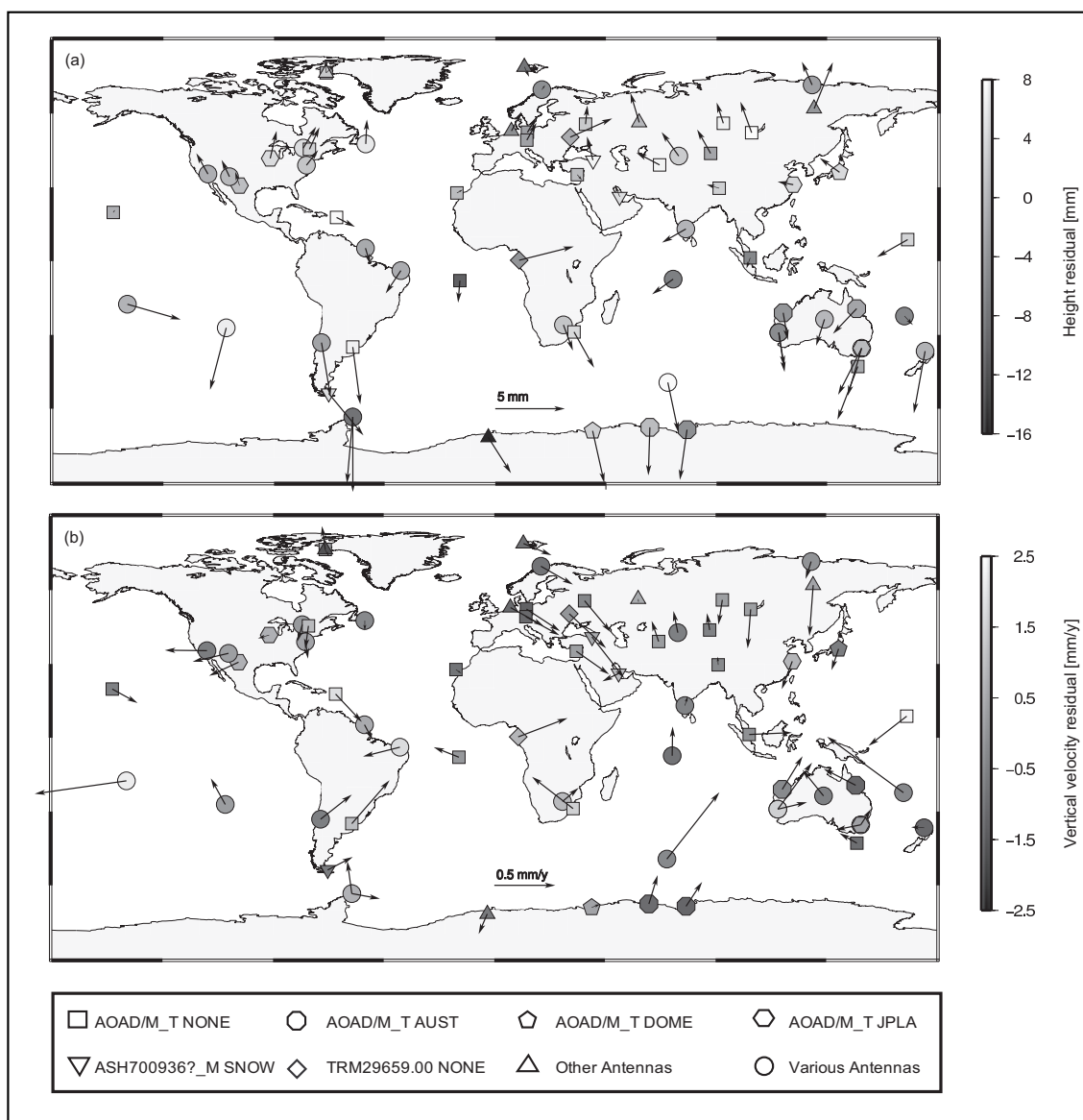
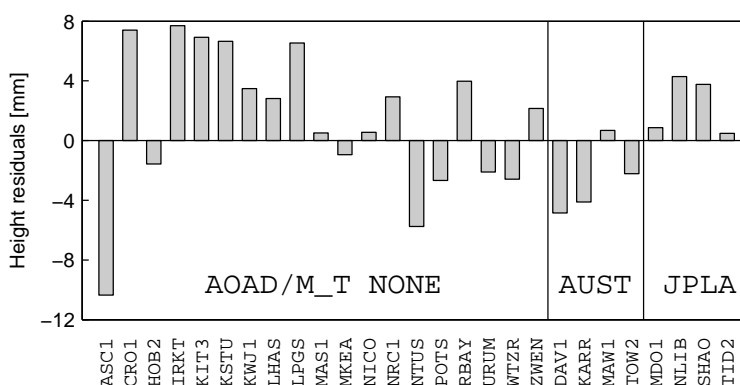


Fig. 9.2: Residuals of a 14-parameter similarity transformation between the solutions IGS01 and IGS05: (a) coordinate residuals; (b) velocity residuals. Only the 66 datum stations used for the estimation of the transformation parameters are shown.

Fig. 9.3: Station height residuals of a 14-parameter similarity transformation between the solutions IGS01 and IGS05 for datum stations with the same antenna/radome configuration. Only the three most commonly used antennas AOAD/M_T NONE, AOAD/M_T AUST and AOAD/M_T JPLA are shown. No radome calibration was applied for the AUST and JPLA radomes.



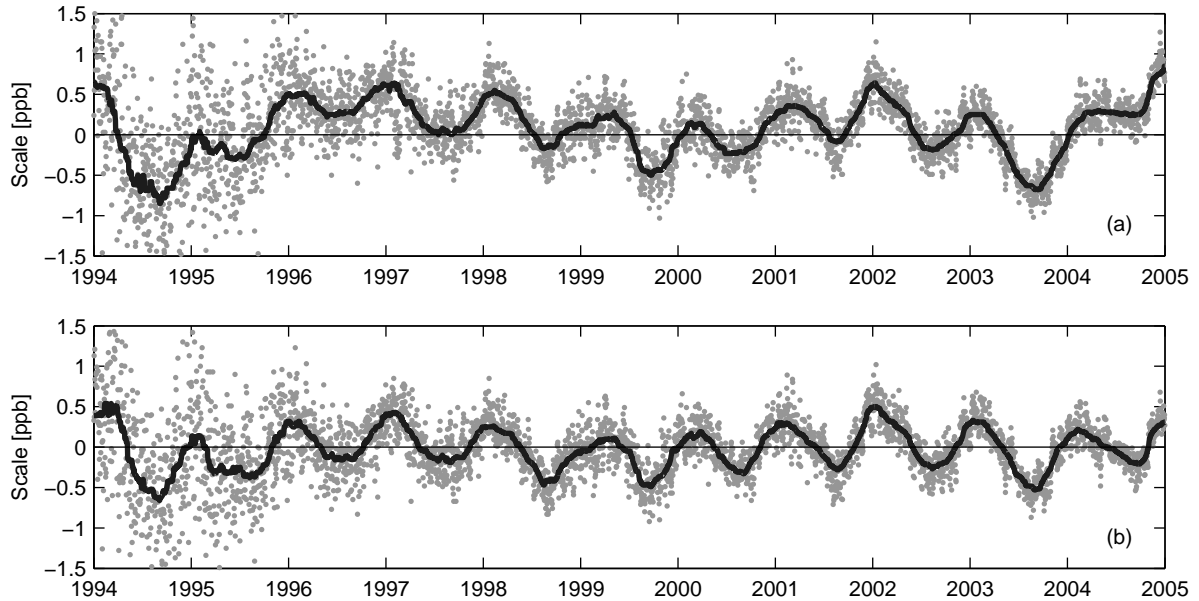


Fig. 9.4: Scale time series of the solutions IGS01 (a) and IGS05 (b) w.r.t. the corresponding reference frames. The solid lines were smoothed with an 80-day median filter.

Terrestrial Scale

The large scale drift of the relative model and the biggest drift of TUM04 amongst the absolute models can be explained by erroneous vertical satellite antenna offsets combined with changes in the satellite constellation (*Ge et al., 2005*). According to *Zhu et al. (2003)* the effect of applying incorrect z -offsets on the global scale Δs in ppb can be described by the empirically determined rule of thumb

$$\Delta s = -7.8 \sum_{i=1}^n \frac{\Delta b_i}{n} \quad (9.1)$$

where Δb_i is the difference between the true z -offset and the offset applied for satellite i in meters and n is the number of satellites. This scale error changes, whenever the satellite constellation changes. Eq. 9.1 cannot be applied to the results discussed in this section as only the effect of different offsets is taken into account. As for the solutions listed in Tab. 9.1 also different PCVs have been applied, only a qualitative analysis of the results is possible. Fig. 9.4 shows the scale time series w.r.t. the corresponding reference frames of the solutions IGS01 and IGS05. Only the datum stations have been used for the estimation of the scale factor within a 7-parameter similarity transformation (Eq. 2.17). As the scale has been determined w.r.t. the TRF computed from the same solution, no drift is contained in the scale time series.

Compared to Block IIR-A, the z -offsets of the Block IIR-B satellites are smaller by a factor of about two (see Fig. 9.1b). As identical z -offset values are applied for Block IIR-A and IIR-B in solution IGS01 (see Tab. 7.1), the scale behavior of this solution changes dramatically the more of these satellites are in orbit (four IIR-B satellites were launched between December 2003 and November 2004, see Tab. 4.2). The different scale behavior between 1994 and 1996 cannot be explained by changes in the satellite constellation. The reason for that effect is unknown; a possible explanation might be the sparse tracking network that is also responsible for the larger scatter in these years.

9.2.2. Station Coordinate Time Series

The histograms in Fig. 9.5 show the mean coordinate changes for all stations between the solutions IGS01 and IGS05 (mean differences of coordinate time series). Reference frame effects have been removed by daily three-parameter similarity transformations (translations only). The changes in the horizontal component range from -8 to $+6$ mm for the north and -5 to $+5$ mm for the east component. A major part of these changes might be caused by considering azimuth-dependent receiver antenna PCVs for solution IGS05 which

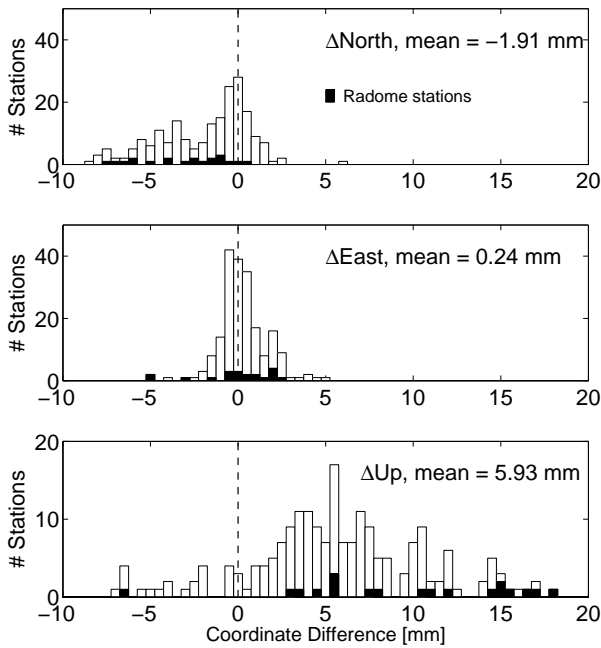


Fig. 9.5: Histograms of the mean coordinate changes between the time series with a relative (IGS01) and an absolute APCM (IGS05). Sites with calibrated antenna/radome combinations are given in black. Three stations with height changes larger than 20 mm (PIMO: 20.8 mm, CONZ: 24.0 mm, GOUG: 28.3 mm) are not displayed.

are ignored in solution IGS01. The large mean change in the height component of +6 mm is primarily related to the scale difference between the two solutions (see Tab. 9.2): the scale difference of 0.78 ppb between the solutions IGS01 and IGS05 corresponds to 5 mm at the Earth’s surface. With -7 to $+28$ mm, also the spectrum of changes in the station height is much larger than for the horizontal component. In particular, some sites with calibrated radomes show large height changes that will be discussed in the next paragraph. It is important to note that the coordinate changes shown in Fig. 9.5 are mean values for a time period of up to 11 years (depending on the observation time of a particular station). On shorter time scales, the differences can be much larger. E.g., *Ferland (2008)* reported a station height change derived from the IGS parallel processing with relative and absolute APCMs of 93.2 mm for Gough Island. The mean height change of GOUG for the time period between 1998 and 2004 from the reprocessing is 28.3 mm. However, after a discontinuity of unknown origin in October 2004, the height difference of the reprocessed series is 90.8 mm. Fig. 9.6 shows the time series of the differences in the station height between the solutions IGS01 and IGS05 as well as the observation rate of the receiver at Gough Island. Before the end of 2001, the tracking rate is quite constant and the height difference only shows a small rate due to the different scale rates of both solutions (see Tab. 9.2). Starting with September 2001 the observation rate rapidly decreases accompanied by an increasing difference in the station height. The station height difference is anti-correlated to the observation rate. In particular, the sharp peak in December 2001 and the bump at the beginning of 2004 can be clearly seen in both time series. At the end of 2004, the coordinate difference reaches values of up to 10 cm. This example impressively shows that even station-specific corrections determined from a limited time interval (like in the IGS parallel processing) are not appropriate for all stations to correct for the coordinate differences induced by different APCMs.

The mean coordinate repeatabilities of weekly solutions based on 1-day NEQs for the year 2004 are given in Tab. 9.3. As regards the horizontal components, there is almost no difference between the various APCMs. The differences of the height component are quite small, but the relative model shows a slightly worse repeatability compared to the absolute models. Although the differences between the absolute models are extremely small, the most sophisticated model IGS05azi shows the smallest repeatabilities for all three coordinate components. The repeatabilities of the time series solutions w.r.t. the TRF solutions already described above are shown in Tab. 9.4. These repeatabilities are larger by a factor of about two compared

Solution	North [mm]	East [mm]	Up [mm]
IGS01	1.66	1.70	5.53
TUM04	1.63	1.67	5.36
TUM05	1.62	1.66	5.27
IGS05	1.62	1.65	5.26
IGS05woR	1.62	1.65	5.27
IGS05azi	1.61	1.64	5.25

Tab. 9.3: Mean coordinate repeatabilities of weekly solutions computed from 1-day NEQs for 2004.

Solution	North [mm]	East [mm]	Up [mm]
IGS01	3.78	4.38	9.77
TUM04	3.76	4.28	9.53
TUM05	3.73	4.26	9.40
IGS05	3.72	4.26	9.37
IGS05woR	3.72	4.26	9.39
IGS05azi	3.67	4.23	9.27

Tab. 9.4: Mean coordinate repeatabilities for combined TRF solutions (1994 till 2004) based on 1-day NEQs.

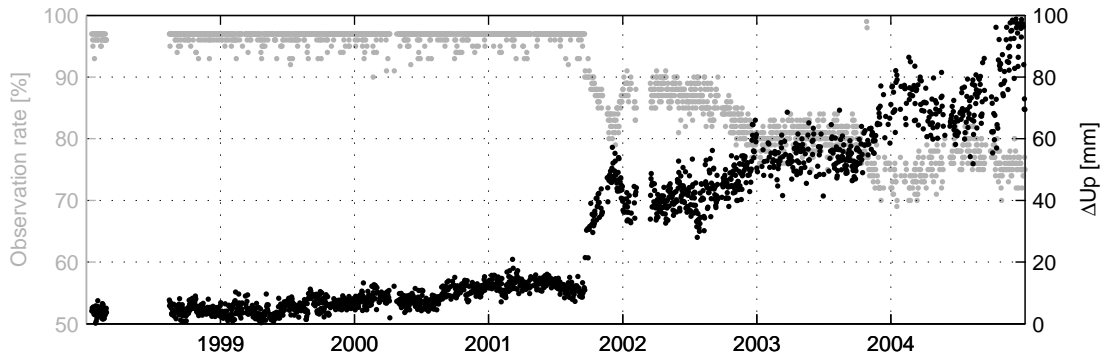


Fig. 9.6: Observation rate and station height difference between the solutions IGS01 and IGS05 for Gough Island (Antarctica).

to the weekly solutions as all signals in the station coordinate time series deviating from the linear model of the TRF solution (e.g., atmospheric and hydrological loading) lead to increased repeatability values. Like for the weekly solutions, the differences of the horizontal repeatabilities are very small. Compared to IGS05azi, the height repeatability of IGS01 is 0.5 mm worse indicating that the model deficiencies of the relative APCM introduce artificial signals that degrade the coordinate time series.

Effect of Radome Calibrations

The effect of radome calibrations can be studied in more detail by comparing the solutions IGS05 and IGS05woR. All sites of the network that tracked the GPS observations with a calibrated antenna/radome combination (unfortunately only 21 out of 108 sites that were at least temporarily equipped with a radome) are listed in Tab. 9.5. For each site, the mean coordinate changes in a local system between the solutions IGS05 and IGS05woR are given. For all the corresponding antennas without radome whose radome variants are listed in Tab. 9.5, absolute robot calibrations with elevation- and azimuth-dependence are available. For some combinations (indicated by a "c") only converted relative calibrations with pure elevation-dependence are available.

In the case of an identical or a similar antenna (e.g., antennas of the group ASH700936?_M are equally constructed), the coordinate changes are very similar for most of the sites. The horizontal changes are on the level of up to 1 mm for most sites whereas the height changes range from about -1 to $+1.5$ cm. E.g., the SNOW radome causes a mean height change of 6.8 ± 1.2 mm for the Ashtech antennas ASH700936?_M. It is worthwhile to mention that the height changes of sites with the converted ASH700936A_M calibrations do not significantly differ from those of sites with robot-calibrated ASH700936 antennas. The horizontal changes are smaller than 1 mm except for the antenna ASH700936C_M, where the east component changes by more than 4 mm. For the antenna ASH700936E the height change is larger by a factor of almost two compared to the other ASH700936 antennas. For the two sites equipped with a SCIT radome, the height change is the smallest and also the height change caused by the LEIS radome is much smaller than that of the SNOW radome. This fact might be explained by the shape of the radomes: in general spherical radomes (LEIS, SCIS, SCIT, UNAV) have a smaller influence on the phase center position than conical radomes (SNOW and TCWD). However, the UNAV radome causes height changes of more than 1 cm despite the spherical shape. The antenna TRM29659.00 together with a TCWD radome shows the largest difference between the height changes of sites equipped with the same antenna/radome combination: for GOUG the height changes by almost $+1.5$ cm and VESL is the only site with a negative height change when ignoring the radome calibrations. VESL is also the only station with a positive height change when switching from IGS01 to IGS05 (not shown here). This strange behavior has also become evident in the IGS parallel processing with the relative and the absolute IGS APCMs (Gendt, 2005) and might be caused by site-specific effects.

Both sites with the TRM29659.00 antenna and the UNAV radome also show large shifts in the horizontal components: about 4.5 mm for the north and 6.5 mm for the east component. These changes are caused by deficiencies of the calibration of the antenna with radome: whereas the calibration of the antenna *without* radome is a robot calibration including zenith- and azimuth-dependent corrections, the calibration *with* radome is a converted field calibration with zenith-dependent corrections down to 10° only. Neglecting the azimuth-dependence of the PCVs is the explanation for the significant horizontal as well as vertical (about

Antenna	Cal.	Site	Start	End	ΔN	ΔE	ΔU	
ASH700936A_M	SNOW	c	DUM1	20 12 1997		0.5	1.0	5.6
			JOEN	15 06 1995		-0.1	0.6	5.7
ASH700936B_M	SNOW	r	MONP	31 03 1994	22 03 2000	-0.1	0.5	6.1
ASH700936C_M	SNOW	r	RIOG	12 11 1996		-1.1	4.2	6.1
			SCUB	01 04 1998		-2.0	4.3	8.8
			UNSA	03 12 1998	21 05 2001	-1.2	4.7	6.9
ASH700936D_M	SNOW	r	RAMO	10 06 1998	17 07 2000	-0.4	-0.6	6.3
			TRAB	08 12 1999		0.8	-1.1	8.5
ASH700936E	SNOW	r	HNPT	22 05 2000		1.4	1.8	15.9
ASH701945B_M	SCIS	c	MONP	22 03 2000		1.1	1.1	6.7
			SIO3	12 04 2000		1.1	1.1	7.5
ASH701945B_M	SCIT	c	GLPS	06 01 2003		1.9	1.8	0.1
ASH701945B_M	SNOW	c	RAMO	17 07 2000		0.4	-2.5	9.3
ASH701945C_M	SCIT	c	BREW	08 11 2001		0.8	1.7	2.9
ASH701945C_M	SNOW	r	KIRU	12 03 2003		-0.4	-1.4	7.0
ASH701946.3	SNOW	r	GOPE	04 10 2000		-2.5	0.4	12.8
LEIAT504	LEIS	r	MALD	12 08 1999		-0.9	-1.9	3.4
TRM29659.00	TCWD	r	GOUG	08 01 1998		0.6	-1.7	14.5
			VESL	18 12 1997		-0.4	-2.5	-10.6
TRM29659.00	UNAV	c	MANA	13 05 2000		-3.9	-6.1	12.5
			SCOB	07 08 1997	26 07 2004	-4.9	-7.3	10.0

Tab. 9.5: Sites with calibrated antenna/radome combinations and the effect of different [APCMs](#) on their station positions. Position changes between the solutions IGS05 with and IGS05woR without radome calibrations are given in millimeters. The column *Cal.* indicates whether the calibration of the antenna/radome combination is an absolute robot calibration with azimuth- and elevation-dependent [PCVs](#) (r) or a converted relative calibration with elevation-dependence only (c). If no end time is given, the antenna/radome combination was still in use on 31 December 2004.

11 mm) displacement of the sites equipped with this type of antenna and emphasizes the importance of a proper and consistent calibration of *all* antenna/radome combinations.

Discontinuities

As already described in Sect. 4.2.2, a large fraction of the discontinuities in [GPS](#) coordinate time series is related to equipment changes (in particular antenna or radome changes) that have to be considered when computing a reference frame solution or analyzing time series. As all coordinate estimates of the [TRF](#) solutions refer to the same epoch, the absolute value of the discontinuities can be directly derived from the differences of the coordinate estimates before and after the discontinuities. The height discontinuities should be especially large when comparing solutions including radome calibrations (IGS05) with solutions ignoring them (IGS01 and IGS05woR) as radomes in particular affect the height component. Unfortunately, the number of discontinuities with changes from an antenna without radome to an antenna with calibrated radome is rather small. The three discontinuities of this type are listed in Tab. 9.6. For the Geodetic Observatory Pecny tracking station (GOPE, Czech Republic) the sign of the height discontinuity differs when comparing IGS05 and IGS01, but the absolute value is only slightly smaller for IGS05. Surprisingly, the discontinuity is smallest when the radome calibration is ignored (IGS05woR). This fact could indicate that the type mean radome calibration is not appropriate for the GOPE antenna due to deviations of the individual antenna or radome from the type mean.

Fig. 9.7 shows the time series of the up component of the Horn Point site (HNPT, USA) for the solutions IGS05woR and IGS05. In May 2000 the [AOAD/M_TA_NGS](#) antenna without a radome was replaced by an ASH700936E antenna with SNOW radome. In the IGS05woR time series a clear discontinuity of -15.8 mm is visible as the result of the non-consideration of the radome. If the radome calibration is considered (IGS05), only a very small discontinuity of -0.5 mm (not significant) remains. For SIO3 (La Jolla, USA) the height change gets significantly smaller when applying the radome calibration, but the height change is still larger than 2 cm. One reason for that large height discontinuity in spite of applying a radome calibration is probably the fact that the antenna/radome calibration for that site is only a converted one.

Site	Date	Ant. before	Ant. after	Sol.	ΔN	ΔE	ΔU
					[mm]	[mm]	[mm]
GOPE	04 10 2000	TRM14532.00	ASH701946.3	IGS05	-4.9	4.7	10.5
		NONE	SNOW	IGS01	-2.6	4.4	-13.6
		Geo++	Geo++	IGS05woR	-2.5	3.8	-2.1
HNPT	22 05 2000	AOAD/M_TA_NGS	ASH700936E	IGS05	-2.4	3.8	-0.5
		NONE	SNOW	IGS01	-4.2	2.4	-15.8
		Geo++	Geo++	IGS05woR	-3.3	3.4	-16.2
SIO3	12 04 2000	AOAD/M_TA_NGS	ASH701945B_M	IGS05	0.0	0.2	-23.4
		NONE	SCIS	IGS01	0.7	0.3	-32.1
		Geo++	NGS conv.	IGS05woR	0.3	0.3	-30.3

Tab. 9.6: Discontinuities due to equipment changes from an antenna without radome to an antenna with calibrated antenna/radome combination for solutions IGS01, IGS05 and IGS05woR.

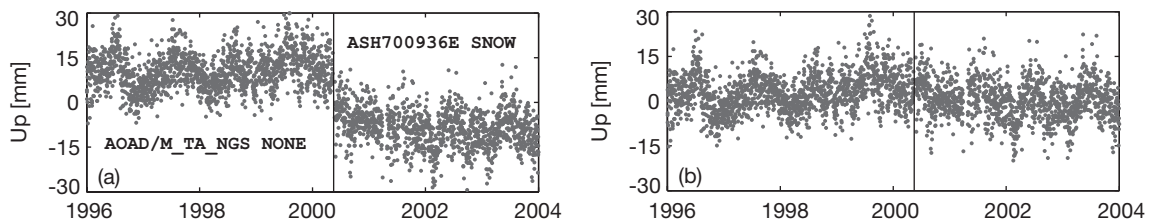


Fig. 9.7: Up component of Horn Point (HNPT): (a) solution IGS05woR: the antenna change from AOAD/M_TA_NGS NONE to ASH700936E SNOW resulting in a discontinuity of -15.8 mm is indicated by a vertical line; (b) solution IGS05: due to a proper calibration of the radome no discontinuity is visible.

All horizontal discontinuities are below 5 mm, in the case of SIO3 even below 1 mm and therefore not significant for this particular site (however, they are smallest for solution IGS05). For GOPE and HNPT, the horizontal discontinuities agree within 2 mm. Like for the vertical component, the horizontal displacement of GOPE is largest for solution IGS05 indicating that there could be some deviation of the individual antenna corrections from the type mean.

These examples again clearly demonstrate the necessity of a proper calibration of all antenna/radome combinations used within the IGS. On the other hand, discontinuities that are related to differences between individual antennas of the same antenna type (manufacturing tolerance) cannot be overcome by using mean values for each antenna type. This problem can only be solved by calibrations for individual antennas which should be a goal for the IGS in the near future.

Elevation Cut-off Angle Dependence

As station heights and antenna phase center corrections are highly correlated, a mismodeling of the phase center corrections induces an elevation cut-off dependence of the estimated station heights (*Hatanaka et al., 2001*). The IGS01 relative APCM shows several deficiencies: (1) the PCVs of the reference antenna AOAD/M_T are assumed to be zero and (2) correction values are only given for elevations down to 10° . Therefore, the PCVs were assumed to be constant for elevations $\leq 10^\circ$ when computing the solution IGS01. *Schmid et al. (2005)* showed for a single global 1-day solution that the scatter of the elevation cut-off angle induced station height changes could be reduced by an absolute APCM. Fig. 9.8 shows histograms for the height changes due to different cut-off angle changes for the solutions IGS05 and IGS01 in October 2002. The histograms show accumulated station numbers for one month, i.e. each daily height change per station contributes to the histogram. Solution IGS05 (including receiver antenna PCVs down to 0°) shows a much sharper histogram than IGS01 when lowering the elevation cut-off angle from 10° to 3° (Figs. 9.8a and 9.8b). The extrapolation of the receiver antenna PCVs below 10° elevation for solution IGS01 causes changes in the station height of up to +20 mm and a mean height change of about +3 mm whereas the maximum height change for solution IGS05 is 10 mm and the mean height change is almost zero. When comparing station heights estimated with cut-off angles of 10° and 15° , the variance of the solutions IGS01 and IGS05 is more

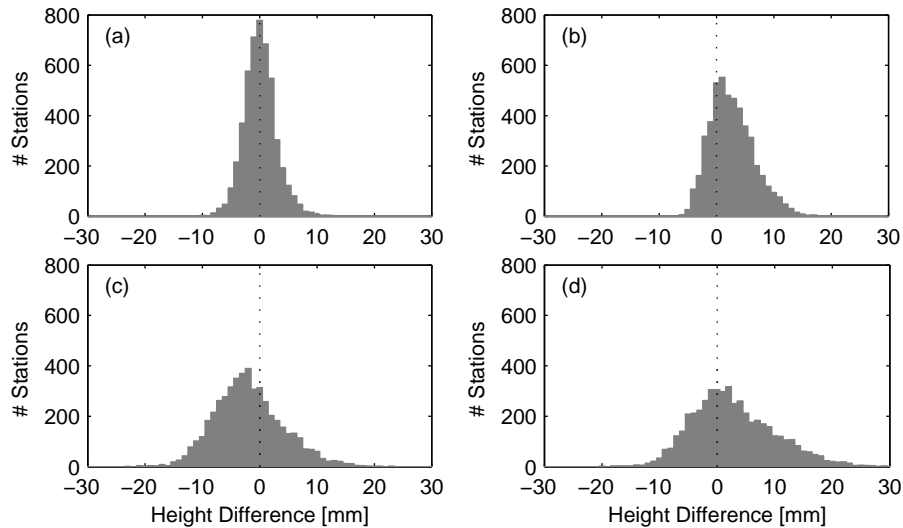


Fig. 9.8: Station height changes between solutions with different cut-off angles and APCMs (October 2002): (a) IGS05 with 3° and 10°, $\Delta h_{\text{mean}}=0.1$ mm; (b) IGS01 with 3° and 10°, $\Delta h_{\text{mean}}=2.7$ mm; (c) IGS05 with 10° and 15°, $\Delta h_{\text{mean}}=-1.9$ mm; (d) IGS01 with 10° and 15°, $\Delta h_{\text{mean}}=2.8$ mm.

similar although the shape of the histogram is still sharper for solution IGS05 and the absolute value of the mean height change is smaller by one third. The remaining height changes of solution IGS05 could be explained by errors of the absolute receiver antenna calibrations or by a mismodeling concerning other parameters or models correlated with the station heights, e.g. the troposphere mapping functions.

9.2.3. Troposphere Parameters

The tropospheric zenith delay is a parameter type that is particularly sensitive to erroneous PCVs as such errors induce an unmodeled elevation-dependent residual signal. As this signal cannot be properly separated from the also elevation-dependent tropospheric delay, erroneous PCVs generate biases in estimated station heights and troposphere zenith delays. Therefore, the comparisons with VLBI troposphere parameters already described in Sec. 6.1.3 allow an independent quality assessment for the effects of different APCMs on the troposphere estimates. The troposphere biases between GPS and VLBI for 25 co-located sites are shown in Fig. 9.9. As for the studies in Sec. 6.1.4, stations with less than 500 common ZWD parameters or with height differences between the two instruments of more than 25 m have been excluded from the comparison and no height correction has been applied for the wet part of the troposphere. The largest mean bias (+6.5 mm) occurs for the relative APCM (solution IGS01). Its absolute value can be reduced by more than a factor of four to -1.5 mm by switching to an absolute APCM with block-specific z -offsets (solution TUM04). A further improvement can be achieved by introducing satellite-specific z -offsets (solution IGS05): the mean bias can be reduced by another factor of five to -0.3 mm. With -0.6 mm, the mean bias of solution TUM05 (not shown in Fig. 9.9) is slightly worse than that of IGS05.

The impact of azimuthal satellite antenna PCVs (IGS05azi) on the troposphere parameters is very small (mean bias of -0.3 mm, the same as for IGS05; standard deviation of the difference between IGS05 and IGS05azi: 0.08 mm; maximum effect of 0.22 mm) and therefore, it will not be discussed here. Brewster (BREW, USA) is the only GPS-VLBI co-location site with a calibrated radome (not shown in Fig. 9.9 due to its small number of 443 common ZWD parameters). By applying this radome calibration, the absolute value of the GPS-VLBI troposphere bias can be reduced from +0.5 to -0.2 mm. For other stations that were partly (e.g., TIDB, FAIR, ONSA and KOKB) or permanently (e.g., CRO1 and FORT) equipped with radomes, the missing calibrations could explain the remaining biases to some extent. On the other hand, Westford (WES2) is a station without a radome but quite a large bias of +4.8 mm. In addition, there are also stations with quite small bias values despite being equipped with an uncalibrated radome (e.g., SHAO and NLIB).

Fig. 9.10 shows the mean differences between GPS ZTD estimates of the solutions IGS01 and IGS05 for all stations sorted by latitude. These biases range from -20 mm (Gough Island, not shown in Fig. 9.10) to

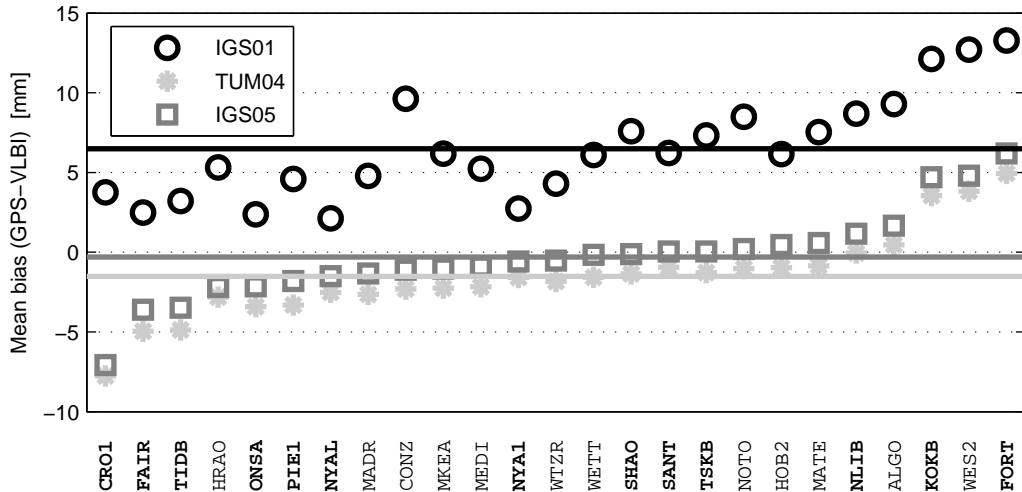


Fig. 9.9: **GPS-VLBI** troposphere biases for different **APCMs**. The mean biases are indicated by horizontal lines: IGS01: +6.5 mm, TUM04: -1.5 mm, IGS05: -0.3 mm. Stations permanently or partly equipped with a radome are given in bold.

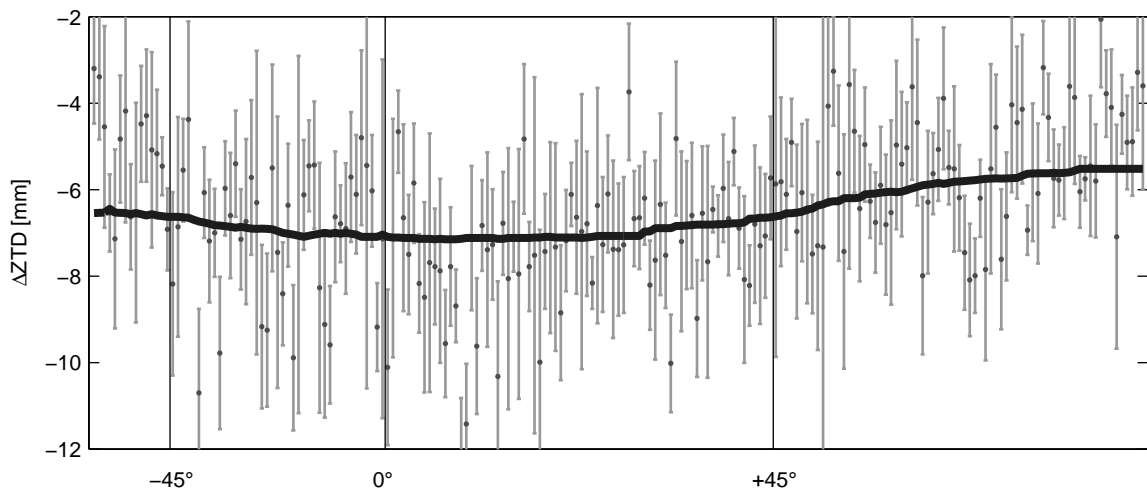


Fig. 9.10: Mean troposphere biases between the solutions IGS01 and IGS05. The stations are sorted by latitude. The error bars indicate the mean scatter for each station. The solid line represents a median value over 50 stations.

-2 mm with a mean value of -6.6 mm. All biases have a negative sign due to the positive scale difference between the solutions IGS01 and IGS05, see Tab. 9.2. The **RMS** values of the **ZWD** difference time series range from 0.5 mm (YAKZ) to 6.2 mm (RIOP) with a mean of 1.7 mm. These quite large biases were one reason for the discontinuation of the combined **IGS** troposphere product (see Sec. 6.1.1) after switching from the relative to the absolute **APCM** in November 2006. The reason for the slight latitude-dependence of the bias values is unknown. However, a relation to the geometry-related observation distribution that also depends on the latitude seems to be possible.

The difference time series of **ZWD** parameters estimated with relative and absolute **APCMs**, respectively, are quite sensitive to equipment changes and changed tracking conditions. As an example, Fig. 9.11 shows the difference time series of the estimated **ZWD** of GOPE for the solutions IGS01 and IGS05. The periods with different tracking equipment are separated by vertical lines. The first antenna/receiver change coincides with a change of the receiver cut-off angle from 15° to 5° resulting in a decreased scatter of the difference time series. The decrease of the absolute **ZWD** difference in the second half of 2001 correlates well with an increase of the observation rate computed by **teqc** from about 80 to 90% (not shown here). The reason for the increasing scatter in the second half of 2004 is unknown.

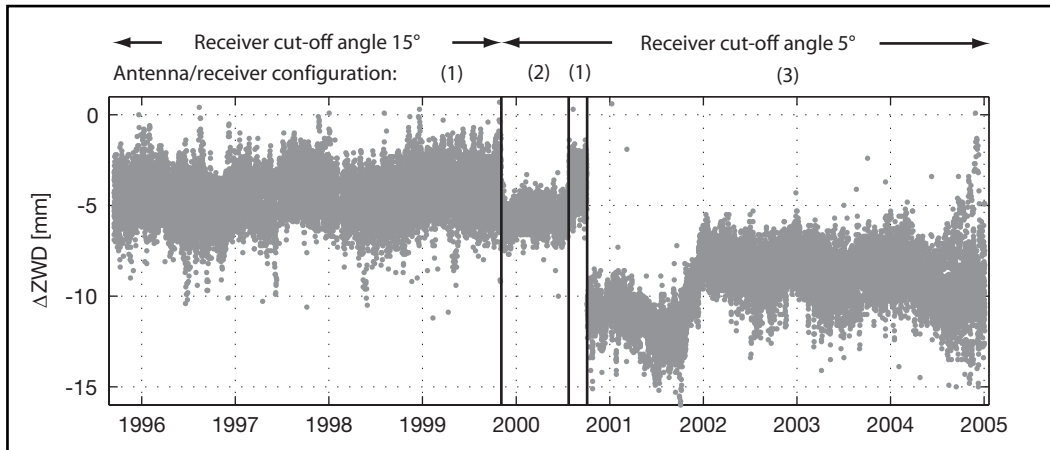


Fig. 9.11: Troposphere ZWD differences between the solutions IGS01 and IGS05 for GOPE. Periods with a different antenna/receiver configuration are separated by vertical lines: (1) TRM14532.00 NONE/TRIMBLE 4000SSE; (2) ASH701073.3 SNOW/ASHTECH Z18; (3) ASH701946.3 SNOW/ASHTECH Z18.

9.2.4. Satellite Orbits

An improved modeling of the satellite antenna phase center also affects the orbit quality. The RMS of a 3-day orbit fit through three consecutive 1-day orbits can be used to quantify the internal orbit consistency of the daily solutions. The mean RMS differences within the 11-year time interval for each individual satellite when switching from a relative (IGS01) to an absolute APCM with block-specific (TUM04) or satellite-specific z -offsets (IGS05) and the effect of azimuthal satellite antenna PCVs (IGS05azi) are shown in Fig. 9.12. A positive sign of the RMS difference indicates an improvement (RMS reduction) of solution 2 compared to solution 1. The Block IIR satellites (in particular the Block IIR-B satellites) show the largest improvement in the orbit consistency due to their large PCV values (see Fig. 9.1a). As no distinction was made between Block IIR-A and Block IIR-B in solution TUM04, a major part of the improvement for the Block IIR-B satellites when comparing the solutions IGS01 and IGS05 (Fig. 9.12b) can be attributed to the consideration of an individual phase pattern for this block type. Only a minor part of the improvement can be due to the consideration of satellite-specific z -offsets as, the offset differences between the individual satellites of this block type are smaller than for the Block II/IIA and IIR-A satellites (see Tab. 3.3 and Fig. 9.1b).

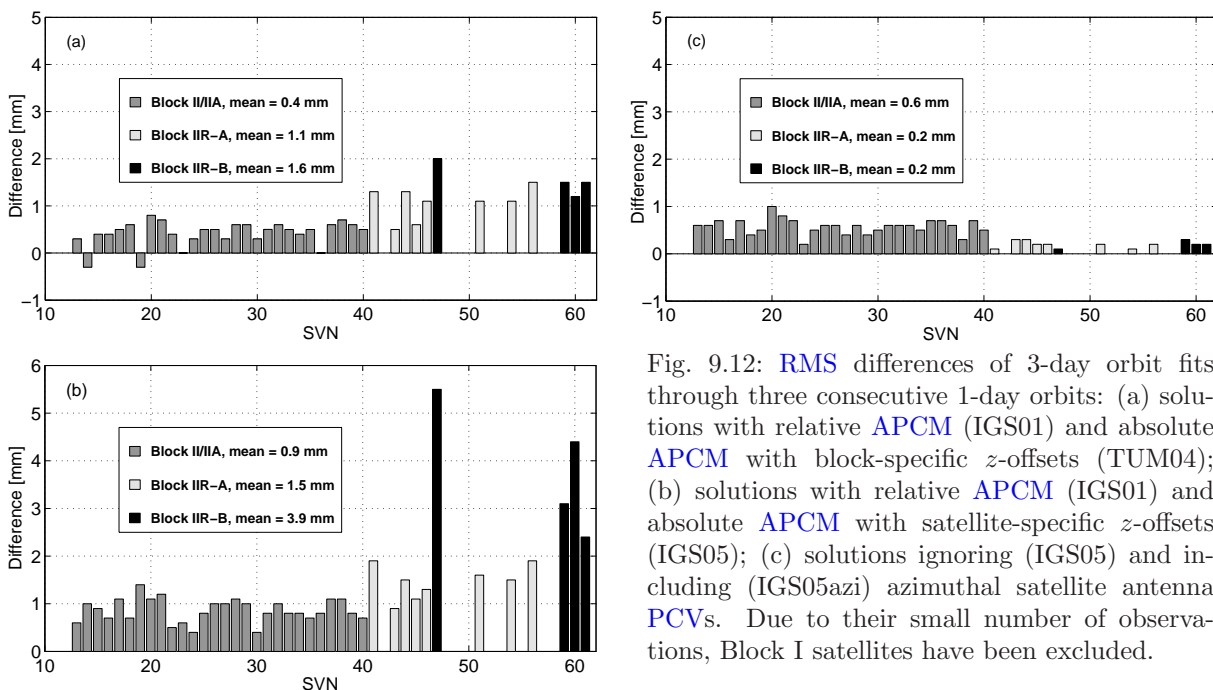


Fig. 9.12: RMS differences of 3-day orbit fits through three consecutive 1-day orbits: (a) solutions with relative APCM (IGS01) and absolute APCM with block-specific z -offsets (TUM04); (b) solutions with relative APCM (IGS01) and absolute APCM with satellite-specific z -offsets (IGS05); (c) solutions ignoring (IGS05) and including (IGS05azi) azimuthal satellite antenna PCVs. Due to their small number of observations, Block I satellites have been excluded.

The comparison of the solutions IGS01 and TUM04 (Fig. 9.12a), shows a degradation for the two Block II satellites with the largest z -offsets (SVN 14 and 19), and for two Block IIA satellites with large z -offsets (SVN 23 and 36) the RMS does not change. By additionally taking into account the z -offset variations within the different satellite blocks the RMS improves by a factor of two for Block II/IIA and by a factor of 1.4 for Block IIR-A, emphasizing the importance of considering individual z -offsets (Fig. 9.12b). The improvements due to considering the azimuthal PCVs of the satellite antennas are smaller than those due to absolute PCVs or satellite-specific z -offsets. However, Fig. 9.12c shows that the orbit fits consistently improve for all satellites indicating that the azimuthal PCVs have a systematic effect on the orbit consistency, although this effect is small.

9.2.5. Earth Rotation Parameters

As a consequence of the systematic station coordinate changes induced by the application of different APCMs, the pole coordinates also change systematically. As the different APCMs mainly affect the station height, the effects on the pole coordinates (linked to the horizontal coordinate components only) are much smaller than for the parameters discussed above. The offsets and STD values of solution IGS01 and the solutions with absolute APCMs w.r.t. solution IGS05 are given in Tab. 9.7. The offsets as well as the STD values are largest for solution IGS01, probably due to the horizontal coordinate changes induced by the differences between the zenith-dependent receiver antenna PCVs of solution IGS01 and the zenith- and azimuth-dependent PCVs of solution IGS05. The differences for the solutions applying absolute APCMs without azimuthal satellite antenna PCVs (namely, TUM04, TUM05 and IGS05woR) are very small with values below $1 \mu\text{as}$ for the x-pole and $2 \mu\text{as}$ for the y-pole. IGS05woR shows the smallest offsets as the radome calibrations mainly affect the station height that is not related to polar motion.

Solution	X-Pole		Y-Pole	
	Offset [μas]	STD [μas]	Offset [μas]	STD [μas]
IGS01	35.1	64.9	34.2	69.7
TUM04	0.3	38.6	1.8	41.6
TUM05	0.9	20.0	-1.2	21.0
IGS05woR	0.2	14.5	-1.2	14.7
IGS05azi	7.5	41.8	4.1	44.0

Tab. 9.7: ERP offsets and STDs of solutions with different APCMs w.r.t. solution IGS05.

10. Summary, Conclusions, and Outlook

The Global Positioning System provides the possibility to monitor different parameters of the Earth system. In the past, interpretations of GPS-derived long time series were difficult due to inconsistencies caused by changes in the processing as regards, e.g., modeling, parameterization and the definition of the geodetic datum. This problem can only be overcome by a complete and homogeneous reprocessing starting with the raw RINEX observation data. Such a reprocessing of a global network including 202 stations and covering a time period of more than a decade of GPS observations has been conducted for this thesis. With the Bernese GPS Software, all relevant parameters of global GPS solutions, namely station coordinates, troposphere zenith delays and gradients, satellite orbits and Earth orientation parameters as well as auxiliary parameters like differential code biases, ionosphere parameters and ambiguities have been estimated. Although the setup of the processing, the detection of outliers and discontinuities as well as the processing itself were time-consuming, the benefits of the reprocessing justify this effort by far. As shown in this thesis, the quality and homogeneity of all types of parameters estimated within the reprocessing could be significantly improved, in particular in the first years.

The repeatability of the station coordinates could be improved by a factor of up to three in the early years. The median repeatabilities of the reprocessed solution are 1.3 mm for the horizontal components and 3.7 mm for the height component. Comparisons of co-located GPS sites show a consistency level of a few millimeters for the horizontal and half a centimeter for the vertical component. The velocities of these sites agree on the level of a few tenths of a mm/y and 1 mm/y, respectively. The troposphere zenith delays of the GPS/GPS co-locations are free of significant drifts and show STDs of a few millimeters. Comparisons of GPS-derived troposphere zenith delays with VLBI estimates result in biases below 5 mm and STDs between 5 and 8 mm. The consistency of the satellite orbits (evaluated by orbit fits) is on the few centimeter level and could be improved by a factor of up to two. In 1994 and 1995, SLR range residuals are 30–40% smaller for the reprocessed orbits than for the IGS or CODE orbits. Comparisons of the reprocessed ERPs with geophysical angular momentum series show higher correlations and smaller residual RMS values compared to operational series. The GPS-derived subdaily ERP model TUM05G has a precision of about 1–2 μs for polar motion and 0.1–0.3 μs for UT1. Comparisons with models based on VLBI observations or altimetry data indicate an accuracy level of 4–7 μs and 0.3–0.6 μs , respectively. The GPS-derived nutation model TUM05N differs by only 3.0–4.5 μs from the official IAU2000A model, an improvement of 10–44% compared to a model computed from the operational CODE series.

Another advantage of the reprocessing capabilities described in this thesis is the possibility to check different modeling or processing options for a considerable amount of data. Once an automated processing chain is set up, such checks can be performed in a convenient way. Two examples of different modeling strategies have been studied in more detail: (1) the effect of up-to-date troposphere mapping functions as well as a priori hydrostatic troposphere zenith delays based on numerical weather models, and (2) the impact of different antenna phase center models. For both, absolute APCMs and mapping functions/hydrostatic a priori delays based on numerical weather models, it could be demonstrated that the advanced modeling significantly improves the consistency and accuracy of the estimated parameters. Whereas the IGS already switched to an absolute APCM, mapping functions and a priori delays from numerical weather models are not used by the IGS ACs at the moment. Beneath the advantages discussed above, the reprocessing also revealed deficiencies of current GPS processing strategies and models. Due to the homogeneity of the reprocessed series, systematic effects show up even more clearly than in inhomogeneous series. On the other hand, however, it is obvious that the reprocessing cannot overcome data problems like multi-path and environmental effects or effects related to receiver tracking performance.

In 2004, the IGS recognized the necessity of a coordinated reprocessing effort of the IGS ACs. One recommendation of the IGS 2004 Workshop and Symposium in Bern was that “The ACs should be prepared to reprocess the IGS data. The detailed procedure should be discussed after the absolute antenna phase center variation models are decided”. After a call for participation in July 2005 (IGSMail 5175), a special session on “Reprocessing Issues, Standardization, New models” was held at the IGS 2006 Workshop in Darmstadt. One important recommendation of this workshop was that “(efficient) reprocessing must become a permanent feature of the IGS”. In summer 2007, an IGS reprocessing pilot project covering a period of three

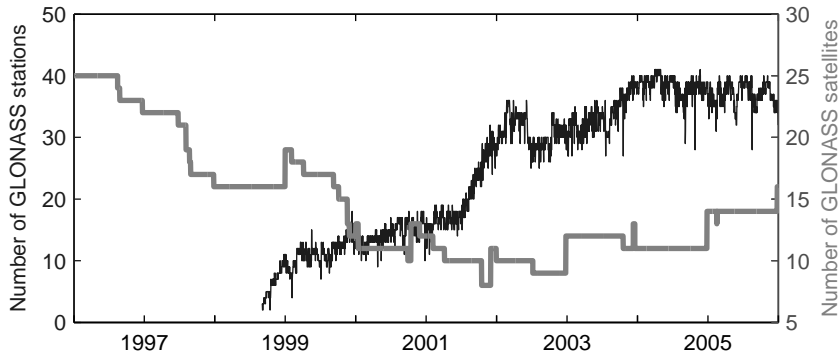


Fig. 10.1: Evolution of the number of [IGEX/IGS GLONASS](#) tracking stations (black) and satellites (gray).

months started. After analyzing the results of this test period, the first [IGS](#) reprocessing campaign started in February 2008. Two sessions dealing with reprocessing issues at the [IGS](#) 2008 Workshop in Miami Beach emphasize the importance of this reprocessing campaign for the [IGS](#). The generation of a first combined reprocessed set of [IGS](#) products based on the contributions of most [ACs](#) is an important task for the near future. However, the [IGS](#) reprocessing will be an iterative process. E.g., the full consistency of the [APCM](#) and the [TRF](#) cannot be achieved by one iteration: the [APCM](#) currently applied by the [IGS](#) reprocessing [ACs](#) was fixed to the scale of [ITRF2000](#). As satellite-specific vertical antenna offsets are included in the [SINEX](#) submissions of the [ACs](#), a new [APCM](#) can be determined from the [IGS](#) reprocessing and aligned to the latest release of the [ITRF](#). That [APCM](#) can later be introduced for the second iteration of the [IGS](#) reprocessing to assure consistency between the [TRF](#) and the [APCM](#).

Reprocessed [GPS](#) solutions will provide valuable input for future [ITRF](#) computations. Especially the long-term stability will benefit considerably from homogeneous [GPS](#) time series. In view of the demands of [IAG's](#) project of a Global Geodetic Observing System ([GGOS](#), [Rummel et al., 2005](#)), reprocessed [GPS](#) solutions are essential to provide the aspired accuracy of a [TRF](#) ([Altamimi et al., 2005b](#)) as the basis for a monitoring of the system Earth. E.g., studies of the global sea level rise require a highly accurate reference frame ([Morel and Willis, 2005](#)), as the accuracy of the reference frame is the limiting factor for the accuracy of [GPS](#)-derived vertical velocities ([Kierulf et al., 2008](#)). Although reprocessed troposphere parameters do not seem suitable for climatological studies at present time (see Sec. 6.1.5), longer time series available in a few years might contribute to a monitoring of global change effects related to the atmosphere.

A further step to a rigorous analysis of [GNSS](#) data would be the reprocessing of [GLONASS](#) tracking data together with the [GPS](#) data. The [CODE IGS](#) products are based on such a combined analysis on the observation level since June 2003. Fig. 10.1 shows the evolution of the [GLONASS](#) constellation and the number of tracking stations publicly available at the [IGS](#) and [IGEX DCs](#). Unfortunately, the number of [GLONASS](#) satellites dramatically decreased when most of the tracking stations came up. Since end of 2001, the number of active [GLONASS](#) satellites increases again, and the full operational capability of 24 satellites should be reached by 2009 ([Kuzin et al., 2007](#)).

The different period of revolution of the [GLONASS](#) satellites could help to reduce systematic errors related to the [GPS](#) orbit design, e.g., effects due to the 2:1 resonance of the [GPS](#) orbital period and the sidereal day on subdaily [ERP](#) estimates. The larger number of observations and the improved geometry can improve the estimation of troposphere zenith delays and particularly of the corresponding gradients ([Zarraoa et al., 1998](#)). However, [Bruyninx \(2007\)](#) could show that the station coordinate repeatability of a regional network does not significantly change, if [GLONASS](#) observations are included. In addition, biases between the two different satellite systems have to be accounted for in a combined analysis. Due to the reasons mentioned above, a rigorous combined [GPS/GLONASS](#) reprocessing on the observation level is a beneficial, but challenging task for the future.

Part III.

Appendices

A. Datum Stations

The list of datum stations is based on the list of IGB00 stations. Stations that were excluded from IGB00 due to the fact that they are inactive at present time were added again.

ALGO 40104M002*	Goug 30608M001	MATE 12734M008	SYOG 66006S002*
ALIC 50137M001*	GRAS 10002M006	MAW1 66004M001*	THTI 92201M009*
ARTU 12362M001*	GRAZ 11001M002	MCM4 66001M003	THU1 43001M001*
ASC1 30602M001*	GUAM 50501M002	MDO1 40442M012*	THU3 43001M002*
AUCK 50209M001*	HOB2 50116M004* ^d	MKEA 40477M001*	TIDB 50103M108* ^b
BAHR 24901M002*	HOFN 10204M002	NICO 14302M001*	TIXI 12360M001*
BILI 12363M001	HRAO 30302M004*	NKLG 32809M002*	TOW2 50140M001*
BOR1 12205M002	IISC 22306M002* ^e	NLIB 40465M001*	TRAB 20808M001*
BRUS 13101M004	IRKT 12313M001*	NOUM 92701M003*	TROM 10302M003*
CAS1 66011M001	JAB1 50136M001	NRC1 40114M001*	TRO1 10302M006
CEDU 50138M001	JOZE 12204M001	NTUS 22601M001* ^e	TSKB 21730S005*
CHAT 50207M001	KARR 50139M001*	NYAL 10317M001*	UNSA 41514M001
CHUR 40128M002	KELY 43005M001	OHIG 66008M001*	URUM 21612M001*
COCO 50127M001	KERG 91201M002*	OHI2 66008M005*	VESL 66009M001*
CRO1 43201M001*	KIT3 12334M001*	ONSA 10402M004	VILL 13406M001
DARW 50134M001	KOKB 40424M004	PERT 50133M001	WES2 40440S020
DAV1 66010M001*	KOUR 97301M210*	PETP 12355M002	WSRT 13506M005*
DGAR 30802M001* ^e	KSTU 12349M002*	PIE1 40456M001*	WTZR 14201M010*
DRAO 40105M002	KWJ1 50506M001*	POL2 12348M001*	YAKT 12353M002*
DUBO 40137M001	LAMA 12209M001	POTS 14106M003*	YAR1 50107M004* ^c
EISL 41703M003*	LHAS 21613M001*	RBAY 30315M001*	YELL 40127M003
FLIN 40135M001	LPGS 41510M001*	RIOG 41507M004*	ZIMM 14001M004
FORT 41602M001*	MAC1 50135M001	SANT 41705M003*	ZWEN 12330M001*
GLSV 12356M001*	MALI 33201M001	SCH2 40133M002	
GODE 40451M123*	MANA 41201S001	SHAO 21605M002*	
GOL2 40405S031 ^a	MAS1 31303M002*	STJO 40101M001*	

^a GOLD 40405S031* is used until 31 December 1995

^b TID2 50103M108* is used after 1 November 1997

^c YAR2 50107M004* is used after 1 May 2001

^d station was affected by the 23 December 2004 Macquarie earthquake: not used as datum station for the reference frame solution discussed in Sec. 5.3; pre-elimination between 23 and 31 December 2004 for the reference frame solutions discussed in Sec. 9.2.1

^e station was affected by the 26 December 2004 Sumatra earthquake: not used as datum station for the reference frame solution discussed in Sec. 5.3; pre-elimination between 26 and 31 December 2004 for the reference frame solutions discussed in Sec. 9.2.1

Tab. A.1: Stations used for datum definition. The subset of stable datum stations used for the reference frame solutions discussed in Sec. 5.3 and Sec. 9.2.1 are marked with an asterisk.

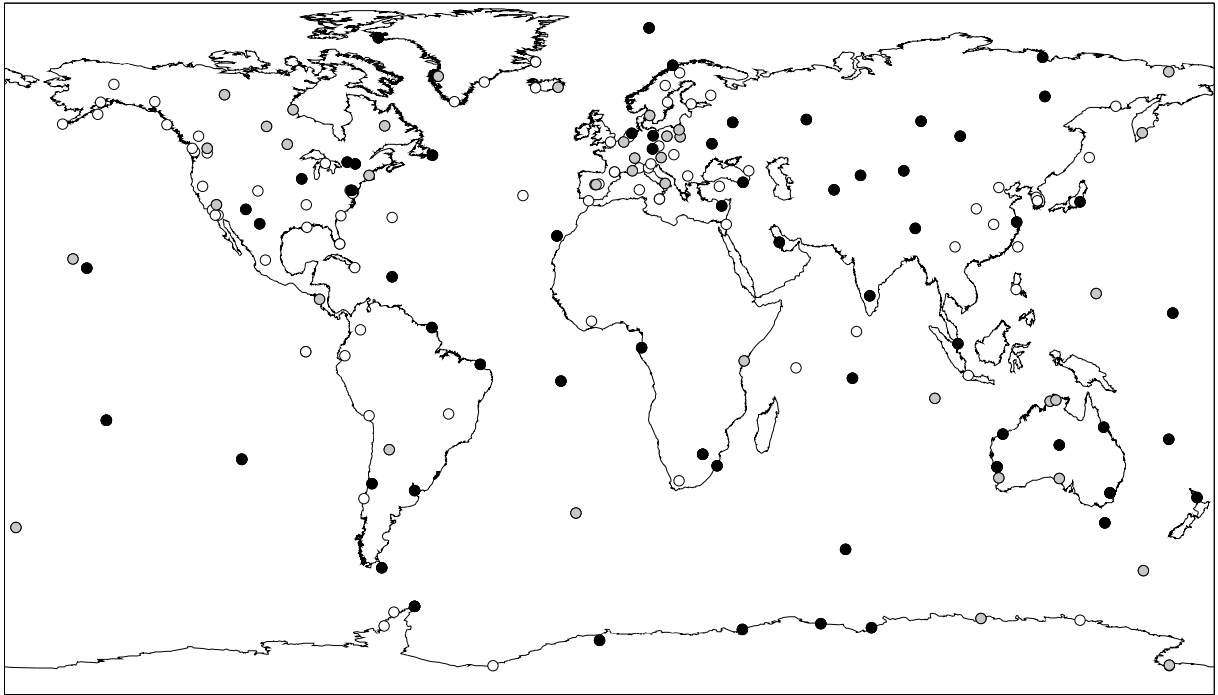


Fig. A.1: Datum stations: stable datum stations used for the reference frame solution are indicated by black circles, other datum stations by gray circles.

Exclusion from Datum Definition

Station	Start	End	Comment
DGAR 30802M001	26. 12. 2004		Sumatra earthquake, IGSSTATION 330
GOUG 30608M001	20. 10. 2004		IGSSTATION 330
IISC 22306M002	14. 11. 2004		IGSSTATION 330
KOKB 40424M004	18. 05. 1996	03. 08. 1996	degraded tracking, see Sec. 4.2.1
	18. 05. 2004		antenna change, IGSSTATION 47
MAC1 50135M001	23. 12. 2004		Macquarie earthquake, IGSSTATION 330
MANA 41201S001	29. 09. 2004		IGSSTATION 330
NTUS 22601M001	26. 12. 2004		Sumatra earthquake, IGSSTATION 330
TR01 10302M006	13. 07. 2004		antenna change, IGSSTATION 123
YAKT 12353M002	01. 01. 2000		snow-induced effects, see Sec. 4.2.1

Tab. A.2: List of stations excluded from datum definition due to systematic effects or recommendations announced via IGSSTATION.

B. Tracking Stations

Abb.	Site	IERS-No.	City/Town	Country	Tect. Plate	Installation	active till	Network	IGb00
AIS1	Annette Island 1	49998S001	Annette Island	USA	North American	19.01.1996		CORS	
ALBH	Albert Head	40129M003	Victoria	Canada	North American	04.05.1992		IGS	
ALGO	Algonquin	40104M002	Algoquin Park	Canada	North American	19.01.1991		IGS	x
ALIC	Alice Springs	50137M001	Alice Springs	Australia	Indo-Australian	15.05.1994		IGS	x
AMC2	Alternate Master Clock	40472S004	Colorado Springs	USA	North American	24.03.1998		IGS	
ANKR	Ankara	49914S001	Ankara	Turkey	Eurasian (Anatolian)	21.06.1995		IGS	
AOML	Atl. Oceanogr. Met Lab	49914S001	Miami	USA	North American	20.11.1997	05.04.2004	IGS	
AREQ	Arequipa Laser Station	42202M005	Arequipa	Peru	South American	01.02.1994		IGS	
ARTU	Arti	12362M001	Arti	Russia	Eurasian	05.08.1999		IGS	x
ASC1	Ascension Island	30602M001	Ascension Island	Ascension Island	South American	20.04.1996		IGS	x
AUCK	Whangaparaoa No 3	50209M001	Whangaparaoa Penins.	New Zealand	Indo-Australian	18.09.1995		IGS	x
BAHR	Bahrain GPS Station	24901M002	Manama	Bahrain	Arabian	20.03.1995		IGS	x
BAKO	Bakosurtanal	23101M002	Cibinong	Indonesia	Eurasian	07.02.1998		IGS	
BAY1	Cold Bay 1	49804S001	Cold Bay	Alaska	North American	05.02.1996		CORS	
BELG	Base Belgrano II	66018M002	Base Belgrano II	Antarctica	Antarctic	03.02.1998		AWI	
BILI	Bilibino	12363M001	Bilibino	Russia	North American	04.09.1999		IGS	x
BJFS	Fangshan	21601M001	Beijing	China	Eurasian	20.09.1995		IGS	
BOGT	Bogota	41901M001	Bogota	Colombia	South American	04.11.1994		IGS	
BOR1	Borowiec	12205M002	Borowiec	Poland	Eurasian	10.01.1994		IGS	x
BRAZ	Brasilia	41606M001	Brasilia	Brazil	South American	28.04.1998		IGS	
BREW	Brewster VLBA	40473M001	Brewster	USA	North American	08.11.2001		IGS	
BRMU	Bermuda	42501S004	Bermuda	Bermuda	North American	12.03.1993		IGS	
BRUS	Brussels	13101M004	Brussels	Belgium	Eurasian	20.10.1993		IGS	x
CAGL	Cagliari	12725M003	Cagliari	Italy	Eurasian	07.04.1995		IGS	
CAS1	Casey	66011M001	Casey	Antarctica	Antarctic	01.01.1994		IGS	x
CEDU	Ceduna	50138M001	Ceduna	Australia	Indo-Australian	15.05.1994		IGS	x
CHA1	Charleston 1	49851S001	Charleston	USA	North American	29.08.1995		CORS	
CHAT	Chatham Island	50207M001	Waitangi	New Zealand	Pacific	04.10.1995		IGS	x
CHB1	Cheboygan 1	49856S001	Cheboygan	USA	North American	14.08.1995		CORS	
CHUR	Churchill	40128M002	Churchill	Canada	North American	13.04.1994		IGS	x
CONZ	Concepcion - TIGO	41719M002	Concepcion	Chile	South-American	16.05.2002		IGS	
COCO	Cocos	50127M001	Cocos Island	Australia	Indo-Australian	03.09.1994		IGS	x
CR01	St. Croix VLBA	43201M001	Christiansted	Virgin Islands	Caribbean	16.01.1994		IGS	x
DAEJ	Taejon	23902M002	Taejon	Korea	Eurasian	19.03.1999		IGS	
DARW	Darwin	50134M001	Darwin	Australia	Indo-Australian	24.03.1994		IGS	x
DAV1	Davis	66010M001	Davis	Antarctica	Antarctic	11.01.1994		IGS	x
DGAR	Diego Garcia Island	30802M001	Diego Garcia Island	U.K. Territory	Indo-Australian	11.03.1996		IGS	x

Abb.	Site	IERS-No.	City/Town	Country	Tect. Plate	Installation	active till	Network	IGb00
DRAO	Dominion R. Astroph. Obs.	40105M002	Penticton	Canada	North American	27.02.1991		IGS	x
DUBO	Lac du Bonnet	40137M001	Lac du Bonnet	Canada	North American	18.10.1996		IGS	x
DUM1	Dumont D'Urville	66020M001	Dumont d'Urville	Terre Adélie ¹	Antarctic	20.12.1997		IGS	
EISL	Easter Island	41703M003	Easter Island	Chile	Pacific/Nazca	01.05.1994	inactive	IGS	x
ENG1	English Turn 1	49866S001	English Turn	USA	North American	25.11.1995		CORS	
FAIR	Gilmore Creek Obs.	40408M001	Fairbanks	USA	North American	17.10.1991		IGS	x
FLIN	Flin Flon	40135M001	CFS Flin Flon	Canada	North American	05.06.1996		IGS	x
FORT	Fortaleza	41602M001	Eusebio, Fortaleza	Brazil	South American	13.05.1993	08.04.2006	IGS	x
GALA	Galapagos Island	42005M001	Galapagos Island	Ecuador	Nazca/Cocos	30.01.1996	inactive	IGS	
GENO	Genova	12712M002	Genova	Italy	Eurasian	23.07.1998		IGS	
GLPS	Galapagos	42005M002	Galapagos Island	Ecuador	Nazca/Cocos	06.01.2003		IGS	
GLSV	Kiev/Golosiiv	12356M001	Kiev	Ukraine	Eurasian	16.12.1997		IGS	x
GODE	Greenbelt	40451M123	Greenbelt	USA	North American	17.04.1993		IGS	x
GOL2 ²	Goldstone	40405S031	Goldstone	USA	North Am./Pacific	11.11.1993		IGS	
GOLD	Goldstone	40405S031	Goldstone	USA	North Am./Pacific	15.12.1989		IGS	x
GOPE	Pecny, Ondrejov	11502M002	Ondrejov	Czech Republic	Eurasian	13.05.1995		IGS	
Goug	Gough Island	30608M001	Gough Island	Saint Helena	African	08.01.1998		IGS	x
GRAS	Observatoire de Calern	10002M006	Caussols	France	Eurasian	22.02.1995		IGS	x
GRAZ	Graz-Lustbuehel	11001M002	Graz	Austria	Eurasian	12.06.1992		IGS	x
GUAM	USGS Guam Observatory	50501M002	Dededo	Guam	Pacific	20.01.1995		IGS	x
HARK	Hartebeesthoek	30302M007	Krugersdorp	South Africa	African	13.06.1997	13.08.2002	IGS	
HART	Hartebeesthoek	30302M002	Krugersdorp	South Africa	African	01.01.1992	10.06.1997	IGS	
HERS	Herstmonceux	13212M007	Hailsham	England	Eurasian	24.03.1992		IGS	
HNPT	Horn Point	49913S001	Cambridge	USA	North American	19.12.1995		IGS	
HOB1	Hobart	50116M003	Hobart	Australia	Pacific	20.02.1993	08.08.1994	IGS	
HOB2	Hobart	50116M004	Hobart	Australia	Pacific	30.11.1995		IGS	x
HOFN	Hoefn	10204M002	Hoefn	Iceland	Eurasian	27.05.1997		IGS	x
HRAO	Hartebeesthoek	30302M004	Krugersdorp	South Africa	African	05.09.1996		IGS	x
IISC	Indian Institute of Science	22306M002	Bangalore	India	Indo-Australian	20.01.1995 ³		IGS	x
INEG	Aguascalientes	40507M001	Aguascalientes	Mexico	North American	19.02.1993		IGS	
IRKT	Irkutsk	12313M001	Irkutsk	Russia	Eurasian	16.09.1995		IGS	x
ISPA	Easter Island	41703M007	Easter Island	Chile	Pacific/Nazca	13.02.2004		IGS	
JAB1	Jabiru	50136M001	Jabiru	Australia	Australian	07.08.1997		IGS	x
JOEN	Joensuu	10512M001	Joensuu	Finland	Eurasian	15.06.1995		EUREF	
JOZE	Jozefoslaw	12204M001	Jozefoslaw	Poland	Eurasian	03.08.1993		IGS	x
JPLM	JPL Mesa	40400M007	Pasadena	USA	Pacific	20.03.1990		IGS	
KARR	Karratha	50139M001	Karratha	Australia	Indo-Australian	14.07.1994		IGS	x
KELY	Kellyville	43005M001	Kangerlussuaq	Greenland	North American	23.07.1995		IGS	x
KEN1	Kenai 1	49995S001	Kenai	USA	North American	31.01.1996		CORS	
KERG	Kerguelen Islands	91201M002	Port aux Francais	Kerguelen Islands	Antarctic	14.11.1994		IGS	x
KIRU	Kiruna	10403M002	Kiruna	Sweden	Eurasian	08.07.1993		IGS	
KIT3	Kitab	12334M001	Kitab	Uzbekistan	Eurasian	01.10.1994		IGS	x
KOD1	Kodiak	40419S001	Kodiak	USA	North Am./Pacific	01.02.1996		CORS	
KOKB	Kokee Park	40424M004	Kokee Park, Waimea	USA	Pacific/South Bismarck	05.10.1990		IGS	x

¹France²GOL2 and GOLD are sharing the same antenna with an antenna splitter, GOLD is used until 31 December 1995, GOL2 afterwards³data before 2 October 1995 was excluded as another marker was used

Abb.	Site	IERS-No.	City/Town	Country	Tect. Plate	Installation	active till	Network	IGb00
KOSG	Kootwijk	13504M003	Kootwijk	Netherlands	Eurasian	13.06.1994		IGS	
KOUR	Kourou	97301M210	Kourou	French Guyana	South American	06.10.1994		IGS	x
KSTU	Krasnoyarsk	12349M002	Krasnoyarsk	Russia	Eurasian	22.10.1996		IGS	x
KULU	Kulusuk		Kulusuk	Greenland	North American	21.07.1996		DNSC	
KUNM	Kunming	21609M001	Kunming	China	Eurasian	16.06.1998		IGS	
KWJ1	Kwajalein Atoll	50506M001	Kwajalein Atoll	Marshall Islands	Pacific	05.03.1996		IGS	
LAMA	Lamkowko	12209M001	Olsztyn	Poland	Eurasian	01.12.1994		IGS	x
LHAS	Lhasa	21613M001	Lhasa	China	Eurasian	02.05.1995		IGS	x
LPGS	La Plata	41510M001	La Plata	Argentina	South American	20.05.1995		IGS	x
MAC1	MacQuarie Island	50135M001	MacQuarie Island	Australia	Antartic/Pacific	27.06.1995		IGS	x
MADR	Madrid	13407S012	Robledo	Spain	Eurasian	15.12.1989		IGS	
MAGO	Magadan	12354M001	Magadan	Russia	North American	12.11.1997		IGS	x
MALD	Maldives	22901S001	Male Airport	Rep. of Maldives	Indian	12.08.1999		IGS	
MALI	Malindi	33201M001	Malindi	Kenya	African	12.11.1995		IGS	x
MANA	Managua	41201S001	Managua	Nicaragua	Caribbean/Cocos	13.05.2000		IGS	x
MAR6	Maartsbo	10405M002	Maartsbo	Sweden	Eurasian	01.08.1993		IGS	
MAS1	Maspalomas	31303M002	Maspalomas	Spain	African	11.04.1994		IGS	x
MASP	Maspalomas	31303M001	Maspalomas	Spain	African	22.06.1992	11.09.1994	IGS	
MATE	Matera	12734M008	Matera	Italy	Adriatic-African	01.01.1991		IGS	x
MAW1	Mawson	66004M001	Mawson	Antarctica	Antarctic	01.01.1994		IGS	x
MCM1	McMurdo		Ross Island	Antarctica	Antarctic	31.10.1993	inactive		
MCM4	McMurdo	66001M003	Ross Island	Antarctica	Antarctic	25.01.1995		IGS	x
MD01	McDonald Obs. Site	40442M012	Fort Davis	USA	North American	03.06.1993		IGS	x
MEDI	Medicina	12711M003	Medicina/Bologna	Italy	Adriatic-African	28.07.1995		IGS	
MEM2	Memphis 2	49867S002	French Bayou	USA	North American	26.07.1995		CORS	
METS	Metsahovi	10503S011	Kirkkonummi	Finland	Eurasian	30.04.1992		IGS	
MIA1	Atl. Oceanogr. Met Lab	49914S002	Miami	USA	North American	24.08.1995	01.06.1998	CORS	
MKEA	Mauna Kea	40477M001	Mauna Kea	USA	Pacific	08.08.1996		IGS	x
MONP	Monument Peak	40497M004	Laguna Mountains	USA	North Am./Pacific	31.03.1994		IGS	
NANO	Nanoose Bay	40138M001	Nanoose	Canada	North American	01.01.1998		IGS	
NICO	Nicosia-Athalassa	14302M001	Nicosia	Cyprus	African	14.05.1997		IGS	x
NKLG	N'Koltang	32809M002	Libreville	Gabon	African	10.02.2000		IGS	x
NLIB	North Liberty VLBA site	40465M001	North Liberty	USA	North American	05.03.1993		IGS	x
NOT1	Noto-Radioastronomy Station	12717M004	Noto	Italy	Adriatic-African	15.09.2000		IGS	
NOTO	Noto-Radioastronomy Station	12717M003	Noto	Italy	Adriatic-African	02.02.1995	07.09.2000	IGS	
NOUM	Noumea	92701M003	Noumea	France	Indo-Australian	08.12.1997		IGS	x
NRC1	Ottawa NRC	40114M001	Ottawa	Canada	North American	01.06.1994		IGS	x
NTUS	Nanyang Tech. Univ.	22601M001	Singapore	Singapore	Eurasian	26.06.1997		IGS	x
NYA1	Ny-Ålesund	10317M003	Ny-Ålesund	Norway	Eurasian	01.06.1997		IGS	
NYAL	Ny-Ålesund	10317M001	Ny-Ålesund	Norway	Eurasian	01.01.1993		IGS	x
OHI2	O'Higgins	66008M005	O'Higgins	Antarctica	Antarctic	14.02.2002		IGS	x
OHIG	O'Higgins	66008M001	O'Higgins	Antarctica	Antarctic	14.02.1995	16.02.2002	IGS	
ONSA	Onsala	10402M004	Onsala	Sweden	Eurasian	01.07.1993		IGS	x
PALM	Palmer Station	66005M001	Palmer Station	Antarctica	Antarctic	19.01.1998			
PAMA	Papeete	92201M003	Papeete	Tahiti	Pacific	21.06.1992	inactive	IGS	
PDEL	Ponta Delgada	31906M004	Ponta Delgada	Portugal	Eurasian	16.01.2000		IGS	
PENC	FOMI Sat. Geod. Obs.	11206M006	Penc	Hungary	Eurasian	01.03.1996		IGS	
PERT	Perth	50133M001	Perth	Australia	Indo-Australian	18.08.1993		IGS	x

Abb.	Site	IERS-No.	City/Town	Country	Tect. Plate	Installation	active till	Network	IGb00
PETP	Petropavlovsk	12355M002	Petropavlovsk-Kamchatka	Russian Fed.	Pacific/North Am. PB	10.10.1998		IGS	x
PIE1	Pietown VLBA Site	40456M001	Pie Town	USA	North American	29.12.1992		IGS	x
PIMO	Manila Observatory	22003M001	Quezon City	Phillipines	Phillipinian	07.05.1997		IGS	
POL2	Poligan IVTAN 2	12348M001	Bishkek	Kyrgyzstan	Eurasian	25.05.1995		IGS	x
POTS	Potsdam	14106M003	Potsdam	Germany	Eurasian	01.10.1994		IGS	x
QAQ1	Qaqortoq	43007M001	Qaqortoq	Greenland	North American	15.10.2001		IGS	
QUIN	Quincy	40433M004	Quincy	USA	North American	06.09.1992		IGS	
RAMO	Mitzpe Ramon	20703S001	Mitzpe Ramon	Israel	African	10.06.1998		IGS	
RBAY	Richardsbay	50136M001	Richardsbay	South Africa	African	10.05.2000		IGS	x
REYK	Reykjavik / Iceland	10202M001	Reykjavik	Iceland	North American	02.11.1995		IGS	
RIOG	Rio Grande	41507M004	Rio Grande	Argentina	South American	12.11.1996		IGS	x
RIOP	Riobamba	42006M001	Riobamba	Ecuador	South American	08.04.1996		IGS	
SANT	Santiago	41705M003	Santiago	Chile	South American	04.02.1992		IGS	x
SCH2	Schefferville	40133M002	Schefferville	Canada	North American	29.06.1997		IGS	x
SCOB	Scorsbysund	43006M001	Scorsbysund	Greenland	North American	07.08.1997		DNOSC	
SCUB	Santiago de Cuba	40701M001	Santiago de Cuba	Cuba	North American	31.05.1995		IGS	
SEY1	Seychelles	39801M001	La Misere	Seychelles	African	15.05.1995		IGS	
SFER	San Fernando	13402M004	San Fernando (Cadiz)	Spain	Eurasian (Iberian)	18.12.1995		IGS	x
SHAO	Sheshan	21605M002	Sheshan	China	Eurasian	20.01.1995		IGS	
SI03	Scripps	40460M004	La Jolla	USA	North American	26.07.1993		IGS	
SMRT	Base San Martin		Base San Martin	Antarctica	Antarctic	22.04.1999		AWI	
SOFI	Sofia	11101M002	Sofia	Bulgaria	Eurasian	19.05.1997		IGS	
SOL1	Solomons Island	49907S001	Solomons Island	USA	North American	09.12.1993		IGS	
STJO	St. John's	40101M001	St. John's	Canada	North American	24.05.1992		IGS	x
SUTH	Sutherland	30314M002	Sutherland	South Africa	African	05.12.1997		IGS	
SUWN	Suwon	23903M001	Suwon-shi	Korea	Eurasian	15.03.1995		IGS	
SYOG	Syowa	66006S002	East Ongle Island	Antarctica	Antarctic	15.03.1995		IGS	x
TAEJ	Taejon	23902M001	Taejon	Korea	Eurasian	26.10.1994	inactive	IGS	
TAHI	Papeete	92201M006	Papeete	Tahiti	Pacific	07.04.1997	inactive	IGS	
TAIW	Taipei	23601M001	Taipei	Taiwan	Eurasian	20.10.1993	inactive	IGS	
THTI	Papeete	92201M009	Papeete	Tahiti	Pacific	22.11.1998		IGS	x
THU1	Thule 1	43001M001	Thule	Greenland	North American	02.05.1995	12.01.2003	IGS	
THU3	Thule 3	43001M002	Thule	Greenland	North American	01.09.2001		IGS	x
TID2 ⁴	Tidbinbilla 2	50103M108	Tidbinbilla	Australia	Indo-Australian	30.10.1997		IGS	
TIDB	Tidbinbilla	50103M108	Tidbinbilla	Australia	Indo-Australian	15.12.1989		IGS	x
TIXI	Tixi	12360M001	Tixi	Russia	Eurasian/North Am.	08.10.1998		IGS	x
TLSE	Toulouse	10003M009	Toulouse	France	Eurasian	04.01.2001		IGS	
TOUL	Toulouse	10003M004	Toulouse	France	Eurasian	20.01.1997	03.01.2001	IGS	
TOW2	Townsville	50140M001	Cape Ferguson	Australia	Indo-Australian	17.01.1995		IGS	x
TRAB	Trabzon	20808M001	Trabzon	Turkey	Eurasian - Anatolian	08.12.1999		IGS	x
TRO1	Tromsø	10302M003	Tromsø	Norway	Eurasian	31.05.1997		IGS	x
TROM	Tromsø	10302M003	Tromsø	Norway	Eurasian	01.01.1990		IGS	
TSKB	Tsukuba	21730S005	Tsukuba	Japan	North American	20.09.1995		IGS	x
UNSA	UNSA Salta	41514M001	Salta	Argentina	South American	26.01.1995		IGS	x
URUM	Urumqi	21612M001	Urumqi	China	Eurasian	01.04.1998		IGS	x
USNA	U.S. Naval Academy	49908S001	Annapolis	USA	North American	13.01.1995	inactive	IGS	

⁴TID2 and TIDB are sharing the same antenna with an antenna splitter, TIDB is used until 31 October 1997, TID2 afterwards

Abb.	Site	IERS-No.	City/Town	Country	Tect. Plate	Installation	active till	Network	IGb00
USNO	U.S. Naval Obs.	40451S003	Washington	USA	North American	24.04.1997		IGS	
USUD	Usuda	21729S007	Usuda	Japan	Pacific	16.07.1990		IGS	
VEVE	Venezia	12741M001	Venezia	Italy	Adriatic-African	23.03.1995		IGS	
VESL	Vesleskarvet	66009M001	Sanae IV	Antarctica	Antarctic	18.12.1997		IGS	x
VILO	Vilhelmina	10424M001	Vilhelmina	Sweden	Eurasian	01.08.1993		EUREF	
VILL	Villafranca	13406M001	Villafranca	Spain	Eurasian	12.11.1994		IGS	x
WES2	Westford	40440S020	Westford	USA	North American	08.02.1993		IGS	x
WETT	Wetzell	14201M009	Koetzting	Germany	Eurasian	24.06.1992	02.02.1997	IGS	
WHIT	Whitehorse	40136M001	Whitehorse	Canada	North American	09.06.1995		IGS	
WILL	Williams Lake	40134M001	Williams Lake	Canada	North American	06.10.1993		IGS	
WSRT	Westerbork	13506M005	Westerbork	Netherlands	Eurasian	01.06.1997		IGS	x
WTZR	Wetzell	14201M010	Koetzting	Germany	Eurasian	09.02.1995		IGS	x
WUHN	Wuhan	21602M001	Wuhan City	China	Eurasian	27.01.1995		IGS	
XIAN	Shaanxi Observatory	21614M001	Lintong	China	Eurasian	20.05.1996		IGS	
YAKT	Yakutsk	12353M002	Yakutsk	Russian Fed.	Eurasian	24.04.2000		IGS	x
YAKZ	Yakutsk	12353M001	Yakutsk	Russian Fed.	Eurasian	12.11.1997	21.06.2001	IGS	
YAR1 ⁵	Yaragadee	50107M004	Mingenew	Australia	Indo-Australian	03.12.1990	inactive	IGS	x
YAR2	Yaragadee	50107M004	Mingenew	Australia	Indo-Australian	08.06.1996		IGS	
YARR	Yaragadee	50107M006	Dongara	Australia	Indo-Australian	17.09.1998		IGS	
YEBE	Yebes	13420M001	Yebes	Spain	Eurasian	14.10.1999		IGS	
YELL	Yellowknife	40127M003	Yellowknife	Canada	North American	21.01.1991		IGS	x
YKRO	Yamoussoukro	32601M001	Yamoussoukro	Ivory Coast	African	18.07.1999		IGS	
YSSK	Yuzhno-Sakhalinsk	12329M003	Yuzhno-Sakhalinsk	Russia	Eurasian/North Am.	28.07.1999		IGS	x
ZECK	Zelenchukskaya	12351M001	Zelenchukskaya	Russia	Eurasian	11.07.1997		IGS	
ZIMM	Zimmerwald	14001M004	Zimmerwald	Switzerland	Eurasian	01.05.1993		IGS	x
ZWE2	Zwenigorod	12330M003	Zwenigorod	Russia	Eurasian	26.10.2004		IGS	
ZWEN	Zwenigorod	12330M001	Zwenigorod	Russia	Eurasian	08.03.1995	inactive	IGS	

Tab. B.1: List of [GPS](#) tracking stations used for reprocessing.

⁵YAR1 and YAR2 are sharing the same antenna with an antenna splitter, YAR1 is used until 31 May 2000, YAR2 afterwards

C. Discontinuities in Coordinate Time Series

Station	Epoch	Comment
AIS1 49998S001	17. 04. 1996	unknown
ALBH 40129M003	14. 04. 1994	antenna change
	08. 09. 2003	radome change
AMC2 40472S004	25. 08. 1999	antenna cable
	14. 06. 2002	antenna/receiver change
	15. 10. 2002	unknown
ANKR 20805M002	19. 09. 1998	antenna change
	17. 08. 1999	Kocaeli earthquake (Mw 7.6)
	12. 11. 1999	Turkey earthquake (Mw 7.2)
AREQ 42202M005	23. 06. 2001	Peru earthquake (Mw 8.4)
ARTU 12362M001	23. 12. 1999	unknown
	02. 02. 2000	unknown
BAKO 23101M002	20. 09. 1999	antenna change
	07. 09. 2001	unknown
	06. 10. 2001	antenna change
BILI 12363M001	15. 01. 2002	unknown
	03. 03. 2002	unknown
BOR1 12205M002	31. 05. 1999	antenna change
BRMU 42501S004	12. 03. 2003	antenna/receiver change
	02. 07. 2004	unknown
BRUS 13101M004	27. 04. 2000	antenna change
CAGL 12725M003	11. 07. 2001	antenna/receiver change
CAS1 66011M001	01. 03. 1997	different velocity rate
	07. 11. 1997	unknown
CEDU 50138M001	22. 04. 2004	unknown
CHA1 49851S001	22. 04. 1997	unknown
CHAT 50207M001	23. 02. 2000	unknown
CHUR 40128M002	11. 01. 2005	antenna change
COCO 50127M001	18. 06. 2000	South Indian Ocean earthquake (Mw 7.6)
DARW 50134M001	19. 10. 2001	antenna change
	14. 12. 2001	antenna change
DGAR 30802M001	26. 12. 2004	Indian Ocean earthquake (Mw 9.0)
DRAO 40105M002	10. 02. 1994	antenna/receiver change
	12. 04. 1995	unknown
DUBO 40137M001	08. 01. 1997	antenna change
	04. 10. 1999	antenna/receiver change
	13. 10. 2002	unknown
DUM1 91501M001	26. 03. 1998	unknown
FAIR 40408M001	03. 11. 2002	Denali fault earthquake (Mw 7.9)
FLIN 40135M001	07. 01. 1997	antenna-/receiver change
GOL2 40405S031	16. 10. 1999	Hector Mine earthquake (Mw 7.2)
GOPE 11502M002	04. 11. 1999	antenna/receiver change
	24. 07. 2000	antenna/receiver change ¹
	04. 10. 2000	antenna/receiver change ¹
GOUG 30608M001	20. 10. 2004	unknown
GRAS 10002M006	23. 04. 2003	antenna/receiver change
GRAZ 11001M002	01. 06. 2001	receiver change
	22. 03. 2005	antenna change

¹*Kaniuth and Huber (2003)*

Station	Epoch	Comment
GUAM 50501M002	26. 04. 2002	Mariana Island earthquake (Mw 7.1)
HART 30302M002	27. 05. 1997	antenna moved, IGSMail 1618
HERS 13212M007 ²	21. 03. 1999	unknown
	08. 06. 2001	unknown, IGSMail 3373
HNPT 49913S001	22. 05. 2000	antenna/receiver change
HOB2 50116M004	23. 12. 2004	Macquarie Island earthquake (Mw 8.1)
HOFN 10204M002	21. 09. 2001	antenna change
IISC 22306M002	26. 12. 2004	Indian Ocean earthquake (Mw 9.0)
JOZE 12204M001	06. 12. 2004	unknown
JPLM 40400M007	14. 06. 1994	antenna/receiver change
	16. 10. 1999	Hector Mine earthquake (Mw 7.2)
JAB1 50136M001	04. 03. 2003	antenna/receiver change
KELY 43005M001	14. 09. 2001	antenna/receiver change ³
KIRU 10403M002	29. 09. 2000	antenna change
	08. 04. 2001	unknown
KOKB 40424M004	01. 08. 1996	antenna change
	14. 10. 2002	antenna/receiver change
	18. 05. 2004	antenna change
KOSG 13504M003	18. 03. 2003	unknown
KUNM 21609M001	26. 12. 2004	Indian Ocean earthquake (Mw 9.0)
LAMA 12209M001	09. 04. 2000	start antenna problem
	06. 10. 2000	antenna change ¹
MAC1 50135M001	04. 01. 2001	receiver change
	23. 12. 2004	Macquarie Isl. earthquake (Mw8.1)
MADR 13407S012 ⁴	03. 10. 1996	receiver change
	30. 06. 2000	receiver change
MAGO 12354M001	17. 07. 2000	antenna cable (IGSMail 2950)
	13. 10. 2002	unknown
	02. 11. 2003	unknown
MALD 22901S001	28. 05. 2000	unknown
MALI 33201M001	23. 10. 1997	antenna-/receiver change
MANA 41201S001	11. 10. 2004	unknown
MATE 12734M008	09. 07. 1996	antenna/receiver change
	18. 06. 1999	antenna/receiver change
MCM4 66001M003	06. 02. 1999	unknown
	03. 01. 2002	receiver change
NANO 40138M001	09. 01. 2003	antenna/receiver change
NTUS 22601M001	26. 12. 2004	Indian Ocean earthquake (Mw 9.0)
ONSA 10402M004	02. 02. 1999	antenna change ¹
PENC 11206M006	22. 05. 2003	antenna/receiver change
PERT 50133M001	05. 06. 2003	antenna change
PETP 12355M002	15. 01. 2005	unknown
PIMO 22003M001	26. 12. 2004	Indian Ocean earthquake (Mw 9.0)
QAQ1 43007M001	30. 12. 2003	antenna change
QUIN 40433M004	06. 03. 1993	unknown
RAMO 20703S001	17. 07. 2000	antenna change ⁵
	19. 03. 2004	antenna change, monument repaired
REYK 10202M001	21. 06. 2000	Iceland earthquake (Mw 6.4)
SFER 13402M004	02. 06. 1998	antenna change
	05. 03. 2002	antenna/receiver change
	08. 06. 2003	unknown
SI03 40460M004	12. 10. 1994	antenna/receiver change
	16. 10. 1999	Hector Mine earthquake (Mw 7.2)

² *Bryuninx et al. (2003)*

³ According to IGSSATION 835 the antenna height reported in the log file (and also used for the reprocessing) before this date was wrong. This discontinuity might vanish if the correct antenna height is used for the whole time interval.

⁴ *Ferraro and Vespe (2000)*

⁵ *Bryuninx et al. (2006), Wdowinski et al. (2004)*

Station	Epoch	Comment
	12. 04. 2000	antenna change
SUWN 23903M001	14. 02. 2000	antenna/receiver change
TAIW 23601M001	11. 07. 1994	unknown
	17. 01. 1995	unknown
TLSE 10003M009	01. 12. 2003	antenna change
TR01 10302M006	22. 12. 1998	antenna change ¹
	13. 07. 2004	antenna change
UNSA 41514M001	11. 07. 2001	antenna change
USUD 21729S007	05. 09. 2004	unknown
VENE 12741M001	24. 08. 1999	unknown
	01. 02. 2001	antenna change
VILL 13406M001	28. 09. 2004	antenna change
WES2 40440S020	22. 05. 1997	antenna/receiver change
	30. 06. 1997	antenna change
	01. 06. 1998	antenna/receiver change
	22. 08. 2000	antenna change
	27. 07. 2001	antenna/receiver change
WUHN 21602M001	26. 01. 2002	pillar replacement ⁶
YELL 40127M003	22. 08. 1996	antenna change
	03. 11. 2000	unknown
	09. 03. 2001	unknown
YSSK 12329M003	25. 09. 2003	Hokkaido earthquake (Mw 8.3)
ZECK 12351M001	12. 07. 2001	antenna/receiver change
ZIMM 14001M004	06. 11. 1998	antenna change

Tab. C.1: List of discontinuities detected in the station coordinate time series. For earthquakes the magnitude is given in brackets.

⁶according to IGSSTATION 1423 a new granite pillar was set up in January 2002

D. Subdaily ERP Model TUM05G

Amplitudes of UT1

Tide	l	l'	F	D	Ω	T	Period [h]	u_j^c [μ s]	u_j^s [μ s]
σ	0	0	2	2	2	-1	27.848	-0.27	-1.04
$2Q_1$	2	0	2	0	2	-1	28.006	0.04	-0.99
Q_1'	1	0	2	0	1	-1	26.873	-0.45	-0.97
Q_1	1	0	2	0	2	-1	26.868	-2.52	-5.38
ρ_1	-1	0	2	2	2	-1	26.723	-0.41	-0.97
O_1'	0	0	2	0	1	-1	25.823	-2.37	-3.30
O_1	0	0	2	0	2	-1	25.819	-12.68	-17.66
	-1	0	2	0	2	-1	24.849	0.36	0.25
M_1	1	0	0	0	0	-1	24.833	0.65	1.03
N_1	0	1	2	-2	2	-1	24.132	-0.30	-0.45
P_1	0	0	2	-2	2	-1	24.066	-2.87	-5.95
S_1	0	1	0	0	0	-1	24.000	-0.40	0.75
K_1''	0	0	0	0	-1	-1	23.938	-0.17	-0.33
K_1	0	0	0	0	0	-1	23.934	8.78	17.54
K_1'	0	0	0	0	1	-1	23.931	1.19	2.38
ψ_1	0	-1	0	0	0	-1	23.869	-0.24	0.40
ϕ_1	0	0	-2	2	-2	-1	23.804	0.21	0.21
J_1	-1	0	0	0	0	-1	23.098	0.72	1.18
OO_1	0	0	-2	0	-2	-1	22.306	0.49	0.70
OO_1'	0	0	-2	0	-1	-1	22.303	0.31	0.45
η_1	-1	0	-2	0	-2	-1	21.578	0.18	0.12
η_1'	-1	0	-2	0	-1	-1	21.575	0.09	0.06
$2N_2$	2	0	2	0	2	-2	12.905	-0.40	0.63
μ_2	0	0	2	2	2	-2	12.872	-0.66	0.49
N_2	1	0	2	0	2	-2	12.658	-1.73	3.33
ν_2	-1	0	2	2	2	-2	12.626	-0.34	0.72
M_2'	0	0	2	0	1	-2	12.422	0.33	-0.54
M_2	0	0	2	0	2	-2	12.421	-8.77	14.35
L_2	-1	0	2	0	2	-2	12.192	0.32	-0.61
T_2	0	1	2	-2	2	-2	12.016	0.22	1.05
S_2	0	0	2	-2	2	-2	12.000	-0.86	7.53
R_2	0	1	0	0	0	-2	11.984	0.65	0.06
K_2	0	0	0	0	0	-2	11.967	0.30	1.55
K_2'	0	0	0	0	1	-2	11.966	0.09	0.46
M_3	0	0	3	0	3	-3	8.280	-0.09	0.00
Small	3	-1	2	0	2	-2	13.143	-0.03	0.00
Small	1	1	2	0	1	-2	12.678	0.01	-0.09
Small	0	0	0	-2	2	-2	11.575	0.02	0.07
Small	0	0	0	4	1	-1	27.668	-0.01	0.04
Small	1	0	4	-2	2	-1	27.043	-0.08	0.05
Small	0	0	0	1	0	-1	24.771	0.04	-0.03

Amplitudes of Prograde Polar Motion

Tide	l	l'	F	D	Ω	T	Period [h]	p_j^c [μas]	p_j^s [μas]
2Q ₁	-2	0	-2	0	-2	1	28.006	-4.04	-2.44
σ	0	0	-2	-2	-2	1	27.848	-5.90	-1.31
Q' ₁	-1	0	-2	0	-1	1	26.873	-5.80	0.81
Q'' ₁	-1	0	-2	0	-2	1	26.868	-32.22	4.48
ρ_1	1	0	-2	-2	-2	1	26.723	-7.06	-0.12
O' ₁	0	0	-2	0	-1	1	25.823	-25.36	8.49
O ₁	0	0	-2	0	-2	1	25.819	-135.60	45.39
	1	0	-2	0	-2	1	24.849	0.49	-1.95
M ₁	-1	0	0	0	0	1	24.833	8.40	-5.28
N ₁	0	-1	-2	2	-2	1	24.132	1.23	8.26
P ₁	0	0	-2	2	-2	1	24.066	-44.60	28.04
S ₁	0	-1	0	0	0	1	24.000	9.95	-3.60
K'' ₁	0	0	0	0	1	1	23.938	-2.85	1.75
K ₁	0	0	0	0	0	1	23.934	150.30	-92.00
K' ₁	0	0	0	0	-1	1	23.931	20.37	-12.47
ψ_1	0	1	0	0	0	1	23.869	15.21	-4.67
ϕ_1	0	0	2	-2	2	1	23.804	0.50	-2.71
J ₁	1	0	0	0	0	1	23.098	8.22	-7.17
OO ₁	0	0	2	0	2	1	22.306	5.52	-4.65
OO' ₁	0	0	2	0	1	1	22.303	3.51	-2.96
η_1	1	0	2	0	2	1	21.578	0.98	-0.81
η'_1	1	0	2	0	1	1	21.575	0.49	-0.40
2N ₂	-2	0	-2	0	-2	2	12.905	1.67	-1.28
μ_2	0	0	-2	-2	-2	2	12.872	1.18	-2.29
N ₂	-1	0	-2	0	-2	2	12.658	11.53	-11.72
ν_2	1	0	-2	-2	-2	2	12.626	2.15	-1.46
M' ₂	0	0	-2	0	-1	2	12.422	-1.53	2.45
M ₂	0	0	-2	0	-2	2	12.421	40.33	-64.58
L ₂	1	0	-2	0	-2	2	12.192	-0.58	1.55
T ₂	0	-1	-2	2	-2	2	12.016	-1.35	-4.28
S ₂	0	0	-2	2	-2	2	12.000	3.52	-29.19
R ₂	0	-1	0	0	0	2	11.984	4.16	1.55
K ₂	0	0	0	0	0	2	11.967	4.00	-3.15
K' ₂	0	0	0	0	-1	2	11.966	1.20	-0.95
M ₃	0	0	-3	0	-3	3	8.280	-0.27	0.50
Small	0	0	0	-4	-1	1	27.668	0.71	0.57
Small	-1	0	-4	2	-2	1	27.043	-1.19	1.27
Small	0	0	0	-1	0	1	24.771	0.11	-1.50
Small	-3	1	-2	0	-2	2	13.143	0.39	0.55
Small	-1	-1	-2	0	-1	2	12.678	-0.36	-0.09
Small	0	0	0	2	-2	2	11.575	-0.81	-0.04

Amplitudes of Retrograde Polar Motion

Tide	l	l'	F	D	Ω	T	Period [h]	p_j^c [μas]	p_j^s [μas]
$2N_2$	2	0	2	0	2	-2	12.905	0.35	7.16
μ_2	0	0	2	2	2	-2	12.872	0.74	9.10
N_2	1	0	2	0	2	-2	12.658	-1.00	43.63
ν_2	-1	0	2	2	2	-2	12.626	-1.09	7.92
M'_2	0	0	2	0	1	-2	12.422	0.37	-9.74
M_2	0	0	2	0	2	-2	12.421	-9.7	256.62
L_2	-1	0	2	0	2	-2	12.192	0.32	-8.34
T_2	0	1	2	-2	2	-2	12.016	-4.95	5.37
S_2	0	0	2	-2	2	-2	12.000	-63.56	111.68
R_2	0	1	0	0	0	-2	11.984	-3.86	5.58
K_2	0	0	0	0	0	-2	11.967	-13.02	36.15
K'_2	0	0	0	0	1	-2	11.966	-3.91	10.84
M_3	0	0	3	0	3	-3	8.280	-0.20	-0.83
Small	3	-1	2	0	2	-2	13.143	-0.83	1.16
Small	1	1	2	0	1	-2	12.678	0.20	0.41
Small	0	0	0	-2	2	-2	11.575	0.50	-0.09

E. Nutation Model TUM05N

l	l'	F	D	Ω	Period [d]	Component	IAU2000A [μas]	TUM05N [μas]	σ [μas]
1	0	2	4	2	4.083	ψ^s	-16	-18	9
						ψ^c	0	2	9
						ϵ^c	7	7	4
						ϵ^s	0	-1	4
4	0	2	0	2	4.579	ψ^s	-26	-23	10
						ψ^c	0	-4	10
						ϵ^c	11	11	4
						ϵ^s	0	1	4
2	0	2	2	2	4.684	ψ^s	-110	-114	11
						ψ^c	1	-1	11
						ϵ^c	46	48	4
						ϵ^s	0	-5	4
0	0	2	4	2	4.793	ψ^s	-69	-68	11
						ψ^c	0	1	11
						ϵ^c	29	30	4
						ϵ^s	0	0	4
3	0	2	0	2	5.492	ψ^s	-290	-284	13
						ψ^c	2	-1	13
						ϵ^c	123	123	5
						ϵ^s	1	3	5
1	0	2	2	2	5.643	ψ^s	-769	-778	13
						ψ^c	4	-2	13
						ϵ^c	327	328	5
						ϵ^s	2	5	5
1	1	2	2	2	5.731	ψ^s	-59	-68	13
						ψ^c	0	-4	13
						ϵ^c	25	24	5
						ϵ^s	0	6	5
-1	0	2	4	2	5.802	ψ^s	-152	-146	13
						ψ^c	1	-5	13
						ϵ^c	65	65	5
						ϵ^s	0	-3	5
2	1	2	0	2	6.733	ψ^s	41	68	16
						ψ^c	0	7	16
						ϵ^c	-18	-23	6
						ϵ^s	0	-1	6
2	0	2	0	2	6.859	ψ^s	-3105	-3103	16
						ψ^c	13	10	16
						ϵ^c	1324	1316	6
						ϵ^s	6	2	6
0	1	2	2	2	6.961	ψ^s	54	63	16
						ψ^c	0	3	16
						ϵ^c	-23	-19	6
						ϵ^s	0	-6	6
0	0	2	2	2	7.096	ψ^s	-3857	-3861	16
						ψ^c	16	29	16

l	l'	F	D	Ω	Period [d]	Component	IAU2000A [μ as]	TUM05N [μ as]	σ [μ as]
						ϵ^c	1645	1643	6
						ϵ^s	7	10	6
0	1	2	2	2	7.236	ψ^s	-265	-278	17
						ψ^c	1	3	17
						ϵ^c	113	112	7
						ϵ^s	0	5	7
-2	0	2	4	2	7.349	ψ^s	-121	-135	17
						ψ^c	0	6	17
						ϵ^c	52	54	7
						ϵ^s	0	0	7
3	0	2	2	2	8.745	ψ^s	93	116	20
						ψ^c	0	-3	20
						ϵ^c	-40	-42	8
						ϵ^s	0	-8	8
1	1	2	0	2	8.910	ψ^s	248	246	20
						ψ^c	-1	-36	20
						ϵ^c	-106	-106	8
						ϵ^s	0	-8	8
-1	0	4	0	2	9.057	ψ^s	115	127	21
						ψ^c	0	-8	21
						ϵ^c	-49	-53	8
						ϵ^s	0	-9	8
1	0	2	0	2	9.133	ψ^s	-30146	-30154	21
						ψ^c	82	58	21
						ϵ^c	12902	12900	8
						ϵ^s	37	25	8
-1	1	2	2	2	9.313	ψ^s	57	62	22
						ψ^c	0	6	22
						ϵ^c	-24	-22	9
						ϵ^s	0	3	9
1	1	2	0	2	9.367	ψ^s	-288	-276	22
						ψ^c	1	-10	22
						ϵ^c	123	115	9
						ϵ^s	0	3	9
-1	0	2	2	2	9.557	ψ^s	-5964	-5954	22
						ψ^c	15	25	22
						ϵ^c	2554	2554	9
						ϵ^s	7	5	9
1	0	0	2	1	9.627	ψ^s	-97	-106	22
						ψ^c	0	-15	22
						ϵ^c	50	48	9
						ϵ^s	0	6	9
-1	1	2	2	2	9.814	ψ^s	-282	-294	23
						ψ^c	1	-8	23
						ϵ^c	121	124	9
						ϵ^s	0	-7	9
-1	0	0	4	0	10.085	ψ^s	134	131	23
						ψ^c	0	-8	23
						ϵ^c	-4	-11	9
						ϵ^s	0	13	9
0	0	4	2	2	12.663	ψ^s	92	127	29
						ψ^c	0	41	29
						ϵ^c	-40	-57	12
						ϵ^s	0	-2	12

l	l'	F	D	Ω	Period [d]	Component	IAU2000A [μas]	TUM05N [μas]	σ [μas]
2	0	2	2	2	12.811	ψ^s	644	646	30
						ψ^c	-1	-71	30
						e^c	-277	-282	12
						e^s	0	3	12
0	1	2	0	2	13.168	ψ^s	757	736	30
						ψ^c	-1	26	30
						e^c	-325	-331	12
						e^s	0	6	12
0	0	2	0	2	13.661	ψ^s	-227641	-227668	32
						ψ^c	280	247	32
						e^c	97846	97838	13
						e^s	137	153	13
2	0	0	0	0	13.777	ψ^s	2924	2920	32
						ψ^c	-7	-13	32
						e^c	-61	-56	13
						e^s	1	-3	13
0	1	2	0	2	14.192	ψ^s	-714	-712	33
						ψ^c	1	27	33
						e^c	307	311	13
						e^s	0	-4	13
-2	0	2	2	2	14.632	ψ^s	138	148	34
						ψ^c	0	-37	34
						e^c	-59	-55	14
						e^s	0	-12	14
0	0	0	2	0	14.765	ψ^s	6338	6326	34
						ψ^c	-15	-103	34
						e^c	-122	-104	14
						e^s	3	-16	14
0	1	0	2	0	15.387	ψ^s	435	422	35
						ψ^c	-1	-10	35
						e^c	-8	9	14
						e^s	0	-16	14
-2	0	0	4	0	15.906	ψ^s	128	126	37
						ψ^c	0	18	37
						e^c	-2	2	15
						e^s	0	-30	15

F. Abbreviations

AAM	Atmospheric Angular Momentum
AC	Analysis Center
ACC	Analysis Center Coordinator
AIUB	Astronomisches Institut der Universität Bern
AMMM	Autonomous Magnetic Momentum Management
APCM	Antenna Phase Center Model
AR	Ambiguity Resolution
ARP	Antenna Reference Point
AS	Anti-Spoofing
AWI	Alfred-Wegener-Institut für Polar- und Meeresforschung, Bremerhaven
BPE	Bernese Processing Engine
CDDIS	Crustal Dynamics Data Information System
CDP	Crustal Dynamics Project
CEO	Celestial Ephemeris Origin
CIP	Celestial Intermediate Pole
CNRS	Centre National de la Recherche Scientifique, Paris
CODE	Center for Orbit Determination in Europe
CORS	Continuously Operating Reference Stations
COSPAR	Committee on Space Research
CRF	Celestial Reference Frame
Cs	Caesium
CSR	Center for Space Research, University of Texas
CSTG	Commission on International Coordination of Space Techniques for Geodesy and Geodynamics
CWT	Continuous Wavelet Transform
DC	Data Center
DCB	Differential Code Bias
DD	Double-Difference
DEM	Digital Elevation Model
DFG	Deutsche Forschungsgemeinschaft
DGFI	Deutsches Geodätisches Forschungsinstitut, München
DNSC	Danish National Space Center, Copenhagen
DoD	Department of Defense
DORIS	Doppler Orbitography and Radiopositioning Integrated by Satellite

EAMF	Effective Angular Momentum Function
ECCO	Estimating the Circulation and Climate of the Ocean
ECMWF	European Centre for Medium-Range Weather Forecasts
ECOM	Enhanced CODE Orbit Model
EOP	Earth Orientation Parameter
EPN	EUREF Permanent Network
ERP	Earth Rotation Parameter
ESOC	European Space Operations Centre, Darmstadt
ETS	Episodic Tremor and Slip
EUREF	IAG Reference Frame Sub-Commission for Europe
FESG	Forschungseinrichtung Satellitengeodäsie der Technischen Universität München
FFT	Fast Fourier Transform
FT	Fourier Transform
GFZ	GeoForschungsZentrum Potsdam
GGOS	Global Geodetic Observing System
GIM	Global Ionosphere Map
GLONASS	Globalnaya Navigatsionnaya Sputnikovaya Sistema (Global Navigation Satellite System)
GMF	Global Mapping Function
GNSS	Global Navigation Satellite System
GOP	Geodetic Observatory Pecny
GPS	Global Positioning System
GPT	Global Pressure and Temperature Model
GSFC	Goddard Space Flight Center, Maryland
IAA	Institute of Applied Astronomy, St. Petersburg
IAG	International Association of Geodesy
IAU	International Astronomical Union
IERS	International Earth Rotation and Reference Systems Service
IGEX	International GLONASS Experiment
IGRF	International Geomagnetic Reference Field
IGS	International GNSS Service
ILRS	International Laser Ranging Service
IMF	Isobaric Mapping Function
IPG	Institut für Planetare Geodäsie der Technischen Universität Dresden
ITRF	International Terrestrial Reference Frame
ITRS	International Terrestrial Reference System
IUGG	International Union of Geodesy and Geophysics
IVS	International VLBI Service for Geodesy and Astrometry
JPL	Jet Propulsion Laboratory, Pasadena
LEO	Low Earth Orbiter

LLR	Lunar Laser Ranging
LOD	Length of Day
LRA	Laser Retroreflector Array
LSA	Least-Squares Adjustment
LRZ	Leibniz-Rechenzentrum der Bayerischen Akademie der Wissenschaften, München
MEO	Medium Earth Orbiter
MF	Mapping Function
MIT	Massachusetts Institute of Technology, Cambridge, Maryland
MJD	Modified Julian Date
MSLM	Modified Single-Layer Model
MW	Melbourne-Wübbena
NAVSTAR	Navigation System with Time and Ranging
NCEP	National Centers for Environmental Prediction, Camp Springs, Maryland
NEQ	Normal Equation (System)
NGS	National Geodetic Survey, Silver Spring, Maryland
NMF	Niell Mapping Function
NNR	No-Net-Rotation
NNS	No-Net-Scale
NNT	No-Net-Translation
NOAA	National Oceanic and Atmospheric Administration, Washington
NP	Normal Point
NRCan	National Resources Canada, Ottawa
OAM	Oceanic Angular Momentum
PB	Plate Boundary
PCO	Phase Center Offset
PCV	Phase Center Variation
PRN	Pseudo-Random Noise
QIF	Quasi-Ionosphere-Free
Rb	Rubidium
RINEX	Receiver Independent Exchange (Format)
RMS	Root Mean Square
RPR	Radiation Pressure
RW	Reaction Wheel
SA	Selective Availability
SD	Single-Difference
SINEX	Solution Independent Exchange (Format)
SIO	Scripps Institute of Oceanography, San Diego, California
SIP	Stochastic Ionosphere Parameter
SLR	Satellite Laser Ranging

SOPAC	Scripps Orbit and Permanent Array Center, La Jolla, California
STD	Standard Deviation
SVN	Space Vehicle Number
TCG	Geocentric Coordinate Time
TD	Triple-Difference
TDT	Terrestrial Dynamical Time
TEC	Total Electron Content
TECU	Total Electron Content Unit
teqc	Translation, Editing, Quality Check
TRF	Terrestrial Reference Frame
TT	Terrestrial Time
TUD	Technische Universität Dresden
TUM	Technische Universität München
USNO	United States Naval Observatory, Washington
UT	Universal Time
UT1	Universal Time 1
UTC	Universal Time Coordinated
VLBI	Very Long Baseline Interferometry
VMF	Vienna Mapping Function
VTEC	Vertical Total Electron Content
WRMS	Weighted RMS
ZD	Zero-Difference
ZHD	Zenith Hydrostatic Delay
ZTD	Zenith Total Delay
ZWD	Zenith Wet Delay

Bibliography

- Altamimi, Z., P. Sillard, and C. Boucher (2002), ITRF2000: A new release of the International Terrestrial Reference Frame for earth science applications, *Journal of Geophysical Research*, 107(B10), 2214, doi:10.1029/2001JB000561.
- Altamimi, Z., P. Sillard, and C. Boucher (2004), ITRF2000: From theory to implementation, in *V Hotine-Marussi Symposium on Mathematical Geodesy, International Association of Geodesy Symposia*, vol. 127, edited by F. Sanso, pp. 157–163, Springer, Berlin, Heidelberg, New York, ISBN: 3-540-21979-X.
- Altamimi, Z., C. Boucher, and D. Gambis (2005a), Long-term stability of the terrestrial reference frame, *Advances in Space Research*, 36(3), 342–349, doi:10.1016/j.asr.2005.03.068.
- Altamimi, Z., C. Boucher, and P. Willis (2005b), Terrestrial reference frame requirements within GGOS perspective, *Journal of Geodynamics*, 40(4-5), 363–374, doi:10.1016/j.jog.2005.06.002.
- Altamimi, Z., X. Collilieux, J. Legrand, B. Garayt, and C. Boucher (2007), ITRF2005: A new release of the International Terrestrial Reference Frame based on time series of station positions and Earth Orientation Parameters, *Journal of Geophysical Research*, 112, B09401, doi:10.1029/2007JB004949.
- Angermann, D., H. Müller, and M. Gerstl (2002), Geocenter variations derived from SLR data to LAGEOS 1 and 2, in *Vistas for Geodesy in the New Millennium, International Association of Geodesy Symposia*, vol. 125, edited by J. Adam and K.-P. Schwarz, pp. 31–35, Springer, Berlin, Heidelberg, New York, ISBN: 3-540-43454-2.
- Angermann, D., H. Drewes, M. Krügel, B. Meisel, M. Gerstl, R. Kelm, H. Müller, W. Seemüller, and V. Tesmer (2004), ITRS combination center at DGFI – a terrestrial reference frame realization 2003, in *Deutsche Geodätische Kommission, Reihe B*, vol. 313, München.
- Angermann, D., B. Meisel, M. Krügel, H. Müller, and V. Tesmer (2005), Time evolution of the Terrestrial Reference Frame, in *A Window on the Future of Geodesy, International Association of Geodesy Symposia*, vol. 128, edited by F. Sanso, pp. 9–14, Springer, Berlin, Heidelberg, New York, doi:10.1007/3-540-27432-4.2, ISBN: 3-540-24055-1.
- Appleby, G. M., and T. Otsubo (2005), Laser Ranging as a Precise Tool to Evaluate GNSS orbital solutions, in *14th International Workshop on Laser Ranging, Boletín ROA*, vol. 5/2005, edited by J. Garate, J. Davila, C. Noll, and M. Pearlman, Real Instituto y Observatorio de la Armada, San Fernando.
- Argus, D., and R. Gordon (1991), No-net-rotation model of current plate velocities incorporating plate motion model NUVEL-1, *Geophysical Research Letters*, 111(18), 2039–2042, doi:10.1029/91GL01532.
- Árnadóttir, T., S. Hreinsdóttir, G. Gudmundsson, P. Einarsson, M. Heinert, and C. Völksen (2001), Crustal deformation measured by GPS in the South Iceland Seismic Zone due to two large earthquakes in June 2000, *Geophysical Research Letters*, 28(21), 4031–4033, doi:10.1029/2001GL013332.
- Ashby, N. (2003), Relativity in the Global Positioning System, *Living Reviews in Relativity*, 6, available at <http://relativity.livingreviews.org/Articles/lrr-2003-1/>.
- Bar-Sever, Y. E. (1996), A new model for GPS yaw attitude, *Journal of Geodesy*, 70(1), 714–723, doi:10.1007/BF00867149.
- Bassiri, S., and G. Hajj (1993), Higher-order ionospheric effects on the global positioning system observables and means of modeling them, *Manuscripta Geodaetica*, 18, 280–289.
- Berg, H. (1948), *Allgemeine Meteorologie*, Dümmlers Verlag, Bonn.
- Beutler, G. (1993a), The 1992 activities of the International GPS Geodynamics Service (IGS), in *Geodesy and Physics of the Earth*, edited by H. Montag and C. Reigber, pp. 9–13, Springer, Berlin, Heidelberg, New York, ISBN: 3-540-56572-8.
- Beutler, G. (1993b), The 1992 IGS Test Campaign, Epoch'92, and the IGS Pilot Service: An overview, in *Proceedings of the 1993 IGS Workshop*, edited by G. Beutler and E. Brockmann, pp. 3–9, Druckerei der Universität Bern, Bern.
- Beutler, G. (2005), *Methods of Celestial Mechanics Volume II: Application to Planetary System, Geodynamics and Satellite Geodesy*, Springer, Berlin, Heidelberg, doi:10.1007/b137725.

- Beutler, G., E. Brockmann, W. Gurtner, U. Hugentobler, L. Mervart, and M. Rothacher (1994a), Extended orbit modeling techniques at the CODE Processing Center of the International GPS Service (IGS): Theory and initial results, *Manuscripta Geodaetica*, 19, 367–386.
- Beutler, G., I. Mueller, and R. Neilan (1994b), The International GPS Service for Geodynamics (IGS): Development and start of official service on 1 January 1994, *Bulletin Geodésique*, 68(1), 43–51, doi:10.1007/BF00806751.
- Beutler, G., I. Mueller, and R. Neilan (1996), The International GPS Service for Geodynamics (IGS): the story, in *GPS Trends in Precise Terrestrial, Airborne, and Spaceborne Applications, International Association of Geodesy Symposia*, vol. 115, edited by G. Beutler, G. Hein, W. G. Melbourne, and G. Seeber, pp. 3–13, Springer, Berlin, Heidelberg, New York, ISBN: 3-540-60872-9.
- Beutler, G., M. Rothacher, S. Schaer, T. Springer, J. Kouba, and R. Neilan (1999), The International GPS Service (IGS): an interdisciplinary service in support of Earth sciences, *Advances in Space Research*, 23(4), 631–653, doi:10.1016/S0273-1177(99)00160-X.
- Bizouard, C., and D. Gambis (2007), The combined solution C04 for Earth orientation parameters consistent with International Reference Frame 2005, available at http://hpiers.obspm.fr/iers/eop/eopc04_05/C04_05.guide.pdf.
- Blewitt, G., and D. Lavallée (2002), Effect of annual signals on geodetic velocity, *Journal of Geophysical Research*, 107(B7), 2145, doi:10.1029/2001JB000570.
- Bock, H., G. Beutler, S. Schaer, T. Springer, and M. Rothacher (2000), Processing aspects related to permanent GPS arrays, *Earth Planets Space*, 52(10), 657–662.
- Boehm, J., and H. Schuh (2004), Vienna mapping functions in VLBI analyses, *Geophysical Research Letters*, 31, L01603, doi:10.1029/2003GL018984.
- Boehm, J., H. Schuh, V. Tesmer, and H. Schmitz-Huebsch (2003), Tropospheric zenith delays determined by VLBI as a contribution to climatological studies, in *Proceedings of the 16th Working Meeting European VLBI for Geodesy and Astrometry*, edited by W. Schwegmann and V. Thorandt, pp. 237–246, Bundesamt für Kartographie und Geodäsie, Leipzig/Frankfurt am Main.
- Boehm, J., A. Niell, P. Tregoning, and H. Schuh (2006a), Global mapping function (GMF): A new empirical mapping function based on numerical weather model data, *Geophysical Research Letters*, 33, L07304, doi:10.1029/2005GL025546.
- Boehm, J., B. Werl, and H. Schuh (2006b), Troposphere mapping functions for GPS and very long baseline interferometry from European Centre for Medium-Range Weather Forecasts operational analysis data, *Journal of Geophysical Research*, 111, B02406, doi:10.1029/2005JB003629.
- Boehm, J., P. Cervera, H. Schuh, and P. Tregoning (2007a), The impact of tropospheric mapping functions based on numerical weather models on the determination of geodetic parameters, in *Dynamic Planet - Monitoring and Understanding a Dynamic Planet with Geodetic and Oceanographic Tools, International Association of Geodesy Symposia*, vol. 130, edited by P. Tregoning and C. Rizos, pp. 837–843, Springer, Berlin, Heidelberg, New York, doi:10.1007/978-3-540-49350-1_118, ISBN: 3-540-49349-5.
- Boehm, J., R. Heinkelmann, and H. Schuh (2007b), Short note: A global model of pressure and temperature for geodetic applications, *Journal of Geodesy*, 81(10), 679–683, doi:10.1007/s00190-007-0135-3.
- Boucher, C., Z. Altamimi, and L. Duhem (1993), ITRF 92 and its associated velocity field, *IERS Technical Note 15*, Observatoire de Paris, Paris.
- Boucher, C., Z. Altamimi, and L. Duhem (1994), Results and analysis of the ITRF93, *IERS Technical Note 18*, Observatoire de Paris, Paris.
- Boucher, C., Z. Altamimi, and P. Sillard (1998), Results and analysis of the ITRF96, *IERS Technical Note 24*, Observatoire de Paris, Paris.
- Boucher, C., Z. Altamimi, and P. Sillard (1999), The 1997 International Terrestrial Reference Frame (ITRF97), *IERS Technical Note 27*, Observatoire de Paris, Paris.
- Brockmann, E. (1997), Combination of solutions for geodetic and geodynamic applications of the Global Positioning System (GPS), *Geodätisch-geophysikalische Arbeiten in der Schweiz*, 55, Zürich, Switzerland.
- Brunner, F. (2001), personal communication.
- Brunner, F., and M. Gu (1991), An improved model for the dual frequency ionospheric correction of GPS observations, *Manuscripta Geodaetica*, 16, 72–75.
- Bruyninx, C. (2007), Comparing GPS-only with GPS + GLONASS positioning in a regional permanent GNSS network, *GPS Solutions*, 11(2), 97–106, doi:10.1007/s10291-006-0041-9.

- Bruyninx, C., G. Carpentier, and F. Roosbeek (2003), EPN monitoring: Status and plans, in *EUREF Publication No. 12: Report on the Symposium of the IAG Sub-commission for Europe (EUREF) held in Ponta Delgada, 5 - 8 June 2002*, edited by J. Torres and H. Hornik, Mitteilungen des Bundesamtes für Kartographie und Geodäsie Band 29, pp. 32–42, Frankfurt am Main, ISBN: 3-89888-873-8.
- Bruyninx, C., G. Carpentier, and F. Roosbeek (2006), Day-to-day monitoring of the EPN, in *EUREF Publication No. 14: Report on the Symposium of the IAG Sub-commission for Europe (EUREF) held in Bratislava, 2 - 5 June 2004*, edited by J. Torres and H. Hornik, Mitteilungen des Bundesamtes für Kartographie und Geodäsie Band 35, pp. 37–44, Frankfurt am Main, ISBN: 3-89888-795-2.
- Brzezinski, A., C. Bizouard, and S. Petrov (2002), Influence of the atmosphere on earth rotation: What new can be learned from the recent atmospheric angular momentum estimates?, *Surveys in Geophysics*, *23*(1), 33–69, doi:10.1023/A:1014847319391.
- Brzezinski, A., R. Ponte, and A. Ali (2004), Nontidal oceanic excitation of nutation and diurnal/semidiurnal polar motion revisited, *Journal of Geophysical Research*, *109*(B11), doi:10.1029/2004JB003054.
- Campbell, J., B. Görres, M. Siemes, J. Wirsch, and M. Becker (2004), Zur Genauigkeit der GPS Antennenkalibrierung auf der Grundlage von Labormessungen und deren Vergleich mit anderen Verfahren, *Allgemeine Vermessungs-Nachrichten*, *111*(1), 2–11.
- Capitaine, N., P. Wallace, and D. McCarthy (2003), Expressions to implement the IAU 2000 definition of UT1, *Astronomy and Astrophysics*, *406*(3), 1135–1149, doi:10.1051/0004-6361:20030817.
- Cartwright, D. E., and A. C. Edden (1973), Corrected tables of tidal harmonics, *Geophysical Journal of the Royal Astronomical Society*, *33*(3), 253–264.
- Cartwright, D. E., and R. J. Taylor (1971), New computations of the tide-generating potential, *Geophysical Journal of the Royal Astronomical Society*, *23*(1), 45–74.
- Chao, B., D. N. Dong, H. S. Liu, and T. A. Herring (1991), Libration in the Earth's rotation, *Geophysical Research Letters*, *18*(11), 2007–2010, doi:10.1029/91GL02491.
- Chao, B., R. Ray, and G. Egbert (1995), Diurnal/semidiurnal oceanic tidal angular momentum: Topex/Poseidon models in comparison with Earth's rotation rate, *Geophysical Research Letters*, *22*(15), 1993–1996, doi:10.1029/95GL01788.
- Chao, B., R. Ray, J. Gipson, G. Egbert, and C. Ma (1996), Diurnal/semidiurnal polar motion excited by oceanic tidal angular momentum, *Journal of Geophysical Research*, *101*(B9), 20,151–20,164, doi:10.1029/96JB01649.
- Chen, G., and T. Herring (1997), Effects of atmospheric azimuthal asymmetry on the analysis of space geodetic data, *Journal of Geophysical Research*, *102*(B9), 20,489–20,502, doi:10.1029/97JB01739.
- Chen, J., C. Wilson, R. Eanes, and R. Nerem (1999), Geophysical interpretation of observed geocenter variations, *Journal of Geophysical Research*, *104*(B2), 2683–2690, doi:10.1029/1998JB900019.
- Dach, R., G. Beutler, U. Hugentobler, S. Schaer, T. Schildknecht, T. Springer, G. Dudle, and L. Probst (2003), Time transfer using GPS carrier phase: error propagation and results, *Journal of Geodesy*, *77*(1-2), 1–14, doi:10.1007/s00190-002-0296-z.
- Dach, R., U. Hugentobler, P. Fridez, and M. Meindl (Eds.) (2007), *Bernese GPS Software Version 5.0*, Astronomical Institute, University of Bern, Bern, Switzerland.
- Daniel, G., D. Marsan, and M. Bouchon (2006), Perturbation of the Izmit earthquake aftershock decaying activity following the 1999 M_w 7.2 Düzce, Turkey, earthquake, *Journal of Geophysical Research*, *111*, B05310, doi:10.1029/2005JB003978.
- Degnan, J. (1993), Millimeter Accuracy Satellite Laser Ranging, in *Contributions of Space Geodesy to Geodynamics: Technology, Geodynamics Series*, vol. 25, edited by D. E. Smith and D. L. Turcotte, pp. 133–162, American Geophysical Union, Washington, D.C., ISBN: 0-87590-526-9.
- Degnan, J. (1997), Pro 1997 CSTG Satellite and Lunar Laser Ranging - Subcommission Report, in *Commission VIII - International Coordination of Space Techniques for Geodesy and Geodynamics (CSTG): Progress Report 1996*, edited by G. Beutler, H. Drewes, and H. Hornik, no. 13 in CSTG Bulletin, pp. 47–59, Deutsches Geodätisches Forschungsinstitut, München.
- Degnan, J. J., and E. C. Pavlis (1994), Laser ranging to GPS satellites with centimeter accuracy, *GPS World*, *5*(9), 62–70.
- DeMets, C., R. Gordon, D. Argus, and S. Stein (1994), Effect of recent revisions to the geomagnetic reversal timescale on estimates of current plate motions, *Geophysical Research Letters*, *21*(20), 2191–2194, doi:10.1029/94GL02118.

- Dickman, S. R. (2003), Evaluation of effective angular momentum function formulations with respect to core-mantle coupling, *Journal of Geophysical Research*, 108(B3), doi:10.1029/2001JB001603.
- Dieter, G. L., and J. Taylor (1999), GPS Block II operations reach a ten year benchmark: Managing a mature constellation, in *Proceedings of ION GPS-99*, pp. 2261–2268, Nashville, Tennessee.
- Dong, D., P. Fang, Y. Bock, M. Cheng, and S. Miyazaki (2002), Anatomy of apparent seasonal variations from GPS-derived site position time series, *Journal of Geophysical Research*, 107(B4), 2075, doi:10.1029/2001JB000573.
- Dow, J., R. Neilan, and G. Gendt (2005), The International GPS Service: Celebrating the 10th anniversary and looking to the next decade, *Advances in Space Research*, 36(3), 320–326, doi:10.1016/j.asr.2005.05.125.
- Duha, J., G. Afonso, and L. Ferreira (2006), Thermal re-emission effects on GPS satellites, *Journal of Geodesy*, 80(12), 665–674, doi:10.1007/s00190-006-0060-x.
- Eanes, R., and S. Bettadpur (1996), The CSR 3.0 global ocean tide model, *Technical Memorandum CSR-TM-96-05*, Center for Space Research, Austin, Texas.
- Egbert, G. D., A. F. Bennett, and M. G. Foreman (1994), TOPEX/POSEIDON tides estimated using a global inverse model, *Journal of Geophysical Research*, 99(C12), 24,821–24,852, doi:10.1029/94JC01894.
- Eller, T. J., and R. P. Fuchs (2008), A history of magnetic momentum dumping on Global Positioning System (GPS) satellites, in *Spaceflight Mechanics 2008, Advances in the Astronautical Sciences*, vol. 130, edited by J. H. Seago, B. Neta, T. J. Eller, and F. J. Pelletier, pp. 1819–1830, American Astronautical Society, Univelt, Inc., San Diego, ISBN: 978-0-87703-544-2.
- Elosegui, P., J. Davis, R. Jaldehag, J. Johansson, A. Niell, and I. Shapiro (1995), Geodesy using the Global Positioning System: The effects of signal scattering on estimates of site position, *Journal of Geophysical Research*, 100(B6), 9921–9934, doi:10.1029/95JB00868.
- Ergintav, S., R. Bürgmann, S. McClusky, R. Cakmak, R. Reilinger, O. Lenk, A. Barka, and H. Özener (2002), Post-seismic deformation near the Izmit earthquake (17 August 1999, M 7.5) rupture zone, *Bulletin of the Seismological Society of America*, 92(1), 194–207, doi:10.1785/0120000836.
- Estey, L., and C. Meertens (1999), Teqc: The multi-purpose toolkit for GPS/GLONASS data, *GPS Solutions*, 3(1), 42–49, doi:10.1007/s10291-002-0027-1.
- Feissel-Vernier, M., K. Bail, P. Berio, D. Coulot, G. Ramillien, and J.-J. Valette (2006), Geocentre motion measured with DORIS and SLR, and predicted by geophysical models, *Journal of Geodesy*, 80(8-11), 637–648, doi:10.1007/s00190-006-0079-z.
- Ferland, R. (2008), From relative to absolute antenna phase center calibrations: The effect on the SINEX products, in *The International GNSS Service (IGS): Perspectives and Visions for 2010 and Beyond, Proceedings of the IGS Workshop 2006*, edited by T. Springer, G. Gendt, and J. Dow, European Space Operations Centre, European Space Agency, Darmstadt.
- Ferland, R., J. Kouba, and D. Hutchinson (2000), Analysis methodology and recent results of the IGS network combination, *Earth Planets Space*, 52(11), 953–957.
- Ferland, R., G. Gendt, and T. Schöne (2005), IGS reference frame maintenance, in *Celebrating a Decade of the International GPS Service, Workshop and Symposium 2004*, edited by M. Meindl, pp. 13–35, Astronomical Institute, University of Bern, Bern, Switzerland.
- Ferraro, L., and F. Vespe (2000), Trying to understand what is happening in Madrid IGS station, in *EUREF TWG Meeting*, Lisboa.
- Fliegel, H., and T. Gallini (1996), Solar force modeling of Block IIR Global Positioning System satellites, *Journal of Spacecraft and Rockets*, 33(6), 863–866.
- Fliegel, H., T. Gallini, and E. Swift (1992), Global Positioning System radiation force model for geodetic applications, *Journal of Geophysical Research*, 97(B1), 559–568, doi:10.1029/91JB02564.
- Flohrer, C. (2008), Mutual validation of satellite-geodetic techniques and its impact on GNSS orbit modeling, *Geodätisch-geophysikalische Arbeiten in der Schweiz*, 75, Zürich, Switzerland.
- Fraser-Smith, A. C. (1987), Centered and eccentric geomagnetic dipoles and their poles, 1600-1985, *Reviews of Geophysics*, 25(1), 1–16.
- Fritsche, M., R. Dietrich, C. Knöfel, A. Rülke, S. Vey, M. Rothacher, and P. Steigenberger (2005), Impact of higher-order ionospheric terms on GPS estimates, *Geophysical Research Letters*, 32, L23311, doi:10.1029/2005GL024342.
- Gambis, D. (2004), Monitoring Earth orientation using space-geodetic techniques: state-of-the-art and prospective, *Journal of Geodesy*, 78(4-5), 295–303, doi:10.1007/s00190-004-0394-1.

- Gambis, D. (2006), DORIS and the determination of the Earth's polar motion, *Journal of Geodesy*, 80(8-11), 640–656, doi:10.1007/s00190-006-0043-y.
- Ge, M., G. Gendt, G. Dick, F. Zhang, and C. Reigber (2005), Impact of GPS satellite antenna offsets on scale changes in global network solutions, *Geophysical Research Letters*, 32, L06310, doi:10.1029/2004GL022224.
- Gendt, G. (1996), Comparison of IGS troposphere estimations, in *Proceedings IGS 1996 Analysis Center Workshop*, edited by R. Neilan, P. van Scoy, and J. Zumberge, pp. 151–164, IGS Central Bureau, Pasadena.
- Gendt, G. (2005), personal communication.
- Gendt, G., and J. Kouba (2008), Quality and consistency of the IGS combined products, in *The International GNSS Service (IGS): Perspectives and Visions for 2010 and Beyond, Proceedings of the IGS Workshop 2006*, edited by T. Springer, G. Gendt, and J. Dow, European Space Operations Centre, European Space Agency, Darmstadt.
- Gipson, J. M. (1996), Very long baseline interferometry determination of neglected tidal terms in high-frequency Earth orientation variations, *Journal of Geophysical Research*, 101(B12), 28,051–28,064, doi:10.1029/96JB02292.
- Gordon, D., D. MacMillan, and K. Baver (2006), Calc 10 Implementation, in *International VLBI Service for Geodesy and Astrometry 2006 General Meeting Proceedings*, edited by D. Behrend and K. Baver, pp. 291–295, NASA/CP-2006-214140, NASA, Greenbelt.
- Görres, B., J. Campbell, M. Becker, and M. Siemes (2006), Absolute calibration of GPS antennas: laboratory results and comparison with field and robot techniques, *GPS Solutions*, 10(2), 136–145, doi:10.1007/s10291-005-0015-3.
- Gradinarsky, L., J. Johansson, H. Bouma, H.-G. Scherneck, and G. Elgered (2002), Climate monitoring using GPS, *Physics and Chemistry of the Earth*, 27(4-5), 335–340, doi:10.1016/S1474-7065(02)00009-8.
- Gross, R. (1993), The effect of ocean tides on the Earth's rotation as predicted by the results of an ocean tide model, *Geophysical Research Letters*, 20(4), 293–296, doi:10.1029/93GL00297.
- Gross, R. (2007), Combinations of Earth orientation measurements: SPACE2006, COMB2006, and POLE2006, *JPL Publication 07-5*, Jet Propulsion Laboratory, Pasadena, California.
- Gross, R., I. Fukumori, and D. Menemenlis (2003), Atmospheric and oceanic excitation of the Earth's wobbles during 1980–2000, *Journal of Geophysical Research*, 108(B8), doi:10.1029/2002JB002143.
- Gross, R., I. Fukumori, D. Menemenlis, and P. Gegout (2004), Atmospheric and oceanic excitation of length-of-day variations during 1980–2000, *Journal of Geophysical Research*, 109(B01406), doi:10.1029/2003JB002432.
- Gross, R., I. Fukumori, and D. Menemenlis (2005), Atmospheric and oceanic excitation of decadal-scale Earth orientation variations, *Journal of Geophysical Research*, 110, B09405, doi:10.1029/2004JB003565.
- Groten, E. (2000), Report of Special Commission 3 of IAG, in *Towards Models and Constants for Sub-Microarcsecond Astrometry, Proceedings of IAU Colloquium*, vol. 180, edited by K. Johnston, D. McCarthy, B. Luzum, and G. Kaplan, pp. 337–352.
- Guinot, B. (2002), Comparisons of "old" and "new" concepts: Celestial Ephemeris Origin (CEO), Terrestrial Ephemeris Origin (TEO), Earth Rotation Angle (ERA), in *Proceedings of the IERS Workshop on the Implementation of the New IAU Resolutions, IERS Technical Note*, vol. 29, edited by N. Capitaine, N. Gambis, D. McCarthy, G. Petit, J. Ray, B. Richter, M. Rothacher, E. Standish, and J. Vondrak, pp. 45–50, Verlag des Bundesamtes für Kartographie, Frankfurt am Main.
- Haas, R., and J. Wunsch (2006), Sub-diurnal earth rotation variations from the VLBI CONT02 campaign, *Journal of Geodynamics*, 41(1-3), 94–99, doi:10.1016/j.jog.2005.08.025.
- Haas, R., G. Elgered, L. Gradinarsky, and J. Johansson (2003), Assessing long term trends in the atmospheric water vapor content by combining data from VLBI, GPS, radiosondes and microwave radiometry, in *Proceedings of the 16th Working Meeting on European VLBI for Geodesy and Astrometry*, edited by W. Schwegmann and V. Thorandt, pp. 279–288, Bundesamt für Kartographie und Geodäsie.
- Hartinger, H., and F. Brunner (1998), Signal distortion in high precision GPS surveys, *Survey Review*, 34, 531–541.
- Hatanaka, Y., M. Sawada, A. Horita, M. Kusaka, J. Johnson, and C. Rocken (2001), Calibration of antenna-radome and monument-multipath effect of GEONET - Part 2: Evaluation of the phase map by GEONET data, *Earth Planets Space*, 53(1), 23–30.
- Heflin, M., D. Argus, D. Jefferson, F. Webb, and J. Zumberge (2002), Comparison of a GPS-defined global reference frame with ITRF2000, *GPS Solutions*, 6(1-2), 72–75, doi:10.1007/s10291-002-0015-5.
- Hefty, J., M. Rothacher, T. Springer, R. Weber, and G. Beutler (2000), Analysis of the first year of Earth rotation parameters with a sub-daily resolution gained at the CODE processing center of the IGS, *Journal of Geodesy*, 74(6), 479–487, doi:10.1007/s001900000108.

- Heinkelmann, R., J. Boehm, H. Schuh, S. Bolotin, G. Engelhardt, D. MacMillan, M. Negusini, E. Skurikhina, V. Tesmer, and O. Titov (2007), Combination of long time-series of troposphere zenith delays observed by VLBI, *Journal of Geodesy*, 81(6-8), 483–501, doi:10.1007/s00190-007-0147-z.
- Heiskanen, W., and H. Moritz (1967), *Physical Geodesy*, W. H. Freeman and Company, San Francisco.
- Herring, T. (1992), Modeling atmospheric delays in the analysis of space geodetic data, in *Publications on Geodesy (New Series)*, vol. 36, edited by J. de Munck and T. Spoelstra, pp. 157–164, Netherlands Geodetic Commission, Delft, ISBN: 90 6132 243 X.
- Herring, T., and D. Dong (1994), Measurement of diurnal and semidiurnal rotational variations and tidal parameters of Earth, *Journal of Geophysical Research*, 99(B9), 18,051–18,071, doi:10.1029/94JB00341.
- Herring, T., C. Gwinn, and I. Shapiro (1986), Geodesy by radio interferometry: Studies of the forced nutations of the Earth - data analysis, *Journal of Geophysical Research*, 91(B5), 4745–4754, doi:10.1029/JB091iB05p04745.
- Herring, T., B. Buffet, P. Mathews, and I. Shapiro (1991), Forced nutations of the Earth: Influence of inner core dynamics - 3. Very long interferometry data analysis, *Journal of Geophysical Research*, 96(B5), 8259–8273, doi:10.1029/90JB02177.
- Herring, T., P. Mathews, and B. Buffet (2002), Modeling of nutation-precession: Very long baseline interferometry results, *Journal of Geophysical Research*, 107(B4), doi:10.1029/2001JB000165.
- Hofmann-Wellenhof, B., H. Lichtenegger, and J. Collins (2001), *GPS – Theory and Practice*, Springer, Berlin, ISBN: 3-211-83534-2.
- Hreinsdóttir, S., J. Freymueller, H. Fletcher, C. Larsen, and R. Bürgmann (2003), Coseismic slip distribution of the 2002 MW7.9 Denali fault earthquake, Alaska, determined from GPS measurements, *Geophysical Research Letters*, 30(13), 1670, doi:10.1029/2003GL017447.
- Hugentobler, U., T. Springer, S. Schaer, G. Beutler, H. Bock, R. Dach, D. Ineichen, L. Mervart, M. Rothacher, U. Wild, A. Wiget, E. Brockmann, G. Weber, H. Habrich, and C. Boucher (2000), CODE IGS analysis center technical report 1999, in *International GPS Service for Geodynamics 1999 Technical Reports*, edited by K. Gowey, R. Neilan, and A. Moore, IGS Central Bureau, Jet Propulsion Laboratory, Pasadena, California.
- Hugentobler, U., S. Schaer, T. Springer, G. Beutler, H. Bock, R. Dach, D. Ineichen, L. Mervart, M. Rothacher, U. Wild, A. Wiget, E. Brockmann, G. Weber, H. Habrich, and C. Boucher (2001), CODE IGS analysis center technical report 2000, in *International GPS Service 2000 Technical Report*, edited by K. Gowey, R. Neilan, and A. Moore, IGS Central Bureau, Jet Propulsion Laboratory, Pasadena, California.
- Hugentobler, U., D. Ineichen, and G. Beutler (2003), GPS satellites: radiation pressure, attitude and resonance, *Advances in Space Research*, 31(8), 1917–1926, doi:10.1016/S0273-1177(03)00174-1.
- Hugentobler, U., S. Schaer, G. Beutler, H. Bock, R. Dach, A. Jäggi, M. Meindl, C. Urschl, L. Mervart, M. Rothacher, U. Wild, A. Wiget, E. Brockmann, D. Ineichen, G. Weber, H. Habrich, and C. Boucher (2004), CODE IGS analysis center technical report 2002, in *International GPS Service 2001-2002 Technical Report*, edited by K. Gowey, R. Neilan, and A. Moore, IGS Central Bureau, Jet Propulsion Laboratory, Pasadena, California.
- Hugentobler, U., S. Schaer, R. Dach, M. Meindl, and C. Urschl (2005a), Routine processing of combined solutions for GPS and GLONASS at CODE, in *Celebrating a Decade of the International GPS Service, Workshop and Symposium 2004*, edited by M. Meindl, Astronomical Institute, University of Bern, Bern, Switzerland, published on CD-ROM.
- Hugentobler, U., S. Schaer, R. Dach, M. Meindl, C. Urschl, and G. Beutler (2005b), GNSS geocenter for precise point positioning, *Geophysical Research Abstracts*, 7, sRef-ID: 1607-7962/gra/EGU05-A-09651.
- Hugentobler, U., M. Meindl, G. Beutler, H. Bock, R. Dach, A. Jäggi, C. Urschl, L. Mervart, M. Rothacher, S. Schaer, E. Brockmann, D. Ineichen, A. Wiget, U. Wild, G. Weber, H. Habrich, and C. Boucher (2008), CODE IGS analysis center technical report 2003/2004, in *International GNSS Service 2003-2004 Technical Reports*, IGS Central Bureau, Jet Propulsion Laboratory, Pasadena, California.
- ICD-GPS-200 (2000), Interface Control Document - Navstar GPS Space Segment/Navigation User Interfaces, *Tech. Rep. ICD-GPS-200, Revision C*, published on behalf of the Department of Defense by ARNIC Research Corp., available at <http://www.navcen.uscg.gov/pubs/gps/icd200/icd200cw1234.pdf>.
- IS-GPS-200 (2004), Interface Specification - Navstar GPS Space Segment/Navigation User Interfaces, *Tech. Rep. IS-GPS-200, Revision D*, published on behalf of the Department of Defense by ARNIC Research Corp., available at <http://www.navcen.uscg.gov/gps/geninfo/IS-GPS-200D.pdf>.
- Jaldehyag, R., J. Johansson, J. Davis, and P. Elosegui (1996), Geodesy using the Swedish permanent GPS network: Effects of snow accumulation on estimates of site positions, *Geophysical Research Letters*, 23(13), 1601–1604, doi:10.1029/96GL00970.

- Jefferson, D., M. Heflin, and R. Muellerschoen (2001), Examining the C1-P1 pseudorange bias, *GPS Solutions*, 4(4), 25–30, doi:10.1007/PL00012862.
- Johansson, J., J. Davis, H.-G. Scherneck, G. Milne, M. Vermeer, J. Mitrovica, R. Bennett, B. Jonsson, G. Elgered, P. Elósegui, H. Koivula, M. Poutanen, B. Rönnäng, and I. Shapiro (2002), Continuous GPS measurements of postglacial adjustment in Fennoscandia: 1. geodetic results, *Journal of Geophysical Research*, 107(B8), 2157, doi:10.1029/2001JB000400.
- Kammeyer, P. (2000), A UT1-like quantity from analysis of GPS orbit planes, *Celestial Mechanics and Dynamical Astronomy*, 77(4), 241–272, doi:10.1023/A:1011105908390.
- Kaniuth, K. (2005), Co- and post-seismic displacements of permanent GPS stations associated with the December 26, 2004 and March 28, 2005 Sumatra earthquakes, *ZfV*, 130(5), 324–328.
- Kaniuth, K., and P. Häfele (2002), Subsidence of the permanent GPS Station Bogota, in *Vertical Reference Systems, International Association of Geodesy Symposia*, vol. 124, edited by H. Drewes, A. Dodson, L. Fortes, L. Sanchez, and P. Sandoval, pp. 56–59, Springer, Berlin, Heidelberg, New York, ISBN: 3-540-43011-3.
- Kaniuth, K., and S. Huber (2003), An assessment of radome effects on height estimation in the EUREF network, in *EUREF Publication No. 12: Report on the Symposium of the IAG Sub-commission for Europe (EUREF) held in Ponta Delgada, 5 - 8 June 2002*, edited by J. A. Torres and H. Hornik, Mitteilungen des Bundesamtes für Kartographie und Geodäsie Band 29, pp. 97–102, Frankfurt am Main, ISBN: 3-89888-873-8.
- Kaniuth, K., H. Müller, and W. Seemüller (2002), Displacement of the space geodetic observatory Arequipa due to recent earthquakes, *ZfV*, 127(4), 238–243.
- Kaniuth, K., K. Stuber, and S. Vetter (2005), Sensitivität von GPS-Höhenbestimmungen gegen Akkumulation von Schnee auf der Antenne, *Allgemeine Vermessungs-Nachrichten*, 112(8-9), 290–295.
- Kaplan, E. D., and C. J. Hegarty (2006), *Understanding GPS: principles and applications*, 2nd ed., Artech House, Boston, London, ISBN: 1-58053-894-0.
- Kedar, S., H. Hajj, B. Wilson, and M. Heflin (2003), The effect of the second order GPS ionospheric correction on receiver positions, *Geophysical Research Letters*, 30(16), 1829, doi:10.1029/2003GL017639.
- Kenyeres, A., and C. Bruyninx (2004), EPN coordinate time series monitoring for reference frame maintenance, *GPS Solutions*, 8(4), 200–209, doi:10.1007/s10291-004-0104-8.
- Kierulf, H. P., H.-P. Plaa, R. M. Bingley, N. Teferle, C. Demir, A. Cingozc, H. Yildiz, J. Garate, J. M. Davila, C. G. Silva, R. Zdunek, L. Jaworski, J. J. Martinez-Benjamin, R. Orus, and A. Aragon (2008), Comparison of GPS analysis strategies for high-accuracy vertical land motion, *Physics and Chemistry of the Earth*, 33(3-4), 194–204, doi:10.1016/j.pce.2006.11.003.
- Kiser, K., and S. H. Vaughan (1998), GPS IIR joins the GPS constellation, in *Proceedings of ION GPS-98*, pp. 1915–1923, Nashville, Tennessee.
- Koch, K.-R. (1999), *Parameter Estimation and Hypothesis Testing in Linear Models*, 2nd ed., Springer, Berlin, Heidelberg, New York, ISBN: 3540652574.
- Kouba, J. (2002), Relativistic time transformations in GPS, *GPS Solutions*, 5(4), 1–9, doi:10.1007/PL00012907.
- Kouba, J. (2005a), A possible detection of the 26 December 2004 great Sumatra-Andaman Islands earthquake with solution products of the International GNSS Service, *Studia Geophysica et Geodaetica*, 49(4), 463–483, doi:10.1007/s11200-005-0022-4.
- Kouba, J. (2005b), Comparison of polar motion with oceanic and atmospheric angular momentum time series for 2-day to Chandler periods, *Journal of Geodesy*, 79(1-3), 33–42, doi:10.1007/s00190-005-0440-7.
- Kouba, J. (2008), Implementation and testing of the gridded Vienna Mapping Function 1 (VMF1), *Journal of Geodesy*, 82(4-5), 193–205, doi:10.1007/s00190-007-0170-0.
- Kouba, J. (2009), A simplified yaw-attitude model for eclipsing GPS satellites, *GPS Solutions*, 13(1), 1–12, doi:10.1007/s10291-008-0092-1.
- Kouba, J., and Y. Mireault (1999), 1998 Analysis Coordinator report, in *International GPS Service for Geodynamics 1998 Technical Reports*, edited by K. Gowey, R. Neilan, and A. Moore, IGS Central Bureau, Jet Propulsion Laboratory, Pasadena, California.
- Kouba, J., and J. Vondrak (2005), Comparison of length of day with oceanic and atmospheric angular momentum series, *Journal of Geodesy*, 79(4-5), 256–268, doi:10.1007/s00190-005-0467-9.
- Kouba, J., Y. Mireault, G. Beutler, T. Springer, and G. Gendt (1998a), A discussion of IGS solutions and their impact on geodetic and geophysical applications, *GPS Solutions*, 2(2), 3–15, doi:10.1007/PL00000034.

- Kouba, J., J. Ray, and M. Watkins (1998b), IGS reference frame realization, in *Proceedings IGS 1998 Analysis Center Workshop*, edited by J. Dow, H. Kouba, and T. Springer, pp. 139–171, European Space Operations Centre, European Space Agency, Darmstadt.
- Krügel, M., V. Tesmer, D. Angermann, D. Thaller, M. Rothacher, and R. Schmid (2004), CONT02 campaign - combination of VLBI and GPS, in *International VLBI Service for Geodesy and Astrometry 2004 General Meeting Proceedings*, edited by N. R. Vandenberg and K. D. Baver, pp. 418–422, NASA/CP-2004-212255, NASA, Greenbelt.
- Krügel, M., D. Thaller, V. Tesmer, M. Rothacher, D. Angermann, and R. Schmid (2007), Tropospheric parameters: combination studies based on homogeneous VLBI and GPS data, *Journal of Geodesy*, *81*(6-8), 515–527, doi:10.1007/s00190-006-0127-8.
- Kuzin, S., S. Revnivkyh, and S. Tatevyan (2007), GLONASS as a key element of the Russian Positioning Service, *Advances in Space Research*, *39*(10), 1539–1544, doi:10.1016/j.asr.2007.04.073.
- Lambeck, K. (1988), The Earth's variable rotation: some geophysical causes, in *The Earth's rotation and reference frames for geodesy and geodynamics: 128th Symposium of the International Astronomical Union*, edited by A. K. Babcock and G. A. Wilkins, pp. 1–20, Kluwer Academic Publishers, ISBN: 90-227-2657-4.
- Larsen, G. C., and K. S. Hansen (2004), Database on wind characteristics, IEA R&D Wind Annex XVII, *Risø National Laboratory, Risø-R-1472(N)*, Roskilde, Denmark, ISBN: 87-550-3357-1.
- Lavallée, D. A., T. van Dam, G. Blewitt, and P. J. Clarke (2006), Geocenter motions from GPS: A unified observation model, *Journal of Geophysical Research*, *111*, B05405, doi:10.1029/2005JB003784.
- Le Bail, K. (2006), Estimating the noise in space-geodetic positioning: the case of DORIS, *Journal of Geodesy*, *80*(8-11), 541–565, doi:10.1007/s00190-006-0088-y.
- Losinski, J. J. (2000), Operational response to an aging Global Positioning System constellation, in *Proceedings of ION-GPS 2000*, pp. 2543–2546, Salt Lake City.
- Luzum, B., J. Ray, M. Carter, and F. Josties (2001), Recent improvements to IERS Bulletin A combination and prediction, *GPS Solutions*, *4*(3), 34–40, doi:10.1007/PL00012853.
- Macmillan, S., S. Maus, T. Bondar, A. Chambodut, V. Golovkov, R. Holme, B. Langlais, V. Lesur, F. Lowes, H. Lühr, W. Mai, M. Manda, N. Olsen, M. Rother, T. Sabaka, A. Thomson, and I. Wardinski (2003), The 9th-Generation International Geomagnetic Reference Field, *Geophysical Journal International*, *155*(3), 1051–1056, doi:10.1111/j.1365-246X.2003.02102.x.
- Mader, G. (1999), GPS antenna calibration at the National Geodetic Survey, *GPS Solutions*, *3*(1), 50–58, doi:10.1007/PL00012780.
- Marini, J. (1972), Correction of satellite tracking data for an arbitrary tropospheric profile, *Radio Science*, (7), 223–231.
- Marquis, W., and D. Reigh (2005), On-orbit performance of the improved GPS Block IIR antenna panel, in *Proceedings of ION GNSS 2005*, Long Beach, California.
- Mathews, P., T. Herring, and B. Buffett (2002), Modeling of nutation and precession: New nutation series for nonrigid Earth and insights into the Earth's interior, *Journal of Geophysical Research*, *107*(B4), 2068, doi:10.1029/2001JB000390.
- McCarthy, D., and G. Petit (2004), IERS Conventions (2003), *IERS Technical Note 32*, Verlag des Bundesamtes für Kartographie und Geodäsie, Frankfurt am Main.
- Meindl, M., S. Schaer, U. Hugentobler, and G. Beutler (2004), Tropospheric gradient estimation at CODE: Results from global solutions, *Journal of the Meteorological Society of Japan*, *82*(1B), 331–338, doi:10.2151/jmsj.2004.331.
- Melbourne, W. G. (1985), The case for ranging in GPS based geodetic systems, in *Proceedings of the First International Symposium on Precise Positioning with the Global Positioning System*, edited by C. Goad, pp. 373–386, U.S. Department of Commerce, Rockville, Maryland.
- Mendes Cerveira, P., R. Weber, and H. Schuh (2007), The instantaneous Earth rotation - still inaccessible?, *Österreichische Zeitschrift für Vermessung und Geoinformation*, *95*(2), 113–120.
- Menge, F., G. Seeber, C. Völkens, G. Wübbena, and M. Schmitz (1998), Results of absolute field calibration of GPS antenna PCV, in *Proceedings of ION GPS-98*, pp. 31–38, Nashville, Tennessee.
- Mervart, L. (1995), Ambiguity resolution techniques in geodetic and geodynamic applications of the Global Positioning System, *Geodätisch-geophysikalische Arbeiten in der Schweiz*, *53*, Zürich, Switzerland.
- Mervart, L. (2000), Combining of Global Positioning System solutions, 2nd Ph.D. thesis, TU Prague.

- Miller, A. (1976), The climate of Chile, in *Climates of Central and South America, World Survey of Climatology*, vol. 12, edited by W. Schwerdtfeger, pp. 113–145, Elsevier, Amsterdam-Oxford-New York.
- Mireault, Y., and J. Kouba (1999), IGS Earth rotation parameters, *GPS Solutions*, 3(1), 59–72, doi:10.1007/PL00012781.
- Miyazaki, S., K. Larson, K. Choi, K. Hikima, K. Koketsu, P. Bodin, J. Haase, G. Emore, and A. Yamagiwa (2004), Modeling the rupture process of the 2003 September 25 Tokachi-Oki (Hokkaido) earthquake using 1-Hz GPS data, *Geophysical Research Letters*, 31, L21603, doi:10.1029/2004GL021457.
- Montenbruck, O., and E. Gill (2000), *Satellite Orbits: Models, Methods, Applications*, 1st ed., Springer, Berlin, Heidelberg, New York, ISBN: 3-540-67280-X.
- Moore, A. W., and R. E. Neilan (2005), The International GPS Service tracking network: Enabling diverse studies and projects through international cooperation, *Journal of Geodynamics*, 40(4-5), 461–469, doi:10.1016/j.jog.2005.10.009.
- Morel, L., and P. Willis (2005), Terrestrial reference frame effects on global sea level rise determination from TOPEX/Poseidon altimetric data, *Advances in Space Research*, 36(3), 358–368, doi:10.1016/j.asr.2005.05.113.
- Mueller, I. (1993), Planning an international service using the Global Positioning System (GPS) for geodynamic applications, in *Permanent Satellite Tracking Networks for Geodesy and Geodynamics, International Association of Geodesy Symposia*, vol. 109, edited by G. Mader, pp. 1–22, Springer, Berlin, Heidelberg, New York, ISBN: 3-540-55827-6.
- Munekane, H., M. Tobita, and K. Takashima (2004), Groundwater-induced vertical movements observed in Tsukuba, Japan, *Geophysical Research Letters*, 31, L12608, doi:10.1029/2004GL020158.
- Negusini, M., and P. Tomasi (2005), Water vapour content and variation estimated at European VLBI sites, in *Proceedings of the 17th Working Meeting on European VLBI for Geodesy and Astrometry*, edited by M. Vennebusch and A. Nothnagel, pp. 84–89.
- Neilan, R., W. Melbourne, and G. Mader (1989), The development of a global GPS tracking system in support of space and ground-based GPS programs, in *Global Positioning System: An Overview, International Association of Geodesy Symposia*, vol. 102, edited by Y. Bock and N. Leppard, pp. 165–178, Springer, Berlin, Heidelberg, New York, ISBN: 3-540-97266-8.
- Newby, S. (1992), An assessment of empirical models for the prediction of the transionospheric propagation delay of radio signals, M.Sc.E. thesis, University of New Brunswick.
- Niell, A. (1996), Global mapping functions for the atmosphere delay at radio wavelengths, *Journal of Geophysical Research*, 101(B2), 3227–3246, doi:10.1029/95JB03048.
- Niell, A. (2000), Improved atmospheric mapping functions for VLBI and GPS, *Earth Planets Space*, 52(10), 699–702.
- Niell, A. E. (2001), Preliminary evaluation of atmospheric mapping functions based on numerical weather models, *Physics and Chemistry of the Earth, Part A*, 26(6-8), 475–480, doi:10.1016/S1464-1895(01)00087-4.
- Nikolaidis, R. (2002), Observation of geodetic and seismic deformation with the Global Positioning System, Ph.D. thesis, University of California, San Diego.
- Owen, S., G. Anderson, D. Agnew, H. Johnson, K. Hurst, R. Reilinger, Z.-K. Shen, J. Svarc, and T. Baker (2002), Early postseismic deformation from the 16 October 1999 Mw 7.1 Hector Mine, California, earthquake as measured by survey-mode GPS, *Bulletin of the Seismological Society of America*, 92, 1423–1432, doi:10.1785/0120000930.
- Pacione, R., E. Fionda, R. Ferrera, R. Lanotte, C. Sciarretta, and F. Vespe (2002), Comparison of atmospheric parameters derived from GPS, VLBI and a ground-based microwave radiometer in Italy, *Physics and Chemistry of the Earth*, 27(4-5), 309–316, doi:10.1016/S1474-7065(02)00005-0.
- Parkinson, B., and J. J. Spilker (1996), Global Positioning System: Theory and applications, in *Progress in Astronautics and Aeronautics*, vol. 163, Washington.
- Pavlis, E. (1996), The laser retroreflector experiment on GPS-35 and 36, in *GPS trends in precise terrestrial, airborne and spaceborne applications, International Association of Geodesy Symposia*, vol. 115, edited by G. Beutler, G. W. Hein, W. G. Melbourne, and G. Seeber, pp. 154–158, Springer, Berlin, Heidelberg, New York, ISBN: 3-540-60872-9.
- Pavlis, E. (2005), Earth orientation parameters from Satellite Laser Ranging, in *14th International Workshop on Laser Ranging, Boletín ROA*, vol. 5/2005, edited by J. Garate, J. Davila, C. Noll, and M. Pearlman, pp. 128–140, Real Instituto y Observatorio de la Armada, San Fernando.
- Pearlman, M., C. Noll, W. Gurtner, and R. Noomen (2007), The International Laser Ranging Service and its support for GGOS, in *Dynamic Planet - Monitoring and Understanding a Dynamic Planet with Geodetic and Oceanographic Tools, International Association of Geodesy Symposia*, vol. 130, edited by P. Tregoning and C. Rizos, pp. 741–748, Springer, Berlin, Heidelberg, New York, doi:10.1007/978-3-540-49350-1_106, ISBN: 3-540-49349-5.

- Pearlman, M. R., J. J. Degnan, and J. M. Bosworth (2002), The International Laser Ranging Service, *Advances in Space Research*, 30(2), 125–143, doi:10.1016/S0273-1177(02)00277-6.
- Petrov, L. (2007), The empirical Earth rotation model from VLBI observations, *Astronomy and Astrophysics*, 467, 359–369, doi:10.1051/0004-6361:20065091.
- Petrov, L., and J.-P. Boy (2004), Study of the atmospheric pressure loading signal in very long baseline interferometry observations, *Journal of Geophysical Research*, 109, B03405, doi:10.1029/2003JB002500.
- Ponte, R., and A. Ali (2002), Rapid ocean signals in polar motion and length of day, *Geophysical Research Letters*, 29(15), doi:10.1029/2002GL015312.
- Poutanen, M., J. Jokela, M. Ollikainen, H. Koivula, M. Bilker, and H. Virtanen (2005), Scale variations of GPS time series, in *A Window on the Future of Geodesy, International Association of Geodesy Symposia*, vol. 128, edited by F. Sanso, pp. 15–20, Springer, Berlin, Heidelberg, New York, doi:10.1007/3-540-27432-4_3, ISBN: 3-540-24055-1.
- Press, W., and G. Rybicki (1989), Fast algorithm for spectral analysis of unevenly sampled data, *The Astrophysical Journal*, 338, 277–280.
- Rajan, J. A., and J. A. Tracy (2002), GPS IIR-M: Modernizing the signal-in-space, in *Proceedings of ION GPS 2002*, Portland, Oregon.
- Ray, J., D. Dong, and Z. Altamimi (2004), IGS reference frames: status and future improvements, *GPS Solutions*, 8(4), 251–266, doi:10.1007/s10291-004-0110-x.
- Ray, J., J. Kouba, and Z. Altamimi (2005), Is there utility in rigorous combinations of VLBI and GPS Earth orientation parameters?, *Journal of Geodesy*, 79(9), 505–511, doi:10.1007/s00190-005-0007-7.
- Ray, J., D. Crump, and M. Chin (2007), New global positioning system reference station in Brazil, *GPS Solutions*, 11(1), 1–10, doi:10.1007/s10291-006-0032-x.
- Ray, J., Z. Altamimi, X. Collilieux, and T. Dam (2008), Anomalous harmonics in the spectra of GPS position estimates, *GPS Solutions*, 12(1), 55–64, doi:10.1007/s10291-007-0067-7.
- Ray, R. (1999), A global ocean tide model from Topex/Poseidon altimetry: GOT99.2, *Technical Memorandum 209478*, NASA.
- Ray, R. D., D. Steinberg, B. Chao, and D. Cartwright (1994), Diurnal and semidiurnal variations in the Earth's rotation rate induced by oceanic tides, *Science*, 264, 830–832, doi:10.1126/science.264.5160.830.
- Rideout, W., and A. Coster (2006), Automated GPS processing for global total electron content data, *GPS Solutions*, 10(3), 219–228, doi:10.1007/s10291-006-0029-5.
- Rivers, M. H. (2000), 2 SOPS anomaly resolution on an aging constellation, in *Proceedings of ION GPS-2000*, pp. 2547–2550, Salt Lake City, Utah.
- Rogers, G., and H. Dragert (2003), Episodic tremor and slip on the cascadia subduction zone: The chatter of silent slip, *Science*, 300(5627), 1942–1943, doi:10.1126/science.1084783.
- Rothacher, M. (2001), Comparison of absolute and relative antenna phase center variations, *GPS Solutions*, 4(4), 55–60, doi:10.1007/PL00012867.
- Rothacher, M. (2002), Estimation of station heights with GPS, in *Vertical Reference Systems, International Association of Geodesy Symposia*, vol. 124, edited by H. Drewes, A. Dodson, L. Fortes, L. Sanchez, and P. Sandoval, pp. 81–90, Springer, Berlin, Heidelberg, New York, ISBN: 3-540-43011-3.
- Rothacher, M., R. Weber, E. Brockmann, G. Beutler, L. Mervart, U. Wild, A. Wiget, C. Boucher, S. Botton, and H. Seeger (1995), Annual report 1994 of the CODE processing center of the IGS, in *International GPS Service for Geodynamics 1994 Annual Report*, edited by J. Zumberge, R. Liu, and R. Neilan, IGS Central Bureau, Jet Propulsion Laboratory, Pasadena, California.
- Rothacher, M., G. Beutler, E. Brockmann, L. Mervart, S. Schaer, T. Springer, U. Wild, A. Wiget, C. Boucher, and H. Seeger (1996), Annual report 1995 of the CODE analysis center of the IGS, in *International GPS Service for Geodynamics 1995 Annual Report*, edited by J. Zumberge, M. Urban, R. Liu, and R. Neilan, IGS Central Bureau, Jet Propulsion Laboratory, Pasadena, California.
- Rothacher, M., T. Springer, S. Schaer, G. Beutler, E. Brockmann, U. Wild, A. Wiget, C. Boucher, S. Botton, and H. Seeger (1997), Annual report 1996 of the CODE analysis center of the IGS, in *International GPS Service for Geodynamics 1996 Annual Report*, edited by J. Zumberge, D. Fulton, and R. Neilan, IGS Central Bureau, Jet Propulsion Laboratory, Pasadena, California.
- Rothacher, M., T. Springer, S. Schaer, and G. Beutler (1998a), Processing strategies for regional GPS networks, in *Advances in Positioning and Reference Frames, International Association of Geodesy Symposia*, vol. 118, edited by F. Brunner, pp. 93–100, Springer, Berlin, Heidelberg, New York, ISBN: 3-540-64604-3.

- Rothacher, M., T. Springer, S. Schaer, G. Beutler, D. Ineichen, U. Wild, A. Wiget, C. Boucher, S. Botton, and H. Seeger (1998b), Annual report 1997 of the CODE analysis center of the IGS, in *International GPS Service for Geodynamics 1997 Technical Reports*, edited by I. Mueller, R. Neilan, and K. Gowey, IGS Central Bureau, Jet Propulsion Laboratory, Pasadena, California.
- Rothacher, M., G. Beutler, T. A. Herring, and R. Weber (1999a), Estimation of nutation using the Global Positioning System, *Journal of Geophysical Research*, *104*(B3), 4835–4859, doi:10.1029/1998JB900078.
- Rothacher, M., T. Springer, G. Beutler, R. Dach, U. Hugentobler, D. Ineichen, S. Schaer, U. Wild, A. Wiget, E. Brockmann, C. Boucher, E. Reinhart, and H. Habrich (1999b), Annual report 1998 of the CODE analysis center of the IGS, in *International GPS Service for Geodynamics 1998 Technical Reports*, edited by K. Gowey, R. Neilan, and A. Moore, IGS Central Bureau, Jet Propulsion Laboratory, Pasadena, California.
- Rothacher, M., G. Beutler, R. Weber, and J. Hefty (2001), High-frequency variations in Earth rotation from Global Positioning System data, *Journal of Geophysical Research*, *106*(B7), 13,711–13,738, doi:10.1029/2000JB900393.
- Rothacher, M., V. Lechner, and W. Schlüter (2005), Local monitoring of a fundamental GPS site, in *Celebrating a Decade of the International GPS Service, Workshop and Symposium 2004*, edited by M. Meindl, Astronomical Institute, University of Bern, Bern, Switzerland, published on CD-ROM.
- Rülke, A., R. Dietrich, M. Fritsche, M. Rothacher, and P. Steigenberger (2008), Realization of the Terrestrial Reference System by a reprocessed global GPS network, *Journal of Geophysical Research*, *113*, B08403, doi:10.1029/2007JB005231.
- Rummel, R., M. Rothacher, and G. Beutler (2005), Integrated Global Geodetic Observing System (IGGOS) science rationale, *Journal of Geodynamics*, *40*(4-5), 357–362, doi:10.1016/j.jog.2005.06.003.
- Saastamoinen, J. (1973), Contributions to the theory of atmospheric refraction, *Bulletin Geodesique*, *107*, 13–34, doi:10.1007/BF02522083.
- Salstein, D., D. Kann, A. Miller, and R. Rosen (1993), The sub-bureau for atmospheric angular momentum of the International Earth Rotation Service: A meteorological data center with geodetic applications, *Bulletin of the American Meteorological Society*, *74*(1), 67–80.
- Salstein, D., J. Nastula, K. Quinn, D. MacMillan, and P. Mendes Cerveira (2008), Atmospheric excitation on Earth rotation/polar motion at high temporal resolution, in *Proceedings of the Journées 2007 Systèmes de Référence Spatio-Temporels*, edited by N. Capitaine, pp. 177–179, Observatoire de Paris.
- Schaer, S. (1999), Mapping and predicting the Earth's ionosphere using the Global Positioning System, *Geodätisch-geophysikalische Arbeiten in der Schweiz*, *59*, Zürich, Switzerland.
- Scherneck, H.-G. (1991), A parametrized solid Earth tide model and ocean loading effects for global geodetic base-line measurements, *Geophysical Journal International*, *106*(3), 677–694, doi:10.1111/j.1365-246X.1991.tb06339.x.
- Scherneck, H.-G., J. Johansson, H. Koivula, T. Dam, and J. Davis (2003), Vertical crustal motion observed in the BIFROST project, *Journal of Geodynamics*, *35*(4-5), 524–441, doi:10.1016/S0264-3707(03)00005-X.
- Schillak, S. (2004), Analysis of the process of the determination of station coordinates by the satellite laser ranging based on results of the Borowiec SLR station in 1993.5 - 2000.5, Part 1: Performance of the Satellite Laser Ranging, *Artificial Satellites*, *39*(3), 217–263.
- Schlüter, W., and D. Behrend (2007), The International VLBI Service for Geodesy and Astrometry (IVS): current capabilities and future prospects, *Journal of Geodesy*, *81*(6-8), 379–384, doi:10.1007/s00190-006-0131-z.
- Schlüter, W., E. Himwich, A. Nothnagel, N. Vandenberg, and A. Whitney (2002), IVS and its important role in the maintenance of the global reference systems, *Advances in Space Research*, *30*(2), 145–150, doi:10.1016/S0273-1177(02)00278-8.
- Schmid, R., and M. Rothacher (2003), Estimation of elevation-dependent satellite antenna phase center variations of GPS satellites, *Journal of Geodesy*, *77*(7-8), 440–446, doi:10.1007/s00190-003-0339-0.
- Schmid, R., M. Rothacher, D. Thaller, and P. Steigenberger (2005), Absolute phase center corrections of satellite and receiver antennas: Impact on global GPS solutions and estimation of azimuthal phase center variations of the satellite antenna, *GPS Solutions*, *9*(4), 283–293, doi:10.1007/s10291-005-0134-x.
- Schmid, R., P. Steigenberger, G. Gendt, M. Ge, and M. Rothacher (2007), Generation of a consistent absolute phase center correction model for GPS receiver and satellite antennas, *Journal of Geodesy*, *81*(12), 781–798, doi:10.1007/s00190-007-0148-y.
- Seidelmann, P. K. (1992), *Explanatory supplement to the astronomical almanac*, University Science Books, Mill Valley, California, ISBN: 0-935702-68-7.

- Snajdrova, K., J. Boehm, P. Willis, R. Haas, and H. Schuh (2005), Multi-technique comparison of tropospheric zenith delays derived during the CONT02 campaign, *Journal of Geodesy*, 79(10-11), 613–623, doi:10.1007/s00190-005-0010-z.
- Solheim, F., J. Vivekanandan, R. Ware, and C. Rocken (1999), Propagation delays induced in GPS signals by dry air, water vapor, hydrometeors, and other particulates, *Journal of Geophysical Research*, 104(D8), 9663–9670, doi:10.1029/1999JD900095.
- Sovers, O. J., J. L. Fanselow, and C. S. Jacobs (1998), Astrometry and geodesy with radio interferometry: experiments, models, results, *Reviews of Modern Physics*, 70(4), 1393–1454, doi:10.1103/RevModPhys.70.1393.
- Springer, T. (2000), Modelling and validating orbits and clocks using the Global Positioning System, *Geodätisch-geophysikalische Arbeiten in der Schweiz*, 60, Zürich, Switzerland.
- Standish, E. (1998), JPL planetary and lunar ephemerides, DE405/LE405, *Interoffice Memorandum IOM 312.F-98-048*, JPL, Pasadena, California.
- Steigenberger, P., M. Rothacher, R. Dietrich, M. Fritsche, A. Rülke, and S. Vey (2006), Reprocessing of a global GPS network, *Journal of Geophysical Research*, 111, B05402, doi:10.1029/2005JB003747.
- Steigenberger, P., V. Tesmer, M. Krügel, D. Thaller, R. Schmid, S. Vey, and M. Rothacher (2007), Comparisons of homogeneously reprocessed GPS and VLBI long time-series of troposphere zenith delays and gradients, *Journal of Geodesy*, 81(6-8), 503–514, doi:10.1007/s00190-006-0124-y.
- Szeliga, W., T. I. Melbourne, M. M. Miller, and V. M. Santillan (2004), Southern Cascadia episodic slow earthquakes, *Geophysical Research Letters*, 31, L16602, doi:10.1029/2004GL020824.
- Tapley, B., M. Watkins, J. Ries, G. Davis, R. Eanes, S. Poole, H. Rim, B. Schutz, C. Shum, R. Nerem, F. Lerch, J. Marshall, S. Klosko, N. Pavlis, and R. Williamson (1996), The Joint Gravity Model 3, *Journal of Geophysical Research*, 101(B12), 28,029–28,049, doi:10.1029/96JB01645.
- Tesmer, V., and H. Kutterer (2004), An advanced stochastic model for VLBI observations and its application to VLBI data analysis, in *International VLBI Service for Geodesy and Astrometry 2004 General Meeting Proceedings*, edited by N. Vandenberg and K. Baver, pp. 296–300, NASA/CP-2004-212255, NASA, Greenbelt.
- Tesmer, V., H. Kutterer, and H. Drewes (2004), Simultaneous estimation of a TRF, the EOP and a CRF, in *International VLBI Service for Geodesy and Astrometry 2004 General Meeting Proceedings*, edited by N. Vandenberg and K. Baver, pp. 311–314, NASA/CP-2004-212255, NASA, Greenbelt.
- Tesmer, V., J. Boehm, R. Heinkelmann, and H. Schuh (2006), Impact of analysis options on the TRF, CRF and position time series estimated from VLBI, in *International VLBI Service for Geodesy and Astrometry 2006 General Meeting Proceedings*, edited by D. Behrend and K. Baver, pp. 243–251, NASA/CP-2006-214140, NASA, Greenbelt.
- Tesmer, V., J. Boehm, R. Heinkelmann, and H. Schuh (2007), Effect of different tropospheric mapping functions on the TRF, CRF and position time-series estimated from VLBI, *Journal of Geodesy*, 81(6-8), doi:10.1007/s00190-006-0126-9.
- Teunissen, P. J., and A. Kleusberg (Eds.) (1998), *GPS for Geodesy*, Springer, Berlin, ISBN: 3-540-63661-7.
- Thaller, D., R. Dill, M. Krügel, P. Steigenberger, M. Rothacher, and V. Tesmer (2006), CONT02 analysis and combination of long EOP series, in *Observation of the Earth system from space*, edited by J. Flury, R. Rummel, C. Reigber, M. Rothacher, G. Boedecker, and U. Schreiber, pp. 389–411, Springer, Berlin Heidelberg New York, doi:10.1007/3-540-29522-4_26, ISBN: 3-540-29520-8.
- Thaller, D., M. Krügel, M. Rothacher, V. Tesmer, R. Schmid, and D. Angermann (2007), Combined Earth orientation parameters based on homogeneous and continuous VLBI and GPS data, *Journal of Geodesy*, 81(6-8), 529–541, doi:10.1007/s00190-006-0115-z.
- Titov, O., V. Tesmer, and J. Boehm (2004), Occam v6.0 software for VLBI data analysis, in *International VLBI Service for Geodesy and Astrometry 2004 General Meeting Proceedings*, edited by N. R. Vandenberg and K. D. Baver, pp. 267–271, NASA/CP-2004-212255, NASA, Greenbelt.
- Torge, W. (2001), *Geodesy*, deGruyter, Berlin, New York, ISBN: 3-11-017072-8.
- Tregoning, P., and T. Herring (2006), Impact of a priori zenith hydrostatic delay errors on GPS estimates of station heights and zenith total delays, *Geophysical Research Letters*, 33, L23303, doi:10.1029/2006GL027706.
- Tregoning, P., and T. van Dam (2005), Effects of atmospheric pressure loading and seven-parameter transformations on estimates of geocenter motion and station heights from space geodetic observations, *Journal of Geophysical Research*, 110, B03408, doi:10.1029/2004JB003334.
- Tregoning, P., P. Morgan, and R. Coleman (2004), The effect of receiver firmware upgrades on GPS vertical timeseries, in *Cahiers du Centre Europeen du Geodynamique et de Seismologie*, vol. 23, pp. 37–46.

- Urschl, C., W. Gurtner, U. Hugentobler, S. Schaer, and G. Beutler (2005), Validation of GNSS orbits using SLR observations, *Advances in Space Research*, 36(3), 412–417, doi:10.1016/j.asr.2005.03.021.
- Urschl, C., G. Beutler, W. Gurtner, U. Hugentobler, and S. Schaer (2007), Contribution of SLR tracking data to GNSS orbit determination, *Advances in Space Research*, 39(10), 1515–1523, doi:10.1016/j.asr.2007.01.038.
- Urschl, C., G. Beutler, W. Gurtner, U. Hugentobler, and S. Schaer (2008), Validation of GNSS orbits using SLR observations, in *The International GNSS Service (IGS): Perspectives and Visions for 2010 and Beyond, Proceedings of the IGS Workshop 2006*, edited by T. Springer, G. Gendt, and J. Dow, European Space Operations Centre, European Space Agency, Darmstadt.
- van Dam, T., and J. Wahr (1987), Displacements of the Earth's surface due to atmospheric loading: Effects on gravity and baseline measurements, *Journal of Geophysical Research*, 92(B2), 1281–1286, doi:10.1029/JB092iB02p01281.
- Vennebusch, M., S. Böckmann, and A. Nothnagel (2007), The contribution of Very Long Baseline Interferometry to ITRF2005, *Journal of Geodesy*, 81(6-8), 553–564, doi:10.1007/s00190-006-0117-x.
- Vey, S., R. Dietrich, M. Fritsche, A. Rülke, M. Rothacher, and P. Steigenberger (2006), Influence of mapping function parameters on global GPS network analyses: Comparisons between NMF and IMF, *Geophysical Research Letters*, 33, L01814, doi:10.1029/2005GL024361.
- Violet, M., J. Crum, J. Carberry, M. Drake, R. Smetek Jr., M. O'Brine, S. Hutsell, F. Mueller, and J. Saffel (1999), Navigation accuracy or satellite health? Controlling momentum on aging GPS satellites, in *Proceedings of ION GPS-99*, pp. 2269–2279, Nashville, Tennessee.
- Viron, O. d., G. Schwarzbaum, F. Lott, and V. Dehant (2005), Diurnal and subdiurnal effects of the atmosphere on the Earth rotation and geocenter motion, *Journal of Geophysical Research*, 110, B11404, doi:10.1029/2005JB003761.
- Vondrak, J., C. Ron, and R. Weber (2003), Combined VLBI/GPS series of precession-nutation and comparison with IAU2000 model, *Astronomy and Astrophysics*, 397, 771–776, doi:10.1051/0004-6361:20021523.
- Watkins, M., and R. Eanes (1994), Diurnal and semidiurnal variations in Earth orientation determined from LAGEOS laser ranging, *Journal of Geophysical Research*, 99(B9), 18,073–18,080, doi:10.1029/94JB00805.
- Wdowinski, S., Y. Bock, G. Baer, L. Prawirodirdjo, N. Bechor, S. Naaman, R. Knafo, Y. Forrai, and Y. Melzer (2004), GPS measurements of current crustal movements along the Dead Sea Fault, *Journal of Geophysical Research*, 109, B05403, doi:10.1029/2003JB002640.
- Wu, J., S. Wu, G. Hajj, W. Bertiger, and S. Lichten (1993), Effects of antenna orientation on GPS carrier phase, *Manuscripta Geodaetica*, 18, 91–98.
- Wübbena, G. (1985), Software developments for geodetic positioning with GPS using TI-4100 code and carrier measurements, in *Proceedings of the First International Symposium on Precise Positioning with the Global Positioning System*, edited by C. Goad, pp. 403–412, U.S. Department of Commerce, Rockville, Maryland.
- Wübbena, G., M. Schmitz, F. Menge, V. Böder, and G. Seeber (2000), Automated absolute field calibration of GPS antennas in real-time, in *Proceedings of ION GPS-2000*, pp. 2512–2522, Salt Lake City, Utah.
- Wünsch, J. (1991), Small waves in UT1 caused by inequality of the equatorial moments of inertia A and B of the Earth, *Astronomische Nachrichten*, 312(5), 321–325, doi:10.1002/asna.2113120510.
- Xu, G. (2003), *GPS: Theory, Algorithms and Applications*, Springer, Berlin, ISBN: 3-540-67812-3.
- Yinger, C. H. (2002), Operation and application of the Global Positioning System, *Crosslink - The Aerospace Corporation magazine of advances in aerospace technology, Summer 2002*, 12–16.
- Zarraoa, N., W. Mai, E. Sardón, and A. Jungstand (1998), Preliminary evaluation of the Russian GLONASS system as a potential geodetic tool, *Journal of Geodesy*, 72(6), 356–363, doi:10.1007/s001900050175.
- Zeimetz, P., and H. Kuhlmann (2006), Systematic effects in absolute chamber calibration of GPS antennas, *Geomatica*, 60(3), 267–274.
- Zhu, S. Y., and E. Groten (1988), Relativistic effects in GPS, in *GPS-techniques Applied to Geodesy and Surveying, Lecture Notes in Earth Sciences*, vol. 19, edited by E. Groten and R. Strauß, pp. 41–46, Springer, Berlin, Heidelberg, New York, ISBN: 3-540-50267-X.
- Zhu, S. Y., C. Reigber, and Z. Kang (1997), Apropos laser tracking to GPS satellites, *Journal of Geodesy*, 71(7), 423–431, doi:10.1007/s001900050110.
- Zhu, S. Y., F.-H. Massmann, and C. Reigber (2003), Satellite antenna phase center offsets and scale errors in GPS solutions, *Journal of Geodesy*, 76, 668–672, doi:10.1007/s00190-002-0294-1.

- Ziebart, M., S. Edwards, S. Adhya, A. Sibthroe, P. Arrowsmith, and P. Cross (2004), High precision GPS IIR orbit prediction using analytical non-conservative force models, in *Proceedings of ION GNSS 2004*, pp. 1764–1770, Long Beach, California.
- Ziebart, M., A. Sibthroe, P. Cross, Y. Bar-Sever, and B. Haines (2007), Cracking the GPS - SLR orbit anomaly, in *Proceedings of ION GNSS 2007*, pp. 2033–2038, Fort Worth, Texas.
- Zumberge, J., D. Jefferson, M. Hefflin, and F. Webb (1994), Earth orientation results from the Jet Propulsion Laboratory using GPS, *IERS Technical Note, 17*, P-43 – P-47.

An excerpt of Sec. 7 has been published in:

Steigenberger, P., M. Rothacher, M. Fritsche, A. Rülke, and R. Dietrich (2009), Quality of reprocessed GPS satellite orbits, *Journal of Geodesy*, 83(3-4), 241–248, doi: 10.1007/s00190-008-0228-7.

Acknowledgments

First of all I'd like to thank Markus Rothacher for initiating and supervising the [TUM/TUD GPS](#) reprocessing project that provided the basis for this thesis. His detailed knowledge of the Bernese [GPS](#) Software and of global [GPS](#) solutions was substantial for setting up the processing scheme and analyzing the results. Many thanks to Urs Hugentobler who offered me the chance to come back to Munich and finish my thesis at the same institute where I have started it. I am grateful to Robert Weber for the acceptance to co-examine this thesis. I'd like to thank the [CODE IGS](#) Analysis Center team in Bern, in particular Rolf Dach and Stefan Schaer, for their support. The work of Axel Rülke and Mathias Fritsche from the project partner Technische Universität Dresden was essential for the success of the [TUM/TUD](#) reprocessing project. Special thanks go to Mathias Fritsche for proof-reading this thesis. Volker Tesmer ([DGFI](#) Munich) computed the [DGFI VLBI](#) solutions, initiated many interesting discussions and delivered Augustiner to Potsdam. Dan MacMillan provided the [GSFC](#) subdaily [ERP](#) series. Ralf Schmid (Technische Universität München) implemented the estimation of satellite antenna [PCV](#)s in the Bernese [GPS](#) Software, compiled the [TUM](#) antenna phase center models, and helped to improve the English of parts of this thesis. Johannes Böhm (Vienna University of Technology) provided the [ECMWF](#) data for [IMF](#), [VMF1](#), the hydrostatic a priori delays as well as many fruitful discussions. F. B. Madsen ([DNSC](#) Copenhagen), M. Ramatschi ([GFZ](#) Potsdam) and C. Vigny ([CNRS](#) Paris) provided additional [GPS](#) raw data. The [LRZ](#) Linux cluster administrators supported the setup of the processing and the computation of the reprocessed [GPS](#) solutions. The efforts of the [IGS](#), the [ILRS](#) and the [IVS](#) in providing space geodetic observation data are acknowledged. The project "Interpretation globaler geodynamischer Prozesse anhand homogener Langzeitreihen reprozessierter [GPS](#)-Daten" was funded by Deutsche Forschungsgemeinschaft ([DFG](#)).

Curriculum Vitae

Name	Peter Steigenberger
Date of birth	4 August 1976
Place of birth	Gräfelfing, Germany
Nationality	German

Education

Sep. 1983 – Jul. 1987	Grundschule Planegg, Germany
Sep. 1987 – Jul. 1996	Feodor-Lynen-Gymnasium Planegg, Germany
Jun. 1996	Graduated with Abitur

Civilian Service

Aug. 1996 – Aug. 1997	Emergency Medical Services, Malteser Hilfsdienst Gräfelfing, Germany
-----------------------	--

Studies

Nov. 1997 – May 2002	Technische Universität München, Germany: Vermessungswesen (Geodesy and Geoinformation)
Sep. 2002 – May 2002	Diploma thesis: MATLAB Toolbox zur TOPEX/POSEIDON Altimeterdatenverarbeitung
May 2002	Graduated with a Dipl.-Ing. degree (M.Sc.)

Professional Positions

Jun. 2002 – Sep. 2002	Scientific collaborator at Institut für Astronomische und Physikalische Geodäsie, Technische Universität München
Oct. 2002 – Nov. 2005	Scientific collaborator at Forschungseinrichtung Satellitengeodäsie, Technische Universität München
Nov. 2005 – Sep. 2007	Scientific collaborator at GeoForschungsZentrum Potsdam
Since Oct. 2007	Scientific assistant at Institut für Astronomische und Physikalische Geodäsie, Technische Universität München